

Patch-Clamp Analysis

Advanced Techniques

Edited by

Wolfgang Walz
Alan A. Boulton
Glen B. Baker



HUMANA PRESS



NEUROMETHODS ■ 35

Series Editors: Alan A. Boulton and Glen B. Baker

Patch-Clamp Analysis

NEUROMETHODS

Series Editors: *Alan A. Boulton and Glen B. Baker*

37. **Apoptosis Techniques and Protocols**, Second Edition, edited by *Andréa C. LeBlanc*, 2002
36. **Neural Transplantation Methods**, edited by *Stephen B. Dunnett, Alan A. Boulton, and Glen B. Baker*, 2000
35. **Patch-Clamp Analysis: Advanced Techniques**, edited by *Wolfgang Walz, Alan A. Boulton, and Glen B. Baker*, 2002
34. **Cell Neurobiology Techniques**, edited by *Alan A. Boulton, Glen B. Baker, and Alan N. Bateson*, 1999
33. **Molecular Neurobiology Techniques**, edited by *Alan A. Boulton, Glen B. Baker, and Alan N. Bateson*, 1999
32. **In Vivo Neuromethods**, edited by *Alan A. Boulton, Glen B. Baker, and Alan N. Bateson*, 1998
31. **G Protein Methods and Protocols: Role of G Proteins in Psychiatric and Neurological Disorders**, edited by *Ram K. Mishra, Glen B. Baker, and Alan A. Boulton*, 1997
30. **Regulatory Protein Modification: Techniques and Protocols**, edited by *Hugh C. Hemmings, Jr.*, 1997
29. **Apoptosis Techniques and Protocols**, edited by *Judes Poirier*, 1997
28. **Transgenic Xenopus: Microinjection Methods and Developmental Neurobiology**, by *Shlomo Seidman and Hermona Soreq*, 1997
27. **Voltammetric Methods in Brain Systems**, edited by *Alan A. Boulton, Glen B. Baker, and Ralph N. Adams*, 1995
26. **Patch-Clamp Applications and Protocols**, edited by *Alan A. Boulton, Glen B. Baker, and Wolfgang Walz*, 1995
25. **Neurotrophic Factors**, edited by *Alan A. Boulton, Glen B. Baker, and Franz Hefti*, 1993
24. **Animal Models of Drug Addiction**, edited by *Alan A. Boulton, Glen B. Baker, and Peter Wu*, 1992
23. **Practical Cell Culture Techniques**, edited by *Alan A. Boulton, Glen B. Baker, and Wolfgang Walz*, 1992
22. **Animal Models of Neurological Disease, II: Metabolic Encephalopathies and the Epilepsies**, edited by *Alan A. Boulton, Glen B. Baker, and Roger F. Butterworth*, 1992
21. **Animal Models of Neurological Disease, I: Neurodegenerative Disease**, edited by *Alan A. Boulton, Glen B. Baker, and Roger F. Butterworth*, 1992
20. **Intracellular Messengers**, edited by *Alan A. Boulton, Glen B. Baker, and Colin W. Taylor*, 1992
19. **Animal Models in Psychiatry, II**, edited by *Alan A. Boulton, Glen B. Baker, and Mathew T. Martin-Iverson*, 1991
18. **Animal Models in Psychiatry, I**, edited by *Alan A. Boulton, Glen B. Baker, and Mathew T. Martin-Iverson*, 1991
17. **Neuropsychology**, edited by *Alan A. Boulton, Glen B. Baker, and Merrill Hiscock*, 1990
16. **Molecular Neurobiological Techniques**, edited by *Alan A. Boulton, Glen B. Baker, and Anthony T. Campagnoni*, 1990
15. **Neurophysiological Techniques: Applications to Neural Systems**, edited by *Alan A. Boulton, Glen B. Baker, and Case H. Vanderwolf*, 1990
14. **Neuropsychological Techniques: Basic Methods and Concepts**, edited by *Alan A. Boulton, Glen B. Baker, and Case H. Vanderwolf*, 1990
13. **Psychopharmacology**, edited by *Alan A. Boulton, Glen B. Baker, and Andrew J. Greenshaw*, 1989
12. **Drugs as Tools in Neurotransmitter Research**, edited by *Alan A. Boulton, Glen B. Baker, and Augusto V. Juorio*, 1989
11. **Carbohydrates and Energy Metabolism**, edited by *Alan A. Boulton, Glen B. Baker, and Roger F. Butterworth*, 1989
10. **Analysis of Psychiatric Drugs**, edited by *Alan A. Boulton, Glen B. Baker, and Ronald T. Coutts*, 1988
9. **The Neuronal Microenvironment**, edited by *Alan A. Boulton, Glen B. Baker, and Wolfgang Walz*, 1988
8. **Imaging and Correlative Physicochemical Techniques**, edited by *Alan A. Boulton, Glen B. Baker, and Donald P. Boisvert*, 1988
7. **Lipids and Related Compounds**, edited by *Alan A. Boulton, Glen B. Baker, and Lloyd A. Horrocks*, 1988
6. **Peptides**, edited by *Alan A. Boulton, Glen B. Baker, and Quentin Pittman*, 1987
5. **Neurotransmitter Enzymes**, edited by *Alan A. Boulton, Glen B. Baker, and Peter H. Yu*, 1986
4. **Receptor Binding Techniques**, edited by *Alan A. Boulton, Glen B. Baker, and Pavel D. Hrdina*, 1986

NEUROMETHODS ■ 35

Patch-Clamp Analysis

ADVANCED TECHNIQUES

Edited by

Wolfgang Walz

University of Saskatchewan, Saskatoon, Canada

Alan A. Boulton

Alviva Biopharmaceuticals Inc., Saskatoon, Canada

Glen B. Baker

University of Alberta, Edmonton, Canada

HUMANA PRESS



TOTOWA, NEW JERSEY

© 2002 Humana Press Inc.
999 Riverview Drive, Suite 208
Totowa, New Jersey 07512

www.humanapress.com

All rights reserved. No part of this book may be reproduced, stored in a retrieval system, or transmitted in any form or by any means, electronic, mechanical, photocopying, microfilming, recording, or otherwise without written permission from the Publisher.

The content and opinions expressed in this book are the sole work of the authors and editors, who have warranted due diligence in the creation and issuance of their work. The publisher, editors, and authors are not responsible for errors or omissions or for any consequences arising from the information or opinions presented in this book and make no warranty, express or implied, with respect to its contents.

This publication is printed on acid-free paper. ∞

ANSI Z39.48-1984 (American National Standards Institute) Permanence of Paper for Printed Library Materials.

Production Editor: Kim Hoather-Potter.

Cover design by Patricia F. Cleary.

Cover illustration: From Fig. 2B in Chapter 4 "Combined Fluorometric and Electrophysiological Recordings," by Hartmut Schmidt and Jens Eilers, and from Fig. 5C in Chapter 5 "Patch-Clamp Techniques Applied to Brain Slices," by James R. Moyer, Jr. and Thomas H. Brown.

For additional copies, pricing for bulk purchases, and/or information about other Humana titles, contact Humana at the above address or at any of the following numbers: Tel: 973-256-1699; Fax: 973-256-8341; E-mail: humana@humanapr.com or visit our website at <http://humanapress.com>

Photocopy Authorization Policy:

Authorization to photocopy items for internal or personal use, or the internal or personal use of specific clients, is granted by Humana Press Inc., provided that the base fee of US \$10.00 per copy, plus US \$00.25 per page, is paid directly to the Copyright Clearance Center at 222 Rosewood Drive, Danvers, MA 01923. For those organizations that have been granted a photocopy license from the CCC, a separate system of payment has been arranged and is acceptable to Humana Press Inc. The fee code for users of the Transactional Reporting Service is: [1-58829-013-1/02 \$10.00 + \$00.25].

Printed in the United States of America. 10 9 8 7 6 5 4 3 2 1

ISBN 1-58829-013-1

ISSN 0893-2336

Preface to the Series

When the President of Humana Press first suggested that a series on methods in the neurosciences might be useful, one of us (AAB) was quite skeptical; only after discussions with GBB and some searching both of memory and library shelves did it seem that perhaps the publisher was right. Although some excellent methods books had recently appeared, notably in neuroanatomy, it was a fact that there was a dearth in this particular field, a fact attested to by the alacrity and enthusiasm with which most of the contributors to this series accepted our invitations and suggested additional topics and areas. After a somewhat hesitant start, essentially in the neurochemistry section, the series has grown and will encompass neurochemistry, neuropsychiatry, neurology, neuropathology, neurogenetics, neuroethology, molecular neurobiology, animal models of nervous disease, and no doubt many more “neuros.” Although we have tried to include adequate methodological detail and in many cases detailed protocols, we have also tried to include wherever possible a short introductory review of the methods and/or related substances, comparisons with other methods, and the relationship of the substances being analyzed to neurological and psychiatric disorders. Recognizing our own limitations, we have invited a guest editor to join with us on most volumes in order to ensure complete coverage of the field. These editors will add their specialized knowledge and competencies. We anticipate that this series will fill a gap; we can only hope that it will be filled appropriately and with the right amount of expertise with respect to each method, substance or group of substances, and area treated.

*Alan A. Boulton
Glen B. Baker*

Preface

Neher and Sakmann were the first to monitor the opening and closing of single ion channels in the membranes of cells by conductance measurements. In 1976, they used firepolished micropipets with a tip diameter of 3–5 μm to record currents from a small patch of the membrane of skeletal muscles, thereby decreasing background membrane noise. In order to reduce the dominant source of background noise, the leakage shunt under the pipet rim between membrane and glass, the muscle membrane had to be treated enzymatically. Despite these early limitations, a new technique was born—the patch-clamp. The final breakthrough came in 1981 when the same workers, in collaboration with Hamill, Marty, and Sigworth, developed the gigaohm seal. Not only did this improve the quality of recordings, it was now possible to gently pull the membrane patch with the attached pipet off the cell and study its trapped ion channels in isolation. Another offshoot of the gigaohm seal technique was the whole-cell patch-clamp technique, in which the path is ruptured without breaking the seal. This technique is really a sophisticated voltage-clamp technique and also allows for the altering of cytoplasmic constituents if the experimenter so wishes.

The first part of this treatise on *Patch-Clamp Analysis: Advanced Techniques* presents modern developments associated with the basic patch-clamp techniques outlined above. These chapters are supplemented with information on the newest developments in fast external solution switching to study fast inactivating responses as well as the switching of the pipet solution during recordings. The application of the patch pipet technique not only to clean membrane preparations, but also to brain or other tissue slices, was an important development in the last decade. Other offshoots of the patch pipet technique are the loose patch, the perforated patch, as well as the recording from macropatches and the patch-clamp detection technique. These are all introduced and described in detail. Perhaps the recent developments in the patch-clamp field with the biggest impact are the combination of two of the most powerful life science technologies: molecular biology and imaging. This led to the intertwining of the patch pipet with RT-PCR and fluorometric techniques.

The methods associated with the patch pipet are certain to become even more refined in the future, as new applications involving genomics, proteomics, and sophisticated imaging techniques emerge.

Wolfgang Walz
Alan A. Boulton
Glen B. Baker

Contents

Preface to the Series	<i>v</i>
Preface	<i>vii</i>
Contributors	<i>xi</i>
1. Technology of Patch-Clamp Electrodes <i>Richard A. Levis and James L. Rae</i>	<i>1</i>
2. Whole-Cell Patch-Clamp Recordings <i>Harald Sontheimer and Christopher B. Ransom</i>	<i>35</i>
3. Single-Channel Recording <i>David J. A. Wyllie</i>	<i>69</i>
4. Combined Fluorometric and Electrophysiological Recordings <i>Hartmut Schmidt and Jens Eilers</i>	<i>111</i>
5. Patch-Clamp Techniques Applied to Brain Slices <i>James R. Moyer, Jr. and Thomas H. Brown</i>	<i>135</i>
6. Perforated Patch-Clamp Technique <i>Raimondo D'Ambrosio</i>	<i>195</i>
7. Fast-Drug Application <i>Manfred Heckmann and Christian Pawlu</i>	<i>217</i>
8. Pipet Perfusion Methods: <i>Techniques and Applications</i> <i>Gea-Ny Tseng and Minoru Horie</i>	<i>231</i>
9. Patch-Cram Detection of Cyclic GMP in Intact Cells <i>Richard H. Kramer</i>	<i>245</i>
10. Loose-Patch Voltage-Clamp Technique <i>Blake D. Anson and William M. Roberts</i>	<i>265</i>
11. Recording from Macropatches <i>Frances Moody-Corbett and Mark Fry</i>	<i>287</i>
12. Combining Patch-Clamp Techniques with RT-PCR <i>Gerald Seifert, Albert Becker, and Christian Steinhäuser</i>	<i>301</i>
Index	<i>331</i>

Contributors

- BLAKE D. ANSON • *Department of Medicine/Cardiology, University of Wisconsin, Madison, WI*
- GLEN B. BAKER • *Department of Psychiatry, University of Alberta, Edmonton, Canada*
- ALBERT BECKER • *Institute of Neuropathology, University of Bonn, Bonn, Germany*
- ALAN A. BOULTON • *Alviva Biopharmaceuticals Inc., Saskatoon, Canada*
- THOMAS H. BROWN • *Department of Psychology, Yale University, New Haven, CT*
- RAIMONDO D'AMBROSIO • *Department of Neurosurgery, University of Washington, Seattle, WA*
- JENS EILERS • *Department of Neurophysiology, Max-Planck-Institute for Brain Research, Frankfurt, Germany*
- MARK FRY • *Department of Physiology, Dartmouth Medical School, Hanover, NH*
- MANFRED HECKMANN • *Institut für Physiologie, Albert-Ludwigs-Universität, Freiburg, Germany*
- MINORU HORIE • *Department of Cardiovascular Medicine, Kyoto University, Kyoto, Japan*
- RICHARD H. KRAMER • *Department of Molecular and Cell Biology, University of California, Berkeley, CA*
- RICHARD A. LEVIS • *Department of Physiology, Rush Medical College, Chicago, IL*
- FRANCES MOODY-CORBETT • *Division of Basic Medical Sciences, Memorial University of Newfoundland, St. John's, Canada*
- JAMES R. MOYER, JR. • *Department of Psychology, Yale University, New Haven, CT*
- CHRISTIAN PAWLU • *Institut für Physiologie, Albert-Ludwigs-Universität, Freiburg, Germany*
- JAMES L. RAE • *Department of Physiology, Mayo Foundation, Rochester, MN*
- CHRISTOPHER B. RANSOM • *Department of Neurobiology, University of Alabama, Birmingham, AL*
- WILLIAM M. ROBERTS • *Institute of Neuroscience, University of Oregon, Eugene, OR*

HARTMUT SCHMIDT • *Department of Neurophysiology, Max-Planck-Institute for Brain Research, Frankfurt, Germany*

GERALD SEIFERT • *Department of Neurosurgery, University of Bonn, Bonn, Germany*

HARALD SONTHEIMER • *Department of Neurobiology, University of Alabama, Birmingham, AL*

CHRISTIAN STEINHÄUSER • *Department of Neurosurgery, University of Bonn, Bonn, Germany*

GEA-NY TSENG • *Department of Physiology, Virginia Commonwealth University, Richmond, VA*

WOLFGANG WALZ • *Department of Physiology, University of Saskatchewan, Saskatoon, Canada*

DAVID J. A. WYLLIE • *Department of Neuroscience, University of Edinburgh, Edinburgh, UK*

1

Technology of Patch-Clamp Electrodes

Richard A. Levis and James L. Rae

1. Introduction

The extracellular patch voltage-clamp technique has allowed the currents through single ionic channels to be studied from a wide variety of cells. In its early form (Neher and Sakmann, 1976), the resolution of this technique was limited by the relatively low ($\sim 50 \text{ M}\Omega$) resistances that isolated the interior of the pipet from the bath. The high resolution that can presently be achieved with the patch-clamp technique originated with the discovery (Neher, 1981) that very high resistance (tens or even hundreds of $\text{G}\Omega$) seals can form between the cell membrane and the tip of a clean pipet when gentle suction is applied to the pipet interior. Although the precise mechanisms involved in this membrane-to-glass seal are still not fully understood, the importance of the gigaohm seal is obvious. The high resistance of the seal ensures that almost all of the current from the membrane patch flows into the pipet and to the input of the current-sensitive headstage preamplifier. It also allows the small patch of membrane to be voltage-clamped rapidly and accurately via the pipet, and the mechanical stability of the seal is vital to the whole-cell voltage-clamp technique. Of equal importance, the high resistance of the seal greatly reduces the noise it contributes to single-channel measurements. Although the seal can often represent only a small fraction of total patch-clamp noise (particularly as the bandwidth of recording increases), its importance should never be minimized. Without such high-resistance seals, most of the steady progress to reduce background noise levels would not have been possible.

From: *Neuromethods*, Vol. 35: *Patch-Clamp Analysis: Advanced Techniques*
Edited by: W. Walz, A. A. Boulton, and G. B. Baker @ Humana Press Inc., Totowa, NJ

Of course the patch pipet is not simply a tool in the formation of gigohm seals. The pipet serves as a fluid bridge that connects the current-sensitive headstage amplifier input to the surface or interior of the cell. The insulating properties (both resistive and more importantly capacitive) of the glass that forms the wall of the pipet are also crucial to the ability to measure current originating in the patch and to the background noise levels that can be achieved.

For any patch-clamp measurement, several steps are required to construct a proper glass electrode. First, a glass that has optimal properties is selected. The required properties differ substantially for single-channel recordings and whole-cell-current recordings. For single-channel measurements, low noise is the most important electrical parameter, whereas for whole-cell measurements dynamic performance is more important than the contribution of the electrode to the background noise. This is simply because the background noise in a whole-cell recording is dominated by the noise from the electrode resistance (actually the access resistance) in series with the capacitance of the entire cell. The dynamic bandwidth of a whole-cell recording also depends on the same factors. Therefore, the goal in constructing an electrode for whole-cell recording is simply to make it as blunt and as low in resistance as is compatible with sealing it to the cell. In single-channel recordings, the pipet is a major contributor to the background noise and so requires many subtle considerations to produce an electrode optimal for recording single-channel currents.

As a second step in pipet construction, the electrode glass stock is pulled into a pipet with a tip of optimal geometry. This geometry differs for whole-cell and single-channel recordings. In a third step, the outside wall of the pipet is coated with a hydrophobic elastomer possessing good electrical properties. This procedure is essential for low-noise single-channel recordings but can be done much less carefully for whole-cell recordings. Fourth, the tip is firepolished to round it and clean its surface of any thin film of elastomer coating. This step can also be used to adjust the final tip diameter. Firepolishing promotes seal formation but often is not required. After all these procedures, the electrode can be filled and used.

Several general properties of glasses must be considered when trying to construct optimal electrodes for patch clamping (*see* Table 1).

Table 1
Glass Properties

Glass	LF	Log ₁₀ vol. R.	Diel. const.	Softening temp. C°	Description
7940	.0038	11.8	3.8	1580	Quartz (fused silica)
1724	.0066	13.8	6.6	926	Aluminosilicate
7070	.25	11.2	4.1	—	Low-loss borosilicate
8161	.50	12.0	8.3	604	High lead
Sylgard	.58	13.0	2.9	—	#184 Coating compd.
7059	.584	13.1	5.8	844	Barium-borosilicate
7760	.79	9.4	4.5	780	Borosilicate
EG-6	.80	9.6	7.0	625	High lead
0120	.80	10.1	6.7	630	High lead
EG-16	.90	11.3	9.6	580	High lead
7040	1.00	9.6	4.8	700	Kovar seal borosilicate
KG-12	1.00	9.9	6.7	632	High lead
1723	1.00	13.5	6.3	910	Aluminosilicate
0010	1.07	8.9	6.7	625	High lead
S-8250	1.08	10.0	4.9	720	—
7052	1.30	9.2	4.9	710	Kovar seal borosilicate
EN-1	1.30	9.0	5.1	716	Kovar seal borosilicate
7720	1.30	8.8	4.7	755	Tungsten seal borosilicate
7056	1.50	10.2	5.7	720	Kovar seal borosilicate
3320	1.50	8.6	4.9	780	Tungsten seal borosilicate
7050	1.60	8.8	4.9	705	Series seal borosilicate
S-8330	1.70	8.0	4.6	820	—
KG-33	2.20	7.9	4.6	827	Kimax borosilicate
7740	2.60	8.1	5.1	820	Pyrex borosilicate
1720	2.70	11.4	7.2	915	Aluminosilicate
N-51A	3.70	7.2	5.9	785	Borosilicate
R-6	5.10	6.6	7.3	700	Soda lime
0080	6.50	6.4	7.2	695	Soda lime

Thermal properties determine the ease with which desired tip shapes can be produced and they determine how easily the tips can be heat-polished. Optical properties often result in a distinct visual endpoint so that tips can be firepolished the same way each time. Electrical properties are important determinants of the noise the glass produces in a recording situation and determine the size and number of components in the capacity transient following a change of potential across the pipet wall. Glasses are complex

substances composed of many compounds and most of their properties are determined to a first order by the composition of the glass used. Glass composition may also influence how easily a glass seals to membranes and whether or not the final electrode will contain compounds leached from the glass into the pipet-filling solution that can activate, inhibit, or block channel currents.

2. General Properties of Pipet Glass

Before proceeding to the details of electrode fabrication, it is useful to consider in more detail glass properties that are important for patch-clamp pipet construction. We will begin with thermal properties. It is important that glasses soften at a temperature that is easily and reliably achieved. This formerly was a stringent constraint because glasses like aluminosilicates, which melt at a temperature in excess of 900°C, would shorten the lifetime of a puller-heating filament so much that their use was unattractive. Quartz, which melts above 1600°C, could not even be pulled in commercially available pullers and so was not used at all. Today, at least one puller exists that will do these jobs easily (P-2000, Sutter Instruments) and so virtually any kind of glass can be used routinely. It is generally true that the lower the melting temperature of the glass, the more easily it can be firepolished. Low melting-temperature glasses such as those with high lead content can be pulled to have tip diameters in excess of 100 microns and still be firepolished to a small enough tip diameter that the pipet can be sealed to a 7–10 micron diameter cell. With such glasses, one has greater control over the final shape of the tip than is possible with higher melting-temperature borosilicate glasses. Quartz pipets cannot be firepolished with a usual firepolishing apparatus, although with care they can be firepolished in a temperature-controlled flame.

Electrical properties are most important for providing low noise as well as low amplitude, simple time-course capacity transients. As will be discussed later, it is not possible to achieve low background noise without an elastomer coating the outside of the pipet. In general, glasses with the lowest dissipation factors have minimal dielectric loss and produce the lowest noise. There is a wide variety of glasses to choose from that will produce acceptable single-channel recordings although quartz is clearly the best material to date. Good electrical glasses are also necessary for whole-cell recordings not because of noise properties but because they result in the simplest and most voltage and time-stable capacity transients.

Major chemical constituents in glass are important since they determine the overall properties of the glass and because they are potential candidates to leach from the glass into the pipet-filling solution where they can interact with the channels being studied. No glass can be deemed to be chemically inert since even tiny amounts of materials leached in the vicinity of the channels may produce sufficient local concentrations to interact with channels and other cellular processes. Again, quartz would be expected to have fewer chemical impurities than other glasses but every kind of glass should be suspected of having an effect on the channels being measured.

3. Whole-Cell Pipet Properties: Practical Aspects

3.1. Choice of Glass

Modern computerized pipet pullers are capable of pulling glass with almost any thermal properties (with the exception of quartz) into the proper blunt-tipped geometry that is ideal for whole-cell recording. Therefore, almost any glass can be used to form whole-cell pipets. Nevertheless, we feel that some types of glass should usually be avoided, while others have some particularly useful properties for this application.

Soda lime glasses like Kimble R-6 and Corning 080 should not generally be used because of their high dielectric loss. When a voltage step is applied across a patch pipet fabricated from one of these glasses, there will be a large slow component in the resulting capacity transient (Rae and Levis, 1992a). For a 2 mm depth of immersion with a moderate coating of Sylgard 184 to within $\sim 200\ \mu\text{m}$ of the tip we have found following a 200 mV voltage step that the slow component for a soda-lime pipet can be as large as 50 pA 1 msec after the beginning of the step. The slow tail of capacity current can still be as much as 10 pA 10 msec after the step and may require as much as 200 msec to decay to below 1 pA. The time course of this slow tail is not exponential, but more closely approaches a logarithmic function of time. In addition, we have observed that for soda-lime pipets the magnitude of the slow component of capacity current is not always constant during a series of pulses, which occur at rates faster than about 1–2/s. Instead, the magnitude of this component is sometimes observed to decrease with successive pulses. Because of these characteristics, these capacitive currents can possibly be mistaken for whole-cell currents. Heavy Sylgard

coating can reduce the amplitude of the slow component of capacity current for soda-lime glasses, but is generally better (and certainly more convenient) simply to use glasses with lower loss factors (for further discussion *see* Rae and Levis, 1992a).

High lead glasses such as 8161, EG-6, EG-16, 0010, 0120, and KG-12 possess much lower dissipation factors than soda-lime glasses and are particularly useful due to their low melting point. This property allows the construction of initially very large-tipped pipets, which can be subsequently fire-polished to blunt bullet-shaped tips offering the lowest possible access resistance. This, of course, minimizes series resistance. In addition, pipets of this shape also draw in the largest surface-area patch of membrane when suction is applied. This is useful in perforated-patch recordings since the larger area of membrane available for partitioning by amphotericin or nystatin results in the maximum incorporation of perforation channels and thus the lowest access resistance. KG-12 (Friedrich and Dimmock) is a good choice for glasses of this class since it seals well, has good electrical properties, and is readily available.

Pipets for whole-cell recording can be thin-walled by comparison to those for single-channel recording. In whole-cell measurements, other sources of noise far outweigh the contribution from the pipet per se (*see* Subheading 5.8. below). In terms of total background noise, the major consideration in pipet fabrication is simply achieving the lowest possible resistance. Glass with an OD/ID ratio of 1.2–1.4 will have lower resistance for a given outside tip diameter than will thicker-walled glass, and is therefore useful for whole-cell recording. Some precautions are necessary, however, since if the walls become too thin the pipet will more easily penetrate the cell during the attempt to form a seal.

Other glasses that have been successfully used by many laboratories for whole-cell recording include Pyrex (Corning #7740), Kimble's Kimax, and Corning #7056. Schott #8250 or #8330 are also good choices and readily available from Garner Glass (Claremont, CA). Although we usually prefer the high-lead glasses described earlier, these other glasses have produced perfectly acceptable results.

3.2. Pulling Whole-Cell Electrodes

This can be done on any commercially available electrode puller. Here one simply strives for as blunt a taper and as large a tip diameter as is compatible with sealing of the electrode to the cell.

3.3. Elastomer Coating Whole-Cell Electrodes

Elastomer coating of electrodes reduces electrode noise in single-channel recordings. In whole-cell recordings, the noise associated with electrode glass is usually insignificant in comparison to other noise sources and so elastomer coating is not required for noise reduction. Elastomer coating also reduces electrode capacitance. Commercial patch-clamp amplifiers have the ability to compensate about 10 pF of electrode capacitance. For pipets made from glasses with high dielectric constants (e.g., soda-lime and high-lead glasses) immersed deeply into a tissue-bathing solution, the electrode (and holder) capacitance may exceed the compensation range of the electronics. Elastomer coating will help to keep the total electrode capacitance within the compensation range. For whole-cell recordings, it is not usually necessary to paint the elastomer close to the tip. Coating that extends from the top of the shank to 1mm from the tip, is sufficient for whole-cell recordings. Many investigators do not use elastomer coating for whole-cell recordings.

3.4. Firepolishing Whole-Cell Electrodes

Finally to promote gigohm seals and to reduce the possibility of tip penetration into the cell during seal formation, electrode tips should be firepolished. In some cells, fire polishing has proven unnecessary but we have found that sealing is generally promoted by firepolishing the electrode tip, particularly for cells where seal formation is difficult. Whole-cell and single-channel electrodes are firepolished with the same basic apparatus. Fire polishing can be done either using an upright or an inverted microscope. In fact, many investigators have chosen to coat their pipets and firepolish them using an inverted microscope with a 40× or so long working-distance objective. Another very useful approach is to utilize a standard upright microscope equipped with an objective for metallurgical microscopes. Several microscope companies, (Nikon, Olympus, Zeiss) make extra long working-distance high-magnification metallurgical objectives. Most noteworthy are the 100× objectives that have 3–3.5 mm working distances and numerical apertures of 0.8. With these objectives and 15× eyepieces and with the electrode mounted on a slide held in the mechanical stage of the microscope, it is possible to move the electrode tip into the optical field and visualize directly the electrode tip at 1500× magnification. At such high magnifications, it is possible to fire-

polish the tip to a very distinct optical endpoint under direct visualization. This approach ensures very repeatable results from one electrode to the next. The only drawback is that the objectives are quite expensive. The firepolishing itself is accomplished by connecting to a micromanipulator a rod of inert material to which has been fastened a short loop of platinum iridium wire. The ends of this wire must be soldered to two other pieces of wire that can be connected to a voltage or current source to allow current to be passed through the platinum wire. The platinum loop is generally bent into a very fine hairpin so that it can be brought to within a few microns of the electrode tip under direct observation. Because of early reports that platinum can be sputtered from the wire onto the electrode tip and prevent sealing, the platinum wire is generally coated with a glass like Pyrex (Corning #7740) or Corning #7056 to prevent such sputtering. This is done by overheating the platinum wire and pushing against it a piece of electrode glass that has been pulled into an electrode tip. At high temperatures, the glass melts and flows over the platinum wire and ends up thoroughly coating it and forming a distinct bead of glass. If the elastomer has been coated too near the tip, firepolishing causes the tip to droop downward at the juncture where the coating ends. If one desires to paint elastomer extremely close to the tip, it may be necessary to do the majority of the firepolishing before coating and then firepolish lightly again afterwards. As a general rule, firepolishing with the electrode tip close to the heating wire at low temperature produces a tip whose inner walls are parallel and relatively close together. With a hotter heating element and the tip farther away, the tip tends to round more and end up quite blunt.

4. Patch Electrode Fabrication for Single-Channel Recording

4.1. Choice of Glass

There is a limited number of glasses available for single-channel patch clamping. Perhaps the most important feature to consider is the amount of noise in the recording that is due to the pipet itself. This subject is sufficiently important that we include an entire section dealing with noise sources in pipets in hopes that the reader will be able to use the principles to make optimal

pipets for their own recording situation. There is no longer any question, however, that quartz is the best glass if noise performance is important. Quartz itself is quite expensive and requires an expensive laser-based puller, and so probably is not the glass for routine studies. Therefore, we consider other glasses here as well. Garner Glass (Claremont, CA) has been particularly helpful in the development of specialty glasses for patch clamping, although they are no longer able to provide any of the high-lead glasses that we find so useful. Any glass tubing selected for the fabrication of single-channel patch electrodes should have walls of substantial thickness. Wall thickness results in decreased electrical noise and increased bluntness at the tip which prevents penetrating the cell during seal formation. Glass tubing with an OD/ID of 2.0–3.0 is easily obtainable and is expected to yield the lowest background noise levels. Generally, the outside diameter chosen is 1.5–1.7 mm. For single-channel recordings, only the glasses with the best electrical properties should be used if optimal noise performance is desired. Corning glasses #8161 and 7760 were particularly good in this regard but again Corning no longer makes them. Corning #7052 was also quite acceptable but also is not available. Sadly, most of the options for particularly low-noise glasses are running out and so quartz is expected to become increasingly more attractive even given its cost. Readily available glasses like Corning 7740 or Kimble's Kimax are not particularly quiet glasses. High-lead glasses like Kimble's KG-12 give better signal to noise than the Pyrex-type glasses but are substantially worse than the best glasses mentioned earlier. Schott #8250 is readily available and has thermal and noise properties about as good as Corning #7052. Low-noise recordings have also been obtained with Schott #8330 (Benndorf, 1995), a glass with electrical properties about midway between those of Corning #7740 and Schott #8250. For single-channel recordings, one should not choose a glass with a filament fused to the interior wall. Such a filament promotes filling but presumably serves as an internal conduit, which allows fluid to creep up the inside of the pipet even if the pipet has been vacuumed with a suction line. This fluid near the internal filament presumably serves as a noise source, much like the external fluid film that forms in the absence of elastomer coating.

In our experience, it is usually unnecessary to clean electrode glasses prior to pulling. On occasion, however, normally quiet pipet glasses are found to be noisy in use and then it is imperative

to clean the glass for best noise performance. Sonicating the glass in 100% ethanol or methanol in an ultrasonic cleaner is effective for this purpose. Following any cleaning procedure, it is a good idea to place the glass in an oven at around 200°C for 10–30 min to achieve complete drying. Heat treatment of this sort has also proven necessary if low-noise recordings are required in environments where the humidity is exceptionally high.

4.2. Pulling Single-Channel Electrodes

Single-channel pipets made from glasses other than quartz can be pulled on any commercially available patch-electrode puller. Here the tips can be less blunt and higher in resistance. In fact, they can be pulled with a single-stage pull so that the tips are almost perfectly conical. They look similar to tips that might be used for impaling cells although their resistance is 10–50 megOhms or so. The electrode resistance in series with the patch capacitance is a potential noise source (R_e - C_p noise', see Subheading 5.5. below). However, as will be seen, this source of noise may actually be minimized by using high resistance pipets in so far as such high-resistance correlates with small patch area. In addition, sharper tips taper often lead to higher-resistance seals to the membrane. Thus for best noise performance for single-channel recording, it is better not to use the blunt electrode tips that are good for whole-cell situations.

4.3. Coating Single-Channel Pipets with Elastomers

For the lowest-noise recordings, electrodes must be coated with a hydrophobic elastomer to within 100 microns or less of their tip. The closer it can be painted to the tip the better. This coating prevents bathing solution from forming a thin fluid film along the outer surface of the electrode. This thin film of bathing solution would be a substantial noise source. A commonly used compound is Sylgard #184 (Dow Corning, Midland, MI). Sylgard also has exceptional electrical properties (see Table 1) and so improves the electrical properties of most glasses when a thick coat covers the glass surface. Sylgard, meticulously mixed can be stored at -20°C in small-capped centrifuge tubes. The thorough mixing is required to prevent pockets of the compound not adequately exposed to polymerizer. This unpolymerized elastomer can flow to the electrode tip (even against gravity) and render the tips dif-

ficult to seal. At freezer temperatures, the mixed Sylgard can be stored for several weeks. A tube of this freezer-stored Sylgard, when brought to room temperature for use in painting electrodes, will last for several hours before it begins to polymerize. Care must be taken not to open the tube until the contents have reached room temperature to prevent water condensation. Condensed water can degrade the electrical properties of the elastomer and increase noise. The Sylgard is applied to the electrode tip with a small utensil such as a piece of capillary tubing pulled to a reasonably fine tip in a flame. Sylgard is applied using dissecting microscopes at magnifications of 10–30 \times . It is useful, but not required, to modify the dissecting microscope to work in dark field. This can be done inexpensively with a fiber optic ring illuminator connected to a fiber optic light source. The ring illuminator is placed under the stage of the microscope. 3–4 inches above the ring light, dark field illumination is achieved and the walls of the electrode glass show up as bright lines of light against a dark background. Both the Sylgard coat and the tip of the electrode are easily seen with this dark field illumination. The Sylgard must be directed away from the tip by gravity at all times during the painting procedure or the Sylgard may flow over the tip to make firepolishing and/or sealing impossible. The Sylgard can be cured by holding the tip for 5–10 seconds in the hot air stream emanating from a standard heat gun like those used in electronics to heat shrink tubing. Again, the Sylgard must be gravitationally directed away from the tip during this curing process.

While Sylgard is the most commonly used elastomer, there are a number of other elastomers available which are as good as Sylgard in most respects and better in others. RTV615A from General Electric has properties nearly identical to Sylgard and can be used in exactly the same way as is Sylgard. Dow Corning Medical Silastic MDX-4 has dielectric properties slightly better than Sylgard #184 but polymerizes more rapidly at freezer temperatures. To date, it has not offered any obvious improvement in noise on a day to day basis but several of the lowest noise measurements done with quartz electrodes utilized this elastomer. It is considerably more expensive than Sylgard #184. Dow Corning #R-6101 is another excellent elastomer which costs more to buy but probably not to use than Sylgard. R-6101 has the useful property that it does not polymerize appreciably at room temperature and so can be used for up to 12 months without freezing. Its noise properties are as good

(should be a little better) as Sylgard #184 and it does result in low noise when used with quartz or some other very good electrode glass. R-6101 is particularly useful because it does not require mixing and it can be partially cured in an oven to produce any desired viscosity. That viscosity remains quite stable, increasing only slightly over a time period of a year or so. Heating at 95°C for 48 h yields about as high a viscosity as one might desire. Lower temperature or shorter heating times give intermediate viscosities. Because R-6101 shows little tendency to run into the tip of the electrode, it is possible to coat the electrode and then cure the R-6101 in a hot air stream with the tip pointing down rather than up. This procedure results in a bulbous mass of the elastomer that is much thicker along the shank of the pipet than is possible by heat curing with the tip up. This approach is also helped by painting a thin ring of the elastomer as close to the tip as possible, curing it, and then painting the electrode shank with a much thicker layer of elastomer. When this thicker layer is cured tip down, there is very little tendency for the R-6101 to get into the tip and so thicker layers are possible near the tip than with most other coating schemes.

4.4. Firepolishing Single-Channel Pipets

The same principles apply here as in the firepolishing of whole-cell electrodes. The same apparatus is used for both. In general, patch electrodes are firepolished with the tip close to the heating filament with the goal of thickening the glass near the tip in addition to rounding it. For high-resistance seals, it may be useful to firepolish so that the internal walls of the tip become parallel for several microns. This mode of firepolishing will increase the tip resistance a few megohms but will often result in lower noise due to higher-resistance seals (see also discussion of “ R_e - C_p noise”).

4.5. Fabrication Methods Specific to Quartz

Quartz softens at about 1600°C and so no platinum- or nichrome wire-based heat source will melt it. Both of these materials disintegrate long before 1600°C is reached. It can be pulled in a flame but the tip geometry is unreliable with such fabrication techniques. The new laser-based P-2000 electrode puller from Sutter Instruments generates enough heat to pull quartz fairly easily. It begins to have trouble when the glass OD exceeds 1.5 mm. It has no diffi-

culty pulling quartz tubing with an OD/ID = 3 so long as the OD does not exceed 1.5 mm. Since the major reason to use quartz-patch pipets is for the reduction of single-channel background-noise currents, it is best to use quartz with as thick a wall as possible. 1.5 mm OD with 0.5 mm ID produces about the smallest bore that is practical. Even at 0.5 mm ID, there is some difficulty with the internal Ag-AgCl electrode because it must be made of such flimsy silver wire that it is often damaged (bent) or denuded of silver chloride as the electrode is placed into the small bore. IDs of 0.6–0.75 mm make the pipets much easier to use.

Quartz cannot easily be firepolished with any presently available commercial apparatus. Those that firepolish other glasses, including aluminosilicate, do not generate enough heat to firepolish quartz. It is possible to firepolish it in a carefully controlled Bunsen burner, but that approach is sufficiently unreliable that it is best to try to pull tips whose geometry is good enough to allow sealing without firepolishing. That places an additional constraint on the puller because most other glass pullers need only to produce electrode tips that are approximately correct, as the final tip geometry can be customized while firepolishing. With quartz, the tips must be good enough for use immediately after pulling.

Because of the noise produced by a thin-film bathing solution creeping up the outer surface of an electrode, quartz must be elastomer coated like any other glass. This bathing-solution film is such a large noise source that if an elastomer coating is not used to reduce it, there is absolutely no reason to use quartz electrodes for patch clamping. It will not perform appreciable better than poor glasses if this noise source is not eliminated or minimized. Because quartz must be elastomer-coated, it must also be subjected to the heat polisher. While the polisher cannot smooth or round the quartz tip as it does with other glasses, it can burn off any residual elastomer and so should be used with quartz electrodes just before filling.

4.6. Low-Noise Recording

Low noise recording requires meticulous attention to detail. Even with an electrode optimally pulled, coated, and firepolished, there are still many ways in which excess noise can creep in. It is important that the electrodes be filled only to just above the shank. Fluid in the back of the electrode can cause internal noise-

generating films and allow fluid into the holder. It is important for low-noise recordings that a suction line with a syringe needle the correct size to fit into the bore of the pipet be maintained near the experimental setup. This suction line can be used to vacuum fluid from the pipet and ensure none gets into the holder or coats the majority of the back of the electrode. Alternatively, silicone fluid or mineral oil can be used to fill the electrode for a short distance in back of its filling solution. These "oils" are somewhat messy and not really required if a proper suction line for "vacuuming" the electrode interior is used. The internal electrode should be adjusted in length until its tip just comfortably is immersed in the filling solution. In general, the shorter the length of the internal electrode (and of the pipet) the lower the noise will be. Therefore, it is best to use the shortest possible holder and electrode that is practical.

During experiments where low noise is required, it is best to test the noise at intermediate stages. Most modern patch-clamp amplifiers have an RMS noise meter that can be checked to determine the noise levels at any time. This meter should be checked immediately after inserting the electrode into the holder and placing the electrode tip over the bath but before actually immersing the tip in the bath. Poorly filled electrodes, fluid in the holder, a generally dirty holder, and pickup from the environment will show up as elevated noise. What the actual level of the noise will be depends on the noise of the patch clamp amplifier, the kind of holder and electrode glass being used, and on how well the worker has shielded against pickup of electrical interference. Specific examples appear in Levis and Rae, 1993. However, as a general rule, total noise in this situation should not be more than ~10–20% above that of the open-circuit headstage. If you see excess noise, you can remove the electrode, dry the internal electrode, and then test the noise with only the headstage and holder placed above the bath. If this is elevated above what is normal for your setup, either your holder is dirty or you are experiencing pickup from the environment. Environmental pickup can often be seen as noise spikes at discrete frequencies, whereas a dirty holder contributes noise across a broad range of frequencies. You can try to dry the holder by blowing dry, clean air through it, but it is possible that you will have to clean the holder before the noise will go down. This can be done by disassembling it, sonicating it in ethanol, and drying it for sev-

eral hours in an oven at 60–70°C. Because of the time involved in cleaning the holder, it is wise to have two or more holders available when attempting very low-noise recordings.

The noise of your electronics, holder, electrode glass, and elastomer can be determined by making a thin pad of Sylgard and placing it in the bottom of your chamber. You then seal your electrode to it much as you would sealing to a cell. No suction, however, is required to make the seal. You simply push the tip against the Sylgard and a seal forms. The seal should be 200 gigohms or more if you have done it correctly. Under these circumstances, the seal noise is essentially negligible and you are able to quantify the remaining composite noise sources. This noise will depend on how deep the bathing solution is: the deeper the bathing solution, the greater the noise. For most purposes, the bath depth need not be more than 1–3 mm. This simple procedure will let you know what is routinely possible with your setup and give you a baseline for comparing the noise you actually get in experiments. A good seal to a cell will often produce noise that is about the same as the noise you get sealed to Sylgard.

Note, however, that as soon as the electrode tip is placed in the bath, the noise will be enormous since you are now measuring at best the thermal noise of a 1–10 megohm resistance tip. The readings on the noise meter will not be meaningful until you have obtained a gigohm seal. If the seal resistance is <20 gigohms, the majority of the noise will be due to the seal and really low-noise recordings cannot be achieved.

5. Noise Properties of Patch Pipets

5.1. Noise Contribution of the Pipet

The earliest patch pipets were fabricated from “soft” soda-lime glasses. Such glasses were easy to pull and heat-polish to any desired tip geometry, primarily because they soften at relatively low temperatures. Unfortunately such pipets introduced relatively large amounts of noise into patch-clamp measurements. It was soon found that “hard” borosilicate glasses produced less noise, but, owing to their softening at higher temperatures, were somewhat more difficult to pull and heat-polish. Probably as a result of these early findings, it has sometimes been assumed that “hard” high melting-temperature glasses necessarily had better

electrical properties than “soft” low melting-temperature glasses. However, there is no obligatory relationship between the thermal and electrical properties of glass. For example, several low melting-temperature, high-lead glasses (e.g., 8161, EG-6) have been shown to produce less noise than a variety of high melting-temperature borosilicate and aluminosilicate glasses (e.g., 7740, 1720). The reason for these findings becomes clear when the electrical properties of the glasses are considered.

The electrical properties of glass that are important to its noise performance are its dielectric constant and its dissipation factor; the bulk resistivity of a glass might also be important, but is usually sufficiently high to be ignored. The dielectric constant of a substance is the ratio of its permittivity to the permittivity of a vacuum. Thus for pipets of equivalent geometry and depth of immersion, the higher the dielectric constant of the glass, the higher the pipet capacitance. The dielectric constants for glasses commonly used for patch pipet-fabrication range from 3.8 for quartz to more than 9 for some high-lead glasses. The dielectric constant of borosilicates is typically 4.5–6, while that of soda-lime glasses is near 7. The pipet capacitance generates noise by several mechanisms that will be described below. The dissipation factor is a measure of the lossiness of a dielectric material. Ideal capacitors display no dielectric loss and do not generate thermal noise. However, all real dielectrics are lossy and do produce thermal noise; we refer to this as dielectric noise. Glasses with the lowest dissipation factors are the least lossy and generate the least dielectric noise. Quartz is among the least lossy of all practical dielectrics; its dissipation factor, which is in the range of 10^{-5} – 10^{-4} , is far lower than that of other glasses used for patch pipets. Several high-lead glasses have dissipation factors of $\sim 10^{-3}$. The dissipation factor of borosilicates that have been successfully used to fabricate patch pipets varies from about 0.002–0.005. Soda-lime glasses have the highest dissipation factor (~ 0.01), which is the principal reason for their high noise.

The best glasses for patch-pipet fabrication are those with the best electrical properties, i.e., low dissipation factor and low dielectric constant. However, understanding pipet noise requires more than simply understanding the electrical properties of glass. A variety of other factors also influence the noise performance of the patch pipet, e.g., pipet geometry, depth of immersion, and the type and extent of elastomer coating. Here we will summa-

size our present understanding of all major pipet noise sources; more detailed discussions can be found elsewhere (Levis and Rae, 1992, 1993, 1998; Rae and Levis, 1992a,b).

Attaching the electrode holder to the headstage input will slightly increase noise above its minimum level associated with an open-circuit input. The mechanisms involved in generating this noise are discussed elsewhere (Levis and Rae, 1993, 1998). Here we only note that the contribution of the holder by itself to total patch-clamp noise should be very small. Holder noise is minimized by constructing the holder from low-loss dielectric materials, minimizing its size, and always keeping it clean. Shielded holders will produce more noise than unshielded holders.

Simply adding the pipet to the holder (attached to the headstage input) slightly increases the capacitance at the amplifier input. After the pipet has been immersed into the bath and a gigohm seal has been formed, the capacitance at the headstage input is further increased. As will be seen, the capacitance of the immersed portion of the pipet is a consideration in several sources of noise. Here, however, we begin by noting that all of this capacitance will at minimum produce noise because it is in series with the input voltage noise, e_n , of the headstage amplifier. The current noise produced has a power spectral density (PSD, Amp^2/Hz) with rises as f^2 at frequencies above roughly 1 kHz. Of course this noise is correlated with noise arising from e_n in series with other capacitance (amplifier input capacitance, stray capacitance, capacitance of the electrode holder). The total amount of capacitance associated with an immersed pipet can vary from a fraction of a pF up to 5 pF or more. Low capacitance is associated with heavy elastomer coating and shallow depths of immersion. Obviously the amount of noise arising from this mechanism increases as the capacitance associated with the pipet increases. However, regardless of the value of the pipet capacitance, the noise it contributes in conjunction with e_n will be small in comparison with other pipet noise sources described below. For low-noise patch-clamp measurements, it is imperative that the pipet capacitance be minimized. The reason for this will become more clear as other noise sources associated with this capacitance are described.

In addition to the mechanism just described, and to noise arising from the membrane to glass seal (which will be discussed separately), the pipet contributes noise by at least four mechanisms.

Each mechanism will be described below, followed by a summary of pipet-noise sources. Our emphasis is on the minimization of each noise, rather than simply its description.

5.2. Thin Film Noise

Thin films of solution are capable of creeping up the outer surface of the pipet from the bath (Fig. 1A). The noise associated with such films has previously been shown to be very significant (Hamill et. al., 1981). Such a film will have a relatively high distributed resistance, and the thermal voltage noise of this resistance is in series with the distributed capacitance of the pipet wall. It is expected that the PSD of this noise will rise at low to moderate frequencies and then level out at frequencies in the range of several kHz to several tens of kHz. We have estimated with uncoated pipets made from several types of glass that the noise associated with such a film of solution is usually in the range of 100–300 pA rms in a bandwidth of 5 kHz. Evidence for such films has been found in pipets fabricated from all glasses we have tested when elastomer coating has been omitted. However, pipets pulled from GE quartz produce significantly less noise without elastomer coating than any other type of glass. Apparently the surface of this glass is less subject to the formation of such thin films.

Coating the pipet with Sylgard 184 or other suitable elastomers can essentially eliminate the formation of external films of solution and eliminate the otherwise large amounts of noise they produce. These elastomers have a hydrophobic surface that prevents the formation of such films. Sylgard 184 is so effective in this regard that we have been unable to detect any thin film noise in properly coated pipets.

Thin films of solution may also be able to form on the interior surface of the pipet and inside of the holder. To avoid the formation of such films, it is possible after filling the pipet with the desired amount of ionic solution to layer a few mm of paraffin oil or silicone fluid on top of the filling solution. However, we have found that this is usually unnecessary (and it can get messy) if excess solution is carefully suctioned from the back of the pipet as described earlier.

5.3. Distributed RC Noise

Noise will also arise from the thermal voltage noise of the resistance of the pipet-filling solution in series with the capacitance of

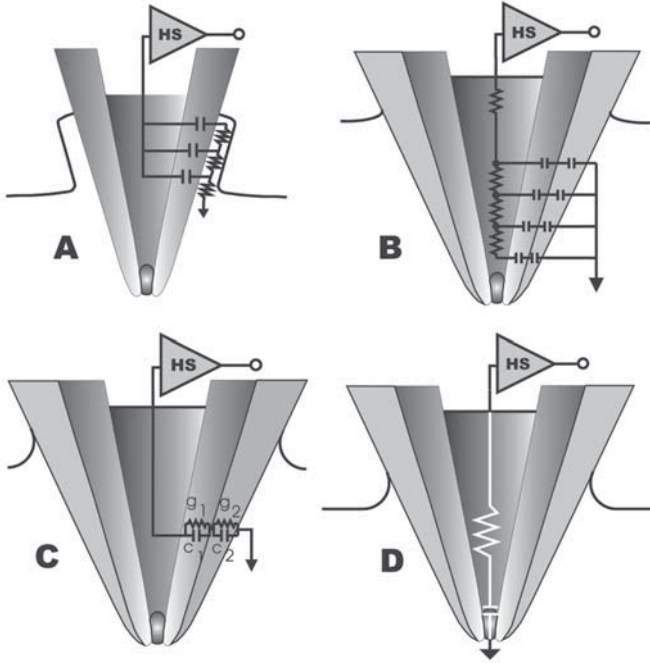


Fig. 1. Simplified circuit representations of the major noise mechanisms of the patch pipet. (A) Thin solution film on the exterior surface of an uncoated patch pipet; noise arises from the thermal voltage noise of the distributed resistance of this film in series with the capacitance of the pipet wall. In (B), (C), and (D), the pipet is shown coated with a suitable elastomer. (B) Distributed RC noise arising from the thermal voltage noise of the distributed resistance of the pipet filling solution in series with the distributed capacitance of the immersed portion of the pipet wall and its elastomer coating. (C) Dielectric noise of the series combination of the pipet (g_1, C_1 , where $g_1 = \omega C_1 D_1$) and the elastomer coating (g_2, C_2 , where $g_2 = \omega C_2 D_2$). In the region immersed in the bath, the glass wall of the pipet and its elastomer coating are represented by ideal lumped capacitances C_1 and C_2 , respectively, in parallel with loss conductances $g_1 = 2\pi f C_1 D_1$ and $g_2 = 2\pi f C_2 D_2$. The thermal noise (dielectric noise) of the coated pipet is then $4kT$ multiplied by the real part of the admittance of the series combination of dielectrics. (D) R_e - C_p noise arising from the thermal voltage noise of the entire (lumped) resistance, R_e , of the patch pipet in series with the patch capacitance, C_p . See text for further details.

the immersed portion of the pipet (Fig. 1B). Most of the resistance of the pipet resides at or near its tip. However, significant resistance is distributed along the shank distal to the tip. This resistance (and its thermal voltage noise) are in series with the capacitance of the pipet wall distributed along the portion that is immersed in the bath. We refer to noise that results as "distributed RC noise." In the frequency range of greatest interest to patch clamping (DC to 100 kHz or more), the PSD of this noise is expected to rise as f^2 . Most of our theoretical predictions of the noise arising from this mechanism (e.g., Levis and Rae, 1992) have relied on idealizations of the pipet geometry. More complicated real-world geometrics and factors such as nonuniform thinning of the pipet wall, which often occurs during pulling, are expected to make such predictions rather imprecise (*see* also Levis and Rae, 1998). Because of this, we chose to study distributed RC noise directly. These experiments used quartz pipets pulled from OD/ID = 2.0 tubing that were coated with Sylgard 184 only to the point where the electrode entered the bath (i.e., most or all of the immersed portion of the pipet was uncoated); immersion depth was ~ 1.8 mm, and the pipets were sealed to Sylgard (seal resistance > 200 G Ω). Our strategy was to vary the ionic strength of the internal filling solution. Changing the ionic strength of the filling solution will change the pipet resistance, but it will have no effect on the pipet capacitance. Because of this, it is expected that for pipets of equivalent geometry and with the same depth of immersion into the bath, the PSD of distributed RC noise will vary as $1/M$, where M is the ionic concentration of the filling solution. The rms noise in any particular bandwidth is expected to vary as $1/M^{1/2}$. In our study of this noise, we used NaCl solutions with concentrations from 1.5 mM to 1.5 M to fill the pipet. As expected, the noise increased as the ionic strength of the filling solution decreased. When the noise component attributable to distributed RC noise was parsed from total noise (and it was the dominant noise source for ionic strength of 15 mM or less), the predicted behavior was reasonably well-confirmed. Also, as expected the PSD of this noise component increased approx as f^2 as frequency increases.

On the basis of these experiments, we concluded that for uncoated quartz pipets that were pulled from OD/ID = 2 tubing and immersed to a depth of about 1.8 mm and filled with 150 mM NaCl (i.e., the ionic strength typical of most experiments) the PSD of distributed RC noise was approximated by $2.5 \times 10^{-38} f^2$ amp²/Hz.

The rms noise contribution in a bandwidth B is then $(8 \times 10^{-39} c_3 B^3)^{1/2}$ amps rms, where c_3 is a coefficient that depends on the type of filter used ($c_3 \approx 1.9$ for an 8 pole Bessel filter). This equation predicts a noise component of ~ 44 pA rms for a 5 kHz bandwidth (-3 dB, 8 pole Bessel filter), or about 123 fA rms in a 10 kHz bandwidth. It must be remembered, however, that these results were for relatively thick walled pipets fabricated from quartz, which has a low dielectric constant of 3.8. It must also be remembered that the pipets were not coated with Sylgard (or other suitable elastomer) in the region immersed in the bath. The capacitance of the wall of the pipet is expected to vary directly with the dielectric constant of the glass (for pipets of the same geometry) and vary inversely roughly in proportion to the log of the OD/ID ratio. The PSD of distributed RC noise should vary in proportion to the pipet capacitance (C_e) squared; rms noise in a given bandwidth will therefore vary linearly with C_e . Thus for an uncoated pipet fabricated from OD/ID = 1.4 tubing from a glass with a dielectric constant of 7.6 (twice that of quartz), the numbers given previously would be expected to increase by a factor of about 4. On the other hand, coating the immersed portion of a pipet with a suitable elastomer will thicken its walls and therefore reduce C_e . Thus very heavy coating of the pipet with an elastomer such as Sylgard 184 can dramatically reduce distributed RC noise, and, with such a coating, the amount of this noise will become almost independent of the type of glass used. In the experiments described above, we measured C_e to be in the range of 1.4–1.8 pF. We have found that using the tip-dip elastomer coating method (Levis and Rae, 1993) to build up a heavy coat of Sylgard all the way to the tip of the pipet, we can obtain values of C_e as low as ~ 0.35 pF for a comparable depth of immersion. This should reduce distributed RC noise to less than 10 fA rms in a 5 kHz bandwidth. Of course, shallow depths of immersion can also reduce distributed RC noise.

From the preceding discussion, it should be clear that the reduction of distributed RC noise is one of the major benefits of coating the immersed portion of the pipet with a low dielectric constant elastomer such as Sylgard 184. This noise component can also be minimized by using thick-walled tubing of glasses with low dielectric constants and by shallow depths of immersion of the pipet into the bath. Distributed RC noise is also expected to depend on pipet geometry, and should be minimized by shapes that reduce the distributed resistance distal to the pipet tip.

5.4. Dielectric Noise

Dielectric noise (Fig. 1C) will also arise from the capacitance of the pipet wall over the region that is immersed in the bathing solution. For pipets fabricated from glasses other than quartz, dielectric noise is likely to be the dominant source of noise arising from the pipet. For a single dielectric with a capacitance C_d and a dissipation factor D , the PSD of dielectric noise is given by:

$$S_d^2 = 4kTDC_d(2\pi f) \text{ Amp}^2/\text{Hz} \quad (1)$$

The rms noise in a bandwidth B is given by:

$$I_d = (4kTDC_dc_2\pi B^2)^{1/2} \text{ Amp rms} \quad (2)$$

where k is Boltzman's constant and T is absolute temperature ($^{\circ}\text{K}$). c_2 is a coefficient that depends of the type of filter used; for an 8 pole Bessel filter with B as the -3 dB bandwidth, $c_2 \approx 1.3$. It is important to note that the PSD of dielectric noise rises linearly with increasing frequency and that the rms value of this noise is proportional to filter bandwidth. This is quite unlike the other noise sources discussed, and is very usefully in experimentally parsing dielectric noise from other types of noise generated by the pipet.

For an uncoated pipet, these equations can be applied simply by noting that C_d is the capacitance of the immersed portion of the pipet (denoted by C_e above), and that D is the dissipation factor of the glass. It is instructive to consider two uncoated pipets with the same geometry both pulled from OD/ID = 1.4 tubing and both immersed to depth of about 2 mm. One pipet is fabricated from quartz ($D = 0.0001$, dielectric constant = 3.8) and the other pipet is fabricated from a borosilicate with $D = 0.005$ and a dielectric constant of 5.0. The capacitance (C_d or C_e) of the quartz pipet should be about 1.5 pF, while that of the borosilicate pipet will be about 2 pF due to its higher dielectric constant. Using these numbers, it can be estimated that the uncoated quartz pipet will produce about 16 fA rms dielectric noise in a 5 kHz bandwidth (-3 dB, 8 pole Bessel filter), while the borosilicate pipet would produce 128 fA rms dielectric noise in the same bandwidth. The superiority of quartz is clear in this case.

Of course the importance of coating the pipet with a suitable elastomer has already been demonstrated regardless of the type

of glass used. Therefore it is necessary to consider the dielectric noise in this more complicated situation. We have presented a more detailed analysis of the dielectric noise in this case elsewhere (Levis and Rae, 1993, 1998). Here we will summarize our most important conclusions. When the pipet is coated with an elastomer it is necessary to derive equations which describe the dielectric noise of the series combination of two different dielectrics with capacitances C_1 and C_2 and dissipation factors D_1 and D_2 (see Fig. 1C and its legend). For $D_1, D_2 \ll 1$, the dielectric noise PSD of the elastomer coated pipet is well approximated by:

$$4kT(2\pi f) \frac{D_1 C_1 C_2^2 + D_2 C_2 C_1^2}{(C_1 + C_2)^2} \text{ Amp}^2 / \text{Hz} \quad (3)$$

and the rms noise in a bandwidth B is approximated by:

$$\{4kTc_2 \pi B^2 \frac{D_1 C_1 C_2^2 + D_2 C_2 C_1^2}{(C_1 + C_2)^2}\}^{\frac{1}{2}} \text{ Amps rms} \quad (4)$$

In these equations C_1 and D_1 are the capacitance and dissipation factor of the glass wall of the pipet and C_2 and D_2 are the capacitance and dissipation factor of the elastomer coating. The capacitance C_1 depends on the depth of immersion, the thickness of the pipet wall, and the dielectric constant of the glass. For a 2 mm depth of immersion, C_1 can vary from as little as about 1 pF for very thick-walled quartz pipets, to more than 6 pF for thin-walled pipets made from glasses with high dielectric constants (e.g., soda-lime and high-lead glasses). Of course the capacitance C_2 of the elastomer coating also depends on the depth of immersion, the dielectric constant of the elastomer, and the thickness of the elastomer coating. Obviously heavy elastomer coating will lead to the smallest values of C_2 . However, it is important to realize that the thickness of the elastomer coating will not be uniform. In particular, it is hard to achieve very thick elastomer coatings near the tip of the pipet. The dip method of elastomer coating (Levis and Rae, 1993) has proved to be useful in building up relatively heavy coats of elastomer all the way to the tip of the electrode, but even with this method the thickness of the coat is still not uniform. Because of this, it is difficult to predict the value of C_2 . However, we have measured the value of C_2 (see Levis and Rae, 1993) to be as little as 0.4–0.5 pF for a 2 mm immersion depth when heavy coatings of

Sylgard were applied with the dip method. With lighter coating, the value of C_2 can easily be much higher (2 pF or more).

The dissipation factor D_1 of the glasses used to fabricate patch pipets have already been discussed; reported values range from as little as 10^{-5} to 10^{-4} for quartz to as much as 0.01 for soda-lime glasses. The dissipation factor D_1 of the elastomer is also very important. Sylgard 184 has a dissipation factor of about 0.002, which is lower than that of most glasses with the notable exception of quartz. Because of this, coating pipets fabricated from glasses other than quartz will significantly reduce their dielectric noise and the relative reduction will be greatest for the poorest (most lossy) glasses. However, the dissipation factor of Sylgard 184 is a factor of 20 or more higher than that of quartz, and predictions based on Equations 3 and 4 indicate that for all realistic values of C_2 coating a quartz pipet with Sylgard will actually increase its dielectric noise relative to that which would have been produced by the pipet alone. This is true despite the reduction in overall capacitance produced by the Sylgard coating. Thus for a quartz pipet with $C_1 = 1.5$ pF and $D_1 = 0.0001$ and a Sylgard coating with $C_2 = 0.5$ pF and $D_2 = 0.002$, equation 4 predicts 30 fA rms of dielectric noise in a 5 kHz bandwidth (-3 dB, 8 pole Bessel filter), while as described earlier, the same pipet without the Sylgard coating would have produced only about 17 fA rms dielectric noise in this bandwidth. Estimates of the dielectric noise of quartz pipets coated with Sylgard and several similar elastomers and sealed to Sylgard have produced values that are in good agreement with the predictions of Equations 3 and 4.

It is apparent from the previous discussion that coating a quartz patch pipet with Sylgard 184 is not desirable in terms of dielectric noise. Nevertheless, coating with Sylgard or some other suitable elastomer is necessary to eliminate thin-film noise and to minimize distributed RC noise. In fact, very heavily Sylgard-coated quartz pipets display the least noise of all pipets, so the small increment in dielectric noise resulting from such coating is more than offset by the benefits in terms of reduction of other types of noise. It is also important to realize that even though Sylgard-coating a quartz pipet will increase its dielectric noise, the final dielectric noise of such a pipet still remains significantly below that of Sylgard-coated pipets fabricated from any other type of glass we have tested. If elastomers with dissipation factors significantly less than that of

Sylgard 184 can be found that are otherwise suitable for coating pipets, they could be effective in lowering the dielectric noise of quartz pipets. It can be appreciated from examination of Equations 3 and 4 that the dissipation factor of such an elastomer need not be less than that of quartz to lower total dielectric noise of a heavily coated pipet. Such elastomers (if found) should also be very beneficial for other types of glass. Dow Corning R-6101 and Q1-4939 both are reported by the manufacturer to have dissipation factors of 0.00025. However, our preliminary measurements of pipets coated with R-6101 have failed to demonstrate any significant noise advantage over pipets coated with similar thicknesses of Sylgard 184. Although we are unable to account for this finding, it certainly seems possible that the true dissipation factor of this elastomer exceeded the value in the manufacturer's data sheet.

Due to the volume of material presented regarding dielectric noise, it is probably worthwhile to summarize our conclusions. For thick-walled quartz pipets with heavy Sylgard coating to the tip and sealed to Sylgard at an immersion depth of ~ 2 mm, our estimates of dielectric noise has generally been in the range of 20–35 fA rms in a 5 kHz bandwidth. On occasion, with actual excised patches and heavily Sylgard-coated patch pipets, our estimates of dielectric noise have been less than 15 fA rms in a 5 kHz bandwidth when the electrode tip has been withdrawn close to the surface of the bath. For other types of glasses, dielectric noise is significantly higher. Our previous measurements of the noise arising from light to moderately Sylgard-coated pipets made from more than 20 different glasses (Rae and Levis, 1984, 1992a), indicated that in a 5 kHz bandwidth and with a ~ 2 mm depth of immersion dielectric noise varied from about 100–200 fA rms. The lowest noise was associated with glasses with the smallest loss factor (i.e., dissipation factor multiplied by dielectric constant), while the highest noise arose from the very lossy soda lime glasses. Recently we have measured a few pipets made from Corning 7052 and 7760 (tubing OD/ID = 1.4) that were heavily coated with Sylgard 184 to the tip by the dip method described earlier. These measurements indicated that dielectric noise could be as low as ~ 70 fA rms in a 5 kHz bandwidth for these glasses (with heavy Sylgard coating) at a 2 mm immersion depth. This is somewhat more noise than would be predicted from Equations 3 and 4, but less than we have estimated previously.

5.5. R_e - C_p Noise

The last pipet-noise mechanism that we will consider is the noise that is expected to arise from the thermal voltage noise of the entire lumped pipet resistance, R_e in series with the capacitance of the patch membrane, C_p ; we refer to this noise source as R_e - C_p noise (*see* Fig. 1D). This noise is expected to have a PSD that increases as f^2 up to frequencies of about $1/2\pi R_e C_p$ (which is usually several hundred kHz); at frequencies below this the PSD is expected to be:

$$S_{ep}^2 = 4\pi^2 e_e^2 C_p^2 f^2 \text{ Amp}^2/\text{Hz} \quad (5)$$

where $e_e^2 = 4kTR_e$, i.e., the thermal voltage noise PSD for the pipet. The rms noise attributable to this mechanism in a bandwidth B is then given by:

$$I_{ep} = \{1.33\pi^2 c_3 e_e^2 C_p^2 B^3\}^{1/2} \text{ Amps rms} \quad (6)$$

where c_3 is a coefficient that again depends on the type of filter used to establish the bandwidth; for an 8 pole Bessel filter with a -3 dB bandwidth of B Hz, $c_3 \approx 1.9$.

For single-channel measurements, patch capacitance typically ranges from approx 0.01–0.25 pF for pipet resistances in the range of 1–10 M Ω (Sakmann and Neher, 1983). As expected, higher values of patch capacitance are associated with lower-resistance pipets. Because of the inverse relationship between R_e and C_p , Equations 5 and 6 predict that the smallest amount of R_e - C_p noise will arise from the smallest patches, even though such patches are obtained with higher-resistance pipets. For example, with $R_e = 10$ M Ω and $C_p = 0.01$ pF, Equation 6 predicts a noise contribution of only about 6 fA rms in a 5 kHz bandwidth (-3 dB, 8 pole Bessel filter). On the other hand, with $R_e = 2$ M Ω and $C_p = 0.25$ pF, the predicted noise is more than 60 fA rms in the same bandwidth. This latter amount of noise can exceed the total of all other pipet-noise sources for quartz pipets, and remains significant even for pipets fabricated from other glasses. Obviously, however, this noise source itself does not depend on the type of glass, but rather on the geometry of the pipet (and, to some extent, on luck).

5.6. Seal Noise

The noise associated with the membrane-glass seal is less easily predicted. It is expected that the PSD of this noise for zero applied

voltage will be given by $4kT \operatorname{Re}\{Y_{sh}\}$, where $\operatorname{Re}\{Y_{sh}\}$ is the real part of the seal admittance. The minimum value of $\operatorname{Re}\{Y_{sh}\}$ is $1/R_{sh}$, where R_{sh} is the DC seal resistance, and this leads to a minimum estimate of the seal noise in a bandwidth B of $(4kTB/R_{sh})^{1/2}$. This is just the thermal current noise of the seal resistance and can be very small for high resistance seals. For example, for a $200 \text{ G}\Omega$ seal and a bandwidth of 5 kHz , $(4kTB/R_{sh})^{1/2} = 20 \text{ fA rms}$. Our measurements from several patches with seal resistances in the range of $40\text{--}100 \text{ G}\Omega$ have shown that the noise attributable to the seal is often indistinguishable from the predicted thermal current noise of R_{sh} (Rae and Levis, 1992b). Nevertheless, it is certainly possible that seal noise may sometimes exceed this minimum prediction. As anyone who has spent much time trying to achieve low noise with the patch-clamp technique knows, there is a great deal of variability in the noise achieved even when all of the precautions we have described have been followed and when very high seal resistances have been obtained. It is certainly tempting to blame some of this variability on the noise associated with the seal.

5.7. Summary of Pipet Noise Sources

It is important to realize that the noise sources described previously (with the exception of noise arising from various capacitances in series with the amplifier's input voltage noise e_n) are all uncorrelated. Uncorrelated noise sources add in an rms fashion. For example, if four uncorrelated noise sources have rms values denoted by E_1 , E_2 , E_3 , and E_4 , then the total rms noise resulting from the summation of these sources is given by $(E_1^2 + E_2^2 + E_3^2 + E_4^2)^{1/2}$. Because of this, the largest individual source of noise will tend to dominate total noise.

Of the noise sources described earlier, only thin-film noise can be completely eliminated (or in any case reduced to negligible levels). Distributed RC noise, dielectric noise, and $R_e\text{--}C_p$ noise can never be eliminated, but they can be minimized. In many cases, precautions taken to reduce one noise source will also be beneficial in reducing other sources of noise. Thus with any type of glass, thick-walled pipets will, all else being equal, have less capacitance, and therefore display less distributed RC noise and dielectric noise. Similarly, shallow depths of immersion will also reduce pipet capacitance and simultaneously reduce distributed RC and dielectric noise. Coating pipets with a heavy layer of a low-loss elastomer

such as Sylgard 184 will also reduce the pipet's capacitance and reduce distributed RC noise for all types of glass. For all types of glass other than quartz, a heavy coat of Sylgard 184 extending as close to the tip as possible will also significantly reduce dielectric noise. In the case of quartz pipets, elastomers with dissipation factors comparable to that of Sylgard 184 will actually somewhat increase dielectric noise. However, within the range of realistic thicknesses of the coating, even for quartz, heavy coatings will generally lead to the least dielectric noise; this is compatible with the requirements for minimizing distributed RC noise in quartz pipets. It is also important to recall that even though Sylgard-coating somewhat increases the dielectric noise of quartz pipets, the final dielectric noise of a heavily Sylgard coated quartz pipet is still much less than that of pipets made from any other type of glass. The major distinction in terms of noise between pipets fabricated from quartz and other types of glasses is, in fact, the much lower dielectric noise of quartz. R_e - C_p noise has often been ignored in the past, and in many situations it is sufficiently small to still be ignored. However, when all other sources of noise have successfully been reduced to the lowest limits presently achievable, it can become significant, and even dominant at very wide bandwidths (Levis and Rae, 1993). R_e - C_p noise is minimized by forming the smallest patch areas that are consistent with the goals of the experiment being undertaken. Although the data is widely scattered, patch area (or patch capacitance) decreases as pipet resistance increases. The net result is that it is predicted that higher-resistance patch pipets with small tips will tend to produce the least amount of R_e - C_p noise. The geometry of such electrodes is not necessarily the best selection for minimizing distributed RC noise, but this can be overcome by heavy elastomer coating. Although we have not systematically studied the relationship between pipet resistance (tip diameter) and noise, it is our experience that the lowest noise patches are usually obtained from small-tipped, high-resistance pipets.

It is difficult to assign values to what can be expected as "typical" or "best-case" noise from pipets fabricated from different glasses in different situations. Nevertheless, some rough estimates can be provided. For low-loss borosilicate, aluminosilicate, or high-lead glasses with moderate Sylgard coating extending to within ~ 100 μm of the tip, it is reasonable to expect that in a 5 kHz bandwidth

total pipet noise (excluding seal noise) as low as 100–120 fA rms can be achieved with a ~2 mm depth of immersion. With very heavy Sylgard coating all the way to the tip, this value should fall to somewhat less than 100 fA rms in this bandwidth. With quartz pipets that are heavily Sylgard coated to the tip we have been routinely able to keep total pipet noise to ~40 fA rms in a 5 kHz bandwidth for a 2 mm immersion depth. With the quartz pipet raised to the surface of the bath with an excised membrane patch, we have occasionally achieved a total noise of the pipet plus seal as low as 30–35 fA rms in a 5 kHz bandwidth; subtracting the thermal current noise of the seal (as judged from its measured resistance) yields an estimate of 10–20 fA rms for total pipet noise in these cases.

5.8. Noise Sources for Whole-Cell Voltage Clamping

While all of the pipet noise mechanisms described earlier with the exception of R_e - C_p noise are present in whole-cell voltage clamping, their relative importance is very much less than is the case for patch voltage-clamp measurements. Of course, this is not because these pipet noise sources have become less in the whole cell situation, but rather because other noise source have become much higher. In the first place, most whole-cell voltage-clamp measurements are made with a patch-clamp headstage amplifier configured with a 500 M Ω feedback resistor. In a 5 kHz bandwidth, this resistor alone will produce 400 fA rms noise, which is more than even soda-lime pipets will produce provided they are reasonably Sylgard-coated. Under most situations, however, the dominant source of noise in a whole-cell voltage clamp will be the thermal current noise of the pipet resistance R_e in series with the cell-membrane capacitance C_m .

As just noted, the whole-cell voltage clamp lacks R_e - C_p noise. The reason for this is simply that the patch membrane has been disrupted, or shorted out, as is the case for perforated patch measurements. However, in the whole-cell situation, the entire cell membrane is in series with the pipet resistance and with the thermal voltage noise of this resistance. The noise produced by this has precisely the same mechanism that underlies R_e - C_p noise, but, since $C_m \gg C_p$, it is of far greater magnitude. It might also be recalled that the time constant $R_e C_p$ will typically be a μ sec or less and so can usually be neglected. However, the time constant $R_e C_m$

is much larger and its effects can not be ignored, either in terms of noise or dynamic performance.

Of course, the electrode resistance R_e is the series resistance in the whole-cell variant of the patch voltage clamp, and many of its effects are well-known and need no further comment here. But it seems that some of its effects can not be emphasized often enough. One of these is the filtering effect that uncompensated series resistance has on the measured current. In the absence of series resistance compensation, this filtering effect (equivalent to a simple RC low-pass filter) limits the actual bandwidth of current measurement to $1/2\pi R_e C_m$. For example, with $R_e = 10 \text{ M}\Omega$ and $C_m = 50 \text{ pF}$, this is $\sim 320 \text{ Hz}$, and it should be remembered that R_e after patch disruption or perforation is usually higher than the pipet resistance that was measured in the bath. With series resistance compensation, this bandwidth limit is increased. We will define α as the fraction of the series resistance compensated ($0 < \alpha < 1$), and $\beta = 1 - \alpha$. With series resistance compensation, the uppermost usable bandwidth is extended to $1/2\pi\beta R_e C_m$. So in the previous example, 90% series resistance compensation ($\beta = 0.1$) will extend the actual bandwidth limit to about 3.2 kHz. It will also greatly increase the noise at this bandwidth. The PSD, S_{em}^2 , of noise arising from the thermal voltage noise of R_e in series with C_m is given by:

$$S_{em}^2 = \frac{4\pi^2 e_e^2 C_m^2 f^2}{1 + 4\pi^2 \beta^2 R_e^2 C_m^2 f^2} \quad (7)$$

where $e_e^2 = 4kTR_e$ is the thermal voltage noise PSD of R_e . Note that this expression takes into account the effects of series resistance compensation. For 100% series resistance compensation ($\alpha = 1$, $\beta = 0$), Equation 7 reduces to $4\pi^2 e_e^2 C_m^2 f^2$, which has exactly the same form as Equation 5.

From Equation 7 it can be seen that the PSD of the noise arising from R_e and C_m rises with increasing frequency as f^2 until it reaches $f = 1/2\pi\beta R_e C_m$. Thereafter, this noise plateaus to a value of $4kT/\beta^2 R_e$, which, of course, is many times larger than the thermal current noise of the feedback resistor. This plateau level of the PSD will be maintained until a frequency where it is rolled off by an external filter (or the inherent bandwidth limit of the electronics). As an example of the magnitude of the noise introduced by this mechanism, consider a rather favorable example for whole-

cell voltage clamping with $R_e = 5 \text{ M}\Omega$ and $C_m = 30 \text{ pF}$. Without series resistance compensation, the "corner frequency" at which the noise PSD plateaus (and the limit of actual bandwidth of current measurement) is at about 1060 Hz. For a -3 dB bandwidth (8 pole Bessel filter) of current measurement only 500 Hz, the noise arising from R_e and C_m would already be nearly 0.5 pA rms, which is more than a very bad electrode would produce in a bandwidth of 5 kHz. By a bandwidth of 1 kHz, the noise would have increased to about 1.3 pA rms. Increasing the bandwidth of current measurement much beyond 1 kHz without series resistance compensation is not justified because the measured current will still be effectively filtered at 1.06 kHz (-3 dB bandwidth of the 1 pole low-pass filter arising from R_e and C_m). This does not, however, mean that setting the external filter to a bandwidth higher than 1 kHz will not add more noise. Increasing the bandwidth of the external filter to 5 kHz will increase the noise to more than 3 pA rms, but it will provide very little signal information that was not contained when the data was filtered at 1 kHz. Series (pipet) resistance compensation can extend the usable bandwidth, but, of course it will significantly increase the noise at external filter bandwidths higher than $1/2\pi R_e C_m$. Thus with 90% series resistance compensation, the maximum usable bandwidth of current measurement is extended to 10.6 kHz. In this case with an external filter (8 pole Bessel) with a -3 dB bandwidth of 5 kHz, the noise is increased to almost 15 pA rms. For a 10 kHz bandwidth the noise will increase to about 40 pA rms. With noises of this magnitude, the pipet noise mechanisms previously discussed become quite insignificant. It can therefore be concluded that many of the characteristics of the pipet that were important to patch clamping are not important to a whole-cell voltage-clamp situation.

The noise arising from R_e and C_m in whole-cell voltage clamping can only be minimized by minimizing R_e and/or C_m . Of course, minimizing C_m means selecting small cells and this is often not possible. In addition, it should also be noted that if you are studying a particular type of channel in a population of cells of various sizes but the channel density is the same in all cases, there is no clear advantage in terms of signal-to-noise ratio of selecting smaller cells. For a constant value of R_e , it is simple to show that at a given bandwidth (below $1/2\pi\beta R_e C_m$) the rms noise will decrease linearly as C_m decreases, but, because the number of channels is

also proportional to C_m , the signal will also decrease linearly with decreasing C_m : Signal-to-noise will be constant. In this case, signal to noise ratio only depends on R_e , and it will improve as $1/R_e^{1/2}$. So the most practical way to minimize this source of noise is to use the lowest-resistance pipets that are capable of sealing to your cells and make every effort to minimize the increase in access resistance that often occurs when the patch is disrupted.

Finally, it is worth emphasizing that another important way of minimizing this noise is to not make the mistake of using a bandwidth of the external filter that is not justified by the situation. Increasing the external bandwidth significantly beyond $1/2\pi\beta R_e C_m$ adds essentially no information about the signal, but it will add additional noise.

6. Recent Developments

Since the last edition of this book was published, there have been some new developments that deserve at least brief mention here. Specifically we will consider ongoing efforts in several laboratories to replace present-day patch pipets with what can generally be called planar electrode techniques. Briefly, these techniques involve a small hole (or holes, a few μm down to less than $1\ \mu\text{m}$ in diameter) in a sheet of a low-loss dielectric material (with a typical thickness of a few hundred microns). Typically the hole expands from a small opening at the upper surface to a much wider diameter at the lower surface, forming a conical or pyramidal "well." This sheet separates two compartments. The uppermost compartment contains a bathing solution and a cell or cells from which measurements are to be made. The lower compartment only contains solution in the small well just mentioned. This very small amount of solution is attached to a patch-clamp amplifier input, while the solution in the upper compartment is grounded. This arrangement can greatly reduce the capacitance associated with the traditional pipet and its holder. It also allows for the possibility of arrays of holes/wells for simultaneous whole-cell recording from numerous cells, with isolation occurring between each of these by the absence of solution except in the wells. More exotic arrangements than those just described are also being considered, but will not be discussed here.

Thus there are two possible benefits of this approach: 1) it can allow for multiple whole-cell measurements to be made simulta-

neously (ultimately with a high degree of automation); and 2) it can potentially reduce the capacitance—and hence the noise—associated with single-channel patch-clamp measurements. To take full advantage of the latter possibility, new lower-capacitance low-noise “headstage” amplifiers must be developed, and it must become possible to form very high-resistance seals.

In general the formation of high-resistance seals has been the greatest problem encountered in the development of such planar electrode (or “sheet/hole”) techniques. However, significant progress has been made over the past year. Klemic et al. (2001) have formed arrays of planar electrodes in a partition formed by micro-molding Sylgard into the desired shape; Sylgard has proved successful in forming gigohm seals. Fertig et al. (2001) have successfully formed tiny (~1 μm diameter) lipid bilayers in “chip electrodes” made from glass or quartz with etched apertures. Farre et al. (2001) have prepared chips for whole-cell recordings with standard optical lithography and etching of silicon wafers covered by silicon nitride (Si_3N_4). More progress in such techniques seems likely in the future.

References

- Benndorf, K. (1995) Low-noise recording, in *Single-Channel Recording* (Sakmann, B. and Weher, E., eds.), Plenum Press, New York, NY, pp.129–145.
- Farre, C., Olofsson, J., Pihl, J., Persson, M., and Orwar, O. (2001) Whole-cell patch clamp recordings performed on a chip. *Biophys. J.* **80**, 338a.
- Fertig, N., Meyer, C., Blick, R. H., and Behrends, J. C. (2001) A microstructured chip electrode for low noise single channel recording. *Biophys. J.* **80**, 337a.
- Klemic, K. G., Baker, W. T., Klemic, J. F., Reed, M. A., and Sigworth, F. J. (2001) Patch clamping with a planar electrode array. *Biophys. J.* **80**, 337a.
- Hamill, O. P., Marty, A., Neher, E., Sakman, B., and Sigworth, F. J. (1981) Improved patch-clamp techniques for high-resolution current recording from cells and cell-free membrane patches. *Pflugers Arch.* **391**, 85–100.
- Levis, R. A. and Rae, J. L. (1998) Low noise patch clamp techniques. *Methods Enzymol.* **293**, 218–266.
- Levis, R. A. and Rae, J. L. (1993) The use of quartz patch pipettes for low noise single channel recording. *Biophys. J.* **65**, 1666–1677.
- Levis, R. A. and Rae, J. L. (1992) Constructing a patch clamp setup. *Methods Enzymol.* **207**, 18–66.
- Neher, E. (1981) Unit conductance studies in biological membranes, in *Techniques in Cellular Physiology* (Baker, P. F., ed.), Elsevier, North Holland, Amsterdam.
- Neher, E. and Sakman, B. (1976) Single channel currents recorded from membrane of denervated frog muscle fibers. *Nature* **260**, 799–802.

- Rae, J. L. and Levis, R. L. (2000) An electrode coating elastomer to replace sylgard 184. *Axobits* **29**, 6-7.
- Rae, J. L. and Levis, R. A. (1992a) Glass technology for patch electrodes. *Methods Enzymol.* **207**, 66-92.
- Rae, J. L. and Levis, R. A. (1992b) A method for exceptionally low noise single channel recordings. *Pflugers Arch.* **42**, 618-620.
- Rae, J. L. and Levis, R. A. (1984) Patch voltage clamp of lens epithelial cells: theory and practice. *Mol. Physiol.* **6**, 115-162.

2

Whole-Cell Patch-Clamp Recordings

Harald Sontheimer and Christopher B. Ransom

1. Introduction

The patch-clamp recording technique, which measures ionic currents under voltage-clamp, was designed to study small patches of membrane in which near-perfect control of the transmembrane voltage can be readily achieved. The recent application of patch-clamp methodology to the analysis of whole-cell current actually defies many of the original design requirements. Nevertheless, whole-cell recordings are routinely used in electrophysiology laboratories to study electrical currents carried by ions through ion channels, neurotransmitter receptors, and electrogenic transporters in cell types of virtually any origin. Since the introduction of the patch-clamp technique in 1981 (Hamill et al., 1981) and the subsequent rapid development of commercial amplifiers, this method of intracellular recording has essentially replaced sharp electrode recordings, particularly in the study of cultured cells.

This procedure and its applications have been the topics of numerous excellent reviews and book chapters (*see Recommended Readings*). In addition to summarizing some basic concepts, this chapter specifically emphasizes hands-on procedures and protocols. It is hoped that the chapter will effectively complement previous accounts of the patch-clamp technique.

2. Principals (Why Voltage-Clamp?)

Electrophysiologists are especially interested in the activity of membrane proteins, which provide conductive pathways through biological membranes: ion channels, transmitter receptors, or electrogenic ion-carriers. Channel activity, whether through voltage-

From: *Neuromethods*, Vol. 35: *Patch-Clamp Analysis: Advanced Techniques*
Edited by: W. Walz, A. A. Boulton, and G. B. Baker @ Humana Press Inc., Totowa, NJ

dependent or ligand-gated ion channels, results in changes of membrane conductance, which can be most conveniently evaluated by recording membrane currents at a constant membrane voltage. Under such "voltage-clamped" conditions, current is directly proportional to the conductance of interest.

A two-electrode voltage-clamp design was first introduced in the seminal studies of Hodgkin and Huxley (1952) for the study of ionic conductances of the squid giant axon. In this application, one of the electrodes serves as voltage sensor, whereas the second functions as a current source both interconnected through a feedback amplifier. Any change in voltage detected at the voltage electrode results in current injection of the proper polarity and magnitude to maintain the voltage signal at a constant level. The resulting current flow through the current electrode is assumed to flow exclusively across the cell membrane and as such is proportional to the membrane conductance (mediated by plasma-membrane ion channels). The major disadvantage of this technique, however, is its requirement for double impalement of the cell, which restricts its application to rather large cells ($>20\text{ }\mu\text{m}$) and prevents study of cells embedded in tissue.

In an attempt to solve this problem, single-electrode switching amplifiers were developed that allowed the use of one electrode to serve double duty as voltage and current electrode. For short periods of time, the amplifier connects its voltage-sensing input to the electrode, takes a reading, and subsequently connects the current source output to the same electrode to deliver current to the cell. This approach, however, is limited in its time-resolution by the switching frequency between the two modes, which must be set based on the cell's RC time constant (the product of cell input resistance and capacitance). Both single-electrode switch clamp and double-electrode voltage-clamp allow direct measurement of the cells voltage and avoid the introduction of unknown or unstable voltage-drops across the series resistance of the current passing electrode.

The whole-cell patch-clamp technique similarly uses only one electrode. However, in contrast to aforementioned techniques, it uses the electrode continuously for voltage recording and passage of current. Consequently, the recording arrangement contains an unknown and potentially varying series resistance in form of the electrode and its access to the cell. For the technique to deliver

satisfactory results, it is essential that this series resistance be small relative to the resistance of the cell. Numerous measures are taken to satisfy these requirements (*see below*) including the use of blunt, low-resistance electrodes, small cells with high impedance, and electronic compensation for the series resistance error. When effectively utilized, the whole-cell technique can yield current recordings of equal or superior quality to those obtained with double- or single-electrode voltage-clamp recordings.

3. Procedure and Techniques

3.1. Pipets

In contrast to sharp electrode recordings that utilize pipets with resistances of $>50\text{ M}\Omega$, comparatively blunt low-resistance ($1\text{--}5\text{ M}\Omega$) recording pipets are used for whole-cell patch-clamp recordings. This is done for at least two reasons: 1) series resistance should ideally be two orders of magnitude below the cell's resistance, and 2) blunt electrodes ($1\text{--}2\text{ }\mu\text{m}$) are required to achieve and maintain mechanically stable electrode-membrane seals.

As described in Chapter 1 (Levis and Rae), electrodes can be manufactured from a variety of glass types. Although it has been frequently reported that glass selection has a significant influence on the quality of seal or the frequency at which good seals are obtained, little scientific evidence supports this notion. In our laboratory, we have found it to be more critical that glass pipets are thoroughly cleaned by soaking in acetone for $1/2\text{ h}$ followed by drying at 180°C in a lab oven. To achieve the shape ideal for sealing membrane patches, electrodes are pulled from capillary glass pipets in a two- or multistage process using commercially available pullers, such as those of Narashige, Brown-Flaming, and others. An additional step of firepolishing the tips of pipets can significantly improve the likelihood of seal formation. As an added benefit, the tips of pipets with very low resistance (steep, tapering tip) can be firepolished to reduce the tip diameter to appropriate levels. Cell surfaces can also be enzymatically cleaned during isolation and culturing procedures, or just prior to each experiment. Once an appropriate set of variables, i.e., cell preparation, glass type, electrode resistance, and shape, is identified, the success rate for stable electrode-membrane seals should be between 50–90%.

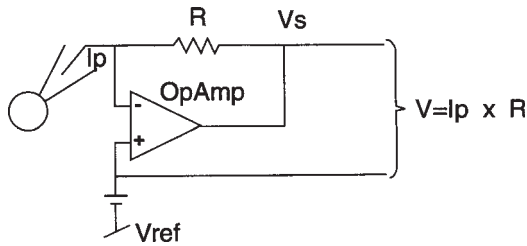


Fig. 1. Scheme of current-to-voltage converter (for details, *see* Sigworth, 1983). Abbreviations used: Pipet current I_p , feedback resistance R , operational amplifier OpAmp, reference potential V_{ref} , voltage source V_s .

3.2. Electronic Components of a Setup

The electronic components of a patch-clamp setup are comparatively few: A patch-clamp amplifier, oscilloscope, stimulator, computer, an optional external signal filter, and VCR recorder. High-quality patch-clamp amplifiers are available from a number of manufacturers. At present, most laboratories utilize either a List EPC 9 or an Axon Instruments Axopatch 200 amplifier. These amplifiers are overall similar in design and are both equipped with multi-stage Bessel filters, variable gain settings, and at least 2 feedback resistor settings for whole-cell and single-channel recordings.

The single most important electronic component of a patch-clamp amplifier is the current-to-voltage converter, which is contained in the headstage. Its characteristics are described in detail elsewhere (Sigworth, 1983; *see* Fig. 1). Current flow through the electrode (I_p) across a resistor of high impedance (R) causes a voltage drop that is proportional to the measured pipet current (I_p). An operational amplifier (OpAmp) is used to automatically adjust the voltage source (V_s) to maintain a constant pipet potential (V_p) at the desired reference potential (V_{ref}). As the response of the OpAmp is fast, it can be assumed that for all practical purposes $V_p = V_{ref}$. When current flows across the membrane through ion channels, V_p is instantaneously displaced from V_{ref} . The OpAmp alters V_s to generate an I_p that will exactly oppose the displacement of V_p from V_{ref} . Thus, the current measured during a patch-clamp experiment (membrane current flow) is equal and opposite to I_p . In their whole-cell mode, patch-clamp

amplifiers use a 500 M Ω feedback resistor allowing to measure currents of up to 20 nA. For some amplifiers a low gain 50 M Ω headstage is available that can pass currents of up to 200 nA, however, its use sacrifices the use of capacitance and series resistance compensation.

Although some amplifiers, such as the Axopatch 1 D, have built-in stimulators, most electrophysiologists prefer the use of an external stimulator that offers greater versatility. Low-cost microcomputers serve as both digital stimulator and on-line recorder. While the use of a microcomputer is not essential, the growing number of affordable high-quality hard- and software products have made computers and D/A(digital-analog)-A/D converters standard laboratory equipment. Data can be collected and digitized on-line at up to 330 kHz and can be stored to the hard disk of a computer. All necessary components can be purchased at a price well below that of an external stimulator alone.

Most patch-clamp amplifiers are equipped with 4 pole Bessel filters, which are of sufficient quality to filter data. However, the use of an external 8 pole Bessel filter (such as a Frequency Devices, Series 920) allows the selection of a wider range of cutoff frequencies and has better frequency responses, specifically a sharper roll-off (See Subheading 4.1, Filtering).

Additional equipment is recommended for specific data collection needs. If data is to be collected for extended periods of time, and if the sampling rates are roughly 10–40 kHz, a VCR tape recorder is a useful interim storage medium. Data analysis can subsequently be done by playing data back off-line to a computer equipped with an A/D converter. The introduction of larger hard drives and convenient inexpensive means to back up data digitally (JAZ disks, CD burners) have made the use of VCR data storage less popular. Even in the presence of a computer-based data-acquisition system, oscilloscopes are a convenient means for monitoring data collected by either microcomputer or VCR, and are essential for the “debugging” of environmental electrical noise from a recording setup.

3.3. Recording Configuration

The whole-cell patch-clamp recording setup closely resembles that used for sharp electrode intracellular recordings (Fig. 2A). An electrically grounded microscope on an isolation table serves as the foundation of the recording setup. A recording chamber is mounted to the stage of the microscope (Fig. 2B). Alternatively, if

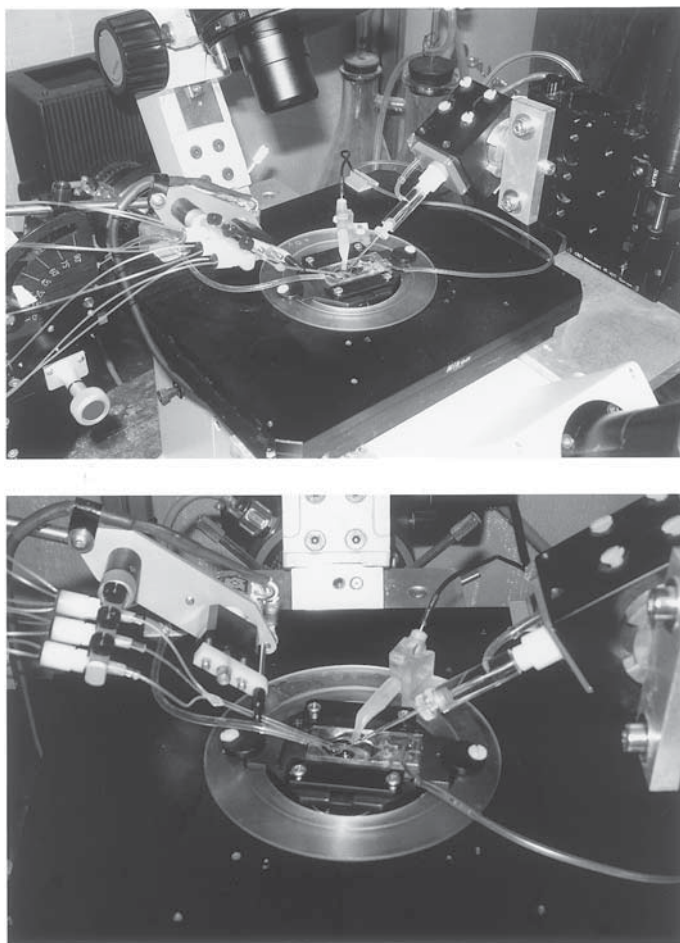


Fig. 2. Whole-cell patch-clamp setup (A) and recording chamber (B). Photomicrographs of a typical recording setup based on a Nikon Diaphot microscope. (A) Patch-clamp headstage with electrode holder mounted on a swivel PVC clamp and attached to 3-axis manipulator constructed from 3 series 420 microtranslation stages (Newport Inst.) (B) Close-up view of flow-through recording chamber. Chamber from Warner Instruments modified after our own design.

constant perfusion is not desired, a 35 mm petri dish can be used as recording chamber, in which case, cells may be grown directly on the 35 mm dish. To use Normarski optics, we prefer the use of a Plexiglas recording chamber, which has a glass coverslip as the base (Fig. 2B). Various types of recording chambers are commercially available, all of which serve well for most purposes. Electrodes are typically placed under visual control (400 \times) onto a cell by use of a high-quality, low-drift micromanipulator. Numerous hydraulic, piezoelectric, and mechanical designs are commercially available, each offering unique benefits. Hydraulic manipulators, such as Narishige model MO-203 combine precise movement with large travel, are very versatile and easy to use. Piezoelectric manipulators, such as the Burleigh PCS 500, only allow 70 μ m of travel, and as such are only useful when used in combination with a coarse positioning manipulator. Piezoelectric systems provide excellent stability and are the instruments of choice for excising patches for single-channel recordings (*see* Chapter 3, this volume). Stable, low-cost mechanical manipulators (such as Soma instruments series 421) can be assembled from single-axis translation stages. Their modular design, combined with micrometer screws and DC motors- (e.g., model 860A) make them extremely versatile. The arrangement shown in Fig. 2A includes three 421 stages of which the X and Y axes are controlled manually by micrometer screws, whereas the Z axis for electrode placement on the cell uses an 860A DC motor controlled by a hand-held battery operated manipulator (model 861). This arrangement has proven to be very stable and relatively inexpensive.

3.4. Experimental Procedure

During electrode placement, electrode resistance is monitored continuously by applying a small voltage pulse (1–5 mV, 2–10 ms) to the electrode (Fig. 3A). Once in contact is made with the cell, electrode resistance spontaneously increases by 10–50%. Application of gentle suction to the electrode by mouth or a small syringe quickly results in the formation of a gigaseal (Fig. 3B). At this point, seal quality can be improved by applying a negative holding potential to the pipet. In this cell-attached configuration, pipet capacitance transients (C_p) are reduced using the fast compensation adjustment at the amplifier (Fig. 3C). This compensation of pipet capacitance is essential for proper series resistance compensation. Should compensation be incomplete, coating of future electrodes

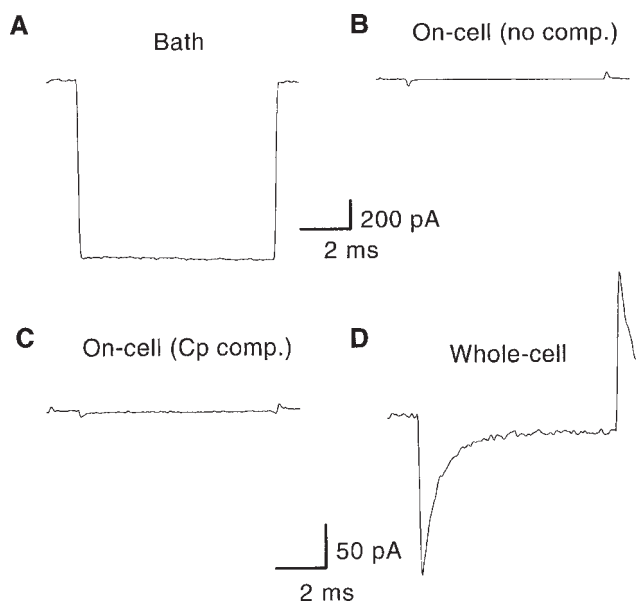


Fig. 3. Oscilloscope traces before and during establishment of whole-cell recording. (A) Electrode in bath ($V = 0$ mV). (B) On cell after formation of giga-seal ($V = 0$ mV). (C) As in (B) after C_p compensation. (D) After rupturing patch, whole-cell configuration but prior to cell capacitance and series resistance compensation ($V = -80$ mV).

with Sylgard (Dow Corning) or lowering the bath perfusion level is recommended to reduce the residual transients and improve C_p compensation. Following pipet capacitance cancellation, a brief pulse of suction will rupture the membrane patch under the electrode providing low-resistance access to the cell. This also results in large capacity transient arising from the added membrane capacitance (Fig. 3D). Immediately after rupturing the membrane, a reading of the cell's potential should be obtained (at $T = 0$) as this access potential is as close to the actual resting potential reading that can be obtained. Within minutes of establishing a whole-cell configuration, the pipet contents will equilibrate with the cells cytoplasm and will impose an artificial ionic potential across the membrane. Next, by adjusting the capacitance and series resistance (R_s) compensation and gradually increasing the % compen-

sation, effective R_s compensation should be possible under most circumstances. Ideally, access resistance should be <10 MOhm prior to activating R_s compensation. Under these conditions 80% compensation results in a <2 MOhm residual uncompensated series resistance. Series resistance and capacitance compensation result in a change of the step waveform applied without actually changing access resistance or the cell capacitance per se (*see below*). The procedure for establishing whole-cell configuration and all necessary compensations are nicely illustrated in the manuals of both the List EPC7 and Axon Axopatch 1 D amplifiers.

Due to the intracellular perfusion of cytoplasm with pipet solution, it is advisable to wait several minutes prior to obtaining recordings to assure that this dialysis has reached a steady-state. Diffusion rates depend on molecular weight and charge of the diffusing particle, such that longer diffusion times are expected for relatively large, uncharged molecules as compared to small ions. For substances of molecular-weight 23–156,000 diffusion rates have been determined in adrenal chromatin cells, and these suggest that complete dialysis of these small cells occurs on the order of tens to hundreds of seconds (Pusch and Neher, 1988). If dialysis of the cell is incompatible with the experimental design, e.g., when ionic currents are studied that are under control of second messengers, the perforated-patch method should be used instead (*see Chapter 6, this volume*).

4. Data Evaluation and Analysis

4.1. Data Filtering/Conditioning, Acquisition, and Storage

4.1.1. Filtering

Data are rarely acquired and stored without further modifications. The analog output of the amplifier is typically amplified to make effective use of the dynamic range of the acquisition device. In the case of an A/D converter, this typically translates to an amplification range of -10 V to 10 V. At the same time, signals are filtered, often using the built-in signal filter.

Filtering of data is both essential and inevitable. Due to the RC components of the cell membrane-series resistance combination, the cell and electrode are essentially a single-stage RC filter. This is important to bear in mind as it can significantly affect the true time-resolution of a recording. Assuming that $R_s \ll$ membrane resistance

(R_m), uncompensated R_s will filter any current flow recorded with a -3dB cut-off frequency described by $F = 1 / (2\pi \cdot R_s \cdot C_m)$. Assuming, for example, a cell capacitance of 20 pF and a series resistance R_s of 10 MOhm , values typical of small-cell recordings, currents across the membrane will be filtered with an effective F of $\sim 800\text{ Hz}$.

Irrespective of the intrinsic filter properties of the analyzed cell, data filtering is essential to reduce signal components that are outside the bandwidth of interest. Filtering “condenses” the time domain of the signal to the domain of interest. The fastest signals recorded under whole-cell conditions are on the order of $200\text{--}500\text{ }\mu\text{sec}$ ($2\text{--}5\text{ kHz}$). Note that this is of the same order of magnitude as the membrane- R_s filter time-constant above. To eliminate high-frequency noise, a low-pass filter is used. An ideal filter has a steep roll-off, and does not greatly distort signals. Four- or 8-pole Bessel filters have excellent characteristics for filtering whole-cell currents. Comparison of the filter characteristics of a 4- and 8-pole Bessel filter are demonstrated by comparing the onset response of a square pulse before and after filtering at various cut-off frequencies (Fig. 4). In these examples, an 8-pole Bessel filter clearly provides excellent signal filtering with least distortions (Fig. 4A–E). However, at cut-off frequencies above 2 kHz , 4- and 8-pole filters do not differ significantly in the onset or settling time.

4.1.2. Sampling Rate and Dynamic Range of Signal

When using an A/D converter to digitize signals, it is important to select the appropriate filter and sampling rates to accurately represent the analog signal of interest. It is inevitable that A/D conversion will reduce the “infinite” dynamic range of the analog signal to a well-defined step-like range of the digital signal. Commonly used 12-bit converters (for example the Axon Digidata 1200) divide the amplitude range into 4096 discrete steps, which at a -10 V to 10 V signal range will yield steps of 4.88 mV . In theory, signals can be sampled at the highest possible rate supported by the A/D converter. However, practical limitations exist. Most affordable A/D boards sample at $100\text{--}330\text{ KHz}$ on a single channel, thus allowing to sample in $3\text{--}10\text{ }\mu\text{sec}$ intervals. Depending on the duration of the signal, sustained sampling at $10\text{ }\mu\text{sec}$ will generate very large amounts of data, requiring significant disk space. A vast majority of this data will not contain necessary information. The Nyquist Sampling Theorem states that the minimum sampling rate (Nyquist frequency) required to accurately

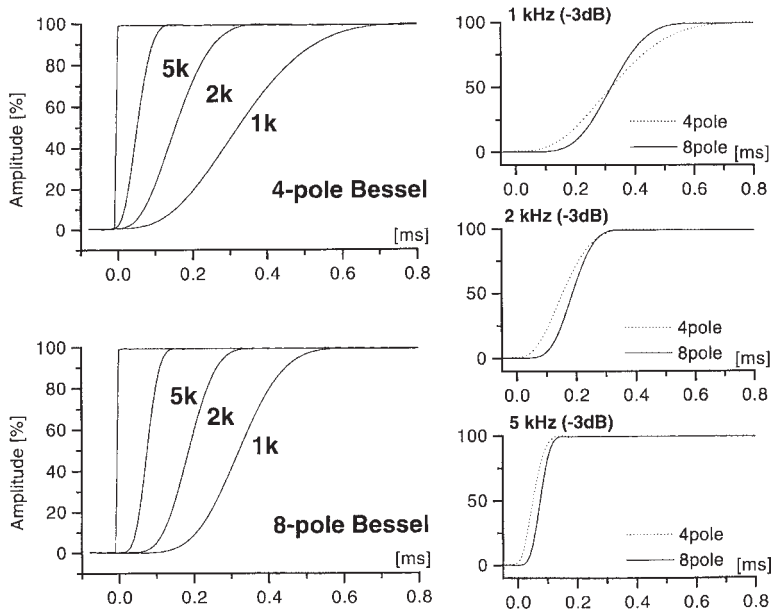


Fig. 4. Frequency response of 4- and 8-pole Bessel filter to square pulse. A 2 ms square pulse was applied to a Frequency Device model 902 8-pole Bessel filter as compared to the built-in 4-pole Bessel filter of the Axopatch 1D amplifier. The graphs illustrate differences in response characteristics at three commonly used -3dB cutoff frequencies (1, 2, and 5 kHz).

represent an analog waveform is twice the signal bandwidth. As a consequence, if the analog filter is set at a -3dB cutoff frequency of 3 kHz, a minimum sampling frequency of 6 kHz or 167 μs intervals is required. While these minimum requirements will allow the reconstruction of data with little error under most circumstances, a sampling frequency 5 times the -3dB frequency is commonly recommended for actual recordings.

4.1.3. Aliasing

The Nyquist Sampling Theorem only applies when sampling data digitally at frequencies between 0 and the Nyquist frequency. If frequencies higher than the Nyquist frequency are sampled, they are “folded back” into the low-frequency domain, a process

called “aliasing.” Essentially these high-frequency signals will affect and distort those signals within the appropriate frequency domain. Aliasing can be prevented if signals above the Nynquist frequency are cut off by a low-pass filter. A proper matching of filter frequency and sampling rate is thus important to accurately reproduce analog waveforms. In practical terms this requires that the cut-off frequency of a low-pass filter be set to no higher than half the sampling frequency. In the previous example, the low-pass filter was set at 3 kHz.

4.1.4. Data Storage

On-line digitization has the advantage that data can be directly stored in computer memory or hard disk. This mode of data storage is preferred as it gives convenient and fast access to the data for future evaluation. Using a 12-bit A/D converter, each data sample uses 2 bytes of information. Thus a 2048 sample trace requires about 4 kbytes of memory or disk-space. A continuous sampling of neuronal discharge at a frequency of 50 kHz generates 100 kbyte of data every second. A 5-min recording would thus require 300*100 kbyte or 30 Mbyte of disk space. It thus becomes apparent that practical limitations exist as to the on-line digitization of data. For prolonged recordings at high frequencies (<40 kHz), a VCR recorder (such as the Neurocorder) may be used as an interim storage for data. Segments can subsequently be played back to the A/D converter for data analysis. For brief signals, on-line storage is not an issue, as hard-disk space has become affordable at <\$0.1 per Mbyte. Recordable CD-R disks are a practical and cheap way to archive data.

4.2. Leak/Subtraction

Currents across a cell membrane consist of two components: ionic current flowing through ion channels of interest, and capacitive current that charges the membrane. Capacitive current contains useful information pertaining to the cell size, as an approximation of cell size (or more precisely, membrane area of the recorded cell) can be derived from the capacitive current. However, in the study of ionic currents, capacitive currents are of relatively little interest. As ideally capacitive currents are linear and not voltage-dependent, they can be subtracted from the signal of interest, through a process called “leak subtraction.” This subtraction can

be done either on-line or off-line. Two protocols for leak subtraction are typically used: 1) If the nature of the experiments permit, currents are recorded sequentially in the absence and presence of specific ion-channel blockers (e.g., TEA, TTX, 4-AP). As specific blockers will eliminate ionic current but should not alter the capacitive or leakage current, subtraction of the two traces/or set of traces should result in the removal of capacitive and leakage currents. 2) If this approach is not possible, P/N leak subtraction as first proposed by Bezanilla and Armstrong (1977) can be obtained. In this subtraction scheme, each "test" voltage step is preceded by a series of N (typically 4) "leak" voltage steps of $1/N$ ($1/4$ or $-1/4$ dependent on polarity) amplitude of the test pulse activated from a potential at which no voltage-activated currents are activated. In a P/4 protocol, these $4 * 1/4$ amplitude traces are summed together (Fig. 5B) and are subtracted from the actual current trace of interest (Fig. 5A) and will isolate the ionic current of interest (Fig. 5C). The example demonstrated in Fig. 5 actually used a P/-4 protocol, in which 4 hyperpolarizing pulses of $-1/4$ amplitude were summed and added to the current trace of interest. It is important to obtain the "leakage" current at potentials at which no voltage-activated currents occur. Most often this can be achieved by stepping to potentials negative of the resting potential (as illustrated). However, some cells express inwardly rectifying (or anomalous rectifying) currents that are active at the resting potential and negative thereof. Under these circumstances leak currents must be recorded at potentials at which the I-V curve is linear and no voltage-dependent currents are activated. Note that subtraction of capacitive and leakage currents is purely cosmetic. It does not actually improve the signal recorded. However, it may allow revealing small current components that would otherwise be hard to identify. If capacitive currents are not of interest, it is recommended that P/4 leak subtraction be performed on-line by the data-acquisition program because it significantly reduces the amount of data stored.

4.3. Determination of Cell Capacitance

Biological membranes are lipid bilayers in which membrane proteins (e.g., ion channels and transporters) are contained. The specific capacitance of biological membranes seems to be fairly constant. It is relatively independent of cell type and a value of

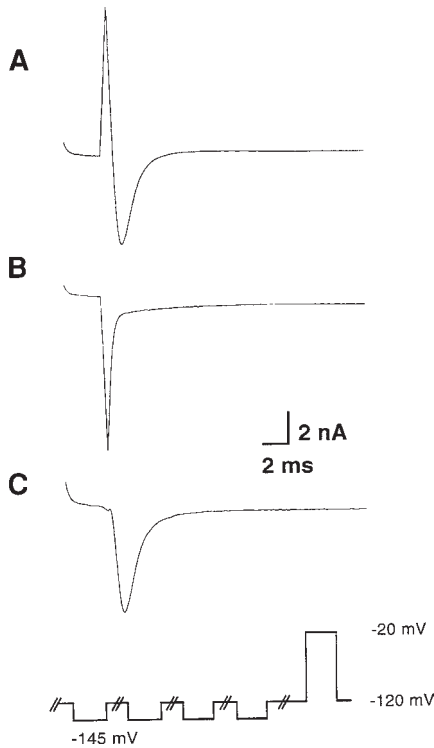


Fig. 5. Capacitive and leakage current subtraction using P/-4 method. (A) Whole-cell current recorded in response to voltage step from -120 mV to -20 mV. (B) Summed response of $4 \times -1/4$ amplitude voltage steps as indicated at bottom of (C). (C) Added response of (A) and (B) eliminating capacitive current.

$1 \mu\text{F}/\text{cm}^2$ is typical. The capacitance cancellation circuits of patch-clamp amplifiers are normally calibrated in pF, and allow direct determination of the cells capacitance by adjusting and minimizing the capacity transients in response to a voltage step as discussed previously. The dial reading provides at least a rough determination of membrane capacitance on which bases estimates can be made as to the membrane area, as 1 pF capacitance represents $100 \mu\text{m}^2$ of membrane.

Capacitance can also be derived from the capacity transient at any time during the recording. In response to a voltage step, capac-

itance is proportional to the integral of the charging transient, thus it can be derived by determining the area under the transient of a currents trace. Neher and Marty (1982) have developed a very sensitive approach of measuring changes in membrane capacitance using a phase-lock amplifier, which measures currents in and out of phase with a sinusoidal voltage change. This approach can resolve capacitance changes of 10 fS and has been used to resolve the fusion of synaptic vesicles by a step increase in capacitance.

4.4. Dissecting Current Components

Whole-cell recordings integrate the response of a large number of potentially heterogeneous ion channels. Separation of these ionic current components is a critical step during or following current recordings. Four methods of current isolation are commonly used to isolate voltage-activated ionic currents:

1. Kinetically:

Certain types of ion channels activate and inactivate much faster than others. For example, Na^+ currents typically activate within 200–300 μsec and inactivate completely within 2–5 msec. In contrast, K^+ currents may take several msec to activate, and often inactivate slowly, if at all. Simple current isolation can thus be accomplished by studying whole-cell currents at different time points following stimulation, e.g., determining Na^+ current amplitudes at 300–500 μsec , and determining K^+ current amplitudes after tens or hundreds of msec.

2. Current subtraction via stimulus protocols:

Voltage-dependence of the steady-state activation and inactivation of currents often allows selective activation of subpopulations of ion channels. For example, low- or high-threshold Ca^{2+} currents can be activated separately by voltage steps originating from different holding potentials. Similarly, depolarizing voltage steps applied from very negative holding potentials (e.g., -110 mV) can activate both transient “A” type (KA) and delayed-rectifying (Kd) K^+ currents (Fig. 6A). Voltage steps applied from a more positive holding potential (e.g., -50 mV) will completely inactivate all KA channels while not affecting Kd activity (Fig. 6B), such that subtraction of currents recorded with these two protocols effectively isolates KA currents (Fig. 6C).

3. Through “Isolation Solutions” (Ion Dependence):

It is common practice to specifically design the composition of ionic solutions to favor movements of desired ions. As mentioned

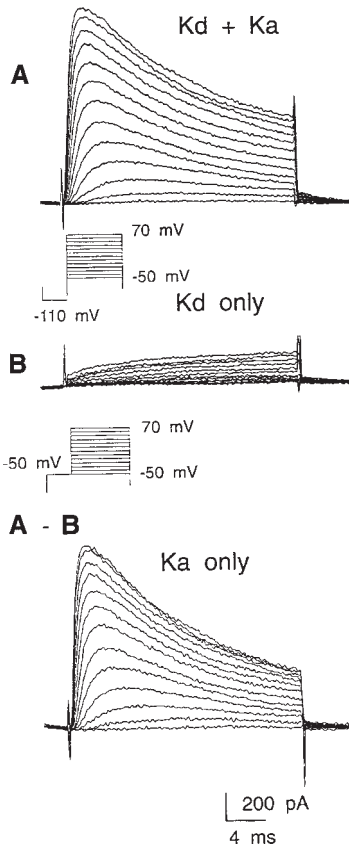


Fig. 6. Isolation of K_a current by subtraction. Current recordings from a spinal-cord astrocyte expressing both transient (K_a) and delayed rectifier (K_d) like K^+ currents. (A) Currents activated from holding potential of -110 mV (step protocol see inset). (B) same cell and same voltage-step protocol but steps originated from holding potential of -50 mV. Subtraction of (A) - (B) yielded K_a currents in isolation.

previously, dialysis of cytoplasm with patch pipet contents occurs rapidly after whole-cell configuration is achieved, thus allowing for manipulation of internal ionic concentrations. This access can be used to block most K^+ channel activity by replacing pipet KCl with impermeant Cs^+ or N-methyl-D-glucuronate (NmDG), thus

Table 1
Commonly Used Ion-Channel Blockers

Channel Type	Compound/Reagent
K ⁺ channels	
Delayed rectifier (Kd)	TEA, Ba ²⁺ , capsaicin, 4-AP, margatoxin
Inward rectifier (Kir)	TEA, Cs ⁺ , Rb ⁺ , Na ⁺ , Ba ²⁺
A	TEA, 4-AP, dendrotoxin
K(Ca)	
Big K	Charybdotoxin, iberiotoxin
Small K	Apamin
K(ATP)	TEA, Cs ⁺ , Ba ²⁺
Na ⁺ channels	TTX, STX, CNQX, agatoxin, Scorpion toxin
Ca ²⁺ channels	
L-type	Nifedipine, verapamil, BayK8644, Cd ²⁺ , La ³⁺
T-type	Ni ²⁺ , La ³⁺
N-type	ω-conotoxin, La ³⁺
P-type	FTX funnel spider toxin
Cl ⁻ /anion channels	Chlorotoxin, avermectin B, NPPB, DIDS, Zn ²⁺

allowing isolation of Na⁺ currents. In a similar fashion, acetate, glucuronate, or isothionate can each be substituted for Cl⁻ ions, and tetramethyl-ammonium chloride (TMA-Cl) can be substituted for Na⁺ ions. It has even been reported that the contribution of one ion-channel population can be determined by replacement of all but the desired ion with glucose or sucrose.

4. Current Isolation Via Pharmacology:

Numerous natural toxins and synthetic pharmacological agents exist that can be used to reduce or eliminate specific voltage-activated ion channel activity (for excellent review, TINS Suppl., VOLUME, 1994). A list of some of the more commonly used agents is shown in Table 1. Many of these agents are effective against one particular type of ion channel, such as Tetrodotoxin and dendrotoxin, which target Na⁺ and K⁺ channels, respectively. The use of these compounds, either alone or in combination, allows the isolation of specific current(s).

Experimentally, currents are best identified pharmacologically by recording a family of current traces in both the absence and

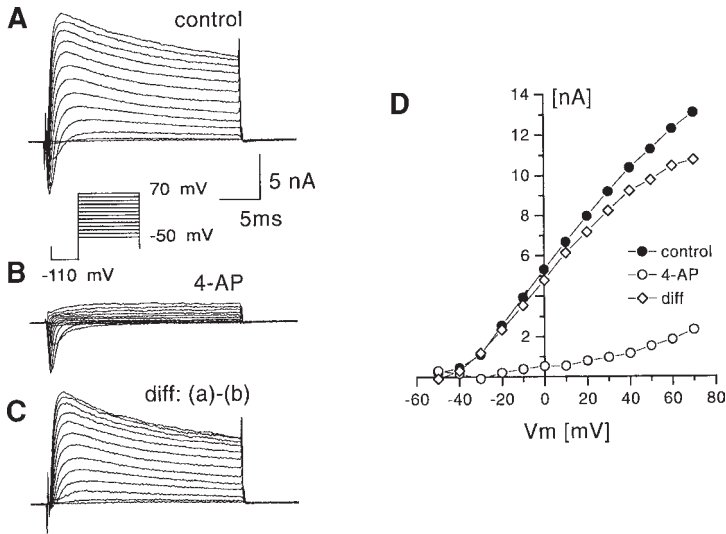


Fig. 7. Pharmacological isolation of 4-AP sensitive K^+ current. (A) Family of current traces recorded from a spinal cord astrocyte using step-protocol indicated in inset. (B) Recording in the same cell using the same stimulus protocol 2 min after application of 2 mM 4-AP. (C) 4-AP sensitive current isolated by subtraction of (A) - (B). (D) Current amplitudes determined 8 msec after onset of voltage steps plotted as a function of applied potential for current traces in (A-C).

presence of drug. This is illustrated in Fig. 7, in which the block of spinal-cord astrocyte K^+ currents by 4-amino pyridine (4-AP) is shown. In the control and treated current traces (Fig. 7A,B), the inward sodium current is unaltered. By subtracting the 4-AP-treated current traces from those of control, one can isolate the current component that is 4-AP-sensitive. As discussed previously, a side benefit to such current subtraction is the elimination of capacitive and leakage currents.

Neurotransmitter-activated currents are perhaps easier to identify and isolate than their voltage-dependent counterparts, as these currents are induced in a time-dependent manner based on the application of exogenous ligands. If need be, ligand-gated current can be isolated from background noise by subtracting recorded currents in the absence and presence of a given ligand.

4.5. I-V Curves

Current-voltage (I-V) relationships are perhaps the most effective way to summarize the behavior of voltage- and ligand-activated ion channels. A number of important and useful parameters that can not be easily accessed from the raw data can be readily derived from these plots, including: reversal potential, ionic dependence/selectivity, voltage-dependence (rectification), activation threshold, slope and cord conductance, as well as overall quality of voltage-clamp. I-V curves can be determined in various ways, examples of which are discussed below.

The factors that determine current flow through an open channel are conductance and driving force. While conductance is proportional to the number of open channels, driving force is defined as the difference between actual voltage and the equilibrium potential for the ion(s) permeating the channel, also known as reversal potential (V_{rev}). Thus current can be described as $I = G (V_m - V_{rev})$.

A plot of I vs V_m is commonly used to derive G (slope) or V_{rev} (X-intercept). The current evoked at a given V_m can be measured using a variety of protocols.

4.5.1. Peak and Steady-State IV Curves

Peak currents are measured as the largest current activated by the applied voltage (Fig. 7C). Thus, if a current has a transient peak current amplitude, such as the KA current in Fig. 7A, analysis software can easily determine maximal current and plot these values against voltage (Fig. 7C). If the current to be studied does not have this defined peak, steady-state values may be used, typically as recorded at the end of a voltage step. This type of analysis was applied to the 4-AP-treated current traces of Fig. 7B, with the resulting amplitudes similarly plotted in Fig. 7C.

4.5.2. Continuous "Quasi Steady-State" I-V Curves

A convenient way to establish I-V curves is by alteration of the membrane potential in a continuous way through a voltage ramp. As this ramp can be applied very slowly, it allows to acquire a "quasi steady-state" I-V relationship. This procedure has proven very useful in determining I-V relationships for transmitter responses. Note, however, that this approach assumes that currents do not inactivate during the length of the voltage ramp. An example of a voltage ramp used to determine the reversal potential of GABA induced currents is illustrated in Fig. 8. A 200 mV, 400 ms voltage

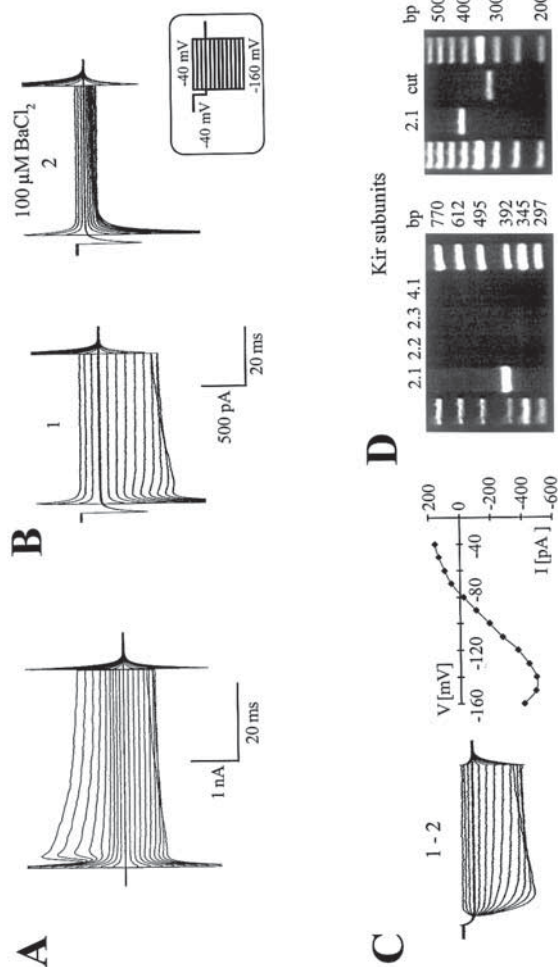


Fig. 6. Kir subunit expression by an individual glial cell. (A) Membrane currents were activated in response to de- and hyperpolarizing voltage steps between -160 mV and $+20$ mV (10 mV increments, holding potential -70 mV). (B) In BaCl₂ solution (2), the cell's resting potential shifted from -72 to -53 mV. (C) gives the Ba²⁺-sensitive current (1-2) with its I/V relation. (D) After recording, the cytoplasm was harvested for RT-PCR analysis. In this cell, gel electrophoresis detected only Kir2.1 cDNA (408 bp; left panel). The second round of Kir2.1 PCR was repeated and the resulting PCR product was cut by *Bsa*HI (318 bp, right panel).

ramp as indicated in the inset to Fig. 8A was applied twice. Once prior to application of GABA (control) and once during transmitter application (GABA). By subtracting the two responses one obtains the transmitter induced current in isolation. As the time axis represents a constant change in the voltage applied, it can be instantaneously replotted as I-V relationship of the transmitter induce current (Fig. 8B). Using this approach I-V curves of transmitter responses can be easily created throughout an experiment. As mentioned earlier, alteration of ionic composition allows to shift the reversal potential and thus allows to determine ion specificity and relative permeabilities.

For those situations where currents inactivate rapidly, some indication as to the reversal potential can be obtained using a single-step protocol from which the reversal potential can be extrapolated. An example of this approach is illustrated in Fig. 8C. Here, a larger concentration of GABA was bath applied which resulted in characteristic receptor desensitization. The cell was maintained at -80 mV and a single 80 mV step (50 ms) was applied prior to and at the peak of the transmitter response. Current levels at the two potentials, -80 mV and 0 mV were then subtracted and plotted as a function of applied potential (Fig. 8D). The line through the two data points clearly does not reflect the true IV relationship of the response, however, it allows to determine with fair accuracy the reversal potential of the response. To obtain a more complete I-V relationship, the two previous voltage steps can be substituted by trains of voltage steps.

I-V plots may also be used to determine the quality of the voltage clamp achieved. If the reversal potential (Equilibrium potential) is known, as is the case when isolation solutions limit ionic movements to only one ion, or when it is clearly established, as in the case of GABA_A receptors that currents are mediated predominantly by one ion. Under the imposed ionic conditions, currents must reverse close to the theoretical equilibrium potential for the permeable ion. In poorly voltage-clamped cells, reversal potential is either not achieved, or at potentials more positive than the equilibrium potential (*see next paragraph for further discussion*).

4.5.3. Conductance-Voltage Curves

If the reversal potential is known, a conductance voltage (G-V) curve can be readily calculated by dividing current at each potential by the driving force ($V - V_{rev}$). These curves are typically sigmoidal

and can be fitted by a multistage Boltzmann function. Provided that current through a single channel is linear, conductance is proportional to the number of open channels. Thus the G-V curve resembles an activation curve.

4.5.3. Steady-State Inactivation Curves

Voltage dependence of current inactivation allows to determine the fraction of channels available for activation as a function of voltage. Currents are activated by a step to potentials at which the largest conductance is achieved. This voltage step is preceded by variable prepulse potentials at which the membrane is maintained for 200–1000ms (Fig. 9A). Current amplitudes at each potential are normalized to the largest current recorded and plotted as a function of prepulse potential (Fig. 9B). These curves can be fitted to a multistage Boltzmann function. In the experiment illustrated, a potential of ~ -80 mV yielded about 50% of Na^+ channels available for activation (dashed line).

4.5.5. Deactivation I-V Curves

As voltage-dependent currents are often also time-dependent, and may activate and/or inactivate in a time-dependent manner, I-V curves as described above cannot distinguish between time- and voltage dependence. An elegant way to determine conductance independent of its time-dependence is provided by analyzing the deactivation process (Fig. 9C,D). Upon termination of the voltage step, deactivation, which is the reversal of activation, results in tail currents (Fig. 9C, dotted line). Immediately after terminating the voltage step, for a brief period of time current continues to flow through open channels and only subsequently terminates with time-dependent channel closure (relaxation of tail currents). Thus, current amplitudes measured at the peak of these tails resembles time-independent current amplitudes, and these typically yield linear I-V curves (Fig. 9D).

4.6. Fitting of Time-Constants

Current activation and inactivation kinetics have been well-described by mathematical models. If the model is known, the data can be fitted to the model and will allow to derive important kinetic properties, such as time-constants for activation (τ_m) and inactivation (τ_h), respectively (Hodgkin and Huxley, 1952). Often

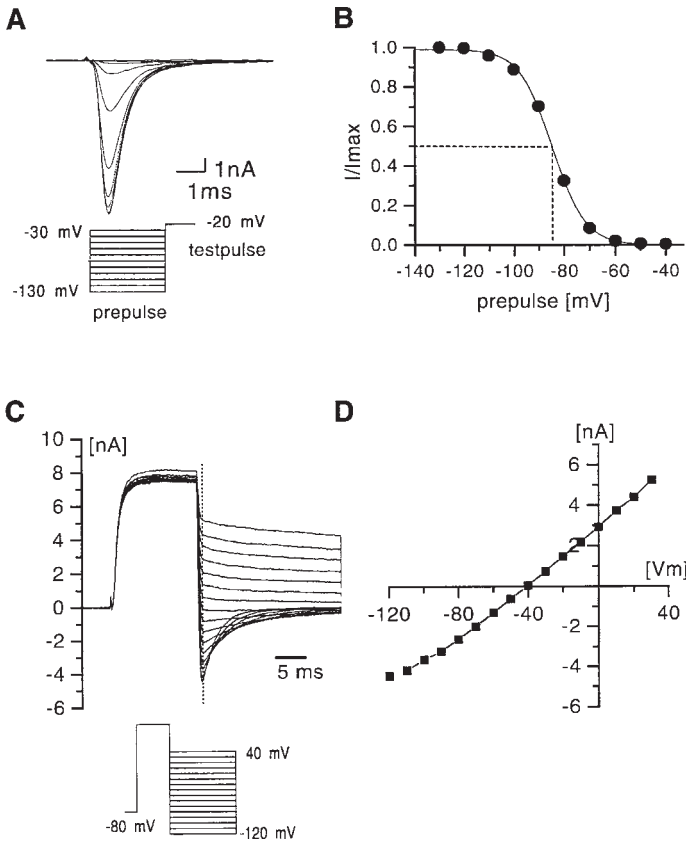


Fig. 9. Steady-state inactivation and tail-current analysis. Current recordings from two different spinal-cord astrocytes. (A) To study steady-state current inactivation, inward Na^+ currents were activated by stepping the membrane to -20 mV for 8 msec. Voltage step was preceded by varying prepulse potential ranging from -130 mV to -30 mV (step protocol *see* inset). (B) Peak current amplitudes in (A) were normalized to the largest current amplitude and plotted as a function of prepulse potential. The data was fitted to a two-stage Boltzmann equation (solid line) to yield steady-state inactivation (h_∞) curve. (C) Tail current analysis. Outward currents were activated by a 15 ms voltage step from -80 mV to 80 mV. This step was followed by a second step to varying test potentials ranging from -30 mV to -120 mV (*see* inset), resulting in "tail" currents. (D) Current amplitude of tail currents was measured 500 usec after stepping potential to second step potential (dotted line) and plotted as a function of applied potential to yield tail current I - V curve.

times the models used are an oversimplification of the true biology. This is particularly true for fitting of whole-cell data for two reasons. First, whole-cell current may be mediated by the combined activation of numerous channels types, and second, even if one can be reasonably sure that currents are mediated by a single-channel population, the biophysics of this channel type, e.g., the number of open and closed states may be unknown.

Fitting routines are an integral part of numerous data-acquisition or data-analysis packages. Most commonly these use either a Simplex or a Levenberg-Marquard algorithm to minimize the least squared error. Both algorithms are capable of producing excellent and fast fitting to small data sets. Examples of Levenberg-Marquard fits are demonstrated for two examples in Fig. 10. These were obtained using the script interpreter of Origin (Mico Cal) by fitting to user-defined functions. The examples illustrated fitted multiple parameters simultaneously. Thus, in a) transient K^+ current activation and inactivation was fitted to a n4g model of the form: $f(t)=AO+A1*(1-EXP(-(t-tO)/\tau m))^4 * (EXP(-(t-tO)/\tau h))$ as used by Connor and Stevens (1971) to describe kinetics of A-currents, in b) Na^+ current activation and inactivation was fitted to the Hodgkin-Huxley equation: $f(t)=AO+A1*(1-EXP(-(t-tO)/\tau m))^3 * (EXP(-(t-tO)/\tau h))$. It is important to keep in mind that data fits are not sufficient to formulate a model, but rather assume that the model is known and used to derive variables such τm and τh contained in the model.

4.7. Data Presentation

Presentation of patch-clamp data has become significantly easier with the advent of micro-computer based data acquisition, virtually eliminating the use of scissors and glue. Digitized data can be easily exported in ASCII format and read into numerous powerful spreadsheet programs (Excel, Lotus, Quattro, SigmaPlot, Origin, PlotIt). More recently, two scientific spreadsheet programs (Origin, PlotIt) have included import modules that allow to import Axon binary data. Thus without prior conversion, axon data files can be imported for plotting, data analysis, and graphing. The authors' laboratory is currently using Origin, which is based on a scientific scripting language LabTalk for which a script interpreter is part of the program. This allows simple programming of frequently used commands or sequences of commands into "macros," which can be assigned to visual buttons on the screen. This allows the computer

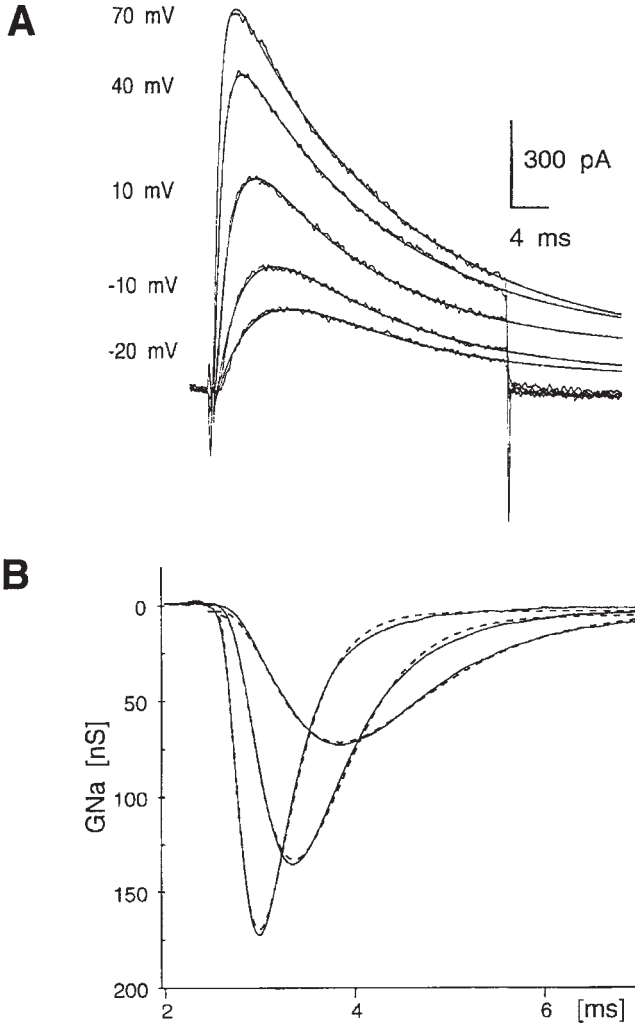


Fig. 10. Fitting of current traces using least squared fit. (A) Transient outward K^+ and (B) inward Na^+ currents were fitted to established kinetic models using a Levenberg-Marquard algorithm to minimize the least squared error. Fitted curves were superimposed on data. The models used were: (A) $n4h$ describing transient K^+ current according to Connor and Stevens (1971): $f(t) = AO + A1 * (1 - \text{EXP}(-(t-tO)/\tau_m))^4 * (\text{EXP}(-(t-tO)/\tau_h))$. (B) the Hodgkin-Huxley (1952) equation to described Na^+ current kinetics: $f(\tau) = AO + A1 * (1 - \text{EXP}(-(t-tO)/\tau_m))^3 * (\text{EXP}(-(t-tO)/\tau_h))$.

literate (nonprogrammer) to design custom data-analysis and graphing schemes. As most of the graphing programs are Windows-based, merging of graphs into word processors or other drawing programs is easy. Finally, high-quality affordable laser printers have made plotters obsolete. Most of these printers, such as the HP Laserjet 4, will readily accept 80g glossy paper, providing a quality printout that is indistinguishable from glossy photographs.

5. Limitations, Pitfalls, and Errors

5.1. Series Resistance and its Consequences

As mentioned previously, the major limitations of the whole-cell patch-clamp recording technique lies in its design as a continuous single-electrode voltage clamp. The continuous use of one electrode for current passage as well as voltage sensor makes true membrane voltage determination impossible. The technique assumes that pipet voltage equals membrane voltage, as voltage commands are imposed on the pipet, not on the cell. However, recording pipet and access resistance (due to potential clogging at the electrode tip) are in series with the current recording and the voltage command. This series resistor in conjunction with the membrane resistance acts as voltage divider to all imposed voltages. Consequently, only in cases where the membrane resistance greatly exceeds the series resistance is an adequate voltage clamp (point clamp) assured. Under experimental circumstances, series resistance accounts for at least 5, more typically 10–15 MOhm. In order to keep the voltage error below 1%, membrane resistance has to be two orders larger than the series resistance, in our example ~1 GOhm. This is hardly the case, and certainly does not hold true during activation of ionic currents! In order to assure best possible recording conditions, the following steps are absolutely necessary:

1. Electrode resistance has to be minimized as much as possible, depending on the size of the cells to be studied. In our experience, and dependent upon the solutions used, cells from 8–40 μm in size can be successfully patched with electrodes 1.5–3 MOhm range. However, once the whole-cell recording configuration has been achieved, it is important to frequently check for adequate compensation. If all compensation mechanisms are turned off, one may see a dramatic decrease in the magnitude of initial capacitance transients observed. The most likely explanation for such a change is the clogging of the electrode tip with cell membrane,

which directly interferes with clear access to the cell's interior. This phenomenon of membrane "healing" around the electrode tip can be prevented by buffering $[Ca^{2+}]_i$ using high concentrations of EGTA or BAPTA. In an acute situation, slight positive or negative pressure can reverse electrode clogging. In our experience, it is possible to achieve access resistances of 5 MOhm prior to series resistance compensation.

2. Series resistance (RS) needs to be compensated for. Most patch-clamp amplifiers provide a positive feedback series resistance compensation circuit, in which a signal proportional to the measured current is added to the command potential. RS is determined by adjusting Rs and Cp controls to square out a command voltage. Subsequently, Rs compensation is activated. Although, theoretically, near 100% compensation is possible, real experiments hardly allow gain setting of more than 50–80%. Rs compensation scales the command input to account for the voltage loss across Rs. Rs compensation is very sensitive to changes in the fast (pipet) capacitance compensation. It is essential to adjust this compensation properly to achieve maximum % compensation settings. Note that continuous bath perfusion may result in some oscillations of the bath fluid level. As a consequence, this would also change the effective capacitance of the pipet and would make the fast capacitance compensation unstable and thereby Rs compensation prone to ringing. Effective compensation under those circumstances thus requires stable bath perfusion level. The problem can be reduced by the use of heavily silylated electrodes which have a much reduced capacitance.

In an ideal case, with Rs of 10 MOhm, a voltage step of 100 mV results in a current flow of 1 nA, and an apparent input resistance $R_{cell}+R_s$ of 100 MOhm. A 1 nA current flow across Rs generates a 10 mV voltage drop across Rs and thus a 10% error. Using Rs compensation assuming an 80% compensation the error is reduced to 2 mV or 2% of command voltage, a tolerable error. However, suppose activation of voltage-dependent channels gives rise to a 5 nA current. During the peak of this response the input resistance falls to 20 MOhm and, in the uncompensated situation, the membrane experiences only a 50 mV voltage drop! Even with 80% compensation, a 10 mV (10%) error still remains.

3. Cells with low input resistances are almost impossible to record from. Should the membrane impedance be <100 MOhm it is advisable to increase it by inclusion of ion channel blockers to

block conductances that are not of immediate interest. Thus, K^+ channel blockers could be included and Cl^- replaced by acetate to allow resolution of small Na^+ currents.

Uncompensated R_s will have two additional detrimental effects on current recordings. It will affect the time response to a voltage change, and it will result in increased signal noise. The transmembrane voltage resulting from a step change in voltage is described by $V_m = V_c [1 - \exp(-\tau/(R_s * C_m))]$ with an effective time-constant of $\tau = RC$ (if $R_s \ll R_m$). Assuming an uncompensated R_s of 10 MOhm and C_m of 100 pF charging of the membrane will be slowed with an effective time-constant (τ) of 1 msec. Unfortunately, R_s will also filter any current flow recorded with this arrangement. In the absence of compensation, this results in a single-pole RC filter with a -3dB frequency described by $F = 1/(2\pi * R_s * C_m)$ resulting in a cut-off frequency (F) of 159 Hz for previous example.

5.2. Voltage-Clamp Errors

Voltage clamp is prone to error, as it makes numerous assumption that may not be valid under the given experimental conditions. It assumes that the cell is isopotential and that the voltage measured at any one point across the membrane is the true membrane voltage. Analogously, current injection, which imposes change to the membrane voltage is thought to be uniformly realized in all parts of the membrane, including distant processes. This, however, is not the case. As a result, two sources of error exist namely voltage (point) and space clamp errors. As illustrated below, whole-cell patch-clamp recordings are even more susceptible to error than classical two electrode recordings, and as such, the experimenter needs to be constantly aware of possible sources of this error.

5.2.1. Space Clamp

Space-clamp limitations are intrinsic to voltage-clamp and do not differ in their principals between different voltage-clamp techniques. Current injected into the cell to maintain or establish a change in membrane voltage will spread radially from the injection site, and decay across distance with the space (length) constant λ . In small-diameter spherical cells, this is a minimal concern. However, in a process-bearing cell, the current signal may have distorted by the time it reaches distant processes hundreds of μm away from the injection site. In the best of circumstances, the signal will be attenuated and the voltage-changes imposed will be

smaller. In the worst case, distant membranes may not experience any voltage change at all.

Double electrode voltage-clamp methods are somewhat advantageous in that they allow to detect space-clamp problems more readily. In this case, the voltage electrode can be inserted at a distance from the current electrode, and closer to the site of interest. Whole-cell recordings clamp the voltage of the electrode tip, and thus provide no means to establish any true recording at a site distant from the electrode. Some investigators have chosen to insert a second patch-clamp or sharp microelectrode into cells to monitor the true voltage changes observed. Space-clamp problems can only be reduced by recording from small cells with simple morphology, ideally spherical cells. Nonspherical cell can sometimes be "rounded-up" by exposure to serum or treatment with dBcAMP. However, often times the most interesting cells bear extensive arborized processes. A second way to assure that injected current can travel further is to increase the cells impedance. Thus it is often possible to block parts of the cells conductance (e.g., K^+ conductance) pharmacologically to effectively increase the length constant (λ) of the cell.

5.2.2. Voltage (Point) Clamp

The whole-cell recording technique effectively voltage-clamps the electrode tip, and, by assuming that its resistance is small relative to the cell's resistance, the cell's voltage is assumed to be clamped. As described earlier, this is only the case if series resistance is small and well-compensated for. Unlike space clamp errors, point-clamp errors can be readily detected and often eliminated. After canceling series resistance error (at least partially, see above) the experimenter can calculate the voltage error, which now is a linear function of current flow. Point-clamp errors produce primarily two distortions to the recorded signal: 1) Slowing of current kinetics and 2) apparent attenuation of true current amplitudes due to uncompensated voltage error. Errors due to slow activation can be readily identified from the current traces.

5.2.3. Determining Quality of Clamp from I-V-Plots

I-V plots are a very sensitive way to evaluate point-clamp errors. Figure 11 demonstrates Na^+ current recordings from 3 different cells of a neuronal cell line (BIO4). Current recordings were obtained under appropriate and poor voltage control (Fig. 11 A-C), and

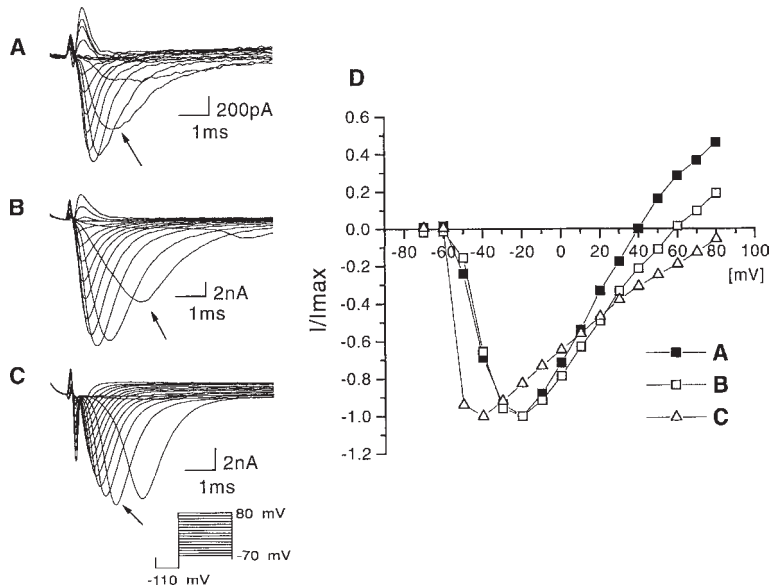


Fig. 11. I-V curves used to judge quality of point-clamp. (A–C) represent families of current recordings from three different B104 cells (neuronal cell line) using the same step protocol indicated in inset. Peak Na⁺ currents at each potential were plotted in (D). Arrows in (A–C) point to current trace in response to a -40 mV voltage step. Only the recording in (A) is under appropriate point clamp. (B) and (C) are distorted by a delay in current activation at threshold (arrows) and by a shift in I-V relationship (D) overestimating the true current reversal potential. E_{Na} was 40 mV.

peak current values were plotted as a function of membrane potential and superimposed in Fig. 11D. Under the imposed ionic gradients of the recordings, the theoretical equilibrium potential for Na⁺ was ~40 mV. The current traces in Fig. 11A yield an I-V plot that reverses close to E_{Na} indicative of proper voltage-control, whereas the traces in Fig. 11B indicate a 20 mV more positive reversal potential, and in Fig. 11C the currents do not reverse at all. Thus the I-V plot directly indicates the severity of the voltage errors in Fig. 11B and C. While the recording in Fig. 11B still yielded the same peak in the I-V relationship (at -20 mV) as the recording in Fig. 11A, the voltage step to -40 mV (arrows in Fig. 11A–C) was significantly delayed. In Fig. 11C, voltage-control is lost at the

threshold of current activation (-50 mV), and currents do not activate in a graded fashion but rather “escape” to reach near-peak amplitude with a severe delay. Similar I-V plots of transmitter-induced currents for which the major ion carrying the response is known (such as GABA) allow to utilize the reversal potential as an indicator for proper voltage control.

We have found that by minimizing R_s and utilizing I-V curves, currents of up to 10 nA can be properly voltage-clamped over a wide voltage range. However, under all these circumstances potential space-clamp errors remain, and most likely currents activated in remote processes are not recorded at all.

6. Special Applications

A number of specialized applications utilize the whole-cell patch clamp recording technique. Three of these, namely perforated patch, patch-slice, and single-cell polymerase chain reaction (PCR) are described in detailed in other chapters of this book. One application worth mentioning is the use of patch-electrodes for dye loading.

As whole-cell recordings allow low resistance access to the cell's cytoplasm, it provides a convenient means to load cells with biological markers such as fluorescence indicators, horseradish peroxidase, or biotin. Loading of cells can be used to address a number of questions:

1. As fluorescence markers may diffuse through gap-junctions, dye-diffusion can be used to search for the existence of gap-junctions between cells. While in principle, numerous low molecular-weight compounds can be and have been utilized for this purpose, Lucifer Yellow (LY) has been a long-time favorite as it is readily retained in cells even after fixation and is among the fluorescence compounds with the highest quantum yields. We have used LY as a pipet solution constituent in numerous recordings and have not detected any interference with our ability to resolve ionic currents. The use of LY to study gap-junction coupling is described in detail elsewhere (Ransom and Sontheimer, 1992).
2. LY may also be used as a cell marker allowing the localization of a cell from which recordings have been obtained. We frequently fill cells with 0.2% LY (potassium or Li^+ salt) during recordings and after fixation utilize cell-specific antibodies to antigenically identify the cell. LY is believed to form covalent

bonds with elements of the cells cytoskeleton, and is retained in cells even after formaldehyde fixation and membrane permeabilization. In some preparations, such as brain slices, LY fills are the only way to resolve the complex arborization of cell processes.

3. Although membrane-permeable AM esters exist for most ratio-metric fluorescent indicator dyes, their characteristics can differ depending on the method of cell loading (Almers and Neher, 1985). Dyes can be readily loaded through a patch pipet through which electrophysiological recordings can be obtained simultaneously while imaging an ion of interest ratiometrically.

7. Conclusions

What started out as a spin-off from single-channel patch recordings has resulted in a technique more useful than its inventors had anticipated (Sigworth, 1986). Its ease-of-use makes whole-cell recordings the most widely used intracellular recording technique to date that in many instances has replaced sharp microelectrode recordings. However, whole-cell patch-clamp recordings are notoriously prone to error and may not always generate accurate recordings. It is thus important to understand the limitations of the technique. If proper care is taken whole-cell patch-clamp allows the study of almost any small cell of interest, and has opened the field of single-cell electrophysiology. Modifications (perforated patch) and applications of the technique to more intact preparations (patch-slice) has provided invaluable insight into nervous system function.

Acknowledgments

During preparation of this manuscript HS was supported by grants RO1-NS31234 and RO1-NS36692 from the National Institutes of Health.

References

- Almers, W. and Neher, E. (1985) The Ca signal from fura-2 loaded mast cells depends strongly on the method of dye-loading. *FEBS Lett.* **192**, 13–18.
- Bezanilla, F. and Armstrong, C. M. (1977) Inactivation of the sodium channel: I. Sodium current experiments. *J. Gen. Physiol.* **70**, 549–566.
- Connor, J. A. and Stevens, C. F. (1971) Voltage clamp studies of a transient outward membrane current in gastropod neural somata. *J. Physiol.* **213**, 21–30.

- Hamill, O. P., Marty, A., Neher, E., Sakmann, B., and Sigworth, F. J. (1981) Improved patch-clamp techniques for high-resolution current recording from cells and cell-free membrane patches. *Pflügers Arch.* **391**, 85–100.
- Hodgkin, A. L. and Huxley, A. F. (1952) A quantitative description of membrane current and its application to conduction and excitation in nerve. *J. Physiol. (London)* **117**, 500–544.
- Hodgkin, A. L., Huxley, A. F., and Katz, B. (1952) Measurement of current-voltage relations in the membrane of the giant axon of loligo. *J. Physiol. (London)* **116**, 424–448.
- Neher, E. (1982) Unit conductance studies in biological membranes. *Techn. Cell. Physiol. P* **121**, 1–16.
- Pusch, M. and Neher, E. (1988) Rates of diffusional exchange between small cells and a measuring patch pipette. *Pflügers Arch.* **411**, 204–211.
- Ransom, B. R. and Sontheimer, H. (1992) Cell-cell coupling demonstrated by intracellular injection of the fluorescent dye Lucifer yellow, in *Electrophysiological Methods for In Vitro Studies in Vertebrate Neurobiology* (Kettemann, H. and Grantyn, R. eds.), Wiley-Liss, New York, pp. 336–342.
- Sigworth, F. J. (1983) Electronic design of the patch clamp, in *Single-Channel Recording* (Sakmann, B. and Neher, E. eds.), Plenum Press, New York, pp. 3–35.
- Sigworth, F. J. (1986) The patch clamp is more useful than anyone had expected. [Review]. *Feder. Proc.* **45**, 2673–2677.

Recommended Readings

For a more in depth description of the patch-clamp technique, the following books are highly recommended (in chronological order):

- Sakman, B. and Neher, E. (eds.) (1983) *Single-Channel Recording*. Plenum Press, New York.
- Ferreira, H. G. and Marshall, M. W. (eds.) (1985) *The Biophysical Basis of Excitability*. Cambridge University Press, London.
- Jones, S. (1990) Whole-cell and microelectrode voltage clamp, in *Neuromethods*, vol. 14, (Boulton, A. A., Barker, G. B., and Vanderwolf, C. H., eds.), Humana Press, Totowa, NJ.
- Hille, B. (2001) *Ionic Channels of Excitable Membranes*. Sinauer, Sunderland, MA.
- Rudy, B. and Iverson, L. E. (eds.) (1992) *Ion Channels, Methods in Enzymology*. Academic Press, San Diego, CA.
- Sherman-Gold, R. (ed.) (1993) *The Axon Guide for Electrophysiology & Biophysics Laboratory Techniques*. Axon Instruments, Inc.

3

Single-Channel Recording

David J. A. Wyllie

1. Introduction

The ability to record the 'real-time' movement of a protein is quite enthralling—in effect this is what we achieve when we record the activity of an individual ion channel. Clearly we do not 'see' amino acids that make up the ion channel undergo the conformational changes that must occur, but we observe the consequences: the current flow through the ion channel pore. The currents that flow are very small, a few picoamperes (10^{-12} A), and, in the case of the nicotinic acetylcholine receptor found at the muscle endplate for example, represent the net movement of about 25,000 monovalent ions per millisecond through the channel pore. These currents are recorded using an electrophysiological technique termed 'patch-clamp recording'. The term 'patch' is self-evident; we record ion channel activity from a small area of membrane. The term 'clamp' refers to the fact that we maintain this membrane at a constant potential (for a description of the electronics that achieve 'voltage-clamp' *see* Chapter 2).

Many texts have been written on single-channel recording and given space limitations; this chapter cannot treat the subject in depth. Rather this chapter has been written to give the reader: (1) a grounding in the fundamentals of single-channel recording, (2) information about what sorts of data that can be obtained from the various recording configurations, and (3) a very brief overview of the analysis of single-channel data records. For a detailed treatment of the subject of single-channel recording and analysis, the reader is referred to several excellent texts (and chapters and references therein) listed at the end of this chapter.

From: *Neuromethods*, Vol. 35: *Patch-Clamp Analysis: Advanced Techniques*
Edited by: W. Walz, A. A. Boulton, and G. B. Baker @ Humana Press Inc., Totowa, NJ

2. Single-Channel Recording

2.1. Resolving Single-Channel Currents Requires Low 'Noise'

Resolving membrane currents that are only a few picoamperes (or in some cases < 1 pA) in amplitude requires that the background noise of the recording is as low as possible. In their seminal paper, Neher and Sakmann (1976) demonstrated that it was possible to observe individual ion channel activity if an electrode was pressed against a muscle fiber and the current flowing in the patch monitored. In 1981, Hamill et al., documented that further improvements in background noise levels were possible if one was able to form a 'gigaseal.' Such high-resistance seals were obtained by applying suction (negative pressure) to the glass patch-pipet when it contacted the surface of the muscle. This reduced the background noise levels by a further order of magnitude (compared to that achieved previously) and consequently increased the temporal resolution of the recording. The formation of a gigohm seal ($>10^9 \Omega$) is therefore the key to obtaining high-quality single-channel current recordings. The noise associated with a current source is determined by the resistance of that source and is described by the following equation:

$$\sigma_n = \sqrt{\frac{4kTf_B}{R}},$$

where σ_n is the root mean square (rms) of the current noise, k = Boltzmann's constant, T = absolute temperature, f_B = the bandwidth of the recording and R = the resistance of the source. Noise of many forms, and from a variety of sources, contributes to the final level of a patch recording; however, the main sources are the feedback resistor in the headstage, the resistance of the patch, the pipet capacitance, and the seal resistance itself. The total rms noise resulting from n uncorrelated sources is given by the following relationship:

$$\sigma_{total} = \sqrt{(\sigma_1^2 + \sigma_2^2 + \dots + \sigma_n^2)},$$

Thus, because of the nature of this relationship, the source with the highest rms noise level will contribute most significantly to the final noise levels. For example, imagine that three noise sources

have rms values of 0.1, 0.2, and 0.4 pA, respectively. The final noise is 0.46 pA and as such noise from the third source would dominate the recording.

Clearly even the best gigaohm seal will not permit the resolution of ion-channel activity if other precautions to reduce noise levels have not been taken, e.g., use of a Faraday cage, good 'earthing' and 'shielding' of equipment, use of anti-vibration air tables. As a guide the resistance between any two (metal) points in the set-up should be less than 1 Ω . To achieve this, earth all equipment to a common point on the electrophysiological set-up: the use of a metal rod that has holes drilled in to accept 4 mm 'in-line' plugs is particularly convenient. Take a single earthing cable from this point to the 'SIGNAL GROUND' point on the back of the patch-clamp amplifier. Ensure that any mains cables are routed well away from cable that connects the headstage to the amplifier. Additionally it is often necessary to construct a shield that can 'screen' the headstage of the patch-amplifier. This can be made from either aluminium foil or fine copper mesh, its essential feature being that it should be easily removable to permit the experimenter to check that all is well with the recording chamber, perfusion system, and so forth during the course of a recording. This shield should also be grounded.

To summarize, a high-resistance seal between the patch-pipet and membrane together with a low noise current to voltage amplifier with the recording made in a well-grounded and shielded environment should permit the high-resolution recording of single-channel currents.

2.2. Patch-Clamp Amplifiers

Single-channel currents are recorded using patch-clamp amplifiers that either use a resistive feedback headstage or a capacitive feedback headstage. Amplifiers such as the Axopatch-1D and List's EPC7 and EPC8 each use resistive feedback. Instead of the resistor in the headstage having a value of 500 M Ω , this is switched to a value of 50 G Ω when the experimenter selects the $\beta = 100$ setting on the Axopatch, or a gain of 50 mV/pA, or above, on the List amplifiers. The theory of the operation of the amplifier is similar to that described for whole-cell recording in Chapter 2, but now the maximum current that can be recorded is 240 pA (12 V \div 50 G Ω). The increase in the resistance of the feedback resistor reduces

the noise level of the recording (*see above*). However the use of resistors with such large resistances introduces two main problems. Noise levels associated with these resistors are considerably higher than those expected from theoretical considerations, and secondly they possess not insignificant capacitance. This latter feature limits the bandwidth of the recording. For example, a 50 G Ω resistor with a stray capacitance of 0.1 pF results in a bandwidth of only 31.8 Hz (obtained from $f_c = 1/2\pi RC$). As this would be useless for recording the fine detail of channel openings and closings, an additional circuit is built in to the amplifier to increase the bandwidth to around 20 kHz (for details, *see Sherman-Gold, 1993; Sigworth, 1995*).

Patch-clamp amplifiers employing a capacitive feedback headstage (e.g., Axopatch 200B) are becoming more popular for the recording of single-channel currents because the noise levels that can be achieved with such amplifiers are less than those obtained with 'traditional' resistive feedback technology. In this sort of headstage a capacitor replaces the resistor in the feedback circuit of the current to voltage convertor. Such a circuit acts as an integrator. By differentiating the slope of the voltage that charges the capacitor, the amount of current passed is determined. The bandwidth of a capacitive current to voltage convertor is wide (70 kHz) and although such scope is not needed, given the fact that most single-channel currents are filtered with low-pass filters with an f_c of 10 kHz (–3 dB) or less, the lower noise levels that can be achieved are very valuable. The drawback of capacitive feedback headstages is that, with time, the voltage across the capacitors reaches that of the supply voltage. When this occurs the capacitor needs to be discharged (the discharge itself only takes about 50 μ s). The frequency of such discharges depends on the amount of current passed. For example, if the discharge is triggered when the voltage reaches 10 V, this would occur every 2 s if the capacitor has a value of 1 pF and the current passed is 5 pA (from $V = Q/C$). Such reset rates are acceptable. Clearly, if the current passed is in the order of several hundred picoamperes, the resets become more frequent (every 20 ms for a current of 500 pA). Therefore in whole-cell recording the capacitive feedback system is less valuable; indeed, the lower inherent noise level of the capacitive feedback system is not much use since noise levels are considerably higher in whole-cell recording (for further details, *see Sherman-Gold, 1993; Sigworth, 1995*).

2.3. Patch-Pipets and Recording Solutions

Patch-pipets ('electrodes') used to study single-channel activity are fabricated usually from "thick-walled" glass. This type of glass gives electrodes with lower noise properties than can be achieved from "thin-walled" glass. Thin-walled glass gives a lower access resistance and hence is preferred for 'whole-cell recording.' Borosilicate glass (e.g., GC150F-7.5, supplied by Harvard Instruments) is well-suited to making patch-pipets. This glass has an outside diameter of 1.50 mm and an inside diameter of 0.86 mm. The "F" refers to the fact that the capillary contains a fine glass filament that makes for the easier filling of the pipet with recording solution and the capillary length of 7.5 cm means that two pipets of usable length can be pulled from each tube.

Patch-pipets are pulled in two stages, using either a horizontal (e.g., Sutter P-97) or vertical (e.g., Narashige PP-830, List L/M 3-PA) puller. The first pull heats the glass rapidly to allow the formation of an 'hour glass' section in the middle of the capillary. With horizontal pullers there is no need to re-center the glass before the second pull since the glass is pulled equally from both sides. However with vertical pullers, since glass is pulled under gravity, re-centering before the second pull is necessary. Pipets used for making isolated patch recordings tend to have higher resistances than those used for whole-cell recording, with resistances of between 5–20 M Ω being common.

The capacitance of patch-pipets, and hence the noise from this source (*see above*), can be reduced by coating the patch-pipet with a coating of Sylgard® 184 resin (Dow Corning). This is a hydrophobic compound that prevents the external recording solution from creeping up the outside of the patch-pipet. Care needs to be taken to avoid blocking the end of the patch-pipet with the resin and therefore it is advisable (although not essential) to apply the resin while viewing under a dissecting microscope. Try to get the coating within 100 μ m of the electrode tip and extend it to beyond where the electrode will exit the solution in the recording chamber. The resin is 'cured' by passing the coated patch-pipet into a heated wire coil. Rotating the patch-pipet during the curing process avoids the build-up of a large amount of Sylgard on one side of the electrode.

Prior to using the patch-pipets for making channel recordings their tips are 'firepolished.' It is a good idea to polish a few electrodes

at a time, use them over the space of a couple of hours, and then polish another batch because small particles of debris can accumulate on the tips over time. Firepolishing involves heating a platinum wire in close proximity to the tip of the patch-pipet. When the wire is heated it will expand and move upwards by several tens of microns, therefore it is important not to have the patch-pipet too close to the wire before heating as one can easily break the pipet with the deflection of the wire. Additionally, it is important to melt a small amount of glass in the form a bead onto the wire to avoid any platinum vapor finding its way onto the pipet tip. Commercial firepolishing units are manufactured by several companies and generally have one low-powered objective that is useful for locating the patch-pipet and placing it near to the wire. A second, higher-powered objective is then used to visualize the actual firepolishing. During the polishing it should be possible to observe a small amount of 'shrinking' (melting) of the tip of the electrode. When using thick-walled glass this is not as dramatic as can be seen with thin-walled glass, and indeed the purpose of the polishing is simply to clean the surface of the pipet tip, rather than change its overall shape. All this being said it is entirely possible to obtain high-quality single-channel recording with pipets that have not been firepolished, although the success rate of obtaining gigaohm seals may be increased with additional polishing. More details regarding the fabrication of and noise properties of patch-pipets are given in Chapter 1.

Most electrophysiologists have their own favourite recipes for 'internal' and 'external' recording solutions and therefore there are no universal standards. To begin with, stick with solutions that have been "tried and tested;" modify these basic recipes, as necessary, once you are confident that you are able to record, routinely, the channel activity of interest to you. Table 1 documents some internal and external recording solutions that this author has used in his studies of both native and recombinant glutamate receptor-channels in outside-out patches.

2.4. Current Conventions in Electrophysiology

Electrophysiologists have agreed on a convention to describe currents recorded in patch-clamp experiments. Positive ions flowing out of the patch-pipet are measured as positive currents and are illustrated as upward deflections on the current trace. Positive ions flowing into the patch-pipet are measured as negative

Table 1
Solutions for Outside-Out Patch Recordings

Internal Solutions							
	mM		mM		mM		mM
CsF	110	CsCl	140	K-gluconate	141	Cs-gluconate	122.5
CsCl	30	NaCl	5	NaCl	2.5	CsCl	17.5
NaCl	4	EGTA	5	HEPES	10	NaCl	8
EGTA	5	HEPES	10	EGTA	11	HEPES	10
HEPES	10	CaCl ₂	0.5			EGTA	0.2
CaCl ₂	0.5					Mg-ATP	2
Mg-ATP	2					Na-GTP	0.3
pH to 7.3 (CsOH)		pH to 7.3 (CsOH)		pH to 7.3 (KOH)			pH to 7.3 (CsOH)
External Solutions							
	mM		mM		mM		
NaCl	125	NaCl	150	NaCl	125		
KCl	3	KCl	2.8	KCl	2.5		
NaH ₂ PO ₄	1.25	HEPES	10	MgCl ₂	4		
HEPES	20	CaCl ₂	2	CaCl ₂	1		
CaCl ₂	0.85			NaHCO ₃	26		
				NaH ₂ PO ₄	1.25		
				Glucose	25		
pH to 7.3 (NaOH)		pH to 7.3 (NaOH)		Bubble with 95% O ₂ + 5% CO ₂			

currents and are illustrated as downward deflections on the current trace. The terms inward and outward refer to the direction of movement of ions flows across the membrane. Thus the net movement of positive ions from the outside of the cell to the inside would be referred to as an inward current, while the net movement of positive ions from the inside of the cell to the outside would be referred to as an outward current. The net movement of negative ions (e.g., Cl⁻ ions in the case of the GABA_A receptor) from the inside of the membrane to the outside would also generate a negative current (and would, by convention be displayed as a downward deflection). Similarly the net movement of anions from the outside of the cell to the inside of the cell would generate a positive current (upward deflection). These conventions can at times become a little confusing. For example in both cell-attached and inside-out membrane patches the net movement of

positive ions in the direction of the outer to inner membrane surface is, by definition, an inward current, but as positive ions are leaving the patch-pipet this would be recorded as a positive (or upward) current. Thus it is common for single-channel currents that have been recorded in these configurations to be inverted so that the inward movement of ions is represented as a downward deflection. Things are much simpler with outside-out membrane patches as the net movement of positive ions from the outer to the inner membrane surface will generate a negative patch current (as, here, positive ions flow *into* the electrode).

2.5. Configurations Used to Record Single-Channel Currents

Single-channel recordings are most commonly made from visualized cells, e.g., in cell culture, acutely dissociated cells, or cells in thin tissue slices. The critical point is that the surface of the cell to be patched is devoid of any material that could prevent the patch-pipet making a high-resistance seal with the cell membrane. When recording from isolated cells this is not generally a problem, but if one records from tissue slices a certain amount of 'cleaning' may be required (*see* Edwards et al., 1989). A good-quality microscope is a real advantage; the choice of an inverted vs an upright microscope if one is recording from acutely isolated or cultured cells is a matter of personal choice to a large extent. However if one plans to record from cells in thin tissue preparations then an upright microscope is essential. The working distance of water-immersion lenses has improved dramatically over the last few years (with little compromise of their numerical apertures) and is common to have more than 3 mm of working distance with a 40× water-immersion lens and around 2 mm with a 63× objective. When recording from isolated cells phase contrast optics are generally all that is required, however, for recording from cells in tissue use of Nomarski (differential interference contrast) optics is preferable. Infrared optics adds considerably more expense, but allows for visualization of cells located deeper in the slice. When considering micromanipulators there are no additional requirements for single-channel recording over and above those needed for whole-cell recording. Indeed it may well be possible to use an old micromanipulator that drifts too much to be of use for whole-cell recording if one is mainly interested in recording from either inside-out or outside-out membrane patches—check those cupboards before spending several thousand dollars on a new one.

There are three basic patch-clamp configurations that can be used to record the activity of single-channel current, each of which have their own advantages (and disadvantages). One needs to decide the nature of the experiment and the type of information required from it before selecting the appropriate configuration. The following is a description of each of the configurations. For each I have selected examples of data that illustrate the sorts of experiments that can be carried out with each configuration.

2.5.1. *The Cell-Attached Patch*

This configuration is the easiest to achieve and causes no disruption to the intracellular composition of the cell under investigation. The cell-attached patch is the starting point for all patch configurations (including whole-cell recordings). The protocol for obtaining the cell-attached configuration is shown below.

2.5.1.1. STEP-BY-STEP PROCEDURE

TO MAKE A CELL-ATTACHED PATCH

1. Apply a small amount of positive pressure to the patch-pipet and then place the pipet tip in the recording bath. Take care not to apply too much pressure, as this will possibly prevent the formation of a gigaohm seal.
2. Offset the pipet current to zero
3. Monitor the electrode resistance while approaching the cell. Voltage-steps of about 5–10 mV can be applied via the patch-clamp amplifier and the current deflection monitored on an oscilloscope. Patch amplifiers such as the Axopatch-1D have an internal oscillator that can be set to 100 Hz to produce voltage steps. The polarity and magnitude of the voltage step can be set by the 'STEP COMMAND.' The Axopatch 200B amplifier supplies a +5 mV 'SEAL TEST' at line frequency, however the polarity and magnitude of this pulse cannot be altered.
4. Immediately before approaching the cell check that there has been no drift in the pipet current (correct if necessary).
5. Observe a small indentation to the cell as the pipet touches the membrane. At this point the size of the current deflections should decrease, indicating an increase in the resistance of the pipet. Remove the positive pressure and observe a further increase in the seal resistance.
6. Monitor the seal resistance. Sometimes a gigaohm seal will form spontaneously without any further intervention on the part of

the experimenter. If the gigaseal does not form apply some gentle negative pressure. This is most easily done by mouth as it gives greater control, however, a syringe may be used.

7. Seal formation is sometimes aided by applying a negative voltage to the pipet. In this author's experience there is no prescribed voltage that routinely works: somewhere in the range of -20 to -40 mV is suggested.
8. When the gigaseal forms the test pulses should cause no detectable deflection on the current trace—all that remains are the capacitive transients indicating the onset and offset of the voltage pulse. Cancel these transients using the controls on the patch-clamp amplifier. You now should have a cell-attached patch.

An immediate question one asks when recording in the cell-attached configuration is: what is the transmembrane potential of the patch of membrane under the patch-pipet? This is not trivial, since in order to answer the question we need to know the resting potential of the cell. If the resting membrane potential (V_{mem}) is known then the patch potential (V_{patch}) can be obtained from:

$$V_{\text{patch}} = V_{\text{mem}} - V_{\text{cmd}}$$

where, V_{cmd} is the command potential set on the patch-clamp amplifier. Estimates of the resting potential can be obtained from the Nernst equation, however, this is unlikely to be very accurate unless a high K^+ concentration is present in the external recording solution. Although the Goldman-Hodgkin-Katz equation may give a better approximation to the resting potential, it is unlikely that one will have accurate values of the necessary permeability ratios.

The Nernst Equation

$$V_{\text{mem}} = \frac{R \cdot T}{z \cdot F} \cdot \ln \frac{[\text{ion}]_{\text{out}}}{[\text{ion}]_{\text{in}}}$$

The GHK Equation

$$V_{\text{mem}} = \frac{R \cdot T}{z \cdot F} \cdot \ln \frac{P_K \cdot [K^+]_{\text{out}} + P_{Na} \cdot [Na^+]_{\text{out}} + P_{Cl} \cdot [Cl^-]_{\text{in}}}{P_K \cdot [K^+]_{\text{in}} + P_{Na} \cdot [Na^+]_{\text{in}} + P_{Cl} \cdot [Cl^-]_{\text{out}}}$$

where, R = Gas constant, T = absolute temperature, F = Faraday's constant, z = ion valency, $[ion]_{out}$ = extracellular concentration of ion, $[ion]_{in}$ = intracellular concentration of ion and, P_K , P_{Na} and P_{Cl} are the permeabilities of K^+ , Na^+ , and Cl^- ions, respectively.

One method that is sometimes employed with cell-attached recording is to raise the extracellular K^+ concentration to depolarize the membrane potential of a neurone to around zero millivolts. The membrane potential of the patch is then equal to the negative of the command potential set by the patch amplifier. One problem with this approach is that the depolarised state of the neurone may alter intracellular processes that regulate the activity of the channels under investigation. In addition, altering the external solution will affect all the other cells in the recording chamber. An alternative method is to record the unitary amplitudes of the channel currents of interest at a variety of applied command potentials. If the unitary single-channel conductance of the channels is known then it is simple to estimate the patch potential that gives the observed single-channel current amplitude: from knowing the command potential set by the patch-clamp amplifier, one can estimate the membrane potential of the cell. It is important to realise that in the cell-attached patch configuration that the patch-clamp amplifier controls only the potential of the membrane patch under the patch-pipet; the remainder of the cell membrane is at the resting potential for the conditions used in the experiment. Apart from the difficulty in estimating the membrane potential of the cell, another disadvantage of this recording method is that if one is studying the activity of ligand-gated ion channels the agonist needs to be included in the patch pipet. Clearly it is important that the agonist concentration selected gives the appropriate amount of activity; it is difficult (though not impossible) to alter the agonist concentration in the pipet solution once the recording has been established.

2.5.1.2. APPLICATION EXAMPLE

As mentioned earlier, the great advantage of the cell-attached patch configuration is that we do not disturb the intracellular environment of the cell. Thus, this configuration allows us to study the actions of drugs that can modulate the activity of ion channels via intracellular signaling pathways. An example of such a use is shown in Fig. 1 (adapted from Selyanko and Sim, 1998).

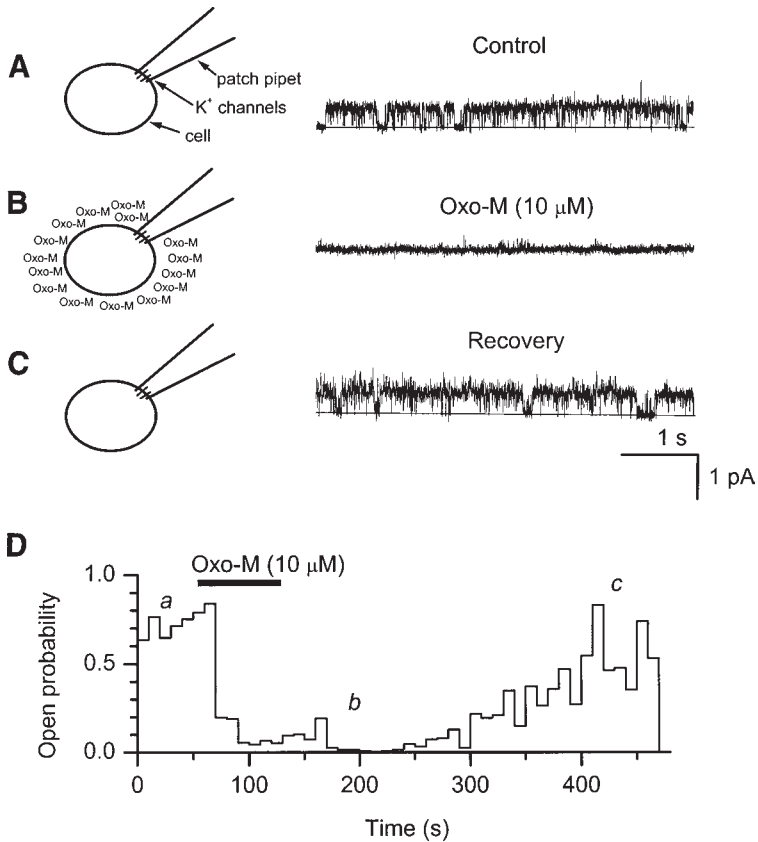


Fig. 1. Oxtremorine-M inhibits the activity of single sustained K⁺-channels. (A) Control level of K⁺-channel activity recorded in a cell-attached patch, the solid line indicates the closed level. (B) Addition of oxtremorine-M (10 μM) to the external bathing solution (and therefore not directly to the area of membrane under the patch-pipet) results in the inhibition of the K⁺-channel activity. (C) Removal of oxtremorine-M allows the K⁺-channel activity to recover. (D) Quantification of the P_{open} of K⁺-channel activity recorded throughout the experiment. Adapted with permission from Selyanko and Sim, 1998.

The upper current trace (Fig. 1A) shows the activity of sustained K⁺ channels under a cell-attached patch-pipet. Openings of the channel are shown as upward deflections to indicate that these are outward currents (the traces have been inverted from what

would actually have been observed). Addition of oxotremorine-M (a muscarinic acetylcholine receptor agonist) to the extracellular bathing solution results in a dramatic reduction of K^+ channel activity (Fig. 1B). Since the agonist was not applied, directly, to the K^+ channels under the patch pipet (and it could not have diffused into this isolated membrane area because of the high-resistance seal between the patch-pipet and the cell membrane), we must assume that the activation of muscarinic receptors results in the production of an intracellular messenger(s) that causes the inactivation of the K^+ channels (middle trace). This effect is reversible since when oxotremorine-M is removed the channel activity returns (Fig. 1C). The plot in Fig. 1D documents the probability of the channel being open (P_{open}) throughout the course of the entire experiment.

2.5.2. The Inside-Out Patch

As the name suggests in this configuration the intracellular face of the lipid bilayer faces the external bathing solution in the recording chamber. To obtain the inside-out patch configuration it is first necessary to obtain a cell-attached patch. Following the formation of the cell-attached patch, pull the patch-pipet away from the cell membrane rapidly; an inside-out patch may form directly, however, it is not uncommon for a membrane vesicle to form. If this is the case an inside-out patch can be made by lifting the patch-pipet from the recording solution for a short period of time; this should burst the vesicle leaving an inside-out membrane patch. The membrane potential of the inside-out patch is simply the negative of the command potential set by the patch-clamp amplifier. As mentioned earlier it is common to invert the current traces recorded in this configuration so that, for example, inward currents are displayed as downward deflections.

2.5.2.1. APPLICATION EXAMPLE

The inside-out mode of patch-clamp recording is ideally suited to the study of agents that modulate the activity of ion channels by interacting with their cytoplasmic domains. Figure 2 shows an experiment where the inside-out configuration has been utilised to study the modulation of large conductance Ca^{2+} -activated K^+ channels (BK channels). K^+ channels of this type are activated by increases in the intracellular Ca^{2+} concentration and therefore are well-suited to being studied using the inside-out patch configuration where

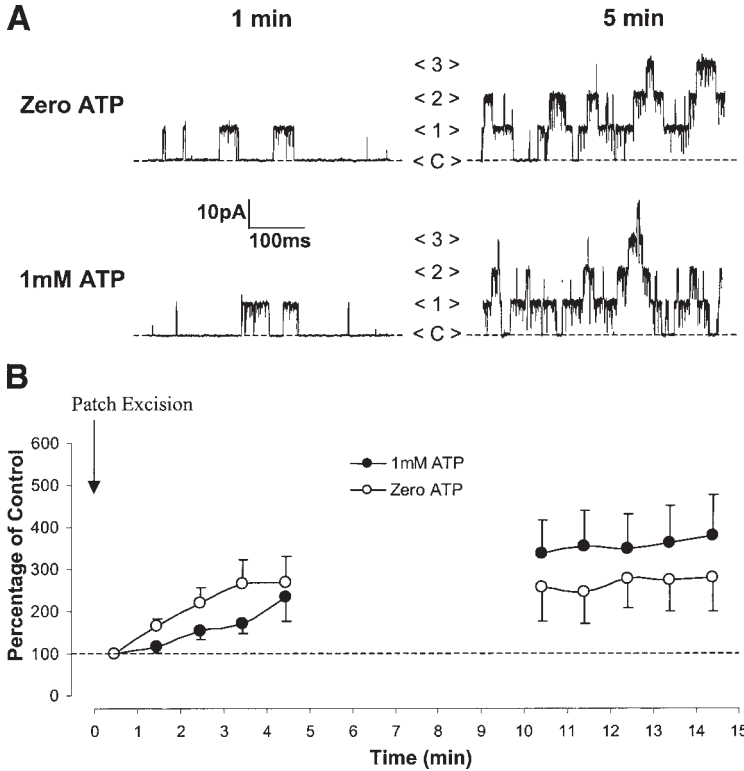


Fig. 2. Inside-out patch recording of BK channels. (A) Representative traces of recordings of S869A BK channels in the absence (P_{open} increases from 0.067 at 1min to 0.467 at 5 min) and presence of ATP (P_{open} increases from 0.045 at 1 min to 0.315 at 5 min, C> indicates the closed state and 1> the number of open channels). (B) Plot of the change in the activity of S869A BK channels in the presence and absence of ATP. In 1 mM ATP the activity of the channel increased and after 15 min has increased to $380 \pm 98\%$ ($n = 25$, $p < 0.05$). In zero ATP the activity of the channel also increased and after 15 min has increased to $279 \pm 80\%$ ($n = 10$, $p > 0.05$). There is no a significant difference between the activity of S869A BK channels in 1 mM ATP and zero ATP after 15 min ($p > 0.05$). All data; mean \pm SEM. Dotted line represents the level of control activity. 0–1 min is the control value for each experimental condition.

one can alter the concentration of Ca^{2+} in the external bathing solution. BK channels normally run-down in the absence of ATP in the solution bathing the intracellular side of the membrane, how-

ever, Fig. 2 illustrates that channels carrying the point mutation, S689A, do not show this phenomenon. In both the absence or presence of ATP (applied to the cytoplasmic face of the channel) there is a 'run-up' of channel activity (unpublished data of Martin Hammond and Mike Shipston, Membrane Biology Group, University of Edinburgh).

2.5.3. The Outside-Out Patch

This is the preferred configuration for the study of ligand-gated ion channels since the external face of the lipid bilayer (and hence the ligand-binding site of the channel) faces the external recording solution permitting the exchange of control and agonist solutions with the membrane patch. The membrane potential of an outside-out patch is simply the value of the command potential set on the patch-clamp amplifier.

2.5.3.1. STEP-BY-STEP PROCEDURE

TO MAKE AN OUTSIDE-OUT PATCH

1. Obtain a cell-attached patch and keep applying the small voltage-steps that were used to monitor the increase in seal resistance during the formation of the cell-attached patch.
2. Set the command potential somewhere between -20 to -40 mV; the precise value will be determined, empirically, by the success of obtaining the whole-cell configuration (*see below*).
3. Apply gentle suction to the patch (suction via mouth gives far better control than is achieved via a syringe). The object here is to rupture the membrane under the patch-pipet without compromising the integrity of the gigaohm seal formed between the patch-pipet and the cell membrane. Successful 'break-through' is most often achieved by applying the suction in brief gentle 'kisses.'
4. Breakthrough will be immediately apparent as the current response to the voltage steps will re-appear on the oscilloscope but now will have large capacitive transients associated with them. The magnitude of the steady-state current trace associated with the voltage-steps gives an indication of the input resistance of the cell. This is now the whole-cell patch-clamp recording configuration.
5. Slowly pull the patch electrode away from the cell. One can generally observe a 'neck' of membrane being pulled away from the cell. Depending on the type of cell, it is not uncommon for

- the need to back the patch-pipet many tens of microns away from the cell. As the outside-out patch forms there will be a reduction in the DC holding current, the noise of the recording and the magnitude of the capacitive currents associated with the voltage-pulses being applied to the patch-pipet.
6. A successful outside-out patch will form if the membrane 'pinches' off the cell and there is no loss in the seal resistance. This takes a little practice and some cells give rise to good quality outside-out patches more readily than others.
 7. To minimize noise levels further the volume of the bathing solution can be reduced so as to leave only the tip of the patch-pipet in the recording solution (this reduces the pipet capacitance). However, care must be taken to avoid the tip leaving the bathing solution. If one is recording the steady-state behavior of a ligand-gated ion channel it is possible to switch off the perfusion after exchanging completely the 'control' bath solution for one that contains agonist. This eliminates noise associated with the perfusion system and there is no danger of the solution level in the bath changing.

2.5.3.2. APPLICATION EXAMPLE

As mentioned earlier the outside-out patch configuration is widely used in the study of ligand-gated ion channels. In addition to being used for studies of the steady-state behavior of ion channels, solutions can be applied rapidly to the outside-out patch in an attempt to mimic more closely the agonist concentration profile that an ion channel might experience following the synaptic release neurotransmitter. Thus outside-out patches are used in concentration-jump experiments. Figure 3 shows an example of channel activity recorded from an outside-out patch in response to a 1 ms application of 1 mM glutamate. The patch was isolated from cell expressing recombinant NR1a/NR2A NMDA receptor channels and was held at -100 mV. The inset shows a sketch of the concentration-jump technique. Two solutions flow from either side of a piece of 'theta' glass: one contains the control solution (glycine alone), while the other contains the 'test' solution (in this case glycine + 1 mM glutamate). The movement of the theta glass is controlled by a piezo crystal. Applying a high voltage to the crystal stack causes its expansion. The patch-pipet is placed a few microns away from the sharp interface that forms between the control and test solutions. Applying a high voltage to the crystal

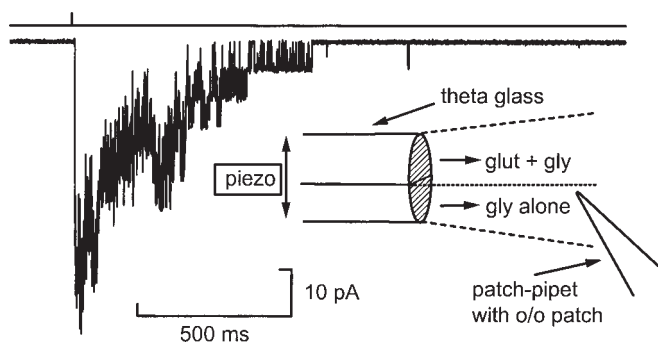


Fig. 3. Use of a 'concentration jump' to activation of NMDA receptor-channels in an outside-out patch. The current trace shows an individual response obtained from an outside-out membrane patch excised from a *Xenopus* oocyte expressing recombinant NR1a/NR2A NMDA receptor-channel. Channel activity was evoked by exposing the patch to a solution containing 1 mM glutamate for 1 ms. Unitary events are clearly discernable in the sweep. The inset shows a cartoon illustration of recording method used in such concentration jump experiments. Current trace originally published in Wyllie et al., 1998; adapted with permission.

for 1 ms cause the theta glass to move and the patch-pipet is exposed to the glutamate-containing solution. In the trace shown, approx 11 individual channels are open simultaneously at the peak of the response. With time, channels close at random, leaving the receptor in a lower affinity state from which agonist dissociation may occur

Figure 4 illustrates another outside-out patch recording. In this case, single-channel events have been recorded at different holding potentials to determine the conductance of the channel under investigation. This property is discussed below.

2.6. Single-Channel Conductance: One of the Signatures of an Ion Channel

Let us assume that we have selected the patch-clamp recording configuration best suited to our channel of interest. Perhaps the most straightforward parameter to measure is the amplitude of the single-channel current. Measuring amplitudes at a variety of holding potentials allows us to determine the conductance of the channel, one of the parameters that defines a channel. Additionally,

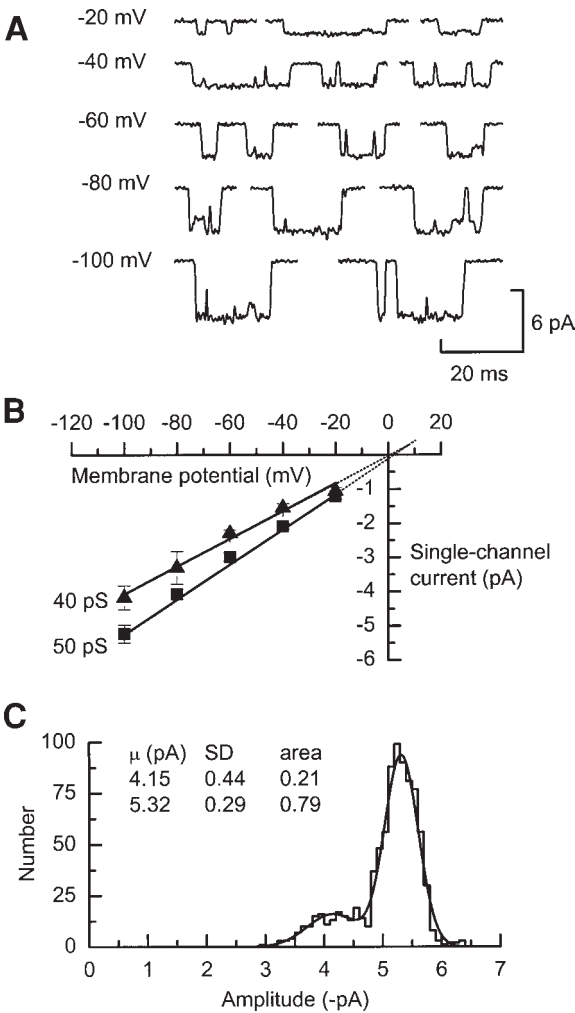


Fig. 4. Current-voltage plot for NMDA receptor-channels. (A) Examples of NMDA NR1a/NR2A(T671A) single-channel currents recorded in an out-side-out membrane patch at the holding potentials indicated. As the holding potential approaches the reversal potential of the current, the driving force decreases and hence the amplitudes of the unitary events becomes smaller. (B) Current-voltage plot indicating the existence of two (50 pS and 40 pS) prominent conductance levels. Extrapolating the least-squares fitted lines to the data gives an estimated reversal potential of +2 mV.

altering the ionic composition of the internal and external recording solution allows us to determine the permeation characteristics of a channel.

An example of a single-channel current-voltage (I/V) plot is shown in Fig. 4B. These data are taken from a study of recombinant NR1a/NR2A NMDA receptors carrying a point mutation in the region of the glutamate-binding site, where an alanine residue replaced the threonine residue at position 671 (Anson et al., 2000). As can be seen from both the single-channel current traces and the I/V plot, two conductance levels are present. The main level has a conductance of 50 pS, while the sublevel has a conductance of 40 pS. These conductance levels are indistinguishable from the conductances of wild-type NR1a/NR2A NMDA receptors and high-conductance NMDA receptors found in central neurones. Extrapolating the fitted lines indicates that the reversal potential of these currents is approx +2 mV—a value that would be expected given that NMDA receptors are nonselective cation channels. The fact that the data sets for both the main and subconductance level are well-fitted with straight lines indicates that the channel is ohmic, i.e., the amplitude of the single-channel current, I_{sc} at any holding potential, V_m , can be determined if we know the channels unitary conductance, g_{sc} and its reversal potential, V_{rev} . Thus from Ohm's Law:

$$I_{sc} = g_{sc}(V_m - V_{rev})$$

2.7. Single-Channel Amplitudes are Described by Gaussian Distributions

Figure 4C shows the amplitude distribution for NMDA single-channel currents recorded at -100 mV. The distribution is well-described by the sum of two Gaussian (or normal) distributions indicating that this NMDA receptor-channel possesses two conductance levels. The distribution of amplitudes that have been measured by taking the mean amplitude of the current when the channel is

(continued) (C) Amplitude histogram for events with durations greater than $2.5T_r$ (415 μ s) that were recorded at -100 mV. The histogram is fitted with a mixture of two Gaussian components with means and standard deviations as indicated. Data adapted with permission from Anson et al. (2000) (A, B) and unpublished (C).

open is, in principle, not actually Gaussian. This is because events with long durations give a more accurate measure of the 'true' amplitude than do shorter duration events (more details can be found in Colquhoun and Sigworth, 1995, Appendix 2). For the histogram shown in Fig. 4C only events with durations greater than 415 μ s have been included in the distribution—this is equal to 2.5 T_r of a 2 kHz filter (*see below*). The equation for a Gaussian distribution is shown below:

The Gaussian Function

$$f(x) = \frac{1}{\sigma\sqrt{2\pi}} \exp\left(-\frac{(x - \mu)^2}{2\sigma^2}\right),$$

where μ is the mean of the distribution and σ^2 is the associated variance. In the next section we shall compare the Gaussian distribution with two other types of distribution that are used to describe the properties of ion channels.

3. Single-Channel Data Analysis

The purpose of this part of the chapter is to introduce the reader to the elementary basics and concepts involved in the analysis of single-channel data. For the rigorous discussion of the topics mentioned here, the reader is referred to texts contained in, for example, *Single-Channel Recording* (1995), *Microelectrode Techniques* (1994), *Methods in Enzymology – Ion Channels Part B* (1998). These texts, in addition to providing excellent insight into the interpretation of single-channel data, also give considerably more detail about the mathematical background and theory of single-channel analysis than is given here.

3.1. Translating the Single-Channel Data Record in Dwell Time Intervals

Channel data are best stored on videotape or on digital audio tape for subsequent digitization. It is best to record single channels with the minimum of filtering, for example at approx 10–20 kHz (–3 dB or half-power) as it is a simple matter to filter the data more heavily when it comes to the analysis. Most patch-clamp amplifiers have a built-in filter unit, which can be set from around 500 Hz to 50 kHz. It is common to filter data with a low-pass filter

of between 2–5 kHz (–3 dB) when it comes to the final analysis, however, be sure to use a Bessel-type filter to prevent ‘ringing’ that occurs if one filters channels with Tchebychev or Butterworth filters. As a guide it is best to digitize data at 10 times the filter rate, e.g., digitize at 20 kHz if filtering at 2 kHz. If for any reason this is not possible or impracticable then one can digitize as low as five times the final filter level. It is important to be aware of the cascade effect of filters. For Bessel and digital Gaussian filters the final cut-off frequency (f_c) is given by the following relationship:

$$\frac{1}{f_c} = \sqrt{\frac{1}{f_1^2} + \frac{1}{f_2^2} + \frac{1}{f_3^2} + \dots \frac{1}{f_n^2}},$$

where f_1, f_2 etc., are the –3 dB values of the various filters used in the cascade series. For example, if one has filtered single-channel data at 10 kHz using the Bessel filter on the patch-clamp amplifier and then filters the data using another filter set at 5 kHz, then the final cut-off frequency is not 5 kHz but 4.47 kHz. To achieve a final cut-off frequency of 5 kHz, one would need to filter the data at 5.77 kHz (–3 dB). However, if one has filtered the data using a filter setting of 20 kHz on the patch-clamp amplifier and then filtered at 5 kHz, the final cut-off frequency would be 4.85 kHz, which would probably be acceptable for most applications. Thus the take-home message is to use a minimum amount of filtering when recording the data onto tape.

From the channel data record we need to obtain two things: (1) the amplitude of the event, and (2) the time that the channel spends at that amplitude level. Thus for a channel that opens to only one conductance level our ‘idealized’ data record would consist of a series of dwell-time intervals with an amplitude of 0 pA (corresponding to closed channel) and a series of dwell times with an amplitude corresponding to the open state of the channel. There are two main single-channel analysis methods of obtaining this data set: the ‘threshold crossing’ method and the ‘time-course fitting’ method.

3.1.1. The Threshold-Crossing Method

In this type of analysis an ‘event’ is detected when the rising phase (opening) of the channel crosses some pre-set threshold; its duration measured by the falling phase (closing) re-crossing

this level. This sounds rather straightforward and in a sense it is; however, many pitfalls await the unwary.

1. The presence of multiple conductance levels in a data record means that determining the 50% threshold values is ambiguous and there is no satisfactory way to measure records with multiple conductance levels by threshold-crossing methods.
2. The best resolution (*see below*) that can be achieved is less than that which can be achieved with time-course fitting.
3. A drifting baseline and/or instability of channel amplitudes can cause havoc with the analysis.

This method of idealizing the data record can be quick, especially if you do not check the validity of the fit to your data! It is essential to *look* at your data beforehand to determine its suitability to this method of analysis. The Strathclyde Electrophysiology Software suite of programs (available from <http://www.strath.ac.uk/Departments/PhysPharm/>) contains software for 50% threshold-crossing analysis as does the pClamp8® software supplied by Axon Instruments and Bruxon Corporation's TAC® single-channel software.

3.1.2. *The Time-Course Fitting Method*

Only one analysis program exists that allows time-course fitting of single-channel data – SCAN (Single-Channel Analysis, written by David Colquhoun and available from <http://www.ucl.ac.uk/Pharmacology/dc.html>). Make no mistake about it, time-course fitting is considerably slower than the 50% threshold-crossing method (if you don't [!], check the fits obtained from threshold crossing), but in the end not only will you have examined every single-channel transition in your data record, you will be able to fit data records that contain events with multiple conductance levels and impose a significantly better resolution on the idealized record. Each amplitude is fitted as it is seen on the screen with no need for predetermined 'windows.' In time-course fitting, one fits each transition with a square pulse with an amplitude equal to that of the channel transition and that has been filtered at exactly the same f_c as the data record (or, better in principle, with the experimentally determined step response of the entire recording system). More details about both these methods can be found in Colquhoun and Sigworth (1995).

3.2. Setting the Resolution

Before any analysis of the channel record can be conducted one needs to impose an acceptable resolution on the data set so that incompletely resolved transitions are clearly distinguished from the baseline noise, but, at the same time, making sure that as few as possible 'real' transitions are missed. It should be said that the presence of multiple conductance levels complicates this further, since incompletely resolved current amplitudes are not always transitions to the same conductance level.

As mentioned earlier one needs to determine the final filter cut-off frequency of the data record. Bessel-type filters with four or eight poles are sufficiently close in their response characteristics that they approximate Gaussian filters. In this case such filters have rise times (T_r) that are equal to $0.3321/f_c$, where f_c is the -3 dB frequency of the filter. For example a data record filtered at 10 kHz during the recording and then filtered subsequently at 3 kHz prior to digitization gives an effective overall filtering of 2.87 kHz (-3 dB) and therefore the corresponding T_r is 116 μ s. Furthermore, the maximum amplitude, A_{\max} , of a low-pass filtered square pulse of duration, d , is given by the equation:

$$A_{\max} = A_o \operatorname{erf} \left(\frac{0.886d}{T_r} \right),$$

where erf is the error function and is given by:

$$\operatorname{erf}(x) = \int \frac{2 \exp(-x^2)}{\sqrt{\pi}} dx,$$

and, A_o is the amplitude of the original unfiltered pulse.

With ratios of d/T_r of 1.0, 1.5, 2.0, and 2.5 this gives values of A_{\max}/A_o of 0.790, 0.940, 0.988, and 0.998, respectively. Thus a low-pass filtered pulse of duration $2.5T_r$ reaches 99.8% of its original amplitude. This is why it is common, when fitting amplitude histograms to include only events that have durations greater than $2.0T_r$ or $2.5T_r$.

The probability that an event with amplitude A_{\max} arises from random baseline noise is given by the false event rate (Colquhoun and Sigworth, 1995):

$$\text{false event rate} \approx f_c \exp \left[-0.5 \left(\frac{A_{\max}}{\sigma_n} \right)^2 \right],$$

where σ_n is the rms of the baseline noise in the channel recording.

Typically, minimum resolvable open and shut times are chosen to give false-event rates of less than 10^{-6} per second. As a further check of the suitability of a chosen resolution, open and shut histograms can be constructed with a very much unrealistic resolution (e.g., 10 μ s), which of course will give a very high false-event rate. When these histograms are displayed on an arithmetic scale (see below) the value at which events start to be ‘missed’ gives an indication of the upper limit of the resolution that can be obtained in a particular experiment. As a guide, if one analyses channels with a ‘full’ amplitude of approx 5 pA in a recording with a baseline noise level of around 100–130 fA (2 kHz, –3 dB) then it should be possible to set the resolution between 40–50 μ s.

3.3. Channel Life-Times are Distributed Exponentially

In the analysis of single-channel events we attempt to understand the average behavior of a channel by studying many hundreds or thousands of *individual* events; there is no point in trying to estimate the mean open time of a channel by simply measuring half a dozen event durations. The random nature of the dwell times (both shut times and open times) means that we need to use probability distributions to describe their behavior. In addition to the Gaussian distribution that we encountered when discussing the distribution of single-channel amplitudes, the two most common distributions encountered in single-channel analysis are the exponential distribution and the geometric distribution.

Figure 5A,B compares the features of a Gaussian (normal) distribution with that of an exponential distribution. The Gaussian distribution shown in this figure has a mean equal to 1 and a standard deviation (SD) of 0.2. The *mean*, *median*, and *mode* each have the same value in a normal distribution (in this example these are all 1). The curve is therefore symmetrical around the mean. In addition 95.4% of all values occur ± 2 SD of the mean. In contrast, the exponential distribution is very different from the normal distribution. The median occurs at a value equal to 0.693 of the mean value. This is sometimes referred to as the half-life (c.f., radioactive decay). Thus 50% of events have a value less than or equal

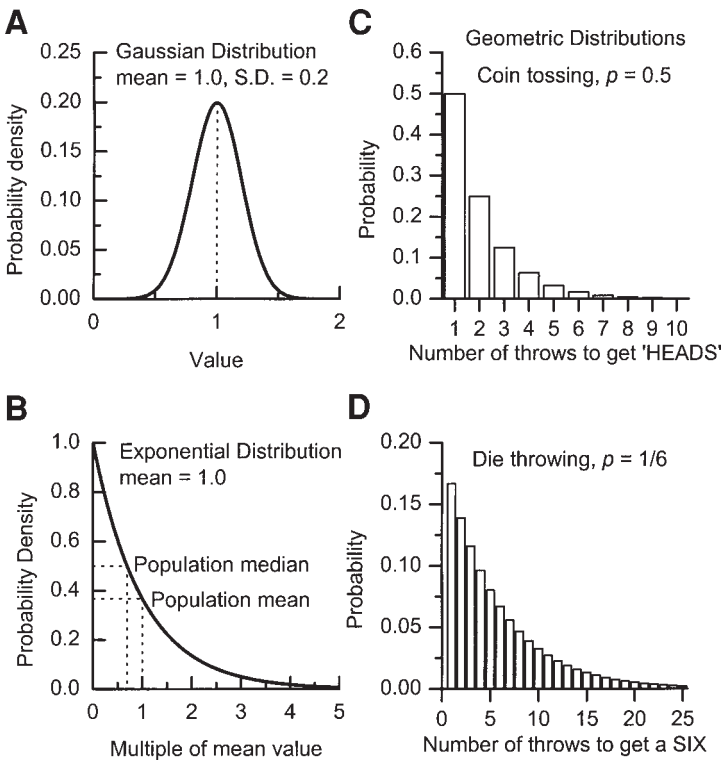


Fig. 5. Examples of Gaussian, exponential, and geometric distributions. (A) A Gaussian (normal) pdf with a mean equal to 1 and a standard deviation of 0.2. (B) An example of an exponential pdf with a mean equal to 1. Dashed lines show where the median and mean occur in such distributions. (C,D) Geometric distributions for coin tossing and die throwing. In each histogram the probability given refers to the probability that the n th trial is the *successful* trial (i.e., there have been $n-1$ 'failures' up to this point).

to the median value. The mean value of an exponential distribution occurs when the curve has decayed to $1/e$ of the initial starting value; referred to as an e -fold decay (where e is the universal constant = 2.7182818...). The mean value is also referred to as the time-constant (symbol τ) of the exponential distribution. For a process that is described by single exponential component 36.79%

of events have a value greater than the mean (63.21% have a values smaller than the mean). The mean and median for the curve shown in Fig. 5B are indicated by dashed lines.

Channel dwell times are distributed exponentially (*see below*). This is a consequence of the fact that single-channel events display a Markov (or memoryless) type of behavior. Two examples of Markov processes are shown in Fig. 5. Figure 5C plots the number of trials (tosses of coin) needed to get a 'head' against the probability. Thus $P = 0.5$ for a single trial, $P = 0.25$ for it taking 2 attempts, $P = 0.125$ for it taking 3 attempts. In Fig. 5D, the plot shows number of die casts required to obtain a six. In each plot the probability of the $n + 1^{\text{th}}$ trial being *the* successful trial is a constant factor ($5/6$) less than the n^{th} trial. In each of these examples, the cumulative probability can be obtained by adding all the individual probabilities that precede a particular trial. For example, when tossing a coin, one will obtain a head three times out of four in a trial of two tosses. What is the analogy with an ion channel? In this case we are interested in the amount of time a channel spends in a particular state (either open or closed). For the sake of argument let us assume that the channel is open. All the bonds in the protein will be bending and stretching until at some point they find themselves in a conformation so close to the transition state that the protein crosses the energy barrier and flips into the shut conformation. There are so many of these bending and stretching events that the protein does not 'know' how close any particular set came to causing the channel to close. It is memoryless. The fact that a success occurs (the channel closes) is therefore independent of the number of trials that have taken place. A channel does not 'remember' how long it has been open (or closed) therefore the probability that the channel will close (or open) in the next small time interval is constant. What we find that in this situation is that the probability of a successful trial is very small, but the number of trials is very large. When this happens, the geometric distribution approaches the exponential distribution. For a mathematical answer to this question the interested reader is referred to Colquhoun and Hawkes (1995). The equation describing the geometric distribution is given below.

Geometric Distribution

$$P(r) = p(1 - p)^{r-1} \quad (r = 1, 2, 3, \dots),$$

where $P(r)$ gives the probability of a success requiring exactly r number of trials given that there has been $r - 1$ 'failures' prior to this and the success of any given trial is p .

As stated earlier, channel lifetimes are distributed exponentially and these are described by exponential probability density functions.

Exponential pdf

$$f(t) = \lambda \exp(-\lambda t) \text{ or } f(t) = \tau^{-1} \exp(-t/\tau),$$

where, λ is equal to the *rate-constant* of the distribution (τ is equal to the *time-constant* of the distribution). The term 'probability density function' can be interpreted as meaning the curve such that the *area* under the curve between any two values of the variable is the probability of the variable having a value somewhere between these two points. Put another way, the area under the curve up to a point, t , gives the probability that the lifetime of the channel is less than or equal to t . The total area under such curves is unity; this is simply a consequence of the fact that the open time (or closed time) must have a value of between 0 and ∞ .

It should be noticed that when the number of trials (r) are large and the probability (p) of a success on any given trial is low, the geometric distribution, which is a discontinuous analogue of an exponential function, approaches an exponential distribution. Thus,

$$(1 - p)^r \rightarrow \exp(-pr),$$

as $p \rightarrow 0$ and $r \rightarrow \infty$ (with the product, pr being finite).

3.4. A Simple Two-State Model

Before we consider the analysis of some simulated channel data below, let us consider a very simple scheme. A channel can exist in two states either open (O) or closed (C). The opening rate constant is β and the closing rate constant is α , both have dimensions of reciprocal time (e.g., s^{-1}).



In our two-state model the mean durations of the closed and open states are given by:

$$\text{Mean open time} = \tau_o = \frac{1}{\alpha} \quad \text{Mean closed time} = \tau_c = \frac{1}{\beta}$$

This result is obtained from a very simple rule that applies to any reaction scheme (no matter how complicated) that can be stated as follows: **“The mean duration of an individual state is equal to the reciprocal of the sum of all the rate constants that describe routes for leaving that state.”** These mean values are known as ‘time constants’ and have units of time. The proportion of time that the channel spends in the open state then is given by:

$$\frac{\tau_o}{\tau_o + \tau_c} \quad \text{or} \quad \frac{\beta}{\beta + \alpha}$$

and similarly the proportion of time that the channel spends in the closed state is:

$$\frac{\tau_c}{\tau_o + \tau_c} \quad \text{or} \quad \frac{\alpha}{\beta + \alpha}$$

The distribution of open times is described by the following pdf:

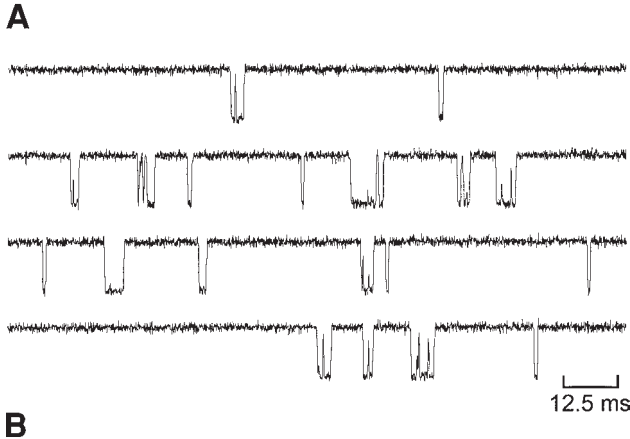
$$f(t) = \alpha \exp(-\alpha t) \quad \text{or} \quad f(t) = \tau_o^{-1} \exp(-t/\tau_o)$$

While the distribution of closed times is given by:

$$f(t) = \beta \exp(-\beta t) \quad \text{or} \quad f(t) = \tau_c^{-1} \exp(-t/\tau_c)$$

3.5. A Quick Guide to the Analysis of Single-Channel Data

The following is the meant to serve as a very brief guide to the analysis of single-channel data. Figure 6 shows 500 ms of a continuous stretch of single-channel activity simulated with the SCSIM program (<http://www.ucl.ac.uk/Pharmacology/dc.html>) and using the del Castillo-Katz (1957) reaction scheme that is shown below the channel traces. The del Castillo-Katz scheme is the simplest model that can account for the action of a ligand binding to a receptor resulting in the opening of an ion channel. In the scheme the resting state of the channel is denoted by R, the ligand-bound but shut state, AR, and the open state of the channel by AR*. The association and dissociation rate constants are given by



Rate constants used in simulation:

$$k_{+1} = 10^7 \text{ mol}^{-1}\text{s}^{-1}$$

$$k_{-1} = 2500 \text{ s}^{-1}$$

$$\alpha = 1000 \text{ s}^{-1}$$

$$\beta = 5000 \text{ s}^{-1}$$

$$[A] = 10 \text{ } \mu\text{M}$$

Fig. 6. Simulation of single-channel data using the del Castillo-Katz reaction scheme. (A) 500 ms of continuous channel activity simulated using the del Castillo-Katz reaction scheme and with the rate constants shown in (B). Note that channel openings tend to occur in trains or bursts of openings that contain relatively short closed periods. Bursts, in turn, are separated from each other by longer closed periods.

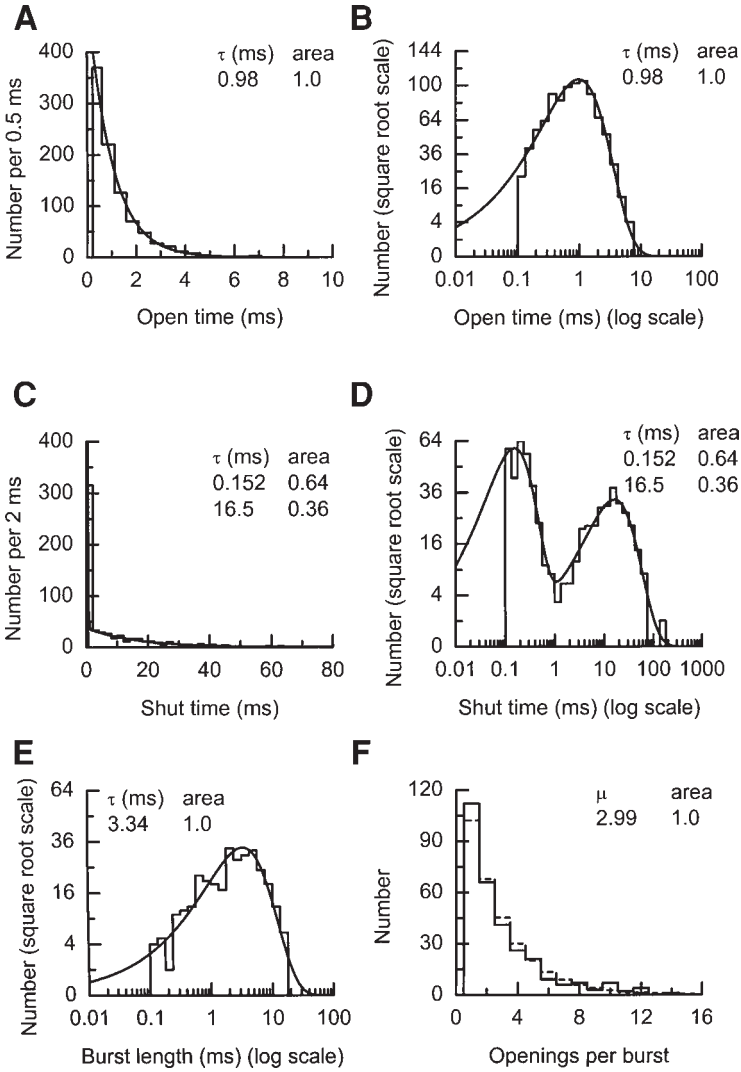
k_{+1} and k_{-1} respectively, while the opening rate constant is denoted by β and the closing rate constant by α . For the simulation, the values for the rate constants chosen were as follows: $k_{+1} = 1 \times 10^7 \text{ mol}^{-1}\text{s}^{-1}$, $k_{-1} = 2500 \text{ s}^{-1}$, $\alpha = 1000 \text{ s}^{-1}$, $\beta = 5000 \text{ s}^{-1}$ and the agonist concentration was set at $10 \text{ } \mu\text{M}$. Inspection of the channel activity shows us four clear things:

1. The amplitude of individual channel openings are very similar (N.B. although these data has been simulated, this can be seen to be true of real channels, e.g., examine the single-channel traces at the different potentials shown in Fig. 4A).
2. The duration of individual openings are not equal.
3. Openings tend to occur in trains or 'bursts' of openings that contain brief closed periods (gaps).
4. Bursts are separated by longer closed periods that, again are not of equal duration.

3.6. Channel Open Times of the Simulated Data Record

Figure 7A shows the distribution of open times—a rather conservative resolution of 100 μs has been imposed on the data. Since there is only one open state in the del Castillo-Katz reaction scheme, open times should be described by a single exponential; this is indeed the case. Now given the rule regarding how one calculates the mean lifetime of any particular state, we would predict that the time constant of the open time distribution should be 1 ms (since $\tau = 1/\alpha = 1/1000 \text{ s}^{-1}$). The fit of the simulated data gives a time constant of 0.98 ms, which is a good approximation given the fact that we only simulated 2000 intervals (1000 openings and 1000 closings). The continuous line superimposed on the histogram is the exponential pdf. Since the fit of the open time distribution gave an estimate of the time constant of 0.978 ms, this equates to a rate constant, α , equal to 1022.5 s^{-1} . Thus the open time pdf is given by $f(t) = 1022.5e^{-1022.5t} \text{ s}^{-1}$. For illustration the pdf has been multiplied by the number of events that are predicted, by the fit, to be in the distribution (in this case 1008) and then expressed in terms of per 0.5 ms (rather than per second). Therefore the pdf has been multiplied by the factor 1008/2000 (the factor 2000 being obtained from $1 \text{ s} / 0.5 \text{ ms}$).

Fig. 7. Kinetic properties of simulated data. (A, B) Distribution of open times fitted with a single exponential component. The distribution on the left is plotted on a conventional arithmetic scale and distribution has a typical exponential-looking appearance. In (B) the same data are plotted on the logarithmic-square root scale that is now the preferred method for displaying distributions of single-channel dwell times that span a large time range. (C, D) The shut time distribution for the simulated data, where the use of the logarithmic time base makes it easier to see



(continued) the two components in this distribution. (E) Distribution of burst length fitted with a single exponential component. (F) Distribution of the number of individual openings contained within each burst. This data is distributed geometrically. In all cases a resolution of 100 μ s was imposed on both openings and closings.

Therefore, the first point on the pdf would be $1022.5 \text{ s}^{-1} \times 1008 / 2000 = 515$. The distribution to the right (Fig. 7B) again shows the open time pdf, but in this case the time scale has been plotted on a logarithmic scale and a square root scale has been used for the ordinate (Blatz and Magleby, 1986; Sigworth and Sine, 1987). The use of the square-root scale helps to keep the errors associated with the variable bin-width constant. This method of displaying data results in the exponential function becoming a skewed bell-shaped curve, where the 'peak' of the curve occurs at the time constant of the distribution. Plotting dwell-time histograms this way has the great advantage that intervals spanning very large time ranges can be plotted on the same graph with multiple exponential components being easily identifiable. It is important to realize that the logarithmic transformation of the abscissa does not simply arise from plotting the exponential distribution semi-logarithmically. The pdf that is actually plotted in these sorts of displays is given by:

$$\sum a_i \tau_i^{-1} \exp\left(x - \tau_i^{-1} e^x\right),$$

where a_i and τ_i are the relative area and time constant of the i^{th} component of the distribution, respectively, and $x = \log_e t$, where t is equal to the length of the interval (more detailed accounts can be found in Blatz and Magleby, 1986; Colquhoun and Sigworth, 1995; Sine and Sigworth, 1987).

3.7. Channel Shut Times of the Simulated Data Record

The shut time distribution for the simulated data is shown in Fig. 7C (arithmetic scale) and Fig. 7D (logarithmic scale). There are two exponential components in the shut time distribution as a result of there being two shut states in the del Castillo-Katz scheme. In this example the advantage of the logarithmic display is clear: we can see clearly the two components of the distribution, whereas on the arithmetic display the first component cannot be seen clearly. In fact, in this display it has decayed to practically zero within a single bin width. A question that is frequently asked is: can we attribute the time constants obtained from the fit of the pdf to particular states in the model? In our model the mean lifetime of AR (liganded but shut state) is equal to $133.3 \text{ } \mu\text{s}$ (the reciprocal of the sum of 2500 s^{-1} plus 5000 s^{-1}). For the mean lifetime of the R state (unliganded) we need to multiply the associa-

tion rate constant ($10^7 \text{ mol}^{-1}\text{s}^{-1}$) by the ligand concentration ($10 \mu\text{M}$) and take the reciprocal of this, thus we obtain a mean life time of the R state of 10 ms. From the shut time distribution we see that the time constants of the pdf are $152 \mu\text{s}$ (relative area = 0.64) and 16.5 ms (relative area = 0.36). The predicted time constants of the shut time pdf are $132.7 \mu\text{s}$ (relative area = 0.66) and 15.07 ms (relative area = 0.34). These values were determined using the SCBURST program (<http://www.ucl.ac.uk/Pharmacology/dc.html>). The $100 \mu\text{s}$ resolution imposed on the data set means that we will have omitted many events (brief closings) that should have been included in the distribution and thus compromised our ability to determine accurately the time constant of this fast component. In all likelihood we would have obtained an estimate from the fit closer to the predicted time constant if we had set a better resolution. Clearly the predicted value of the fast component of the pdf of *all* shut times ($132.7 \mu\text{s}$) is very close to the value of the mean lifetime of a single sojourn in the AR state ($133.3 \mu\text{s}$). Given the simple kinetic scheme used for this simulation this is not surprising.

However, the same argument cannot be made for the discrepancy between the mean lifetime of the R state (10 ms) and the fit of the data that gives us a value of 16.5 ms. The reason that these two values do not (and would not be expected to) agree is simple. What we observe in the channel record is that the channel is either open or closed; we do not (and cannot) monitor the states that the channel occupies—this can only be inferred, e.g., the brief lifetime of the AR state. Examine the del Castillo-Katz scheme. If the receptor binds the ligand it moves to the AR state, in the AR state it has two options: it can either open or the ligand can dissociate. If the channel opens the shut time is terminated; however, if the ligand dissociates, the channel enters the unliganded shut state and sojourns in three states will be concatenated. As the channel is memoryless, it does not remember that it has visited the AR state and so the process with the same probabilities of transitions happening starts all over again. With the rate constants chosen in this example, two out of three times the channel enters the AR state it will open and on one third of the occasions the ligand will dissociate. Because of this the time constant of the second component in the shut time distribution does not give the *mean* lifetime of the R state. The predicted mean value of the second component of the shut time distribution using the set of rate constants chosen for the simulation is in fact 15.07 ms (obtained from SCBURST).

Therefore, in general it is not possible to equate the time constants obtained from pdfs with the mean life times of channel states. The possible exception to this statement is when the channel enters a 'short-lived' shut state that occurs within a burst of channel openings. However, even in this case the time constant obtained from the fit of the pdf of all shut times will not give this exactly (see above) and neither it is easy to determine the relationship of such short-lived states to other closed states.

3.8. Properties of "Bursts" of Openings in the Simulated Data Record

It was pointed out earlier that one of the features of the simulated data was the fact that channel openings tended to occur in quick succession, with short gaps separating the openings within a burst and longer gaps separating bursts from one and other. Bursts can be thought of as representing the individual activation of a channel. In the case of a ligand-gated ion channel, bursts represent the series of openings initiated by the binding of ligand to its receptor and are terminated by the dissociation of ligand that causes the channel to enter a state from which it cannot open again without re-binding of ligand (for a mathematical treatment of this problem, see Colquhoun and Hawkes, 1982). Colquhoun and Sakmann (1985) documented the burst structure of nicotinic acetylcholine receptors found at muscle endplates of *rana temporaria*. The distribution of gaps *within* bursts were described by two exponential components with means of 20 μ s and (rarely) 0.51 ms when the ligand used was acetylcholine. However, if we study the individual activations (bursts) of NMDA receptors we see that within a single activation, multiple shut time components exist and the values of these range for a few tens of microseconds to several hundred milliseconds depending on the subtype of NMDA receptor (e.g., Gibb and Colquhoun, 1992; Wyllie et al., 1998; for a review see B     et al., 1999). Therefore it is important to realise that gaps within bursts need not be on the submillisecond timescale.

Returning to our simulated data in order to identify the bursts, we need to have a method by which we separate shut times that occur *within* a burst from those that occur *between* bursts. Bursts can then be defined as groups of openings that are separated from another group of openings by a shut time interval greater than a

defined critical gap length (t_c). There is a certain amount of ambiguity as to the optimal value of t_c to select. Three common methods are widely used to estimate the optimal value of t_c . All result in a degree of misclassification of events, i.e., events are deemed to be *within* bursts when in fact they were *between* bursts and vice versa. These methods are as follows: one can either minimize the total number of misclassified events (Jackson et al., 1983), misclassify equal numbers from each component of the shut time distribution (Clapham and Neher, 1984), or misclassify equal percentages from each component of the shut time distribution (Colquhoun and Sakmann, 1985). Taking the last method, the value of t_c can be obtained by solving, numerically, the following equation:

$$1 - \exp(-t_c/\tau_2) = \exp(-t_c/\tau_1),$$

where, τ_1 is the time constant of the longest shut time component containing intervals thought to occur within a burst and τ_2 is the time constant of the component that immediately follows this one in the shut time distribution.

From the shut time distribution of our simulated data (and also knowing the nature of the kinetic scheme that produced the data), it is safe to assume that gaps contained within the first shut time component occur mainly within bursts, while gaps in the second component occur mainly between bursts. The critical gap lengths calculated using each of the methods were as follows: 0.81 ms (minimum total number misclassified), 0.60 ms (equal numbers misclassified), and 0.52 ms (equal percentages misclassified). For the analysis of bursts that follows a t_c of 0.52 ms has been chosen. In our example the estimate of the burst length would be similar if either of the other two values for t_c had been selected. It is important to realize, though, that when the number of events contained within the two components is very different, the first two methods described for obtaining t_c can result in a high proportion of the rarer sort of event being misclassified. Additionally the method of "equal proportions misclassified" always results in a greater number of total misclassified events than would be obtained if one used either of the other two methods. Therefore it is always a good idea to try different methods to see which one gives the most consistent result between different experiments.

With the t_c selected we can now construct the burst length distribution; this is shown in Fig. 7E. Again we have imposed a 100 μ s

resolution on the data and the distribution is well-described by a single exponential function, with a time constant of 3.34 ms. How does this value compare with what we might expect from our model? First we need to estimate the mean number of brief gaps that would be expected to occur in a burst. This is given by the following equation:

$$\text{mean number of brief gaps} = \frac{\beta}{k_{-1}}.$$

Thus the ratio of the opening rate constant to the dissociation rate constant gives the mean number of sojourns in the AR state within a burst. Therefore it follows that the mean number of openings that occur in burst is:

$$\text{mean number of openings per burst} = 1 + \frac{\beta}{k_{-1}}.$$

We can now calculate what the predicted mean burst length should be by:

$$\text{mean burst length} = \frac{1}{\alpha} \left(1 + \frac{\beta}{k_{-1}} \right) + \frac{1}{\beta + k_{-1}} \left(\frac{\beta}{k_{-1}} \right).$$

Therefore we would expect that on average there to be 2 brief gaps per burst, 3 openings per burst and the mean burst length to be 3.27 ms. Thus our estimate of 3.34 ms is a good approximation to the true value. The distribution of the number of openings per burst is not an exponential distribution, but rather it is a geometric distribution. This is plotted in Fig. 7F, where the distribution is best fit with a single geometric component with a mean equal to 2.99 (as predicted).

In general, measurements of burst parameters are less affected by 'missed events' (i.e., events not detected in the analysis because they cannot be differentiated from background noise) than parameters relating to open times and shut times. Furthermore, in the case of ligand-gated ion channels, bursts of channel openings represent single 'activations' of the receptor-channel complex (for example, *see* B     et al., 1999; Wyllie et al., 1998). Therefore it is the properties of such events that need to be studied if we want to relate microscopic single-channel activity to the macroscopic activity of ion channels that mediate a synaptic current.

3.9. Real-Life Example:

The Burst Length Distribution of NMDA Receptors

When it comes to the study of real channels, we need to infer what sort of kinetic scheme can account for the data we observe; in the simulation above we started with a kinetic scheme and demonstrated the sort of channel activity that we might expect, a luxury not afforded to us normally. Nonetheless, simulations of this nature are useful to demonstrate some basic concepts involved in channel kinetics.

When one actually carries out an experiment, we find that open and shut time distributions are rarely as straightforward as those generated from the simulation. The histograms shown in Fig. 8A,B exemplify this point and serve to indicate that there is much to be done when it comes to understanding the behaviour of individual ion channels. Figure 8A shows a shut time distribution, while Fig. 8B shows a burst length distribution for the NR1a/NR2A subtype of NMDA receptor. The shut time distribution contains at least five components and the burst distribution contains six components. The calculated critical gap length of 88 ms was estimated by the method of misclassifying equal numbers of shut time intervals (Clapham and Neher, 1984), where the first four components of the shut time distribution were considered to occur within a burst and the last component was thought to contain intervals that occurred between bursts. The reasoning behind this resulted from the fact that only the time-constant of the fifth component showed significant agonist concentration dependence. An example of a burst of openings present in the last component is shown above the burst-length distribution; note the time-base and the fact that within this burst there is a gap with a duration of many tens of milliseconds (data from Wyllie et al., 1998). As yet we do not have a kinetic scheme that can adequately describe this behavior.

The burst-length distribution illustrated in Fig. 8 was obtained from a steady-state recording of NMDA receptor-channel activity using a low agonist concentration (100 nM) so that individual bursts of openings were, temporally, well-isolated. Clearly during synaptic activation of NMDA receptors the agonist concentration in the synaptic cleft is high (a few millimolar) but decays rapidly (in a few milliseconds). Using the concentration jump technique (e.g., see Fig. 3) we can attempt to mimic this. Figure 9A

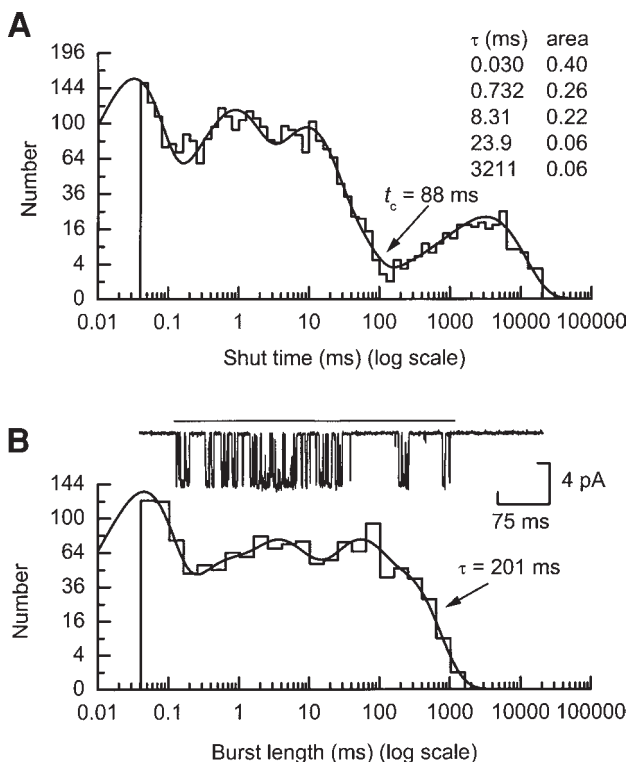


Fig. 8. Example of shut time and burst length distribution for NMDA receptor-channels. **(A)** Shut time distribution for recombinant NR1a/NR2A NMDA receptor-channels activated by 100 nM glutamate (+20 μ M glycine). The distribution is fitted with a mixture of five exponential components with means and relative areas as indicated. **(B)** Burst length distribution for NR1a/NR2A NMDA receptor-channels fitted with a mixture of six exponential components. The most prominent component, in terms of charge transfer, is the last component of the distribution which has a mean of 201 ms. A typical activation from this component is shown above the burst-length distribution. Data adapted with permission from Wyllie et al. (1998).

shows three examples of NMDA receptor-channel bursts evoked by a 1 ms application of 1 mM glutamate. Just as predicted from the steady-state recordings these activations last for several hundreds of milliseconds and contain shut periods that last many tens of milliseconds. These channel activations must have been initi-

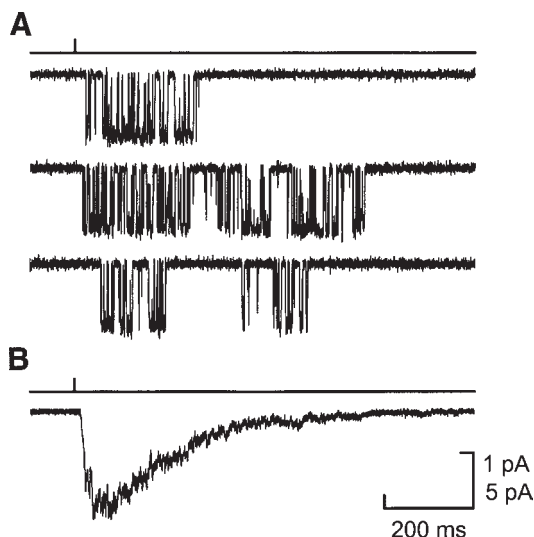


Fig. 9. NMDA single-channels in a 'one-channel' patch. (A) Examples of three individual channel activations (bursts) recorded in a patch containing only one channel. Channel activity was evoked by exposing an outside-out patch containing NR1a/NR2A NMDA receptors channels to glutamate (1 mM) for 1 ms. (B) The average of 248 such jumps gives a current that decays (exponentially) with a time constant of around 250 ms. Data adapted with permission from Wyllie et al. (1997).

ated by the binding of glutamate during the 1 ms exposure of the outside-out patch to the agonist-containing solution. When a large number of such bursts are averaged, we obtain a current that decays with a time constant of approx 250 ms (Fig. 9B). This would be expected (1) from the longest component of the steady-state burst-length distribution (since this is the component that carries the majority of the charge) and (2) from studies of the decay of the NMDA receptor-mediated component of glutamatergic synaptic currents in brain regions where the NR2A NMDA receptor subunit is expressed at high levels (e.g., see Clark et al., 1997).

I hope that this brief overview of the techniques involved in recording and analyzing single-channel data has broken down some of the barriers that prevent many people from using this technique. A frequent reply to the question "Why don't you record some single-channel activity?" is "I'd like to but I'm not very good

at math." Being good at math does not mean that you can obtain good-quality data. Try getting the data first and then seek advice if you find you struggle a bit with the complexities of the analysis! As stated at the beginning of this chapter, watching the movement of single proteins is captivating.

Acknowledgments

Work in my lab is supported by grants from the Wellcome Trust, the BBSRC and The Royal Society. I thank those colleagues who supplied me with illustrations used in this review. I am grateful to David Colquhoun and Phil Larkman for commenting on, and suggesting improvements to, an earlier version of this review. The simulation routine and data analysis programs that have been used and described here are all available (free of charge) from <http://www.ucl.ac.uk/Pharmacology/dc.html>.

References

- Anson, L. C., Schoepfer, R., Colquhoun, D., and Wyllie, D. J. A. (2000) Single-channel analysis of a NMDA receptor possessing a mutation in the region of the glutamate binding site. *J. Physiol.* **527**, 225–237.
- Béhé, P., Colquhoun, D., and Wyllie, D. J. A. (1999) Activation of single AMPA- and NMDA- type glutamate-receptors channels, in *Handbook of Experimental Pharmacology*, vol. 141 (Jonas, P. and Monyer, H., eds.), Springer Verlag, Berlin, pp. 175–218.
- Blatz, A. L. and Magelby, K. L. (1986) Correcting single channel data for missed events. *Biophys. J.* **49**, 967–980.
- Castillo, J. Del and Katz, B. (1957) Interaction at end-plate receptors between different choline derivatives. *Proc. R. Soc. B* **146**, 369–381.
- Clapham, D. E. and Neher, E. (1984) Substance P reduces acetylcholine-induced currents in isolated bovine chromaffin cells. *J. Physiol.* **347**, 255–277.
- Clark, B. A., Farrant, M., and Cull-Candy, S. G. (1997) A direct comparison of the single-channel properties of synaptic and extrasynaptic NMDA receptors. *J. Neurosci.* **17**, 107–116.
- Colquhoun, D. and Hawkes, A. G. (1982) On the stochastic properties of bursts of single ion channel openings and of clusters of bursts. *Philos. Trans. R. Soc. London B* **300**, 1–59.
- Colquhoun, D. and Hawkes, A. G. (1995) The principles of the stochastic interpretation of ion-channel mechanisms, in *Single Channel Recording*, 2nd ed. (Sakmann, B. and Neher, E., eds.), Plenum Press, New York, pp. 397–482.
- Colquhoun, D. and Sakmann, B. (1985) Fast events in single-channel currents activated by acetylcholine and its analogues at the frog muscle end-plate. *J. Physiol.* **369**, 501–557.
- Colquhoun, D. and Sigworth, F. J. (1995) Fitting and statistical analysis of single-channel records, in *Single Channel Recording*, 2nd ed. (Sakmann, B. and Neher, E., eds.), Plenum Press, New York, pp. 483–587.

- Edwards, F. A., Konnerth, A., Sakmann, B., and Takahashi, T. (1989) A thin-slice preparation for patch-clamp recording from synaptically connected neurones of the mammalian central nervous system. *Plüfegers Arch.* **414**, 600–612.
- Gibb, A. J. (1995) Patch-clamp recording, in *Ion Channels: A Practical Approach* (Ashley, R. H., ed.), IRL Press, Oxford, pp. 1–42.
- Gibb, A. J. and Colquhoun, D. (1992) Activation of *N*-methyl-D-aspartate receptors by L-glutamate in cells dissociated from adult rat hippocampus. *J. Physiol.* **456**, 143–179.
- Hamill, O. P., Marty, A., Neher, E., Sakmann, B. and Sigworth, F. J. (1981) Improved patch-clamp techniques for high-resolution current recordings from cells and cell-free membrane patches. *Plüfegers Arch.* **391**, 85–100.
- Jackson, M. B., Wong, B. S., Morris, C. E., Lecar, H., and Christian, C.N. (1983) Successive openings of the same acetylcholine receptor channel are correlated in open time. *Biophys. J.* **42**, 109–114.
- Moss, G. W. J. and Moczydlowski, E. (1995) Concepts of single-channel analysis: inferring function from fluctuations, in *Ion Channels: A Practical Approach* (Ashley, R. H., ed.), IRL Press, Oxford, pp. 69–112.
- Neher, E. and Sakmann, B. (1976) Single channel currents recorded from membrane of denervated frog muscle fibres. *Nature* **260**, 799–802.
- Selyanko, A. A. and Sim, J. A. (1998) Ca^{2+} -inhibited non-inactivating K^+ channels in cultured rat hippocampal pyramidal neurones. *J. Physiol.* **510**, 71–91.
- Sherman-Gold, R. (ed.) (1993) *The Axon Guide for Electrophysiology & Biophysics Laboratory Techniques*. Axon Instruments, Union City, CA.
- Sigworth, F. J. (1995) Electronic design of the patch clamp, in *Single Channel Recording*, 2nd ed. (Sakmann, B. and Neher, E., eds.), Plenum Press, New York, pp. 95–127.
- Sigworth, F. J. and Sine, S. M. (1987) Data transformations for improved display and fitting of single-channel dwell time histograms. *Biophys. J.* **52**, 1047–1054.
- Wyllie, D. J. A., Béhé, P., and Colquhoun, D. (1998) Single-channel activations and concentration jumps: comparison of recombinant NR1A/NR2A and NR1A/NR2D NMDA receptors. *J. Physiol.* **510**, 1–18.
- Wyllie, D. J. A., Edmonds, B., and Colquhoun, D. (1998) Single-channel activations of recombinant NMDA NR1a/NR2A receptors recorded in one-channel patches. *J. Physiol.* **501P**, 13P.

Recommended Reading

- Aidley, D. J. and Stanfield, P. R. (1996) *Ion Channels: Molecules in Action*. Cambridge University Press, Cambridge, UK.
- Ashley, R. H. (ed.) (1995) *Ion Channels: A Practical Approach*. IRL Press, Oxford, UK.
- Conn, P. M. (ed.) (1998) *Methods in Enzymology: Ion Channels* Part B. Academic Press, New York.
- Hille, B. (1992) *Ionic Channels of Excitable Membranes*, 2nd ed. Sinauer Associates, Sunderland, MA.
- Neher, E. and Sakmann, B. (eds.) (1995) *Single Channel Recording*, 2nd ed. Plenum Press, New York.
- Ogden, D. C. (ed.) (1994) *Microelectrode Techniques: The Plymouth Workshop Handbook*, 2nd ed. Company of Biologists Limited, Cambridge.

4

Combined Fluorometric and Electrophysiological Recordings

Hartmut Schmidt and Jens Eilers

1. Introduction

Combined electrophysiological and fluorometric recordings have proven to be a powerful tool, especially in the field of neurobiology. With this combination it became possible to overcome three major limitations of pure electrophysiological measurements. First, high-resolution recordings from cellular compartments distant to the recording electrode became feasible, allowing, for example, the quantification of the occupancy of postsynaptic receptors (Mainen et al., 1999) and the density of voltage-gated Ca^{2+} channels (Sabatini and Svoboda, 2000) at the level of single dendritic spines. Second, the analysis of cellular responses not directly associated with electrical signals became possible. Examples include synaptically evoked Ca^{2+} release from intracellular stores (Takeuchi et al., 1998; Finch and Augustine, 1998) and Ca^{2+} buffering by endogenous Ca^{2+} -binding proteins (Zhou and Neher, 1993). Third, the spatio-temporal extent of second messenger signals, e.g., during subthreshold synaptic activity (Eilers et al., 1995a) and during the induction of synaptic plasticity (Eilers et al., 1997a) can be monitored by means of fluorescence imaging.

In recent years, several technical advances have extended the range of possible applications of fluorescence microscopy. For example, two-photon microscopy (Denk et al., 1990), green-fluorescent proteins (Chalfie et al., 1994), and indicators that use the fluorescence resonance energy transfer (FRET) effect (Adams et al., 1991) opened exciting new avenues for studying cell physiology. In view

From: *Neuromethods*, Vol. 35: *Patch-Clamp Analysis: Advanced Techniques*
Edited by: W. Walz, A. A. Boulton, and G. B. Baker @ Humana Press Inc., Totowa, NJ

of these ongoing developments, combined fluorometric and electrophysiological recordings will continue to be the method of choice for high-resolution *in vitro* and *in vivo* studies.

This chapter aims to give a detailed overview of the special requirements for performing fluorometric measurements in combination with standard patch-clamp recordings. The emphasis will be on dendritic Ca^{2+} measurements in neurons in brain slice preparations since such recordings can encompass significant difficulties arising from the fast timecourse and/or compartmentalization of the postsynaptic signals. However, the methodology is also applicable for other preparations and other signals such as dendritic sodium signals (Rose et al., 1999).

2. Methods

2.1. Recording Setup

2.1.1. Vibration Control

As for standard electrophysiological recordings, good isolation from vibration is also critical for fluorometric experiments. While vibrations will obviously affect the stability of the patch-clamp recording, they will also lead to fluctuations in fluorescence signals, especially when recording from small cellular compartments such as spines, which have to be kept in focus with high precision. Thus, any vibrations of the setup need to be prevented by mounting it on a high-quality air table. In addition, any movements of the fluorescence detector (i.e., camera or confocal system) relative to the microscope body needs to be restricted by a rigid connection between the microscope and the detector system.

If the fluorescence system incorporates a laser, severe vibrations may be introduced by its fan (for air-cooled lasers) or the water flow through its cooling pipes (for water-cooled lasers). Such vibrations are difficult to dampen. Fortunately, most modern laser-based imaging systems use fiber optics to connect the laser to the detector unit. Here, the laser does not have to be located directly on the air table and, therefore, vibrations will cause no problem. However, in some older systems (e.g., the *Odyssey* scanner from Noran, Middleton, WI) the laser is rigidly connected to the imaging system. If critical vibrations occur in these systems, an experienced service engineer could take out the laser and reconnect it via an optical fiber (e.g., from Melles Griot, Irvine, CA).

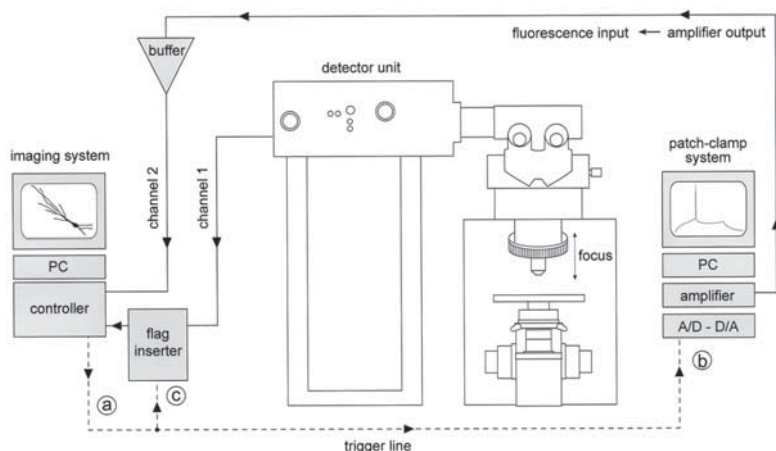


Fig. 1. Schematic drawing of the experimental set-up. The system consists of an upright microscope (center) equipped with a fluorescence detection unit (left) and an electrophysiology unit (right). Focusing moves the nosepiece and the attached objective only. The imaging system can trigger the patch-clamp system (a to b) and/or the flag inserter (c, *see* Fig. 4), which electronically places markers into the fluorescence signal (channel 1) before it is recorded by the imaging system. The electrophysiological signal can be amplified (buffer) and fed into a free channel of the imaging system (channel 2) to allow accurate correlation of electrical and fluorometric responses (*see* Fig. 5).

2.1.2. Microscope

Several important considerations concern the selection of the microscope and its components. Whether the setup is based on an inverted or an upright microscope will be determined by the preparation under study. For work on cultured cells, inverted microscopes are preferable. Here, the objective can be positioned quite close to the specimen because the patch-clamp electrode is above the focal plane. Thus, objectives with a high numerical aperture (NA) can be selected that have a good optical resolution and a high collection efficacy, *see* below. For work on thick samples (e.g., brain slices) upright microscopes (Fig. 1) are preferable because they allow the establishment of the electrophysiological recording under visual control. Suitable objectives, however, will have a slightly reduced NA due to the long working distance required to be able to position the electrode under the objective.

The z-stage should be “fixed” and focusing should only move the “nosepiece” with the attached objective (Fig. 1). With a fixed stage, the specimen is not moved during focusing and the manipulators can be mounted on rigid columns surrounding the microscope (see, for example, mechanical setup from Luigs & Neumann, Ratingen, Germany). For two reasons, the focusing should also not move the trinocular, to which, in most cases, the imaging system will be coupled (see Fig. 1). First of all, some systems (especially confocal laser-scanning systems) have a considerable weight, which may lead to slow defocusing or may indeed not be supported by the focusing unit. Second, as stated earlier, the imaging system should be mounted rigidly on the air table to prevent vibrations. If the system is only attached to the trinocular, the fluorometric recordings will be prone to movement artifacts.

Some patch-clamp experiments may require the use of infrared differential interference contrast (IR-DIC) optics to visualize somata and dendrites in thick samples (Dodt and Zieglgänsberger, 1990). While this technique generates high-contrast images even deep in brain slices, it necessitates the addition of two optical elements between the specimen and the trinocular, namely a prism and a polarizer. During fluorometric recordings, these two elements will block a substantial amount of the emitted fluorescence. However, the light emitted from the fluorescent probes is of ultimate value in fluorescence measurements of living preparations (see below) and, therefore, the loss of photons induced by DIC optics is not acceptable. Thus, the distinct DIC optics (especially the polarizer) should be carefully removed during the fluorescence recording. If the experimental arrangement does not allow this maneuver, the so-called Dodt’s gradient contrast illumination (Schieffer et al., 1999; Luigs and Neumann) may be an attractive solution. This illumination system is based on a simple modification of standard bright field illumination and does not require any special optical elements in the emission light path. In most preparations the resolution is as good as that obtained with IR-DIC.

The most critical optical element is, of course, the objective. Its selection will primarily be based on the requirements of the electrophysiology. Thus, its immersion medium, working distance, and geometry should easily permit patch-clamp recordings. Beside this, for fluorometric recordings the two most important parameters are the wavelength-dependent transmittance and the numerical aperture.

2.1.2.1. TRANSMITTANCE

Standard objectives transmit light efficiently in the visible spectral range but may have serious limitations in the ultraviolet (UV) and infrared (IR) range. Since most available dyes emit light in the blue to yellow range, transmittance will be no problem for *emission*. However, *excitation* of the dyes may require UV (<400 nm) or IR (>800 nm) light. Typical examples include quantitative Ca^{2+} measurements using the fluorescent indicator *Fura-2* (excitation 340–380 nm) and in vivo two-photon microscopy (excitation 760–960 nm). Thus, depending on the experimental conditions (available imaging system, dye to be used, etc.), a UV- or IR-optimized objective may be required. While all major microscopy companies provide such lenses, a comparison between objectives from different companies is difficult. This is due to the fact that most companies do not share the spectral response curves of their objectives with the public. In that respect, a demonstration and direct comparison of suitable objectives may provide useful information on which objective to buy.

2.1.2.2. NUMERICAL APERTURE (NA)

For fluorometric recordings, the NA is of utmost importance. A thorough explanation of the optical and numerical basis of the NA is beyond the scope of this chapter; *see* Lanni and Keller (1999) for details. Generally speaking, the NA describes how much of the emitted fluorescence will be collected by the objective. A higher NA corresponds to a higher collecting efficacy. Note, however, that the NA is not linearly related to the efficacy. For water-immersion objectives NAs of 0.5, 0.7, and 0.9 correspond to collecting efficiencies of 5, 7.5, and 13.5% respectively. Obviously, objectives with as high a NA as possible should be chosen to collect a maximum of the emitted fluorescence.

2.1.3. Imaging System

Today, there is a vast and maybe somewhat confusing diversity in fluorescence detection systems available from commercial suppliers. Choices range from standard camera-based fluorescence systems to confocal laser-scanning microscopes and, more recently, to two-photon microscopes. All these systems have their specific pros and cons, so no single favorite can be recommended. Rather, in the following we will try to list specific requirements that should be

considered when selecting a system for combined electrophysiological and fluorescence recordings.

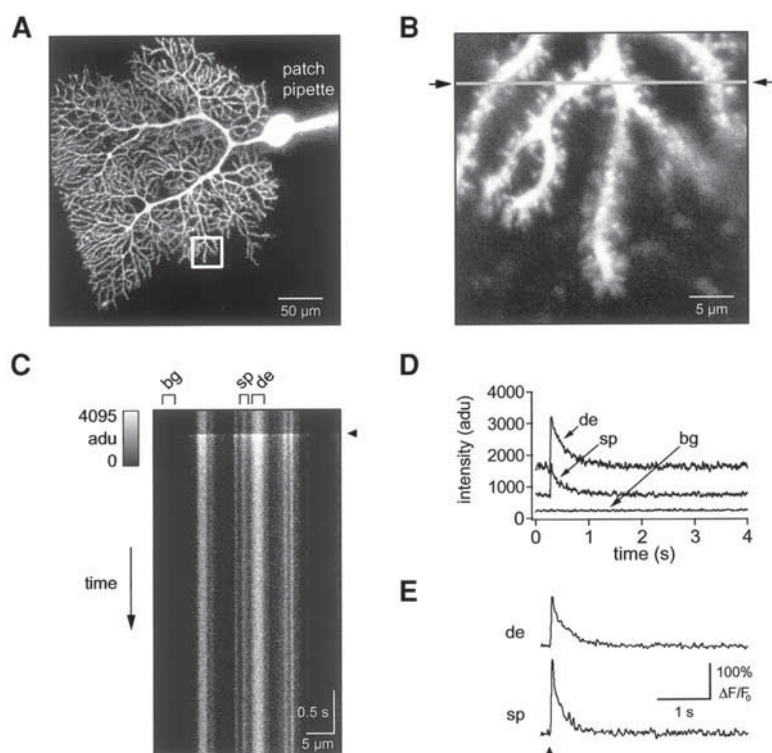
2.1.3.1. TEMPORAL RESOLUTION

Depending on the application, one may have to cope with extremely rapid fluorescence signals. Dendritic Ca^{2+} transients, for example, can have decay time constants well below 100 ms (*see* Fig. 2). In order to quantify reliably such signals, the fluorescence system has to be capable of recording at a comparable speed. Several approaches can be used to fulfill this demand. Thus, some cameras as well as laser-scanning confocal systems (the RCM 8000 from Nikon (Melville, NY and confocal systems from Noran Instruments, not commercially available at present) and two-photon microscopes (Fan et al., 1999) can acquire full images at video rate (*see* Fig. 4). Other systems allow the use of binning, or the selection of regions of interest to sample at rates of tens of Hertz. The highest time resolution is obtained by restricting the acquisition to a single line (the so called line-scan mode) or even a single point. Sample rates of around 500 Hz (line-scan) and 0.5 MHz (point-scan) can be achieved. When deciding on a system, special care should be taken to test the functionality of the hard- and software. Many systems perform brilliantly as long as standard functions are carried out, but crash—more or less systematically—as soon as one tries to push the temporal resolution to its limits.

2.1.3.2. SPATIAL RESOLUTION

Fluorescence signals may be restricted to small cellular compartments such as submembrane shells (Hernández-Cruz et al., 1990; Eilers et al., 1995b) or dendritic spines (Müller and Connor, 1991; Takechi et al., 1998). For studying such signals, standard

Fig. 2. Line-scan recordings of Ca^{2+} transients in spines and dendrites. (A) Confocal fluorescence image of a Purkinje neuron in a cerebellar-slice preparation. The cell was loaded with the Ca^{2+} indicator *Oregon Green BAPTA-1* via the patch pipet. The white rectangle outlines the region that is shown at higher magnification in (B). The image represents a maximum projection of a stack of 16 x - y images taken at 1 μm z interval. (B) High-resolution image of spiny dendrites taken with an 60 \times objective (0.9 NA) and an additional 10 \times magnification provided by the confocal imaging system. The arrows and the gray line indicate the area in which activity-induced Ca^{2+} transients were monitored in the line-scan mode, *see* (C).



(continued) Note that dendrites that were out of focus appear dim and blurred. (C) Line-scan image (x vs time) of the region outlined in (B) during activation of the afferent climbing fiber. In this and the following figures the timepoint of stimulation is denoted by arrow heads. The stimulation resulted in a suprathreshold EPSP (not shown) and a transient increase in fluorescence in spines and dendrites which reflects a transient increase in the intracellular Ca^{2+} concentration. Three regions (bg, sp, and de; background, spine, and dendrite, respectively) are demarked in which the timecourse of the fluorescence changes were analyzed in detail, see D. The temporal resolution of the acquisition was 2 ms per line. The pixel intensities of the 12 bit images range from 0 (black) to 4095 (white) in arbitrary digital units (adu; left inset). (D) Averaged pixel intensity from the three regions outlined in (C) plotted against time. Note that all values are well above 0 and below 4095 adu, indicating a correct setting of gain and contrast of the imaging system; see text for details. (E) Fluorescence transients in the spine and the dendrite converted to background-corrected $\Delta F/F_0$ values, see text.

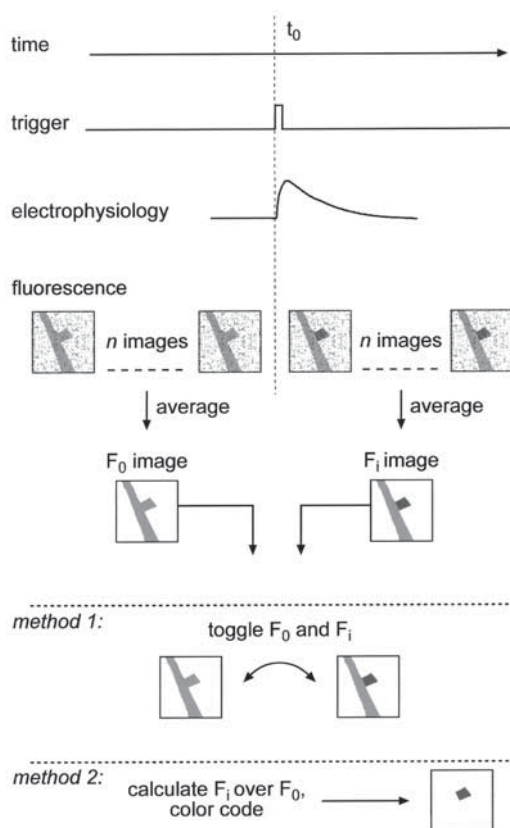


Fig. 3. Algorithm for finding localized and/or minute fluorescence transients. t_0 denotes the timepoint, at which the fluorescence system sends a trigger signal that starts the stimulation of afferent fibers. The electrophysiology trace shows an example EPSP. The rectangles represent simulated images of a dendrite and an adjacent spine with a fluorescence signal restricted to the spine (right images). In addition, the top row of images contain synthetic noise to illustrate the low signal-to-noise ratio of raw recordings. Before and after the stimulation several images are averaged to obtain the F_0 and F_i image, respectively. Differences in the fluorescence intensity can easily be identified either by alternating the display of the F_0 and F_i image at about 1–4 Hz (method 1) or by calculating the ratio of the images and display the result using a color code that emphasizes values different from 1 (method 2).

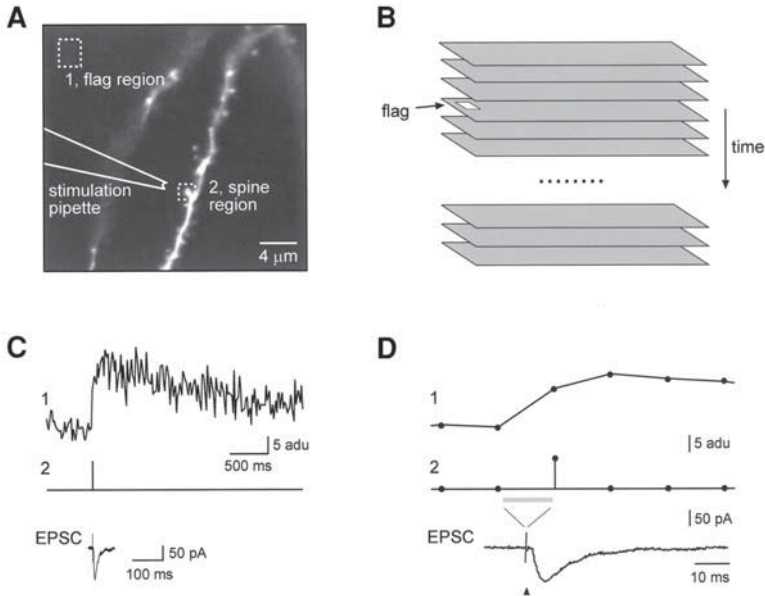


Fig. 4. Synchronizing electrical and fluorometric recordings using the "flag inserter." (A) Confocal image of apical dendrites of a CA 1 pyramidal neuron loaded with *Calcium Green-1*. The dashed boxes delineate the regions that were used for measurement of the fluorescence in the spine and the flag signal generated by the flag inserter circuit, *see* Fig. 1 and text. Afferent fibers were activated with an extracellular stimulation pipet. (B) Schematic illustration of the acquired image sequence. The gray rectangles indicate individual images. The white mark represents the flag that is inserted electronically by the flag inserter. The flag is drawn at a fixed position into the image generated immediately after the timepoint of synaptic stimulation. (C) Activation of the afferent fibers produced an EPSC (bottom trace) and an associated fluorescence increase in the spine (trace 1). The flag signal (trace 2) shows the single data point of maximal intensity (reduced to 5% for clarity) that corresponds to the image into which the flag was inserted. Image acquisition rate was 60 Hz. (D) The fluorometric data from (C) plotted on the same time scale as the EPSC. Individual data points are indicated by closed circles. The flag signal (third data point in trace 2) allowed the EPSC and the fluorescence signal to be correlated with an accuracy of 16.5 ms, indicated by the gray line. Modified from Eilers et al. (1997b).

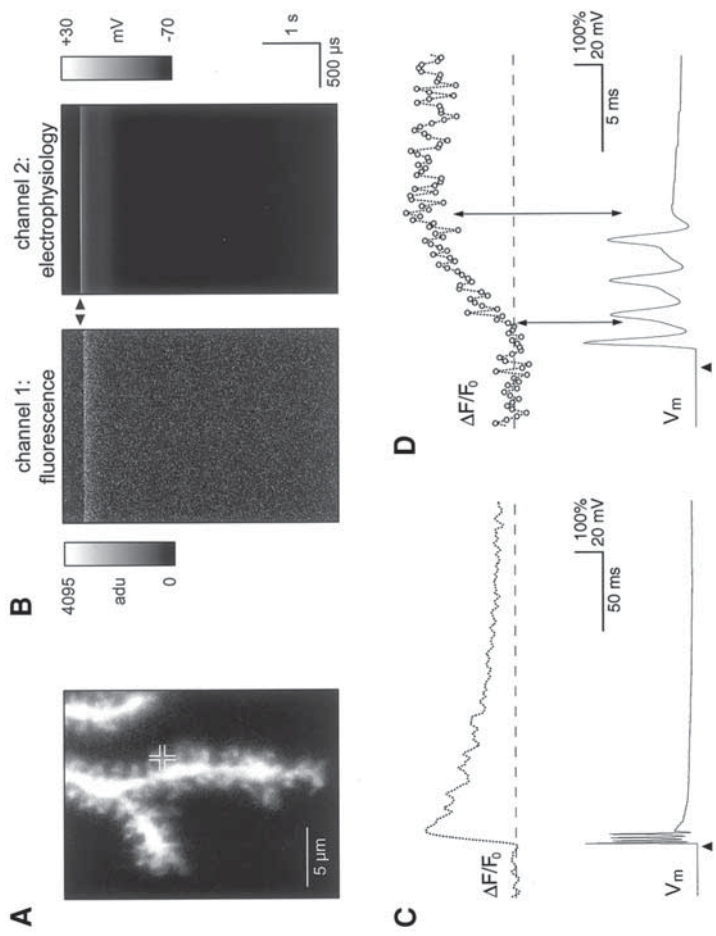


Fig. 5.

fluorescence techniques are of limited use due to image blurring by out-of-focus light. Although such stray light can be mathematically removed from the images off-line (Carrington et al., 1995), this procedure is rather complicated and time-consuming. A simpler, though more expensive alternative is given by confocal laser-scanning microscopy (CLSM; Minsky, 1961) and two-photon microscopy (TPM; Denk et al., 1990). Here, out-of-focus light is either prevented from reaching the detector (CLSM) or is not generated at all (TPM) yielding high-resolution images even in opaque tissue. The examples shown in Figs. 2, 4, and 5 were generated with commercial CLSM systems.

2.1.3.3. EXCITATION LIGHT

Different fluorescence systems will be equipped with different light sources. While camera-based systems usually employ arc lamps equipped with filter wheels or monochromators, confocal systems use lasers for excitation. In both cases severe vibration may occur either due to the cooling device of the laser (*see* Subheading 2.1.1.) or when the filter wheel or monochromator is activated during selection of different wavelengths. Thus, whenever possible, the light source should be connected to the fluorescence

Fig. 5. Simultaneous electrophysiological and fluorometric recordings in the point-scan mode. **(A)** Confocal image of spiny dendrites of a Purkinje neuron loaded with *Oregon Green BAPTA-1*. The cross indicates a single spine from which the fluorescence was sampled in the point-scan mode, *see* (B), channel 1. **(B)** Point-scan recording of the electrical response (channel 2, recorded with a somatic patch pipet) and the fluorometric response (channel 1) in the spine marked in (A) evoked by activation of the afferent climbing fiber. The confocal system allowed the recording of two channels (sampling rate 0.5 MHz). While the fluorescence signal was recorded into the first channel, the cell's membrane potential (V_m) was fed into channel 2 (*see* text for details). The arrow heads denote the timepoint of stimulation. Note that both, the x and the y axis of the images represent time. **(C)** Signals from B (covering the first 200 ms of the climbing fiber response) plotted against time. The fluorescence was binned to 0.5 kHz and converted to $\Delta F/F_0$ values. The electrical signal (V_m) includes the so-called complex spike, the typical response to climbing fiber stimulation. **(D)** Horizontal expand of (C). Note that the start and the end of the rising phase of the Ca^{2+} transient can be correlated to distinct components of the complex spike (arrows).

system via an optical fiber to prevent these vibrations from affecting the electrophysiological recordings and/or the optical resolution (*see* Subheading 2.1.1.). Furthermore, the fluorescence system should permit simple and vibration-free exchange of its optical elements, such as barrier filters and dichroic mirrors. Thus, switches and turrets should operate smoothly and no strong solenoids should be used for shuttering the excitation light.

2.1.3.4. SOFTWARE

Fluorescence responses may have small amplitudes and fast kinetics and, thus, may be hard to detect by eye. For the detection of such signals the acquisition software should provide simple measurement tools, such as a quick brightness vs time analysis from selected regions of interest. Also, a basic macro language that allows the programming of simple acquisition protocols (*see* Fig. 3) is extremely helpful in detecting minute fluorescence signals. The idea is to be able to judge during or immediately after a recording whether it was successful or not.

2.1.3.5. HARDWARE

The fluorometric system should be able to start the acquisition of the electrophysiology system. This will facilitate recordings in which either small and fast responses need to be identified or in which the electrophysiological response needs to be correlated with the fluorescence signal with a high temporal precision. For this purpose a trigger signal (a in Fig. 1) from the fluorescence unit should be available that either signals the acquisition status (active/inactive) or can be set by macro commands of the fluorescence software. This output will in most cases be a "TTL" (transistor-transistor logic, 0 V and 5 V representing "off" and "on" respectively) line that can directly be connected to a corresponding input (b in Fig. 1) of the electrophysiological unit. Most patch-clamp acquisition software allows acquisition to be triggered by an external stimulus, thus, the described trigger line can be used to have the fluorescence unit control the exact timepoint of, for example, a somatic depolarisation or synaptic stimulation. Figures 2–5 illustrate recordings in which this capability was of critical importance for successful recordings.

The trigger output can also be used to automatically place a marker into the stream of the fluorescence data (c in Fig. 1). For

this function, an appropriate electronic device ("flag inserter" in Fig. 1) needs to be added that, when triggered, electronically inserts a marker, the "flag" into the fluorescence data, *see* Fig. 3B. During the recording as well as during playback of the data, the flag will be a clearly recognizable indicator of the timepoint of stimulation. While electronic circuits for this purpose are not commercially available, they can easily be constructed. For video-rate fluorescence imaging, an appropriate circuit has been published (Eilers et al., 1997b) which could be adapted to different fluorescence systems.

For highest demands in temporal correlation, a free fluorescence input of the imaging system can be used for recording electrophysiological in parallel with fluorometric data ("channel 2" and "channel 1," respectively, in Fig. 1). An example of this application is shown in Fig. 5. Note that the output impedance of the electrophysiological signal (usually in the range of 500 Ω) must match the input impedance of the fluorescence input (usually about 50 Ω). Also, the fluorescence input will most likely expect positive voltage signals while the electrophysiological signal (membrane voltage or current) will be of negative polarity. Thus, an amplifier ("buffer" in Fig. 1) needs to be incorporated that inverts and amplifies the electrophysiological signal before it is fed into the fluorescence system.

Grounding of electrophysiological setups is somewhat complicated by incorporating fluorescence equipment. Cameras and lasers, for example, generate high-frequency electrical noise. Furthermore, since any modification of the ground connections of these devices is not recommendable for safety reasons, ground loops will also be a problem. In this respect, it may be helpful to electrically isolate critical equipment by connecting it to the microscope with plastic adapters only.

Finally, it should be possible for the user to easily align the fluorescence detection unit. Both, the overall transmittance and the optical resolution should be carefully checked on a regular basis. For this purpose mixed stained pollen grains (Carolina Biological Supply Co., #304264) can be used as a simple but reliable test specimen. These pollen grains are stained with different fluorescent dyes and can easily be visualized with most fluorescence optics. They possess small protrusions that allow the optical resolution of fluorescence systems to be checked and adjusted.

2.2. Recordings

As stated earlier, we will focus on the methodology for fluorometric Ca^{2+} measurements in neurons. Thus, the emphasis will be on suitable indicators and analysis steps. However, the guideline is also applicable to fluorometric measurements of signaling molecules different from Ca^{2+} , such as Cl^- , Na^+ , or cAMP.

2.2.1. Fluorescence Ca^{2+} Indicators

The selection of an appropriate indicator dye is governed by several parameters, the most obvious one being its excitation spectrum. Depending on the fluorescence system in use, only certain wavelengths may be available. Confocal laser-scanning microscopes, for example, are usually equipped with ion lasers that emit only at a few distinct wavelengths and, in most cases, do not allow excitation in the UV range. In contrast, a broad spectrum of different dyes can be excited with monochromators (Uhl, 1999) or two-photon microscopes (Xu et al., 1996). Note that excitation as well as emission spectra of most commonly used dyes are available from Molecular Probes. The second critical parameter concerns the expected magnitude of the Ca^{2+} signal to be studied and the affinity of the Ca^{2+} indicator. As a rule of thumb, Ca^{2+} indicator dyes allow measurements in the range of 0.1 to 4 times their dissociation constants (K_D). Thus, for example, a high-affinity Ca^{2+} indicator with a K_D of 300 nM allows measurements in the range from 30–200 nM. Note that the exact value of the K_D depends on several parameters, including the pH, osmolarity, temperature, and the concentration of other divalent ions such as Mg^{2+} . Thus, for quantitative measurements, the K_D should be determined specifically for the intracellular solution use. For this purpose, ready-made calibration kits (e.g., C-3273, Molecular Probes) and the public domain software *MaxChelator* (available from www.stanford.edu/~cpatton), that calculates the equilibrium concentration of Ca^{2+} , Mg^{2+} , and EGTA, are available.

Additional criteria for selecting an indicator include its resting fluorescence, i. e., the brightness of the dye at the intracellular calcium concentration ($[\text{Ca}^{2+}]_i$) at rest. For recordings from fine cellular structures, such as dendritic spines, dyes are preferable that exhibit a substantial resting fluorescence (such as *Oregon Green BAPTA-1*). Otherwise, fine structures may be too dim to be seen

under resting conditions and/or no reasonable baseline recording may be obtained (*see below*). Finally, if possible a dye should be chosen that allows the quantification of Ca^{2+} signals by means of ratiometric recordings. Unfortunately, such dyes either require UV excitation (*Fura-2* and *Indo-1*) or are inherently dim (*Fura Red*). In conclusion, no single dye can be recommended as the gold standard. A good starting point, however, is the high-affinity indicator *Oregon Green BAPTA-1* (Molecular Probes), which can be excited by most light sources and has a substantial fluorescence at resting $[\text{Ca}^{2+}]_i$.

Once an indicator dye has been selected, the next question is at what concentration it should be used. On the one hand, the dye concentration needs to be high enough to allow fluorescence measurements with a reasonable signal-to-noise ratio. On the other hand, for most applications, the concentration should be as low as possible for the following reasons: 1) any Ca^{2+} indicator will act as a buffer that reduces the amplitude and prolongs the duration of Ca^{2+} transients (Neher, 1999); 2) Ca^{2+} indicators may have unexpected pharmacological side-effects. Most commonly used Ca^{2+} indicators, for example, block IP 3 receptors at submillimolar concentrations (Morris et al., 1999). We routinely use a dye concentration of 20–50 μM for somatic and 100–200 μM for dendritic recordings. However, these values should be optimized for the required spatio-temporal resolution and the sensitivity of the fluorescence detector in use.

2.2.2. Solutions

Solutions used in combined fluorometric and patch-clamp recordings are similar to those used in standard patch-clamp recordings. Our standard extracellular saline contains (in mM): 125 NaCl, 2.5 KCl, 1.25 NaH_2PO_4 , 26 NaHCO_3 , 1 MgCl_2 , 2 CaCl_2 , 20 glucose, pH 7.3 to 7.4 when gassed with 95% O_2 and 5% CO_2 . Depending on the experimental requirements, various intracellular solutions can be used. As an example, one of our standard pipet solutions contains (in mM): 104 K-gluconate, 8 KCl, 2.5 Mg-ATP, 0.25 GTP, 8 HEPES; 0.1 *Oregon Green BAPTA-1*; adjusted to pH 7.3 with KOH). Note that no Ca^{2+} buffers like EGTA or BAPTA are included in addition to the Ca^{2+} indicator dye. These would buffer Ca^{2+} transients and, thereby, reduce the fluorometric signal. However, when low-affinity Ca^{2+} indicator dyes like *Magnesium Green* are used in

long-lasting whole-cell recordings, EGTA or BAPTA may be included to compensate for possible wash-out of endogenous Ca^{2+} buffers (Zhou and Neher, 1993).

For efficient use of the expensive indicator dyes, we prepare a concentrated (125%) solution of the intracellular solution from which the dye has been omitted as well as a concentrated (about 2 mM) stock solution of the indicator dye dissolved in double-processed water (Sigma, #W-3500). Both solutions should be kept at -20°C for no longer than 2 wk. Suitable quantities of these two solutions are mixed (and sonicated) on a daily basis. Before use, the solution should be filtered with syringe filters (Nalgene, #180-1320). Metal needles must not come into contact with the indicator dye or the pipet solution. They release trace amounts of metals to which the indicator dyes may be extremely sensitive and which may render the dyes Ca^{2+} -insensitive (Gryniewicz et al., 1985). For the same reason, the intracellular solution should be prepared using double-processed water only.

2.2.3. Patch-Clamp Recordings

Seal formation and whole-cell recordings are similar to standard patch-clamp recordings. Low-resistance pipets should be used to allow fast dye loading (*see below*). We routinely use 4–5 M Ω pipets (measured with the intracellular solution mentioned earlier) for somatic recordings from cerebellar Purkinje neurons. When approaching the cell, the application of strong positive pressure should be avoided. Otherwise, the surrounding tissue will be stained by dye ejected from the pipet, which may reduce the optical resolution during the fluorometric recordings. We use the following protocol for patching cells located close to the surface of the slice preparation: when entering the bath and when approaching the cell, weak positive pressure is applied to the pipet to prevent extracellular solution from entering the pipet; immediately before the cell is contacted, a strong but brief (<1 s) pressure pulse is given to clean the surface of the cell; then the pressure is relieved and weak suction is applied to facilitate seal formation (Eilers and Konnerth, 1999).

After the whole-cell configuration is established, equilibration of the cytosol with the indicator dye is determined by three factors: the series resistance (R_s ; Pusch and Neher, 1988), the mobility of the dye molecules (Pusch and Neher, 1988), and the cell geometry (Rexhausen, 1992). In cells that possess an elaborate dendritic tree,

such as cerebellar Purkinje neurons (Fig. 2), the time constant for loading remote dendrites may be as slow as 30–45 min (Rexhausen, 1992). Under such conditions, R_s should be optimized to accelerate dye loading. Thus, the initial pipet resistance should be as low as tolerated by the cells under investigation. Furthermore, after breaking into the cell, R_s should be monitored and kept as low as possible. We rather aggressively try to keep R_s low during the first 10–15 min of the whole-cell recordings. While we lose some cells by this approach, we mostly obtain recordings that stay stable for at least 60–120 min.

2.2.4. Data Acquisition

High-resolution fluorescence recordings from living preparations require delicate tuning of different parameters, most notably of the excitation intensity. This is due to the fact that the generation of fluorescence is inevitably associated with phototoxic damage and dye bleaching. Photodamage may be evident from local swelling (blebbing) of the cell or from a decrease in the membrane resistance with a resulting increase in holding current and reduced excitability (altered waveform of spikes, reduced number of spikes). More subtle signs of photodamage include Ca^{2+} transients that, in contrast to the normal case (Fig. 2D,E), do not fully return to baseline. Thus, the excitation intensity should be reduced as much as possible and appreciable noise needs to be accepted in the fluorescence data. This is especially important for line scan and point-scan recordings (Figs. 2 and 5, respectively), in which the excitation is centered on restricted cellular regions. For these recordings, the excitation intensity should be reduced by a factor of at least 10 (line scan) and 100 (point-scan) compared to the intensity used to scan the whole field of view.

The signal-to-noise ratio should *not* be improved by simply increasing the dye concentration because of the side effects discussed in the previous section. Rather the detection efficacy should be improved by using objectives with a high NA and by optimizing gain and offset of the fluorescence detector. Figure 2D shows an example where the dynamic range of the detector was used properly. The fluorescence signal was sampled by a 12 bit analog/digital (A/D) converter. Thus, values between 0 and 4095 arbitrary digital units (adu) could be obtained. Note that the peak of the fluorescence transient did not saturate the A/D converter (<4095 adu) and that the background signal was close to, but well above 0 adu. The

latter point is critical for a correct quantification of the fluorescence data (*see below*). Unfortunately, some fluorescence systems perform an automatic offset calibration, which may set the offset too high. This may lead to an overestimate of the background intensity and to errors in the quantification of the fluorescence signals. To avoid saturation of the detector, so called look-up tables (LUTs), available in most fluorescence systems, should be used to inspect the data. LUTs use distinct colors to highlight fluorescence intensities that are either close to 0 adu or to saturation (4095 adu in our system) and, thereby, provide an easy tool to adjust the gain and the offset correctly.

To effectively reduce photodamage, the periods of excitation should be kept as short as possible especially if high-magnification is employed that focuses the excitation light on small cellular regions (*see Fig. 2B*). The trigger lines described under Subheading 2.1.3. and in Fig. 1 are designed to fulfill this purpose. The line-scan recording illustrated in Fig. 2 represents an example where the fluorescence detection unit triggered the electrophysiology system, that, in turn, stimulated an afferent excitatory fiber after a fixed interval of 300 ms (Fig. 2C). Thus, the length of the baseline recording was short but well-defined. Manual triggering of the stimulation may have resulted in a baseline recording that was too long or too short.

When fluorescence responses are spatially restricted, for example to single dendritic spines, they might be hard to detect by eye. Photodamage will occur if the cell is screened too long during the search for the active site. Figure 3 displays a simple search algorithm that aids the identification of localized and/or fast responses. The implementation of the algorithm critically depends on the capabilities of the fluorescence system. While some systems allow the use of macro commands (e.g., *MetaFluo*, Universal Image Corp., West Chester, PA), others may be limited to predefined commands that cannot be modified. However, even in such systems it may be possible to implement the algorithm by acquiring two images (each representing an average of n images) with the stimulation occurring after the first averaged image.

The timed stimulation illustrated in Fig. 2 already provides a rough estimate of the temporal relationship of the electrical and fluorometric signals. In the case of video-rate fluorescence microscopy (Inoué and Spring, 1997), a more accurate correlation can be obtained by a special electronic circuit (Eilers et al., 1997b and

Fig. 1) that electronically marks the timepoint of stimulation. This method achieves a resolution of 16.5 ms (Fig. 4) or 60 μ s (not illustrated, *see* Eilers et al., 1997b), which is sufficient for most applications. This approach has the additional advantage (e.g., for failure analysis) that the occurrence of stimulation is indicated even if no cellular responses was evoked. If a perfect correlation between the electrical and fluorometric signals is required, the regimen illustrated in Fig. 5 could be used. Here, the electrical signal was fed into a free input channel of the fluorescence system which was sampled in parallel to the standard fluorescence signal (*see* also Fig. 1). Thus, both signals were acquired simultaneously by the same instrument. This approach allows a correlation, for example, between the cell's spike pattern and the onset and duration of dendritic Ca^{2+} transients.

2.3. Analysis

The first step in the analysis of fluorescence data is the definition of so-called regions-of-interests (ROIs), in which the amplitude and timecourse of responses is to be quantified, *see* Figs. 2C and 4A. The software of the fluorescence detection unit will allow the definition of ROIs of arbitrary shape and size. (Note that in line-scan recordings, a ROI will be a horizontal line.) It is important that the ROIs are set correctly. If a ROI is drawn too small, i.e., if it does not cover the entire cellular region in which the signal is to be analyzed, part of the fluorescence signal is lost and the signal to noise ratio is decreased. If the ROI is set too large, i.e., if it also covers inactive parts of the cell or unstained areas, the amplitude of the signal will be reduced due to the averaging of active and inactive areas. Furthermore, the data should be inspected using look-up tables (*see* above) and parts of the cell in which the signal was saturated should not be included in the analysis. Note that for a quantitative analysis of the fluorescence data, the background signal needs to be measured in an unstained region of the preparation. If the software of the fluorescence system does not allow the analysis of ROIs, the public domain software *NIH image* (available from rsb.info.nih.gov) may be used for this purpose.

Once the ROIs are defined, the software will allow the averaged intensity from individual ROIs to be plotted vs time and the data to be export to external programs. Since the following analysis steps are well-defined and stereotype, they may be automated. In our hands, the analysis program *Igor Pro* (Wavemetrics, Lake

Oswego, OR) provides a simple but powerful programming environment. With this software, all of the analysis steps outlined below can be programmed, allowing the analysis of even hundreds of data traces with a single keystroke.

In the following we describe the quantification of fluorescence data using the simple $\Delta F/F_0$ method which can be applied to any fluorescence recording. The more complex quantification of ratiometric recordings (e.g., *Fura 2*, *Indo-1*, or a mixture of *Fluo 3*/*Fura Red*) is beyond the scope of this chapter, *see* Grynkiewicz et al. (1985) and Helmchen (1999) for details. The $\Delta F/F_0$ method corrects for variations in excitation intensity, dye concentration, and thickness of the cellular structures. Let's consider the example shown in Fig. 2D. Fluorescence signals were recorded from a dendrite, a spine, and the background. Obviously, the signal recorded from the dendrite is larger (in absolute numbers) than that recorded from the spine. Most probably this is due to the fact that the dendrite is thicker than the spine and, thus, more dye molecules were excited when the dendritic area was scanned. Alternative explanations could be that the dye concentration in the spine was lower than that in the dendrite or that somehow the illumination of the field of view was inhomogeneous, directing less excitation light onto the spine than onto the dendrite. Whatever the correct explanation, we would like to know whether the response, i.e., the Ca^{2+} transient, was larger in the dendrite than in the spine. To answer this question we have to:

1. subtract the background from both the dendritic and the spine signal;
2. average the baseline of the two background-corrected traces (this yields two F_0 values);
3. subtract each F_0 value from the corresponding fluorescence traces (to obtain ΔF traces); and
4. divide both ΔF traces by the corresponding F_0 value.

In the resultant ratios, any of the uncertain parameters mentioned earlier (thickness of the structure, dye concentration, and excitation intensity) are canceled out and only the relative change in fluorescence remains, *see* Fig. 2E. Note that this is only true if the cell did not change its size (important for recordings from muscle cells), the dye concentration did not change significantly, and the excitation intensity was constant during the recording (4 s in Fig. 2). If we

finally assume that both compartments had the same Ca^{2+} concentration during the baseline recording, the amplitude of the $\Delta F/F_0$ signals is solely dependent on the amplitude of the Ca^{2+} transient in the spine and the dendrite. Thus, we can directly compare the two signals and find, in our example, that the spine signal was considerably larger than the dendritic one. The $\Delta F/F_0$ method also allows the comparison of successive recordings from the same cell and even from different cells. It should be kept in mind, however, that only minor differences in the dye concentration will be cancelled out. Larger difference and the associated difference in Ca^{2+} buffering may affect the amplitude and timecourse of the signals.

Acknowledgment

We thank T. D. Plant for helpful comments on the manuscript. This work was supported by grants from the Deutsche Forschungsgemeinschaft to J.E.

List of Selected Suppliers

www.carolina.com	Carolina Biological Supply Co. (test slides)
www.image1.com	Universal Image Corp. (acquisition software)
www.luigs-neumann.com	Luigs & Neumann (Dodt gradient-contrast illumination)
www.mellesgriot.com	Melles Griot (fiber optics)
www.molecularprobes.com	Molecular Probes (fluorescent probes)
rsb.info.nih.gov	<i>NIH image</i> and <i>ImageJ</i> (image analysis software, public domain)
www.stanford.edu/~cpatton	Chris Patton, <i>MaxChelator</i> (program for determining the free metal concentration in the presence of chelators, public domain)
www.wavemetrics.com	Wavemetrics: <i>Igor</i> (programmable graphing and analysis software)

References

- Adams, S. R., Harootunian, A. T., Buechler, Y. J., Taylor, S. S., and Tsien, R. Y. (1991) Fluorescence ratio imaging of cyclic AMP in single cells. *Nature* **349**, 694–697.
- Carrington, W. A., Lynch, R. M., Moore, E. D., Isenberg, G., Fogarty, K. E., and Fay, F. S. (1995) Superresolution three-dimensional images of fluorescence in cells with minimal light exposure. *Science* **268**, 1483–1487.
- Chalfie, M., Tu Y., Euskirchen, G., Ward, W. W., and Prasher, D. C. (1994) Green fluorescent protein as a marker for gene expression. *Science* **263**, 802–805.
- Denk, W., Strickler, J. H., and Webb, W. W. (1990) Two-photon laser scanning fluorescence microscopy. *Science* **248**, 73–76.
- Dodt, H. U. and Zieglgänsberger, W. (1990) Visualizing unstained neurons in living brain slices by infrared DIC-videomicroscopy. *Brain Res.* **537**, 333–336.
- Eilers, J., Augustine, G. J., and Konnerth, A. (1995a) Subthreshold synaptic Ca^{2+} signalling in fine dendrites and spines of cerebellar Purkinje neurons. *Nature* **373**, 155–158.
- Eilers, J., Callewaert, G., Armstrong, C., and Konnerth, A. (1995b) Calcium signaling in a narrow somatic submembrane shell during synaptic activity in cerebellar Purkinje neurons. *Proc. Natl. Acad. Sci. USA* **92**, 10,272–10,276.
- Eilers, J., Takechi, H., Finch, E. A., Augustine, G. J., and Konnerth, A. (1997a) Local dendritic Ca^{2+} signaling induces cerebellar LTD. *Learn. Mem.* **4**, 159–168.
- Eilers, J., Hof, D., and Konnerth, A. (1997b) The Fliginserter: a reliable event marker for video recordings. *J. Neurosci. Methods* **78**, 151–156.
- Eilers, J. and Konnerth, A. (1999) Dye loading with patch-pipettes, in *Imaging Neurons: A Laboratory Manual* (Yuste, R., Lenny, F., and Konnerth, A., eds.), Cold Spring Harbor Laboratory Press, New York, pp. 35.1–35.10.
- Fan, G. Y., Fujisaki, H., Miyawaki, A., Tsay, R. K., Tsien, R. Y., and Ellisman, M. H. (1999) Video-rate scanning two-photon excitation fluorescence microscopy and ratio imaging with cameleons. *Biophys. J.* **76**, 2412–2420.
- Finch, E. A. and Augustine, G. J. (1998) Local calcium signalling by inositol-1,4,5-trisphosphate in Purkinje cell dendrites. *Nature* **396**, 753–756.
- Grynkiewicz, G., Poenie, M., and Tsien, R. Y. (1985) A new generation of Ca^{2+} indicators with greatly improved fluorescence properties. *J. Biol. Chem.* **260**, 3440–3450.
- Helmchen, F. (1999) Calibration of fluorescent calcium indicators, in *Imaging Neurons: A Laboratory Manual* (Yuste, R., Lenny, F., and Konnerth, A., eds.), Cold Spring Harbor Laboratory Press, New York, pp. 32.31–32.11.
- Hernández-Cruz, A., Sala, F., and Adams, P. (1990) Subcellular calcium transients visualized by confocal microscopy in a voltage-clamped vertebrate neuron. *Science* **247**, 858–862.
- Inoué, S. and Spring, K. R. (1997) *Video Microscopy-The Fundamentals*, 2nd ed. Plenum Press, New York.
- Lanni, F. and Keller, H. E. (1999) Microscopy and microscope systems, in *Imaging Neurons: A Laboratory Manual* (Yuste, R., Lenny, F., and Konnerth, A., eds.), Cold Spring Harbor Laboratory Press, New York, pp. 1.1–1.72.
- Mainen, Z. F., Malinow, R., and Svoboda, K. (1999) Synaptic calcium transients in single spines indicate that NMDA receptors are not saturated. *Nature* **399**, 151–155.

- Minsky M. (1961) Microscopy apparatus. U.S. patent No. 3013467.
- Morris, S. A., Correa, V., Cardy, T. J., O'Beirne, G., and Taylor, C. W. (1999) Interactions between inositol trisphosphate receptors and fluorescent Ca^{2+} indicators. *Cell Calcium* **25**, 137–142.
- Müller, W. and Connor, J. A. (1991) Dendritic spines as individual neuronal compartments for synaptic Ca^{2+} responses. *Nature* **354**, 73–76.
- Neher, E. (1999) Some quantitative aspects of calcium fluorimetry, in *Imaging Neurons: A Laboratory Manual* (Yuste, R., Lenny, F., and Konnerth, A., eds.), Cold Spring Harbor Laboratory Press, New York, pp. 31.31–31.11.
- Pusch, M. and Neher, E. (1988) Rates of diffusional exchange between small cells and a measuring patch pipette. *Pflügers Arch.* **411**, 204–211.
- Rose, C. R., Kovalchuk, Y., Eilers, J., and Konnerth, A. (1999) Two-photon Na^+ imaging in spines and fine dendrites of central neurons. *Pflüg. Arch.* **439**, 201–207.
- Rexhausen, U. (1992) Bestimmung der Diffusionseigenschaften von Fluoreszenzfarbstoffen in verzweigten Nervenzellen unter Verwendung eines rechnergesteuerten Bildverarbeitungssystems. University of Göttingen, Diploma thesis.
- Sabatini, B. L. and Svoboda, K. (2000) Analysis of calcium channels in single spines using optical fluctuation analysis. *Nature* **408**, 589–593.
- Schiefer, J., Kampe, K., Dodt, H. U., Zieglgänsberger, W., and Kreutzberg G. W. (1999) Microglial motility in the rat facial nucleus following peripheral axotomy. *J. Neurocytol.* **28**, 439–453.
- Takechi, H., Eilers, J., and Konnerth, A. (1998) A new class of synaptic responses involving calcium release in dendritic spines. *Nature* **396**, 757–760.
- Uhl, R. (1999) Arc lamps and monochromators for fluorescence microscopy, in *Imaging Neurons: A Laboratory Manual* (Yuste, R., Lenny, F., and Konnerth, A., eds.), Cold Spring Harbor Laboratory Press, New York, pp. 2.1–2.8.
- Xu, C., Zipfel W., Shear, J. B., Williams, R. M., and Webb, W. W. (1996) Multiphoton fluorescence excitation: new spectral windows for biological non-linear microscopy. *Proc. Natl. Acad. Sci. USA* **93**, 10,763–10,7658.
- Zhou, Z. and Neher, E. (1993) Mobile and immobile calcium buffers in bovine chromaffin cells. *J. Physiol.* **469**, 245–273.

5

Patch-Clamp Techniques Applied To Brain Slices

James R. Moyer, Jr. and Thomas H. Brown

1. Techniques for Preparing Healthy Brain Slices

Brain slices have become an integral part of synaptic and cellular physiology since the pioneering studies by Henry McIlwain (Li and McIlwain, 1957; Yamamoto and McIlwain, 1966). The hippocampal slice preparation was first brought to the United States from Per Anderson's lab—initially by Tim Teyler followed shortly after by Phil Schwartzkroin. Over the years the development of the *in vitro* brain-slice preparation has enabled electrophysiologists to study various aspects of the nervous system in an isolated preparation that still retains many of the brain's complement of neuronal connections. Through the use of brain-slice preparations, much has been learned about the intrinsic properties and morphology of different populations of neurons, about connectivity between different cell types within or between brain regions, about the quantal nature of transmitter release, and about various forms of synaptic plasticity. Although other reduced preparations such as dissociated cells or partially dissociated slices are useful for evaluating single-channel and certain voltage-clamp data, the aforementioned questions are more easily addressed using brain slices. This first section focuses on some of the important aspects of preparing and maintaining healthy brain slices along with some of the rationales for selecting certain procedures.

From: *Neuromethods*, Vol. 35: *Patch-Clamp Analysis: Advanced Techniques*
Edited by: W. Walz, A. A. Boulton, and G. B. Baker @ Humana Press Inc., Totowa, NJ

1.1. Recording and Cutting Solutions

A major value of the *in vitro* brain slice preparation is the ability to vary in a systematic and controlled manner the extracellular and even the intracellular environment of the neurons under study. To obtain and maintain healthy brain slices, it is important not only to choose the appropriate incubation and recording solutions for a specific set of experiments, but it is also important to select an appropriate cutting solution in which to prepare the brain slices. This section reviews some of the ways to prepare and modify recording and cutting solutions to obtain healthy brain slices.

1.1.1. Recording Solutions for Work with Rat Brain Slices

Selection of an appropriate artificial CSF (aCSF) for use in brain-slice studies depends to some extent on the specific preparation. For example, the composition of aCSF for recording from neurons in rat brain slices should at least be similar to that found in rat CSF. The following is a listing of compounds found in rat CSF: Na^+ 156 mM, Cl^- 126 mM, K^+ 2.8 mM, glucose 65 mg/dl (~ 3.6 mM), lactate 2.8 mM, pH 7.35, 302 mOsmol (Sharp and La Regina, 1998). In addition, calcium concentrations in rat CSF have been reported to be about 2.2 mM (*see* Table 2.6 on page 24 of Davson et al., 1987), which is comparable to other species including cat, dog, goat, and humans (*see* Tables 2.2–2.6 in Davson et al., 1987).

For recording, we use the following aCSF (mM): 124 NaCl, 2.8 KCl, 2 CaCl_2 , 2 MgSO_4 , 1.25 NaH_2PO_4 , 26 NaHCO_3 , 10 D-glucose, 0.4 sodium ascorbate, pH 7.4, 295 mOsmol. Historically, glucose concentrations are much higher in brain-slice studies than they are in the living brain (typically 10–26 mM compared with 4 mM). This has its roots in early studies that had difficulty obtaining healthy brain slices using lower concentrations of glucose. Some laboratories claim that using much higher concentrations of glucose (~ 26 mM) is helpful, possibly because the higher concentrations of glucose gets converted to lactate which has been suggested to be essential during recovery from an hypoxic event (Schurr et al., 1997a; Schurr et al., 1997b), such as happens during brain slicing. While we do not use lactate in our own experiments, it may be beneficial in minimizing the anoxic insult inherent in decapitation and preparation of brain slices.

We prepare three different stock solutions for making aCSF. They are made approximately every 2–3 wk, and we advise that the stocks be replaced if they are more than 1 mo old. We use a NaCl stock solution (10X), a sulfate and phosphate stock solution (10X of each of KCl, MgSO_4 , NaH_2PO_4) and a CaCl_2 stock solution (100X). The aCSF is made fresh daily by weighing and adding the appropriate amount of glucose, bicarbonate, and ascorbate to the stock solutions. We always add the CaCl_2 stock solution last and only after adding about 75% of the total volume of water required. If we add the CaCl_2 stock solution earlier or before increasing the volume of water, the solution becomes cloudy due to precipitation of calcium carbonate.

Some researchers supplement their cutting and recording solutions with antioxidants to reduce oxidative cellular damage. Studies have shown that oxidative damage can have detrimental effects on neurons through, for example, mitochondrial damage and membrane lipid peroxidation (Kovachich and Mishra, 1980; Keller et al., 1998; Mattson, 1998). The addition of small quantities of antioxidants such as sodium ascorbate (vitamin C) can ameliorate destructive membrane lipid peroxidation as measured by the accumulation of malonaldehyde as well as edema through water gain (Kovachich and Mishra, 1980; Kovachich and Mishra, 1983; Rice, 1999; Brahma et al., 2000). The range of Vitamin C levels commonly used in aCSF is between 0.4 and 1.0 mM (Rice et al., 1994; Borst et al., 1995; Hoffman and Johnston, 1998). We use 0.4 mM sodium ascorbate in both our cutting and recording solutions. Although glutathione is also an excellent antioxidant, it is not taken up by neurons and does not lead to neuronal preservation (Rice et al., 1994). Some researchers also include an ATP regenerative system (e.g., phosphocreatine, creatine phosphokinase, pyruvate, and ATP) in their aCSF solution to offset the rapid depletion of ATP that occurs immediately after decapitation and preparation of brain slices. For example, 2 mM pyruvate has been shown to protect neurons against oxidation from hydrogen peroxide generation (Desagher et al., 1997), so we have used pyruvate when working with aged tissue.

1.1.2. Selecting an Appropriate Recording Solution

The specific questions to be addressed dictate the ionic and pharmacological composition of the recording solution. For example,

when studying calcium currents it is important to isolate them from other contaminating currents, such as those produced by Na^+ and K^+ conductances. This is often done pharmacologically by adding to the aCSF antagonists such as tetrodotoxin, which blocks sodium channels (Narahashi et al., 1964; Narahashi, 1974), and tetraethylammonium chloride (TEA), 4-aminopyridine (4AP), or internal cesium ions, which block potassium channels (see Chapter 7 of Johnston and Wu, 1995; see also Chapters 2 and 3 of Hille, 2001). It may also be important to conduct ion substitution studies. For example, if a current of interest is suspected to be carried by Na^+ ions, it is important to evaluate the current as a function of changes in the concentration of Na^+ in the aCSF. To maintain osmolarity and charge balance, this is done by substituting various concentrations of NaCl with an equal concentration of a compound such as choline chloride. In this case the cation, choline, substitutes for Na^+ but is impermeant. In this way the effects of sodium concentration on the current as well as its reversal potential can be obtained.

In the course of pharmacological studies, certain divalent cations are added to the recording solution to, for example, block certain currents. In these cases, care should be taken to prevent precipitation. This can be accomplished by removing certain phosphates or sulfates and replacing them with appropriate salts to maintain charge and osmolarity balance. Other studies may necessitate changing the ratio of Ca^{2+} and Mg^{2+} , which will alter neurotransmitter release as well as, for example, the voltage-dependence of NMDA receptors.

1.1.3. Composition of Different Cutting Solutions

For cutting brain slices, researchers originally relied on using their standard recording solution. Although this has led to some high-quality data in a variety of laboratories, intracellular recordings were difficult to obtain in certain brain regions. For example, obtaining stable, high-quality intracellular recordings from healthy facial nucleus motoneurons from adult rats was not feasible until George Aghajanian's group discovered the benefits of replacing NaCl in their cutting solution with an equimolar concentration of sucrose (Aghajanian and Rasmussen, 1989). This replacement was believed to decrease the neurotoxic effects of passive chloride influx followed by cell swelling and lysis during the decapitation and slice

preparation processes. Many laboratories, including our own, have discovered the value of minimizing excitotoxic damage during slice preparation. In brain-slice studies, it is now common to use a *neuro-protective* cutting solution.

Sucrose is not the only compound used in place of NaCl during the preparation of brain slices. Some laboratories have also tried choline-chloride, with excellent results (e.g., Hoffman and Johnston, 1998). Different laboratories also block glutamate-induced excitotoxic damage by including in the cutting solution one of several glutamate-receptor antagonists, such as kynurenic acid, which is a nonselective blocker of NMDA and AMPA/kainate receptors (Christie et al., 1995; Magee et al., 1996).

We have found that a sucrose-based cutting solution works quite well for obtaining stable, long-term, whole-cell recordings (WCRs) as well as synaptically-evoked currents. The composition of our sucrose-CSF (in mM) is as follows: 206 sucrose, 2.8 KCl, 1 CaCl₂, 1 MgCl₂, 2 MgSO₄, 1.25 NaH₂PO₄, 26 NaHCO₃, 10 D-glucose, ascorbic acid 0.4, pH 7.4, 295 mOsmol. As with our recording solution (described earlier in Subheading 1.1.1.), our sucrose-CSF is made fresh daily by weighing and adding the appropriate amount of sucrose, bicarbonate, glucose, and ascorbate to the appropriate amount of stock solutions (including a 100X stock solution of MgCl₂). As is the case for preparing the recording solution, if a concentrated stock solution of calcium chloride is used, it should be added last after a sufficient volume of water has been added (about 50–75% of desired volume). Otherwise the solution will become cloudy, which can sometimes be removed by oxygenation with carbogen gas (95% O₂–5% CO₂).

Our cutting solution is designed to protect neurons in multiple ways. Replacing NaCl with an iso-osmolar concentration of sucrose serves two functions: (1) it reduces sodium influx, which occurs with the tendency of neurons to depolarize during the anoxia that accompanies decapitation, dissection, and slicing; and (2) it minimizes excitotoxic cell swelling from passive chloride influx followed by cation and water entry (Rothman, 1985). We also elevate the Mg:Ca ratio from 1:1 to 3:1. This minimizes calcium influx caused by glutamate-induced depolarization (Feig and Lipton, 1990; Choi, 1992; Choi, 1994). Also, our inclusion of 0.4 mM ascorbic acid helps to reduce oxidative damage. We find that this cutting solution yields healthy slices from both juvenile, adult, and aged animals (*see* Subheading 1.4. and 1.5. below for additional details).

1.2. Making an Incubation Chamber for Maintaining Healthy Slices

One of the most important aspects of in vitro neurophysiology is maintaining a supply of healthy brain slices while one is being used for recording. In the earliest sharp-electrode and field-potential studies, this was not a problem because an interface chamber with adequate room for several slices was used. However, for studies using other kinds of chambers (and also to keep fresh slices free from various drug exposures) a separate chamber is used to hold additional slices. The methodology has evolved over the years from placing brain slices into a glass vial (where they sink to and rest on the bottom) containing aCSF that is oxygenated through a tube placed into the vial to more sophisticated holding chambers where the slices rest atop a nylon mesh, which permits exposure of aCSF from both surfaces of the slice. Several different holding chamber designs can be found elsewhere (Edwards and Konnerth, 1992; Moyer et al., 1992; Sakmann and Stuart, 1995; Moyer and Brown, 1998).

1.2.1. Making and Assembling an Incubation Chamber

The slice incubation chamber used in our laboratory results in nearly 100% healthy slices that can be maintained for 6–12 h (Moyer and Brown, 1998). We use a 24-well chamber so that individual slices are kept separate from each other and in exact order, facilitating identification of slices located at a specific rostro-caudal or dorso-ventral level. The design is simple and can be easily made in only a few hours. The following section outlines the steps involved in making such a chamber (Fig. 1A).

We use a standard 24-well culture dish with the bottom cut off and sanded. We drill holes through the walls of each row and column of wells so that the wall of each well has four holes for diffusion of aCSF. The dish is then cut in half to yield two 12-well chambers. Two pieces of the foot portion of standard nylon hosiery are cut away and stretched across the bottom of each chamber, and rubber bands are used to hold the nylon taut. The nylon is then glued to each chamber using a cyanoacrylate (Krazy Glue Pen). The glue is carefully applied onto the nylon hosiery that contacts the bottom of each well and the bottom edges of each chamber. After the chambers dry overnight, excess nylon hosiery is cut away using a sharp razor blade. Eight glass legs, which serve to ele-

vate the chamber and prevent it from floating, are made by cutting pieces from a standard glass stirring rod. Four legs are glued to the four corners of each chamber using a clear silicone-based sealant like that used for aquariums. The chambers are allowed to dry overnight, after which they are submerged in de-ionized water for several days prior to use.

1.2.2. Oxygenation of Brain Slices in the Incubation Chamber

To oxygenate our solutions we use coarse fritted glass bubblers rather than extra-coarse. We prefer the coarse fritted glass bubbler because they release small bubbles and are resistant to clogging. The fritted glass bubblers themselves are only ~20 mm long but they are joined at the end of a 22 cm Pyrex tube. We cut away the Pyrex tube by scoring it with a diamond knife, wrapping it in a KimWipe, gripping each side of the score with pliers and snapping it in two. The bubbler can then be attached to Tygon tubing connected to a multi-line manifold that permits regulation of the airflow from the 95% O₂/5% CO₂ (carbogen) air tank to each of the bubblers. Oxygenation should be just sufficient to maintain a pH of ~7.4; excess oxygenation can be detrimental to the slices.

The two 12-well chambers are placed inside a large Pyrex staining dish, like those used for histological staining. One fritted glass bubbler is placed at either side of the dish and the third is placed between the two incubation chambers (*see* Fig. 1A). We place a thin Plexiglas lid (with a handle glued to the center) inside the dish. It is cut to a size appropriate for lowering into the dish yet remaining 2–3 cm above the top of the incubation chambers. The lid keeps a layer of moistened carbogen gas above the slices.

With the chambers inside the staining dish, we set the level of the aCSF so that it is sufficient to cover the brain slices and allow fluid exchange between wells via the holes that were drilled through each chamber. It has been suggested that brain slices remain healthiest in interface chambers (for useful discussion, *see* Aitken et al., 1995), so we try to keep the fluid level as low as possible and our recording chamber (discussed later) is an interface-type design. Although we have not tried to use a true interface chamber as an incubation chamber for our visually guided whole-cell recording studies, it may result in even healthier brain slices.

To maintain adequate circulation of oxygenated-aCSF, we place the entire apparatus on top of a stir plate, equipped with a heater

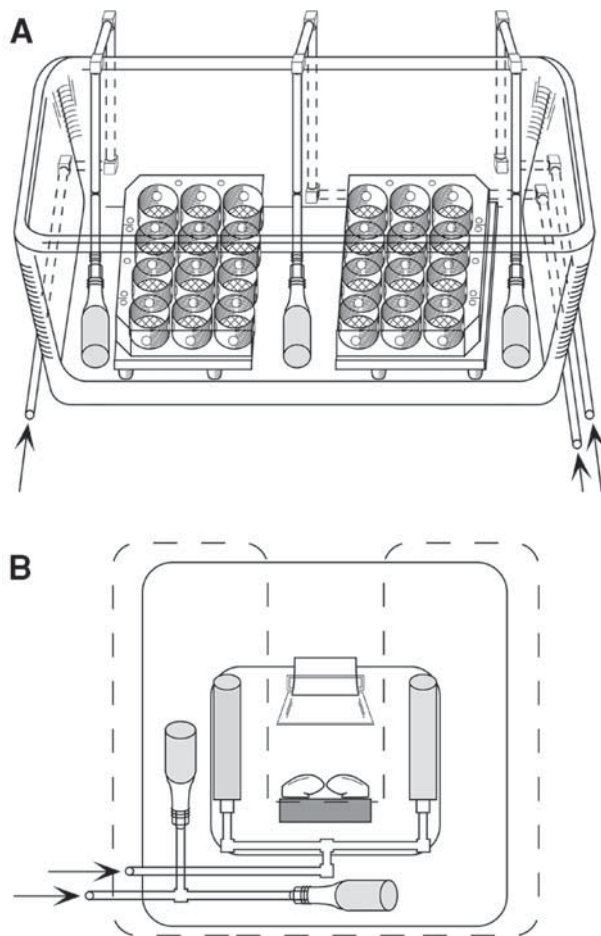


Fig. 1. Design of our brain slice incubation and cutting chambers. **(A)** Schematic diagram of the 24-well slice incubation chamber assembly. Three fritted glass bubblers are used to deliver carbogen gas (95% O₂–5% CO₂). Not shown is a stir plate and miniature stir bar used to gently distribute the oxygenated aCSF. **(B)** Schematic of the stainless-steel vibratome cutting tray (74 × 74 × 9 mm). Small gas dispersion tubes are used to oxygenate the sucrose-CSF during slice preparation. These dispersion tubes are secured by small silver wires that are glued in place by silicone sealant placed on the outer side and bottom surface of the tray. The sucrose-CSF located in the outer chamber of the vibratome is also oxygenated through two fritted glass bubblers. A 4% (w/v) agar

control, and use a small stir bar to gently circulate the aCSF. The slices are also kept at the desired temperature using the heater control. Temperature is monitored using an external fish tank thermometer that sticks to the outside of the staining dish.

1.3. Cutting Brain Slices:

Tissue Chopper vs Vibrating Microtome

Brain slices were first used for electrophysiology by Henry McIlwain (Li and McIlwain, 1957; Yamamoto and McIlwain, 1966). Originally, a tissue chopper was used to cut slices that were typically 300–500 μm thick (Skrede and Westgaard, 1971; Duffy and Teyler, 1975; Schwartzkroin, 1975; Schwartzkroin and Andersen, 1975; Alger and Teyler, 1976). While this technique of using a tissue chopper was used for some time (and still is in some electrophysiology labs), we and others have recognized the value of cutting slices using a vibrating microtome (e.g., Keenan et al., 1988; Moyer et al., 1992; Lipton et al., 1995; Moyer and Brown, 1998).

When we look at the cut surface of the slice it is much smoother when we cut using a vibratome (high vibration amplitude, slow advance speed, cold cutting saline) than when we use a tissue chopper. Our observations are done using a 10 \times air objective or a 40 \times water objective with infrared-filtered light and differential interference contrast (IR-DIC) connected to a digital enhancement device (described in detail in Subheading 2.1.). We also noted that the slices were visibly more healthy (see description of healthy neurons in Subheading 2.2.2.) when we use a vibrating microtome.

Other scientists have confirmed our observations at the metabolic level. For example Charlie Taylor's group stained for mitochondrial activity using 2,3,5-triphenyltetrazolium chloride (TTC) (Watson et al., 1994) and saw more uniform and greater staining throughout brain slices prepared using a vibratome, whereas slices prepared using a McIlwain tissue chopper had much less staining (see discussion in Aitken et al., 1995). It is not surprising that the vast majority of neurophysiologists now use a vibrating microtome

(continued) block, indicated by the dark-gray shaded rectangle, is used to support the brain tissue during cutting. Also shown is a thin Plexiglas lid used to minimize fluid loss by splashing (dashed lines). Arrows in (A) and (B) indicate flow of carbogen gas. Reprinted from Fig. 1 of Moyer and Brown (1998) with permission from Elsevier Science.

with a cold cutting solution when preparing brain slices for in vitro electrophysiology.

1.4. Preparation of Brain Slices from Juvenile Animals

Visually guided, patch-clamp recordings in brain slices are usually done using juvenile rats (2–4 wk). Historically, the reason for the extensive use of young animals is twofold. First, young tissue is much more resilient to the trauma of the slice preparation than adult tissue. That is, there is a much greater margin of error present at each different step in the preparation of slices when using juvenile rats (Keenan et al., 1988; Moyer and Brown, 1998). Second, it is much easier to see individual cells clearly in brain slices prepared from very young rats, perhaps because myelination is not completed in juvenile rats, which allows visualized recordings to be made at greater depths within the slice. The ability to see clearly within a brain slice facilitates proper placement of the patch pipet on the soma, dendrite, or axon of the neuron of interest.

Prior to decapitation, the rat pup (or other juvenile animal) is anesthetized usually with a volatile anesthetic such as halothane or isoflurane. These are preferable to injected anesthetics, such as pentobarbital, because volatile anesthetics like halothane diffuse out of the brain tissue quite rapidly and are less likely to alter neuronal function. We typically place about 1–2 mL of halothane onto a paper towel located within an inhalation narcosis chamber. The rat pup is then placed inside the chamber and removed only after being deeply anesthetized, as evidenced by a lack of movement and slow respiration. This latter point is vital because we have found that if the rat is decapitated after breathing has ceased, the slices are less healthy.

Consistency is one of the most important procedural rules for making healthy brain slices. Consistency is vital not only for finding a set of parameters or procedures that work well, but also for reducing variability among experiments. Day-to-day variability in the slice preparation will likely result in variability in the quality of the data recorded. To help us remain consistent, we time our dissections with a digital stopwatch and record our dissection times onto a data sheet (see Fig. 2). We record the following dissection information: 1) time to remove brain from the animal and place it into a small beaker of ice-cold oxygenated sucrose-CSF, 2) time when brain is removed from the beaker and blocked,

3) time when each hemisphere is glued to the vibratome tray, 4) time when the first useable slice is cut, 5) time when the last slice was obtained, 6) number of slices, and 7) thickness of slices. We also record the temperature of the cutting solution at the start and finish of slicing as well as the temperature of the incubation temperature. Figure 2A shows an example of our data sheet with entries from the dissection of a juvenile rat. Care and consistency will maximize the number of dissections from which usable data are obtained and result in greater consistency among different users within the same lab.

Regarding removal of the brain, faster is better as long as adequate care is taken to prevent damage to the brain. We like to get the brain out in 30–45 s. With practice this speed is not difficult to achieve. For rats younger than 6 or 7 wk of age, we expose the skull by cutting with a scalpel from the nose to the back of the skull. We then use a small pair of scissors (~2.5 cm blade length) to make three cuts. The first is along the occipital suture. The second is a caudal-to-rostral cut along the sagittal suture. The third is across the skull, at the end of the second cut. These cuts leave two plates of skull covering each hemisphere. A small pair of mini bone rongeurs (Roboz, RS-8310) is used to grasp the back of each skull flap and lift firmly upward and outward to remove the skull covering each hemisphere. This must be done carefully, without rotating the wrist. Otherwise the temporal lobes will get cut by the ventral portion of each plate of skull. Any extra pieces of skull that do not come off cleanly are then quickly removed with the rongeurs to prevent damage during brain extraction.

After the brain is fully exposed, we quickly cut away the cerebellum and insert a periosteal elevator (Biomedical Research Instruments, #48-1460) along the front portion of the brain and slide it forward to cut the olfactory bulbs. We prefer the periosteal elevator because it is slightly curved and very smooth, making it less likely to damage the brain, unlike a narrow spatula. Holding the head nearly upside down the frontal portion of the brain is gently pushed out of the skull and the optic nerves are severed. The brain is then pushed out of the skull cavity and into a beaker of ice-cold, oxygenated sucrose-CSF. In older rats, the skull is too thick to cut with scissors, so we use a larger pair of rongeurs (Roboz, RS-803) to remove the skull. We start at the base of the skull and remove the skull behind the occipital suture by gripping it along the suture

A DATE: / /			B DATE: / /		
	DISSECTION by:			DISSECTION by:	
Perfusion:	Yes	(No)		(Yes)	No
Abdominal Cut:				0:00	
Descending Aortic Clamp:				:46	
Cut Right Atrium:				:52	
Perfuse Left Ventricle:				1:00	
Fluid from Atrium is Clear:				1:42	
Decapitate:	0:00			1:51	
Removal of brain:	:33			2:25	
Dissection Start:	3:25		4:01		
Brain Glued:	Left	Right	Left	Right	
	3:56	4:05	4:32	4:42	
Removal of 1st Slice:	6:02	6:02	6:56	6:56	
Removal of Last Slice:	10:16	10:16	12:28	12:28	
Number of Slices:	6	6	6	6	
Slice Thickness:	300 μ / (400 μ) / 500 μ / μ		300 μ / (400 μ) / 500 μ / μ		
Temperature (°C)	sucrose aCSF <u>1</u> °C to <u>1</u> °C normal aCSF <u>20.5</u> °C to <u>23</u> °C		sucrose aCSF <u>0</u> °C to <u>-1</u> °C normal aCSF <u>23</u> °C to <u>24</u> °C		
Rat Information:	Rec'd: / / weaned: / / Age: <u>15</u> (d) wk / mo / yr Wt: <u>42</u> (g) / kg Sex: (M) / F Protocol #		Rec'd: / / weaned: / / Age: <u>3</u> d / wk (mo) / yr Wt: <u>312</u> (g) / kg Sex: M / (F) Protocol #		
Additional Comments:	slices done @ : a.m. / p.m.		slices done @ : a.m. / p.m.		

Fig. 2. Sample dissection time sheet and dissection times. (A) Dissection times from a 15-d-old male rat pup. (B) Dissection times from a 3-mo-old female rat in which an intracardiac perfusion was performed. All times are in a minutes and seconds. Zero time denotes the onset of the first anoxic

and lifting upward. Then we gently grip the skull with the tips of the rongeurs and lift the plate of skull covering each hemisphere. If done swiftly and forcefully, the skull separates along the sagittal suture and the entire skull covering one hemisphere comes free. The same approach is used to remove the skull covering the other hemisphere. The brain is removed from the skull as described earlier for juvenile rats.

All of our dissection tools are chilled in a beaker of ice-cold sucrose-CSF. After the brain is removed it is put into a small beaker (50 mL) containing ice-cold, oxygenated sucrose-CSF from which it is quickly transferred to a larger beaker (250 mL) containing the same solution. The purpose of the intermediate beaker of cold sucrose-CSF is to wash off excess blood. We let the brain chill for around 3 min. Of course, if the brain is hemisected prior to removal from the skull less time is needed to chill each hemisphere thoroughly. The brain is then transferred onto a piece of filter paper, which is placed on top of an ice-packed petri dish, so that the blocking or dissection occurs *on ice*. The brain is then glued onto a vibratome tray in front of and touching a rectangular agar block (4% agar) that was previously glued to the tray. The agar block supports the tissue during slicing (Fig. 1B). The tray is immediately filled with ice-cold oxygenated sucrose-CSF. The tray and main vibratome chamber have bubblers to oxygenate continuously the sucrose-CSF (Fig. 1B). We use a temperature-controlled vibratome for cutting 400 μm slices, and we cut at a temperature of about 1°C (Moyer and Brown, 1998). As each slice is cut it is removed from the vibratome tray using the back end of a 3.5-inch glass dropper and placed in a well within our slice incubation chamber (discussed earlier, see Fig. 1A) and kept at about 24°C until used in an experiment. We have done a series of temperature studies and found that if slices are removed and placed into the incubation chamber at a temperature less than 10°C and allowed to warm to room temperature, or if they are kept at less than or equal to 10°C for 10–20 min and then transferred to room temperature, *nearly every cell in the*

(*continued*) event. For a standard dissection this occurs at the time of decapitation, whereas when a perfusion is performed the first anoxic event occurs when the diaphragm is cut during the perfusion procedure. The time required to remove the brain is about the same: 33 s for the juvenile and 34 s for adult. Notice also that the *removal of first slice* times are comparable (left and right refer to brain hemisphere).

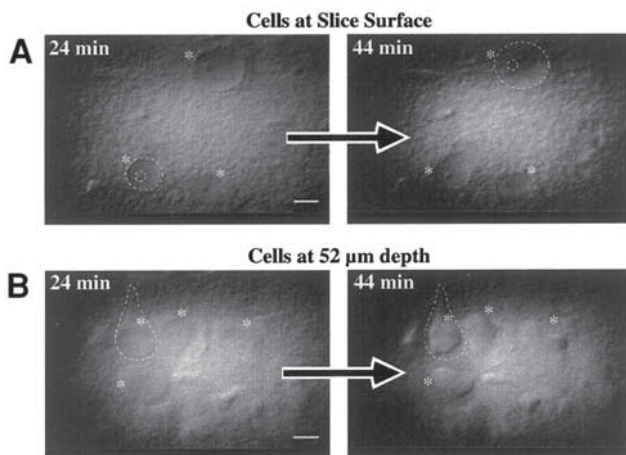


Fig. 3. Recovery of neurons as a function of time after slicing. IR-DIC videomicrographs of perirhinal layer V neurons in brain slices shortly after decapitation (24 min, left panels) and about 44 min later (right panels). (A) Cells located near the cell surface are unhealthy and do not recover. (B) Cells located 52 μm beneath the slice surface initially appear unhealthy but recover over time. Asterisks indicate several cells monitored over time. Adapted from Fig. 3 of Moyer and Brown (1998) with permission from Elsevier Science.

slice is dead (see description of dead cells in Subheading 2.2.1.) (Moyer and Brown, 1998). Thus, we place the slices directly into a chamber with aCSF at room temperature or a few degrees cooler. In our studies, slices are used only after a 45 min to 1 h recovery period. After 45 min, the slices look normal and the cells are easily patchable (see Fig. 3). This procedure yields beautiful looking, healthy neurons that are easily patched and typically remain stable for 2–3 h (see Fig. 4). Using these procedures, we have maintained stable WCRs for as long as 4–5 h.

1.5. Preparation of Brain Slices from Adult and Aged Animals

Preparing brain slices from older animals (adult and aged) requires particular attention to small details regarding both the solutions and the dissection. One obvious difficulty is that the skull of older animals is much thicker and can be more difficult to remove. For

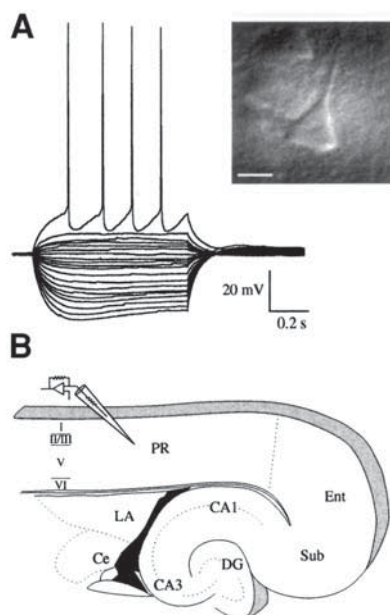


Fig. 4. Use of IR-DIC video-enhanced microscopy for pre-selecting neurons in 400 μm thick brain slices. (A) Voltage traces of a regular spiking layer V pyramidal neuron in perirhinal cortex (left) and the IR-DIC video image (right) of the same cell showing the position of the patch pipet (scale bar is 10 μm). This neuron had a resting membrane potential of -78 mV, an input resistance of 405 M Ω , and remained healthy for nearly 2 h before the experiment was terminated. (B) Schematic diagram of a horizontal brain slice containing perirhinal cortex (*see* Subheading 3.5.). We use slices corresponding to plates 98–100 in a rat brain atlas (Paxinos and Watson, 1998) and recordings are restricted to the rostro-caudal area of about -3.8 to -5.2 mm relative to bregma. Abbreviations: PR perirhinal cortex, Ent entorhinal cortex, Sub subiculum, LA lateral nucleus of the amygdala, Ce central nucleus of the amygdala, DG dentate gyrus.

example, in young adult rats, the skull can be easily removed by gripping it with rongeurs and lifting upward as described earlier (*see* Subheading 1.4.). Large sections of skull covering each hemisphere can be removed intact in this manner. However, in aged rats the bone splinters such that only small pieces are removed, lengthening the process of brain extraction. Thus it is important to work quickly and efficiently with aged animals.

Also, the brain of an older animal is much less resilient. Even a subtle mistake during any step of the dissection process can dramatically affect the quality of the slices and the ability to obtain high-quality recordings from healthy neurons. The following sections describe our approach to working with older animals. The procedures have evolved from years of work in aged rabbit hippocampus (e.g., Moyer et al., 1992; Moyer and Disterhoft, 1994; Moyer et al., 2000b) and recent work in aged rat perirhinal cortex (Moyer and Brown, 1998).

1.5.1. Osmolarity-Matching and Solution Temperatures

We have been recording from neurons in brain slices prepared from aged animals for more than 10 yr. Many of these earlier studies used hippocampal slices from aged rabbits (36–50 mo old). In these studies, sharp electrode recordings were obtained from CA1 and CA3 neurons in slices prepared using both aCSF and sucrose-CSF as the cutting medium (Moyer et al., 1992; Moyer and Disterhoft, 1994; Moyer et al., 1996; Thompson et al., 1996; Moyer et al., 2000b). In the case of the sucrose-CSF cutting solution, the 124 mM NaCl was substituted with an equimolar amount of sucrose. Since a solution with 124 mM NaCl results in a 124 mM concentration of each Na^+ and Cl^- ions, we used 248 mM sucrose (Moyer et al., 1996; Moyer et al., 2000b). This worked fine for cutting isolated hippocampal slices and recording from aged CA1 neurons.

However, when we began doing IR-DIC guided WCRs in rat perirhinal cortex in whole-hemisphere slices, we found that it was extremely difficult to obtain WCRs in neurons from older animals (Moyer and Brown, 1998). One major problem was that the tissue was difficult to cut, so we used a much slower cutting speed and performed intracardiac perfusions (*see* Subheading 1.5.2.). After these adjustments, we could get a gigaohm seal but after going whole-cell the membrane would often re-seal in the electrode tip. Thus our overall success rate was much lower than in juvenile tissue. When we checked the osmolarity of the sucrose-CSF cutting solution, we found that it was much higher than the aCSF, so we reduced the sucrose concentration until the osmolarity matched that of the aCSF (~290 mOsmol).

To achieve the WCR success rate in aged tissue that we obtained in juvenile tissue, we also adjusted the incubation temperature. Many important pumps and enzymes are temperature-sensitive, and since we were cutting slices at an extremely low tempera-

ture—to minimize or slow down cellular damage due to the decapitation and removal of blood supply—we figured that these aged slices may need to go back to a warm temperature faster than juvenile tissue. We therefore introduced another step, a pre-incubation in an identical separate holding chamber at 35–37°C for 30–45 min before placing slices into the main incubation chamber at 24°C. Other laboratories have been using a similar pre-incubation step for juvenile tissue because the cells are easier to patch (Borst et al., 1995; Hestrin and Armstrong, 1996; Magee et al., 1996; Markram et al., 1997a; Jung et al., 2001). After adjusting the osmolality and adding a 30-min pre-incubation at ~35°C, we were able to patch neurons routinely in brain slices prepared from older animals.

1.5.2. Benefits of Performing Intracardiac Perfusions

Several researchers have demonstrated the utility of hypothermia for obtaining healthy brain slices (e.g., Okada et al., 1988; Newman et al., 1992; Saeed et al., 1993). For example, George Newman's group found that anesthetizing the animal and placing the body on a bed of ice until the rectal temperature was 31°C increased the percentage of healthy CA1 pyramidal neurons in hippocampal slices relative to slices prepared under normal conditions (Newman et al., 1992). When making slices from the isolated hippocampus of adult or aged animals, the brain is hemisected, which facilitates rapid cooling of the brain. Also, using a vibratome to cut chunks of hippocampus did not present any unusual difficulties. Thus, in past studies where we made hippocampal slices from adult and aged rabbits, no intracardiac perfusion was performed (Moyer et al., 1992; Moyer and Disterhoft, 1994; Moyer et al., 1996; Moyer et al., 2000b).

When we began preparing brain slices from adult and aged rats without dissecting out the hippocampus, we found that the cortex (with which the blade made initial contact) was more likely to compress and tear rather than be cut smoothly through, even at slow cutting speeds (Moyer and Brown, 1998). Thus, the cortex was damaged during the cutting, even though the hippocampus was in relatively good condition.

The difficulties encountered in using older animals forced us to consider performing intracardiac perfusions. An intracardiac perfusion has another obvious benefit: removing red blood cells, which also stain when tissue is reacted for biocytin (which we

included in our pipets for obtaining cellular morphology). Intracardiac perfusion prior to preparing brain slices is therefore also beneficial for minimizing background staining in biocytin reactions. Once we began performing intracardiac perfusions and preincubating the slices at 35°C for 30 min (*see* Subheading 1.5.1.), we were able to readily obtain stable WCRs from adult and aged perirhinal cortical neurons (Moyer and Brown, 1998; McGann et al., 2001).

Intracardiac perfusions are performed by first anesthetizing the rat using Nembutal (80–90 mg/kg, i.p.). After the rat is unresponsive to a foot pinch, the chest cavity is opened by cutting across the abdomen just below the sternum and then cutting up the sternum. The diaphragm is then carefully cut and the descending aorta is clamped using hemostats to prevent perfusion of the lower body and accelerate perfusion of the brain. The body cavity is exposed by clamping the ribs on each side with hemostats. If necessary, any connective tissue is cut to free the heart from the chest cavity. The right auricle is cut and the left ventricle pierced with an 18–23-gauge needle through which ice-cold, oxygenated sucrose-CSF is pumped using a perfusion pump (Mityflex, ANKO, Bradenton, FL). After about a 1 min perfusion (assuming a good clamp on the descending aorta), the efflux from the right auricle should be clear. About 20 s later the rat is decapitated, the brain is removed, and slices are prepared as described above for juvenile rats. The only difference is that we only let the brain chill for 1 min or less prior to starting the dissection. The overall amount of time it takes to get the first brain slice is therefore similar between juvenile and adult or aged animals (compare Figs. 2A and 2B).

2. Using IR-DIC for Visualizing Neurons in Brain Slices

The original extracellular and intracellular hippocampal brain slice studies used a simple dissecting microscope to see the principal cell layers (CA1–4, dentate granule cells). The dissecting scope allowed scientists to direct their electrodes to the appropriate general regions without difficulty. For intracellular studies, the high packing density of neuronal somata within the hippocampus facilitated obtaining intracellular recordings using sharp electrodes. This was because significantly more light passed through the densely packed cell body layers (which have a convenient laminar organization) relative to the rest of the brain slice. The

anatomy of the hippocampus made it an ideal preparation for intracellular and extracellular studies, without the need to visualize the neurons. With the development of the patch-clamp technique in the mid 1970s (Neher and Sakmann, 1976) and its application to brain slices (Blanton et al., 1989; Edwards et al., 1989), the ability to see neurons facilitated placement of the larger diameter patch pipet on specific neuronal targets such as somata, dendrites, or axons.

2.1. Benefits of Infrared Light and Digital Enhancement

The first attempts to visualize central nervous system (CNS) neurons were by Yamamoto in 1975. However, this study used conventional microscopy, where silhouettes of larger cell somata were only poorly discernible and dendrites or small neurons were not observable (Yamamoto, 1975). In February of 1978 Yamamoto's group also published a paper in which they demonstrated visualization of cerebellar neurons in very thin brain slices (40–120 μm), this time using Nomarski optics (Yamamoto and Chujo, 1978). Under these conditions, both Purkinje cells and smaller neurons were visible. In this study they placed a glass microelectrode near visualized cells and recorded extracellular spike discharges. Five months later, Takahashi also published a paper in which he visualized motoneurons in thin spinal-cord slices (130–150 μm) using Nomarski optics. However, in this study he actually obtained intracellular recordings from the identified motoneurons (Takahashi, 1978). In 1980, Llinás and Sugimori used Hoffman modulation microscopy to visualize cerebellar Purkinje cell somata and obtain intracellular recordings from identified neurons in very thin cerebellar slices (200 μm). These early attempts at visualizing neurons in brain slices were breakthroughs, but they suffered from the inability to clearly resolve neurons in slices thicker than 100–200 μm . Such thin sections result in large numbers of unhealthy neurons due to damage at the slice surface as well as incomplete dendritic arbors, even in the deepest cells.

Brian MacVicar was the first to publish a manuscript describing the application of infrared (IR) light and a video camera for visualizing neurons in brain slices (MacVicar, 1984). The use of IR-filtered light has tremendous advantages over previous studies using visible spectrum light. The longer wavelength of IR light allows it to penetrate deeper into the tissue with less scattering relative to shorter wavelength visible light (Gibson, 1978; MacVicar,

1984). The technique of visualizing cells using IR-filtered light and a video camera obviates the need for using extremely thin sections (Keenan et al., 1988; Edwards et al., 1989).

In the late 1980s, Brown and Keenan were the first to combine videomicroscopy with differential interference contrast (DIC) microscopy and IR-filtered light to visualize amygdala and hippocampal neurons (Brown and Keenan, 1987; Keenan et al., 1988). Using an inverted microscope, they explored the benefits of DIC-microscopy using a video contrast-enhancement device in rat brain slices as a function of thickness (150–450 μm) and age (7 d to adult). This study represented a major breakthrough in the ability to resolve cellular and subcellular details in brain slices used for patch-clamp recordings. Their goal was to push the limits of optical resolution, and later they combined these methods with confocal laser-scanning microscopy for imaging of somatic and dendritic Ca^{2+} (Jaffe and Brown, 1994a, 1994b, 1997; Brown and Jaffe, 1994).

Two years later, Dodt and Zieglgänsberger used an inverted microscope in conjunction with IR-DIC video-enhanced microscopy to show numerous examples of healthy, patchable neocortical, and hippocampal neurons in brain slices. In this study they compared the depth of visualization beneath the slice surface as a function of slice thickness and found that in 400 μm -thick slices from adult rats, neurons could be visualized at depths of up to 40 μm (Dodt and Zieglgänsberger, 1990). Shortly thereafter, Bert Sakmann and colleagues obtained in brain slices the first examples of whole-cell recordings from neurons pre-selected using IR-DIC video-enhanced microscopy (Stuart et al., 1993).

The benefit of IR-DIC video-enhanced microscopy to *in vitro* neurophysiological studies resulted in a tremendous increase in the number of laboratories using the technique since the early 1990s. In our studies, we use an upright microscope (Zeiss Axioskop) equipped with a 40X water immersion objective (0.75 NA), infrared filtered light, DIC optics, and a Hamamatsu C2400 video camera and video enhancement device for visualization of the cell and patch electrode (Keenan et al., 1988; Xiang et al., 1994; Moyer and Brown, 1998; Xiang and Brown, 1998). Although the blind approach to patch clamping (Blanton et al., 1989) is still used in many laboratories, it is hard to imagine any neurophysiologist ever going back to the blind method once he or she has used IR-DIC video-enhanced microscopy for visualizing neurons in brain slices.

2.2. Selecting Healthy Neurons

In any given slice there are both healthy patchable neurons and unhealthy neurons. The less healthy or unhealthy cells can either be unpatchable or result in a cell that dies shortly after beginning an experiment. In this section we will describe how to distinguish between healthy and unhealthy neurons.

2.2.1. Characteristics of Dead or Unhealthy Neurons

Dead neurons are always present within the first 25 μm below the surface of a brain slice (*see* Fig. 3). They have a characteristic swollen appearance, and in many cases all that can be discerned is a large nucleus and a prominent nucleolus. In fact Brown and colleagues, in their efforts to approach the limits of resolution using video-enhanced DIC showed numerous examples of subcellular structures (Keenan et al., 1988). Over time, these dead cells often become invisible. Figure 5A illustrates two examples of these round, transparent, dead neurons that cannot be patched. They explode under the positive pressure of the electrode as it gets close. In addition to these dead cells, there are also cells that appear unhealthy because they have swollen, two-dimensional, or shrunken appearances. These cells are all different from the dead cells mentioned earlier in that significant dendritic structure can still be seen. The somatic images of neurons with a two-dimensional appearance can be shown to lack depth when focusing up and down. High-resistance gigaohm seals cannot be formed on swollen cells. However, gigaohm seals can often be formed on cells that appear two-dimensional or shrunken (*see* Subheading 3.4.), but subsequent WCRs from these cells are difficult to obtain even using an enormous amount of suction.

One last example of unhealthy neurons is worth mentioning. Using DIC videomicroscopy alone, these cells look normal and healthy. However, using the IR-filtered light, it is clear that their nucleus is indeed visible (Fig. 5B). Close inspection using IR-DIC videomicroscopy reveals that these cells look quite normal except that their somatic membrane is to various degrees translucent, such that the nucleus is readily or only slightly apparent. We have attempted to patch such unhealthy cells and found that high-quality WCRs can be obtained from these cells, but within 10–30 min the cell becomes unhealthy. This is evident by a reduction in membrane

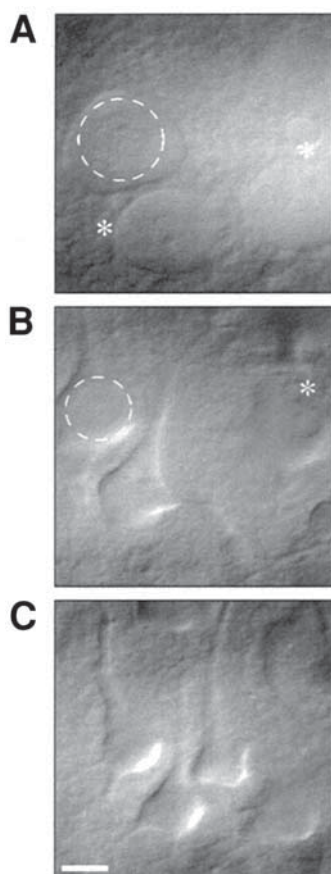


Fig. 5. IR-DIC videomicrographs of visually unhealthy and healthy neurons in 400 μm thick brain slices. (A) Several examples of dead neurons in layer V of perirhinal cortex (PR). The only structures visible are a round soma and a prominent nucleus—presumably due to breakdown of the somatic membrane. In one cell the nucleus is outlined by a dashed circle and another is indicated by an asterisk. (B) Several examples of unhealthy neurons in layer V of PR. In these cells, the nucleus is clearly visible through the somatic membrane (outlined by dashed circle in far left cell and indicated by an asterisk in far right cell). In all other respects these would look like healthy patchable neurons without the IR-DIC video-enhancement. In fact, some of them can be patched but the cell usually dies within 5–30 min (see dimple caused by patch pipet on soma of middle cell) (C) Examples of healthy patchable pyramidal cells in layer

potential, input resistance, and action potential amplitude. An obvious benefit to IR-DIC videomicroscopy is the ability to distinguish between such unhealthy neurons and the healthy neurons that can remain stable for several hours without electrophysiological deterioration (*see* Subheading 2.2.2.).

2.2.2. Characteristics of Healthy, Patchable Neurons

Visually healthy and patchable neurons are easy to distinguish from dead or unhealthy neurons using IR-DIC videomicroscopy. The nucleus is not visible in healthy neurons. Instead, the cell membrane appears smooth and bright (*see* Fig. 5C). There are no outward blebs or small round indentations in the somatic-cell membrane. In addition, healthy patchable neurons look more three-dimensional while many unhealthy neurons look more two-dimensional. This can be appreciated by focusing up and down through the neuron of interest. Generally, one will initially encounter several examples of unhealthy cells as described in Subheading 2.2.1. before finding one that is quite healthy and patchable. With practice it is not uncommon to obtain healthy recordings from 80–100% of all neurons selected for WCRs.

2.2.3. Considerations Regarding Cell Depth

In the early efforts at obtaining intracellular recordings from visually-identified neurons, very thin slices were used and cells were close to the surface (Yamamoto, 1975; Takahashi, 1978; Yamamoto and Chujo, 1978; Llinás and Sugimori, 1980). Similarly, early attempts to visualize neurons for patch-clamp recording employed the advantages of slices that were quite thin (Keenan et al., 1988; Edwards et al., 1989). Although thin slices ($\leq 150\ \mu\text{m}$) facilitated visualization of neurons, they were not well-suited for use in preparations outside the cerebellum. With the use of infrared light (MacVicar, 1984) and eventually the adaptation of IR-DIC videomicroscopy (Dodt and Ziegglänsberger, 1990) to brain-slice preparations, it became easier to visualize neuronal structures deeper into

(continued) V of perirhinal cortex. These cells resemble those seen in (B), however, in these cases the nucleus is not visible. In our many years of using IR-DIC video-enhanced microscopy, we have found that only cells without a visible nucleus, like those in panel C, yield healthy stable long-term whole-cell recordings (e.g., 1–5 h). Scale bar is $10\ \mu\text{m}$ (A–C).

the slice. For greater neuronal integrity of both dendritic structure and afferent fibers, it is better to use 400–500 μm slices (thicker slices are generally less healthy and visualization is very difficult). Although high-quality WCRs from surface cells can be obtained (Jaffe and Brown, 1997), we select neurons that are deeper than 50 μm , preferably 70–140 μm below the slice surface (Moyer and Brown, 1998; Xiang and Brown, 1998; Faulkner and Brown, 1999; McGann et al., 2001; Moyer et al., 2001).

3. Recording from Neurons in Brain Slices

Patch-clamp recording from neurons in brain slices using IR-DIC videomicroscopy has become more widespread in the last five years. With practice it is not uncommon to obtain stable recordings from 80–100% of all neurons selected for WCRs. Of course this estimate assumes minimal difficulties from mechanical sources such as manipulator drift or debris in the electrode tip. In this section we will discuss several issues that are important for obtaining patch-clamp recordings: the selection of the intracellular pipet solution, use of an agar bridge, and liquid-liquid junction potentials. In the last section we will describe the procedures involved in obtaining whole-cell recordings in brain slices and show some examples of the kinds of high-quality data that can be obtained using this technique.

3.1. Selecting an Appropriate Patch Pipet Solution

A wide range of patch-pipet solutions are used depending upon the experimental design (for review see Kay, 1992). A major consideration, when doing whole-cell patch-clamp recordings, is that the contents of the pipet will diffuse throughout the cell and dilute all of the intracellular contents normally present in a neuron. It is therefore advisable to select an intracellular solution that does not adversely affect neuronal function or cause significant run-down of recorded currents.

The major intracellular ions are usually potassium (or some other monovalent cation such as cesium if the goal is to block potassium currents) in conjunction with some negatively charged monovalent anion. The three most common examples of these ions in patch-pipet solution are K-gluconate, KCl, and K-methylsulfate. We use a K-gluconate-based pipet solution and find that it works

quite well with little run-down or alterations of neuronal firing properties over 2–5 h time span (in conjunction with other important ingredients as described below). A chloride-based intracellular solution is excellent for minimizing the liquid-liquid junction potential because chloride is a major part of the ground wire and the aCSF (*see* Subheading 3.3.). A K-methylsulfate-based intracellular pipet solution has been shown to preserve better or minimize run-down of calcium-activated potassium currents (Zhang et al., 1994). It is not surprising that some researchers in the field of aging use a K-methylsulfate-based pipet solution in their patch pipet (e.g., Power et al., 2001), since studies using sharp microelectrodes demonstrated that calcium-activated potassium currents underlying the slow afterhyperpolarization (AHP) are enhanced during aging (Landfield and Pitler, 1984; Moyer et al., 1992),.

Aside from the major ionic species, a number of other ions and chemicals are generally present in standard intracellular patch-pipet solutions. Our standard patch-pipet solution contains each of the following (in mM): 110 K-gluconate, 10 HEPES, 1.0 EGTA, 20 KCl, 2.0 MgCl_2 , 2.0 Na_2ATP , 0.25 Na_3GTP , 10 phosphocreatine (di-Tris), pH 7.3, 290 mOsmol. We also make up a separate identical batch of pipet solution that contains 0.5% biocytin for intracellular labeling and identification of neuronal morphology. Both solutions are aliquoted into small micro-centrifuge tubes and stored at -20°C . Each day fresh patch-pipet solutions are thawed and filtered (using a $0.2\text{ }\mu\text{m}$ syringe filter) before use. We fill the tip of the patch pipet with standard patch solution and then back-fill the pipet with biocytin-patch solution. This minimizes biocytin diffusion throughout the slice prior to obtaining a gigaohm seal.

Different laboratories use different concentrations of ions in their patch-pipet solution and, depending upon the goal of their work (e.g., isolation of specific ionic channels), researchers may add other ions or compounds, such as cesium to block potassium currents (*see* earlier paragraph) or QX-314 to block sodium currents (Frazier et al., 1970). We include GTP in our pipet solution to conserve G-protein mediated responses (Trussell and Jackson, 1987). We also include an ATP regenerative system to prevent run-down of calcium channels (Forscher and Oxford, 1985) and supply energy for other intracellular phosphorylation reactions (Kay, 1992). We also include a small amount of EGTA to buffer slightly the intracellular calcium concentration. Of course, BAPTA is a

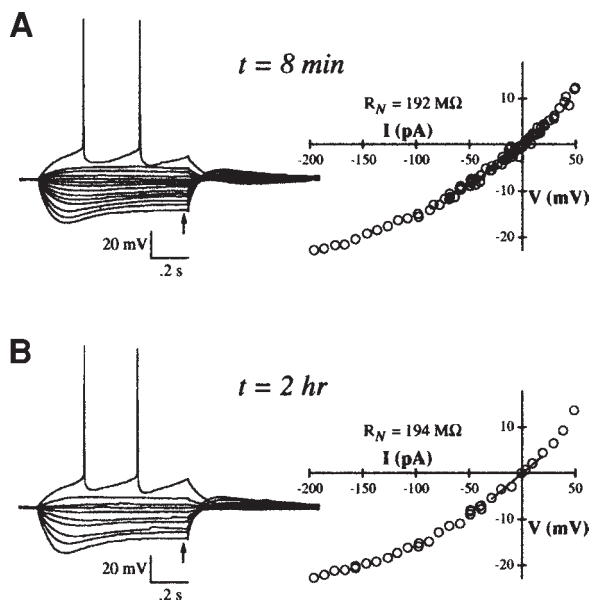


Fig. 6. Whole-cell recordings in brain slices are stable over long time periods. (A) Voltage traces and voltage-current (V-I) relation of a layer V pyramidal neuron in rat perirhinal cortex (PR). The data were collected shortly after establishment of the whole-cell configuration (resting membrane potential -78 mV). (B) Whole-cell recording from the same cell 127 min later. No changes in resting membrane potential, discharge pattern, action potential characteristics, spike threshold, or input resistance were seen over the 2-h time period. Arrows in (A) and (B) indicate the point at which the V-I relation was measured.

much faster calcium chelator than EGTA. Thus BAPTA is recommended in cases where the rapid elimination of intracellular calcium buildup is required (Tsien, 1980).

We routinely obtain stable recordings using this pipet solution and have held cells for several hours without changes in action potential properties, input resistance, or resting membrane potential (Fig. 6). For example, when a neuron has a burst spiking, regular spiking, late spiking, single spiking, or fast spiking discharge pattern at the start of an experiment, that discharge pattern is

maintained for many hours during our whole-cell recordings (Moyer and Brown, 1998; Faulkner and Brown, 1999; Beggs et al., 2000; McGann et al., 2001; Moyer et al., 2002).

3.2. Grounding, Shielding, and the Use of an Agar Salt Bridge

Proper grounding is essential for obtaining low-noise patch-clamp recordings from neurons in any preparation including brain slices. An important aspect of reducing noise is to minimize ground loops as well as magnetic and radiative line-frequency noise from external sources such as computers, monitors, fluorescent lights, and 50 or 60 Hz power lines. Careful grounding of all instruments through low-resistance ground cables and, if necessary, the use of a Faraday cage will generally minimize noise from external sources. Excellent discussions of topics relevant to various noise sources and proper grounding can be found in *The Axon Guide* (Sherman-Gold, 1993). In addition, several other reviews have been published that discuss these topics (e.g., see Levis and Rae, 1992; Penner, 1995).

We ground the bath solution using a sintered silver/silver chloride (Ag/AgCl) wire (for additional information on Ag/AgCl wires see Ives and Janz, 1961; Janz and Ives, 1968; Geddes, 1972; Alvarez-Leefmans, 1992). The sintered Ag/AgCl wire is more durable than a chloridized Ag/AgCl wire, which also works very well (we have used both). The wire is loosely wound into one or more loops and placed into the bath. Since our chambers are not static, we put the Ag/AgCl ground wire at the end of the chamber just prior to where the aCSF flows out. Every couple of weeks we re-chloride the wire by placing it into a vial containing Clorox for 20–30 min (we do the same for the recording wire except in this case we chloridize a bare silver wire). We have also successfully used a DC-power source such as a 1.5 V alkaline battery to chloride our electrodes. In this case, the power source is connected at the positive pole to the Ag/AgCl wire and at the negative pole to another silver wire. Current is passed while both electrodes are immersed in a chloride solution (e.g., 0.1 M HCl). A switch can be used to iteratively reverse the current flow and a potentiometer in series with the power source can be used to adjust the current flow. In our experience chloriding electrodes using Clorox is easier and works just as well.

In our electrophysiology rigs, the Ag/AgCl ground wire is connected to a common copper ground block that is located on, but insulated from, the vibration isolation table. This block has 16 holes for connecting banana jacks from different sources. Grounds from all metallic surfaces (including the headstage, the microscope, the isolation table, the isolated stimulators, the specimen stage, and the manipulators) go through this common ground, which is then connected directly to the signal ground of the patch-clamp amplifier. The Faraday cage can also be grounded through the copper block, but it is also common to ground it through either the instrument rack ground or the ground terminal of a grounded outlet. It is important to make sure that all metallic surfaces near the headstage are properly grounded through the common ground. Failure to ground in this manner will enable the surfaces to act as an antenna and pick up line-frequency signals. Going through a common ground in this manner is an easy way to eliminate ground loops. If additional noise persists, it is important to troubleshoot starting with the amplifier and oscilloscope and add equipment one piece at a time until the noise source is identified. Careful troubleshooting in the beginning will save valuable time in the long run.

As mentioned earlier, we use a sintered Ag/AgCl wire for our ground wire. Of course this wire is perfectly fine as long as a chloride-based aCSF is used and as long as the wire is well-chlorided. For greater stability, many electrophysiologists use a salt bridge. This is particularly useful if the concentration of chloride in the aCSF bath is changed during an experiment. Salt bridges are comprised of a thin agar tube containing KCl throughout. This is made by adding 2–3% agar to a solution of 3 M KCl, boiling the mixture, sucking up it into thin capillary or Teflon tubes (~1 mm), and allowing it to cool. The tubes can also be shaped by gentle heating prior to adding the agar mixture. After cooling, the agar/KCl salt bridge is removed by very gentle pressure applied through a syringe and cut to the appropriate length using a razor blade. One end of the agar tube is in contact with the aCSF bath solution and the other end is in a 3 M KCl solution. When a salt bridge is used, one end of the Ag/AgCl ground wire is in the 3 M KCl solution and the other end goes to the ground block. Thus the ground wire is indirectly in contact with the aCSF bath through the salt bridge. Care should be taken in cases where vastly different aCSF solutions are switched for extended time periods when using a salt bridge (for discussion, *see* Neher, 1992).

3.3. Liquid-Liquid Junction Potentials and Correcting for Them

In electrophysiological studies, liquid-liquid junction potentials (hereafter referred to as liquid junction potentials) arise from differences in ionic composition and ionic mobilities at the junction between two solutions (e.g., the intracellular pipet solution and the extracellular bath solution). Left uncorrected, liquid junction potentials can contribute significantly to errors in membrane potential measurements. Such errors typically range from 1 or 2 millivolts (using KCl electrode solutions) to more than 10 mV (e.g., using gluconate or methylsulfate electrode solutions). With the increased use of whole-cell patch-clamp recordings and the use of charge carriers other than KCl, corrections for liquid junction potentials have become very important. While some authors do correct for liquid junction potentials, others not only fail to correct but they also fail to mention the value of the liquid junction potentials in their studies. Such lack of attention can make it difficult to compare data from different laboratories. The following sections briefly describe how to measure liquid junction potentials as well as how to calculate them using the generalized Henderson Liquid Junction Potential Equation.

3.3.1. Measuring Liquid Junction Potentials

Empirically measuring the liquid junction potential between the bath and pipet solutions is fairly straightforward. Under static conditions (i.e., no flow of fluid) start with a patch pipet filled with the intracellular solution and zero it in the same pipet solution (in current-clamp). Once the potential is zeroed and stable, measure the potential change that results from rapidly switching to the aCSF bathing solution. It is a good idea to switch back to the intracellular solution to verify reversibility. Also, when measuring the liquid junction potential, it is necessary to use a salt bridge if the patch-pipet solution contains a much lower concentration of chloride relative to the aCSF bathing solution. Erwin Neher has recently published a detailed description of how to measure liquid junction potentials along with a listing of approximate junction potentials for some commonly used pipet solutions (Neher, 1992). In our studies, voltages are corrected for a measured liquid junction potential of about +13 mV between the bath and patch-pipet solutions. Corrections are applied according to

the equation $V_M = V_P - V_L$, where V_M is the corrected membrane voltage, V_P is the observed pipet voltage and V_L is the liquid-liquid junction potential (Moyer and Brown, 1998; McGann et al., 2001; Moyer et al., 2002). Our measured liquid junction potential of +13 mV is similar to that obtained theoretically (*see* Subheading 3.3.2.).

3.3.2. Calculating Liquid Junction Potentials

Calculating liquid junction potentials involves the use of the generalized Henderson Liquid Junction Potential Equation (Barry and Lynch, 1991):

$$E^S - E^P = (RT/F)S_F \ln \left\{ \sum_{i=1}^N z_i^2 u_i a_i^P / \sum_{i=1}^N z_i^2 u_i a_i^S \right\} \quad (1)$$

where

$$S_F = \sum_{i=1}^N [(z_i u_i)(a_i^S - a_i^P)] / \sum_{i=1}^N [(z_i^2 u_i)(a_i^S - a_i^P)] \quad (2)$$

and $E^S - E^P$ represents the potential (E) of the solution (S) relative to the pipet (P). The variables u , a , and z represent, respectively, the mobility, activity, and valence of each of the ionic species (i). The constants R , T , and F represent the gas, the temperature (in Kelvin), and the Faraday constants. Thus, $RT/F \ln = 58.2 \log_{10}$ in millivolts at a temperature of 20°C.

Theoretical calculation of liquid junction potentials has become even more convenient with the recent development of JPCalc by Peter Barry (Barry, 1994). This software is inexpensive and can be extended by the user to include the mobilities and valencies of additional ions. We have used JPCalc to calculate the liquid junction potential in our experiments and found the value to be in excellent agreement with our empirical measurements (e.g., liquid junction potential of +13.08 mV when measured compared with +13.0 mV calculated using JPCalc).

Calculations using Eq. 1 (the generalized Henderson Junction Potential Equation) provide an excellent estimate of the liquid junction potential. However, estimates should be carefully checked when high concentrations of divalent ions are used, since most research has been conducted using monovalent ions (Barry and Lynch, 1991). Several excellent reviews of liquid junction potentials along with the mobilities and valencies of some commonly used ions have been published (Barry and Diamond, 1970; Barry and Lynch, 1991; Neher, 1992; Barry, 1994; Ng and Barry, 1995).

3.4. Obtaining Whole-Cell Recordings in Brain Slices

Whole-cell recordings (WCRs) from neurons in brain slices involves obtaining a tight seal between the patch pipet and cell membrane. This is done by applying gentle suction (negative pressure) to gain access to the inside of the cell. There are two basic techniques for obtaining WCRs: the blind approach and the visually-guided approach. Although the blind approach (Blanton et al., 1989) is still used in some laboratories (McKernan and Shinnick-Gallagher, 1997), we believe that IR-DIC videomicroscopy is vastly superior for the reasons discussed earlier (*see* Subheadings 2.1. and 2.2.).

In this section we will describe how to obtain WCRs from neurons in brain slices and illustrate some of the questions that can be addressed using this technique. Although this section focuses on WCRs, the cell-attached, inside-out, outside-out, and perforated patch configurations are also popular (for a brief review, *see* Cahalan and Neher, 1992). Once the whole-cell configuration has been obtained, and a current- and/or voltage-clamp experiment is completed, the somatic cytoplasm and nucleus can be removed and reverse transcriptase polymerase chain reaction (RT-PCR) analyses can be applied to amplify mRNA present in the soma (Martina et al., 1998; Thibault et al., 1998; Sucher et al., 2000).

3.4.1. The Gigaohm Seal and Obtaining Access to the Cell

After waiting 1 h for the slices to recover, a slice is removed from the holding chamber, placed into the recording chamber and secured by placing a net atop the slice. The securing net is made by flattening a piece of silver wire and shaping it to fit in the recording chamber. Then 4 or 5 single strands of nylon hosiery are glued across the wire using cyanoacrylate. When placed on the slice, the nylon hosiery serves to anchor the slice in several locations. After securing the slice, the brain region of interest is identified using a 2.5 \times objective, and the microscope is aligned for Köhler illumination by stopping down the luminous field diaphragm, removing the polarizer, and focusing the condenser (with lens in place) until a crisp outer ring is observed through the oculars. Next we switch to the 40 \times water objective (0.75 NA) and repeat the Köhler illumination alignment and place an infrared light filter directly onto the top of the luminous field diaphragm adjustment knob.

Once the neuron of interest is visualized using a 40 \times water objective (0.75 NA), we pull a patch pipet using a Flaming/Brown micropipet puller (Sutter Instruments, Model P-97). Obtaining the right patch-pipet tip size and geometry are important for achieving a high success rate (for an excellent review, *see* Sakmann and Neher, 1995). The patch pipet is then fire polished and filled with an appropriate patch solution that has been filtered using a 0.2 μ m syringe filter. If necessary, the pipet is first coated with an insulating substance like Sylgard prior to firepolishing the tip. After attaching the pipet to the headstage, positive pressure is applied to the pipet by blowing into a Tygon or Nalgene tube that is directly connected with the pipet holder (we use a stopcock to maintain or release the positive pressure). The pipet is then lowered into the bath and the amplifier voltage is zeroed. After switching to voltage-clamp mode (at 0 mV with tracking on), a 5 mV hyperpolarizing voltage step is applied and the current measured to obtain the pipet resistance (2–5 M Ω for somatic and 5–10 M Ω for dendritic recordings) using Ohm's law.

As the pipet gets closer to the cell, we usually re-apply positive pressure. This helps to clear the membrane of debris. The "plume" of fluid radiating out from the pipet tip increases visibility, which can be helpful in selecting an optimal location on the cell membrane to patch. The pipet is then lowered onto the cell until the positive pressure creates a small "dimple" (*see* Fig. 7A). At this point the positive pressure is quickly removed (by turning the stopcock) and very gentle suction is applied by mouth to form a gigaohm seal (>1 G Ω or 10⁹ Ω), which we estimate by measuring the current in response to a 25 mV hyperpolarizing voltage step. It is important to remove the positive pressure as soon as a small but distinct dimple is visible. Otherwise, the positive pressure will create a *very* large dimple, which may damage the cell membrane (Fig. 7B).

Firepolishing the pipet tip is helpful for obtaining high-resistance seals (our seals are typically about 5 G Ω and we have had seals as high as 25 G Ω). The method of using positive pressure for keeping the pipet clear of debris (Coleman and Miller, 1989) facilitated development of the blind approach to WCR (Blanton et al., 1989). By contrast, in early studies using visualization, it was thought that prior cleaning was necessary. In these cases under visual guidance, suction was applied through a larger pipet filled with aCSF to remove or clean the surface of a neuron from which

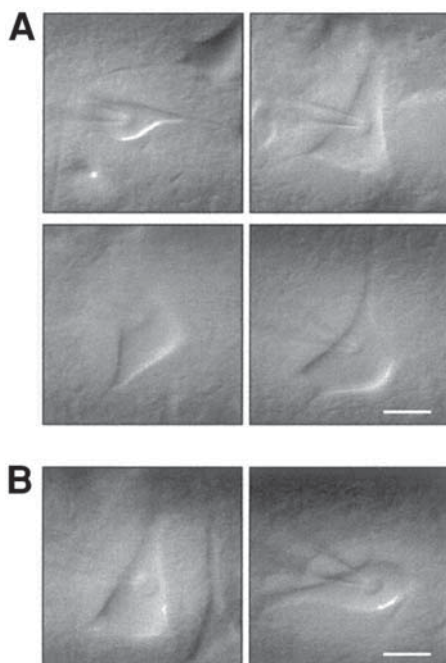


Fig. 7. Examples of the dimple created by positive pressure through the whole-cell patch pipet. (A) IR-DIC videomicrographs of typical dimple sizes. (B) IR-DIC videomicrographs of dimples that are too large. In visually healthy neurons, this results either from excessive positive pressure or failure to quickly release the positive pressure as soon as a dimple is observed. In these cases, obtaining a stable whole-cell recording is unlikely. Scale bar for (A) and (B): 10 μm .

WCRs were to be obtained (for detailed description, *see* Edwards et al., 1989).

After obtaining a stable gigaohm seal, the fast and slow capacitive transients are removed or minimized using dials on the amplifier. Two additional ways to minimize capacitive transients are: (1) by keeping the solution level very low and (2) by coating the pipet with Sylgard or some other insulating compound (which can be made, aliquoted into small micro-centrifuge tubes, and stored at -20°C for several months). The Sylgard should be applied to within 20 μm of the tip and extend back so none of the pipet

glass is in direct contact with the aCSF. The Sylgard can be cured using a heat gun and this should be done before firepolishing the electrode tip (for information regarding tip geometry and patch membrane estimates, *see* Sakmann and Neher, 1995). Unless quartz electrodes are used, coating is extremely important for achieving the low noise necessary for recording single-channel currents in either the cell attached, inside-out, or outside-out configurations. Detailed information regarding different noise sources and types of glass used in patch-clamp recording can be found in the literature (e.g., for review, *see* Sherman-Gold, 1993; Benndorf, 1995).

After cancellation of fast and slow transients, we remove tracking and voltage-clamp the membrane patch at an uncorrected membrane potential of -70 mV before attempting to go into the whole-cell configuration. By clamping the membrane at -70 mV, we eliminate the possibility of the cell rapidly depolarizing upon rupture of the membrane. To break in, extremely gentle suction is applied by mouth every couple of seconds until a sudden increase in the capacitive current is observed as the membrane capacitance of the cell is revealed. If the cell is healthy, little holding current will be required to keep the membrane potential at -70 mV (the actual resting potential can be quickly assessed by switching to $I = 0$ mode (current-clamp with no holding current)). Next the whole-cell capacitance is compensated by adjusting the dial on the amplifier and the series resistance compensated (*see* below).

3.4.2. Series Resistance Compensation and Measurement

In the whole-cell configuration, access resistance (R_a) refers to the resistance to current flow through the pipet tip and into the cell cytoplasm while series resistance (R_s) refers to the combination of R_a and any other external resistances, such as that contributed by an agar salt bridge. Generally, in WCRs these external resistances are small enough to ignore, effectively making $R_a = R_s$. Since the patch-pipet resistance (measured in the bath before forming a gigaohm seal) is part of the R_s , it follows that pipets with larger tip diameters will have both a lower resistance and a lower R_s . Typically, R_s is 2–5 times larger than the pipet resistance. However, in some cases this ratio can be reduced to 2–3 with extremely gentle suction applied to the pipet (e.g., for review, *see* Marty and Neher, 1995).

A major problem associated with attempting to compensate for R_s is the presence of a large uncompensated capacitance. To reduce

the capacitance, it is recommended that the patch pipet be coated with Sylgard as mentioned previously. Such insulation will permit a more accurate determination of the access or series resistance. Uncompensated R_s can lead to significant errors in voltage-clamp experiments. For example, in response to a voltage step the membrane voltage of the cell will settle to its new voltage according to a time constant given by $\tau = R_s C_m$ where C_m is the membrane capacitance. A larger series resistance will significantly reduce the speed of the clamp. Another serious issue regarding uncompensated series resistance is that it can cause the actual membrane potential to deviate from the command potential when ionic current (I) is flowing. The size of this error can be considerable and is given by $R_s I$. Thus, an R_s of only 10 M Ω , will result in a 20 mV error when a current of 2 nA flows. Although it is not possible to compensate fully for series resistance (because amplifiers use positive feedback and "ringing" occurs at 100%) it should be possible to compensate the series resistance by 80% or more.

It is important to check R_s periodically throughout the experiment because it is not uncommon for the patch membrane to re-seal partially or completely. It is usually possible to decrease R_s to its original value with a few gentle suction. Of course, if R_s increases appreciably during an experiment, and repeated attempts to decrease it fail, the experiment should be terminated (for excellent reviews of series resistance and compensation, *see* Armstrong and Gilly, 1992; Marty and Neher, 1995).

3.4.3. Current-Clamp Recordings

In the current-clamp configuration, current is injected into the cell and the membrane voltage is measured. Intracellular current-clamp recordings from neurons in brain slices enables the study of neuronal discharge patterns and membrane voltage in response to both intracellular current injection and synaptic stimulation. Current-clamp studies have been used to probe a wide range of topics including but not limited to synaptic transmission, synaptic plasticity, neuronal connectivity, associative learning, calcium dynamics, aging, and epilepsy (Brown et al., 1979; Barrionuevo and Brown, 1983; Landfield and Pitler, 1984; Kelso et al., 1986; Williams and Johnston, 1988; Deuchars et al., 1994; Moyer et al., 1996; Scharfman, 1996; Thomson and Deuchars, 1997; Moyer et al., 2000b). With the development of the patch-clamp technique (Neher and Sakmann, 1976) and its application to brain slices (Blanton

et al., 1989; Edwards et al., 1989), many researchers are now using whole-cell recordings (WCRs) rather than sharp microelectrodes to probe the neurophysiology of various brain regions (Jaffe and Brown, 1997; Stuart et al., 1997a; Moyer and Brown, 1998; Reyes et al., 1998; Tarczy-Hornoch et al., 1998; Yeckel et al., 1999; Beggs et al., 2000; Johnston et al., 2000; McGann et al., 2001; Power et al., 2001). It should be realized, however, that the patch-clamp amplifier is a current follower (or current to voltage converter) rather than a voltage follower like traditional current-clamp amplifiers. As such, current-clamp recordings from patch-clamp amplifiers may lead to distortions of fast signals (e.g., action potentials) relative to data obtained from WCRs using a current-clamp amplifier (Magistretti et al., 1996).

Comparisons between whole-cell and sharp electrode recordings indicate that in a given class of cells the resting membrane potential is similar, whereas, the input resistance is much higher in WCRs (Staley et al., 1992). Such a large difference in neuronal input resistance is likely due to an artificial leak conductance around the site of the microelectrode impalement. This artifactual leak is not present in WCRs due to the tight gigaohm seal formed between the pipet and cell membrane. Of course, a legitimate concern regarding WCRs is the diffusion of pipet contents into the cell, which may "wash-out" important intracellular constituents. In our current-clamp WCR studies we actually see little or no change in neuronal discharge pattern, spike height, or input resistance over several hours in healthy neurons (*see* Fig. 6). Of course, in cases where the patch pipet drifts or the slice moves slightly (e.g., because of periodic changes in aCSF levels or because the slice is poorly secured), the degradation in neuronal properties over time is not due to "wash out" or "run down" of important intracellular constituents. Such changes in the health of the cell or integrity of the WCR are often due to a mechanical problem or the selection of an unhealthy cell, and it is important to distinguish these situations from genuine run down.

In cases where obvious changes in neuronal properties are observed over time, and run down or wash out are suspected, the perforated patch technique can be employed. After forming a gigaohm seal, instead of using suction or negative pressure to break into the cell, a compound (such as nystatin, amphotericin, gramicidin, or β -escin) that diffuses to the tip of the pipet and forms pores

in the cell membrane is included in the patch-pipet solution. Back-filling the pipet is vital because the presence of these pore-forming compounds at the tip may inhibit the formation of a gigaohm seal. As the pores form, electrical access to the cell interior is slowly achieved over time (e.g., 2–30 min). Two disadvantages of the perforated patch technique are that: (1) dialysis of the cell interior with specific compounds larger than pipet ions is hampered and (2) it takes much longer to obtain a low access resistance (which can be higher than that obtained using WCRs if precautions are not used to minimize access resistance). Advantages of the perforated patch technique include: (1) impermeability to large molecular weight compounds, (2) re-sealing of the membrane in the patch pipet does not occur, and (3) loss of the gigaohm seal is less likely to occur (for reviews of the perforated patch-clamp technique, *see* Sherman-Gold, 1993; Marty and Neher, 1995).

3.4.4. Voltage-Clamp Recordings

In the voltage-clamp configuration, membrane voltage is controlled while the transmembrane current that flows in response to voltage changes is measured (for in-depth reviews of patch-clamp amplifiers, *see* Sherman-Gold, 1993; Johnston and Wu, 1995; Sigworth, 1995; Sigworth et al., 1995). Introduction of the patch-clamp technique (Neher and Sakmann, 1976) with its high signal-to-noise ratio has enabled researchers to study single-channel currents under voltage-clamp conditions in a variety of cell types including central neurons in brain slices. In addition to single-channel studies, whole-cell macroscopic currents (e.g., Jahromi et al., 1999), synaptically evoked currents (e.g., mossy-fiber–CA3 synapses; *see* Xiang et al., 1994), and both the composition and modulation of spontaneous postsynaptic currents (e.g., Jonas et al., 1993; Aghajanian and Marek, 1999) can be studied.

In voltage-clamp studies, it is important to be aware of the space-clamp issue. Simply put, when voltage-clamping neurons, it cannot be assumed that the entire cell is held at the desired membrane potential. With somatic current recordings, distal dendritic membrane may not be at the same membrane potential as the soma. This may also be true for some of the more proximal dendritic membranes. The reader is referred to recent articles for more information on space-clamp errors and analyses of neuronal

electrotonic structure (e.g., Armstrong and Gilly, 1992; Spruston et al., 1993; White et al., 1995; Mainen et al., 1996; Mainen and Sejnowski, 1996; Carnevale et al., 1997).

To minimize space-clamp, some scientists use dissociated cells. This procedure involves enzymatic and mechanical dissociation of neurons from brain slices. Other researchers use the nucleated patch configuration (e.g., *see* Sather et al., 1992; Bekkers, 2000; Korngreen and Sakmann, 2000; Jung et al., 2001). In the latter procedure, a whole-cell recording is first made from the identified cell of interest. Next, negative pressure is applied through the electrode so that the nucleus is brought into contact with the pipet tip. Then, very slowly, the pipet is pulled away from the cell over a period of a minute or so until the nucleus pops out of the somatic membrane, often leaving a thin trail of membrane behind. Pulling must continue until after any trail of membrane is pinched off completely. This results in the formation of a giant outside-out patch of somatic membrane surrounding the nucleus (Jung et al., 1997). The strong negative pressure can then be released but a small amount of pressure should be maintained to keep the nuclear membrane up against the pipet. This nucleated patch configuration can now be used to study somatic channels in voltage-clamp without the worries and artifacts of space-clamp errors.

Since the nucleated patch configuration involves initially obtaining a WCR, one can first obtain current-clamp data before creating the nucleated patch configuration. This way both current-clamp and voltage-clamp data can be obtained from the cell of interest, as well as its morphology provided that biocytin or a fluorescent dye is included in the patch solution. As with voltage-clamp studies in the whole-cell configuration, it is important to use coated electrodes and to compensate for series resistance in the nucleated patch configuration (*see* Subheading 3.4.2.). The series resistance is generally similar in the nucleated patch configuration compared with the whole-cell configuration ($<20\text{ M}\Omega$, e.g., *see* Martina et al., 1998; Bekkers, 2000; Korngreen and Sakmann, 2000).

When the membrane potential of a neuron is stepped to a particular voltage during a voltage-clamp experiment, a leakage current is also generated that is largely carried by K^+ and Cl^- ions. This "leak current" results from a steady outward current through resting conductances, and it varies in a linear manner with hyperpolarizing and depolarizing voltage steps as long as the amplifier does not saturate or receive a signal that is too large to amplify

or filter linearly (Sigworth and Zhou, 1992). Leak currents, however, are often masked by the presence of larger voltage- and/or ion-dependent currents that flow during voltage steps. In order to study directly a current of interest, the leak current can be removed by leak subtraction.

Leak subtraction can be performed both on-line and off-line. One of the most common forms of leak subtraction is referred to as the P/N subtraction method (Bezanilla and Armstrong, 1977). Here P represents the protocol or voltage-step used and N represents both the fraction of the voltage step P that is given to generate the leak current and the number of voltage steps given. For example, with P/N subtraction, the normal voltage step is scaled down by some fraction such as one-fourth. This would correspond to a P/4 protocol, where N is 4 in the denominator. This scaled-down voltage step would then be delivered to the neuron four times and the average of the resulting current scaled back up by a factor of four and subtracted from the current response to the normal voltage step.

For generating the leak subtraction pulses, the membrane potential is held at a more hyperpolarized voltage to minimize contributions from voltage-dependent currents. For example, if an experimental voltage step would normally be from a holding potential of -80 mV to a command potential of $+40$ mV, P would be 120 mV. The leak subtraction steps using a P/4 protocol would involve a step of 30 mV (i.e., P/N would be $120 \text{ mV} / 4$ or 30 mV). Thus the membrane potential would be stepped from -120 to -90 mV four times, and the average of these leak currents would then be multiplied by four (i.e., scaled up) and subtracted from the current elicited by the experimental voltage step protocol (i.e., that produced by the step from -80 mV to $+40$ mV).

In experiments involving voltage steps to a variety of membrane potentials, a set of leak subtraction pulses is generated for each voltage step and the leak currents subtracted. In this manner the leak current is removed from the total current generated by each individual voltage step. Since the holding current will be different between the experimental protocol and the leak protocol (i.e., different amount of current is required to hold a cell at -80 mV compared with -120 mV), each current trace is normalized prior to subtraction. Although it is important to pick a voltage range where voltage-dependent currents are likely to be minimal or absent, it should be noted that neurons generally do not remain

healthy if their membrane potential is held beyond -120 mV for more than a few milliseconds.

3.4.5. *Simultaneous Recordings with Multiple Electrodes*

Recording from multiple neurons or multiple sites on the same neuron is a powerful way to study communication both between and within neurons. The development and application of IR-DIC videomicroscopy to brain slices has facilitated these efforts, especially those involving simultaneous patching of dendrites or axons and the soma in the same cell. Care must be taken, however, to minimize disruption of one recording while obtaining another. We have found that it is helpful to lower both electrodes so they are near the targets of interest. This way, little movement of the electrode is required to actually form the seal. This is especially helpful if the cells of interest are close to each other or if recordings are made from both the soma and proximal dendrite.

Dual recordings have facilitated some elegant studies evaluating the origin of sodium spikes at the soma and their backpropagation into the dendrites (Stuart and Sakmann, 1994; Stuart et al., 1997b). Studies have shown not only that these backpropagating action potentials lead to calcium entry in dendritic spines and shafts (Jaffe et al., 1994; Yuste and Denk, 1995; Jaffe and Brown, 1997), but that in conjunction with an appropriately timed synaptic signal, backpropagating spikes may also contribute to associative synaptic plasticity (Magee and Johnston, 1997; Markram et al., 1997b). Dual somatic and dendritic recordings have also been used to study propagation of synaptic signals from the dendrites to the soma and differences in the density of different potassium conductances as a function of distance from the soma (e.g., see Magee and Johnston, 1995; Hoffman et al., 1997).

Simultaneous recordings from multiple neurons in brain slices are useful for studying neuronal connectivity. Paired recordings from two neurons have been successfully obtained blind using sharp microelectrodes (e.g., Thomson and West, 1993; Deuchars et al., 1994). Recently, simultaneous patch-clamp recordings from multiple, visually-identified neurons has also been performed in brain slices (e.g., see Markram et al., 1997a). Visualization is of obvious benefit for pre-selecting different classes of neurons in specific locations or layers. By recording from two or more neurons it is possible to study not only the nature of their synaptic connec-

tions (i.e., inhibitory, excitatory) but also the frequency-dependent characteristics of the postsynaptic responses as a function of presynaptic firing rate (Galarreta and Hestrin, 1998; Reyes et al., 1998; Gibson et al., 1999). In addition, by filling the pipets with biocytin and obtaining morphological reconstructions, estimates of the number of synaptic contacts between different classes of neurons can be obtained.

A major problem with recording from pairs of neurons in cortical brain slices is the low probability of finding two cells that are synaptically connected—although this percentage probably varies as a function of cell class combination (pyramidal-pyramidal or pyramidal-nonpyramidal) and columnar location (Deuchars and Thomson, 1996; Reyes et al., 1998; Gupta et al., 2000). Recently, Raphael Yuste's group has attempted to overcome the labor-intensive nature of obtaining recordings from synaptically connected pairs of neurons using optical techniques. By bulk-loading the cells with a fluorescent calcium indicator they found that it was possible to identify postsynaptic neurons by stimulating one presynaptic cell and observing those cells whose somatic calcium response is time-locked to the action potentials of the presynaptic neuron (Peterlin et al., 2000). Two drawbacks to this technique are that it does not conveniently reveal inhibitory connections and that all of the cells are loaded with a calcium buffer that could alter the properties of postsynaptic responses. Nevertheless, such a technique could prove to be quite useful for rapidly determining candidate postsynaptic neurons as well as identifying microcircuits within a brain region of interest.

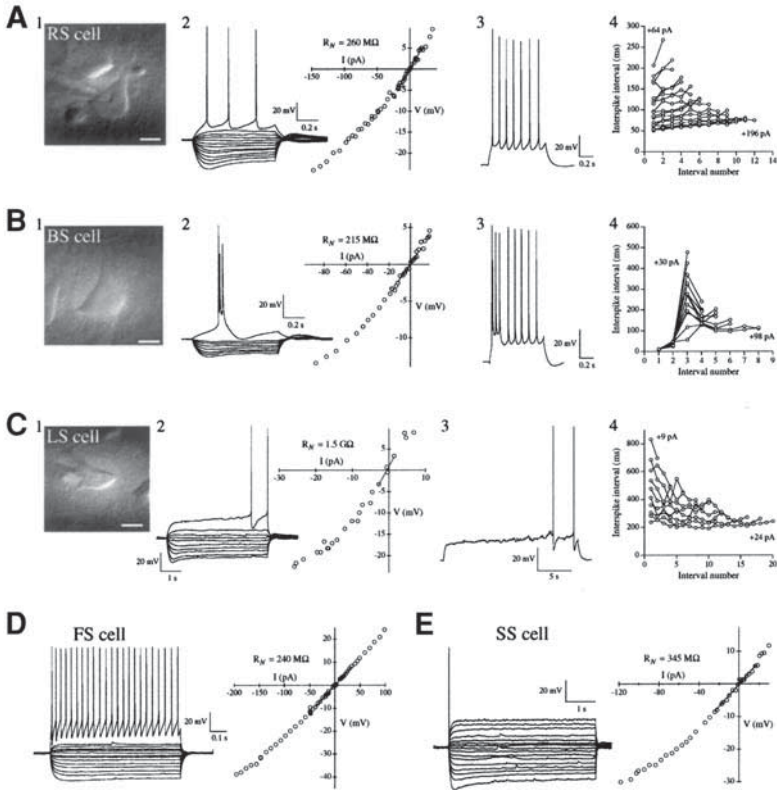
3.5. Use of Patch-Clamp Techniques to Study Perirhinal Cortex

Recently, we have been using whole-cell current- and voltage-clamp recordings in horizontal rat brain slices to study the neurophysiology of perirhinal cortex (Moyer and Brown, 1998; Faulkner and Brown, 1999; Beggs et al., 2000; McGann et al., 2001; Moyer et al., 2002). In these studies we use IR-DIC videomicroscopy to preselect visibly healthy neurons throughout the different layers of perirhinal cortex (PR) and obtain WCRs using pipets filled with biocytin (*see* Subheading 3.1.). This section describes some of the ways in which our use of patch-clamp recordings in brain slices has contributed to understanding this important brain region.

An example of a typical brain slice containing PR is shown in Fig. 4B. Thus far we have identified five distinct discharge patterns among neurons in PR (Fig. 8). Regular spiking (RS) cells fire their first action potential (AP) shortly after onset of the current pulse and exhibit variable amounts of frequency adaptation. Burst spiking (BS) cells fire an initial burst of 2–3 APs shortly after onset of a current pulse followed by a second burst and/or single adapting APs. Late spiking (LS) cells fire their first AP several seconds after onset of the current injection (if the pulse is long enough) followed by sustained firing. We frequently see onset latencies that range from 5–12 s and have seen onset latencies of more than 20 s (depending on the duration of the current step). Fast spiking (FS) cells fire their first AP shortly after onset of a depolarizing current step, are capable of firing at very high frequencies (>100 Hz), and show little or no frequency adaptation. In contrast, single spiking (SS) cells fire only a single AP in response to supra-threshold current steps. These different cell classes in PR have diverse morphologies (Fig. 9), and their distributions vary as a function of layer (*see* legend to Fig. 8).

We have recently been using the patch-clamp technique in brain slices to study spontaneous excitatory PSCs, synaptically evoked PSCs, and the ionic mechanisms underlying firing patterns in PR neurons (Fig. 10; *see* also Moyer et al., 2000a; Moyer et al., 2002). For example, we have recorded and analyzed spontaneous PSCs from visually pre-selected pyramidal neurons in layer V of rat PR. Our analyses indicate that at membrane potentials near rest, the excitatory spontaneous PSCs are ~15 pA in amplitude (Moyer et al., 2002), much smaller than those from neurons in the external capsule and the adjacent lateral amygdala (Faulkner and Brown, 1999). Figure 10A shows the amplitude frequency histograms and examples of spontaneous PSCs recorded in layer V pyramidal neurons in brain slices prepared from both juvenile and aged rats. Alternatively, when monosynaptic currents are evoked by minimal stimulation of layer I, the PSCs are about 40 pA. Interestingly, these monosynaptic currents have long latencies (Fig. 10B).

Fig. 8. Primary classes of neurons in rat perirhinal cortex. (A) IR-DIC videomicrograph and physiology of a regular spiking (RS) pyramidal neuron in layer V. This neuron had a resting membrane potential (E_R) of -76 mV. RS cells comprise ~50% of the pyramidal cells in layer II/III,



(continued) ~76% of the pyramidal cells in layer V, and ~1% of the principal cells in layer VI. (B) IR-DIC image and physiology of a burst spiking (BS) pyramidal neuron in layer V ($E_R = -75 \text{ mV}$). BS cells comprise ~9% of the pyramidal neurons in layer V and only in cells from rats of age 14 d and older. (C) IR-DIC image and physiology of a late spiking (LS) nonpyramidal neuron in layer VI ($E_R = -82 \text{ mV}$). Notice the unusually long latency to first spike in panel 3 (delay of 16 s in response to a 20 s, 8 pA current injection). LS cells comprise ~50% of the pyramidal cells in layer II/III, ~14% of pyramidal cells in layer V, and ~90% of the principal cells in layer VI. (D) Physiology of a fast spiking (FS) nonpyramidal neuron in layer I ($E_R = -78 \text{ mV}$). FS cells are located in layers I, II/III, V, and VI and are easily identified by their small soma size ($\leq 10 \text{ }\mu\text{m}$, see Fig. 1 of McGann et al., 2001). (E) Physiology of a single spiking (SS) nonpyramidal neuron in layer VI ($E_R = -82 \text{ mV}$). SS cells comprise ~7% of the principal neurons in layer VI.

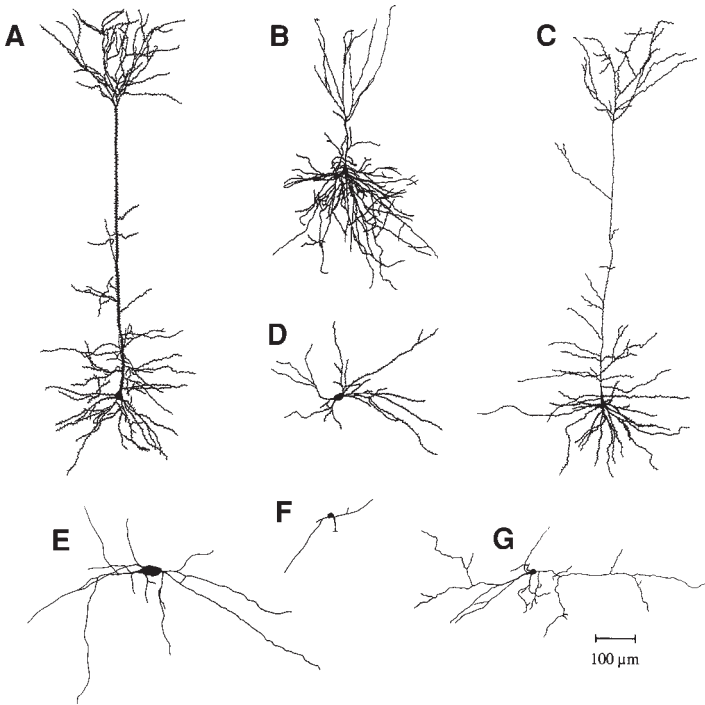


Fig. 9. Morphological examples from each of the five cell classes in rat perirhinal cortex. (A) Burst spiking (BS) spiny pyramidal neuron in layer V. Notice the thick apical dendrite typical of BS pyramidal cells. (B) Late spiking (LS) spiny pyramidal neuron in layer II/III. (C) Regular spiking (RS) spiny pyramidal neuron in layer V. Notice the relatively thin apical dendrite typical of RS pyramidal neurons. (D and E) LS spiny and aspiny nonpyramidal neurons located in layer VI. (F) Fast spiking aspiny nonpyramidal neuron in layer VI. (G) Single spiking aspiny nonpyramidal neuron in layer VI. All neurons are oriented with the pial surface at the top and the external capsule at the bottom.

By obtaining video captures of the brain slice along with the locations of the recording and stimulating electrodes we were able to get a rough estimate of conduction velocity. This is done by rotating out the 40 \times water objective, rotating in a 2.5 \times air objective (which can easily be done without adversely affecting the neuronal recording) and obtaining a video capture at low power. When electrode distance was plotted against onset latency, the slope of

the linear regression suggested a conduction velocity of ~ 0.16 m/s (Moyer et al., 2002). This value agrees well with velocities previously reported in unmyelinated fibers (for example, *see* Berg-Johnsen and Langmoen, 1992) and suggests that PR layer V pyramidal neurons receive at least some of their inputs from small diameter unmyelinated fibers. This is not surprising because PR has a relatively low myelin content compared with other cortical regions (Zilles and Wree, 1995).

The patch-clamp technique in conjunction with IR-DIC videomicroscopy has also facilitated our efforts to investigate the ionic mechanisms underlying late spiking in PR neurons (Moyer et al., 2000a). To approach this question, we are focusing our attention on neurons in layer VI because about 90% of the principal neurons (i.e., all cells larger than those easily identified as a population of small fast-spiking neurons) are late spiking (McGann et al., 2001). Preliminary voltage-clamp data suggest the presence of a slowly-inactivating potassium current that is pharmacologically blocked by low 30 μ M concentrations of 4-aminopyridine (4-AP; *see* Fig. 10C1). This current may at least partly underlie late spiking because, under current-clamp conditions, 4-AP not only blocks late spiking in PR neurons (Fig. 10C2), but it has also been shown to block late spiking in other cell types including medium spiny striatal neurons (Nisenbaum et al., 1994). The extent to which the ionic currents underlying late spiking vary as a function of layer or cell type in PR and whether they are the same or different from those in other brain regions remains to be determined. Our electrophysiological and morphological data are also used in guiding computational modeling studies aimed at exploring the theoretical implications of the various firing patterns in PR. For example, since PR has such a high percentage of LS cells—more than any other cortical region studied to date—we developed a computational model to explore the temporal properties of these neurons and how they could theoretically participate in learning (Tieu et al., 1999; McGann and Brown, 2000). Given the large numbers of LS neurons and relative lack of myelin, we tend to think of PR as “slow” or “thinking” cortex. That is, PR does not appear to be a region of high throughput to other regions such as the amygdala or hippocampal formation.

We are also interested in determining how neurons in PR change during the aging process, which should not be a problem since we have already adapted visually guided patch-clamp recordings

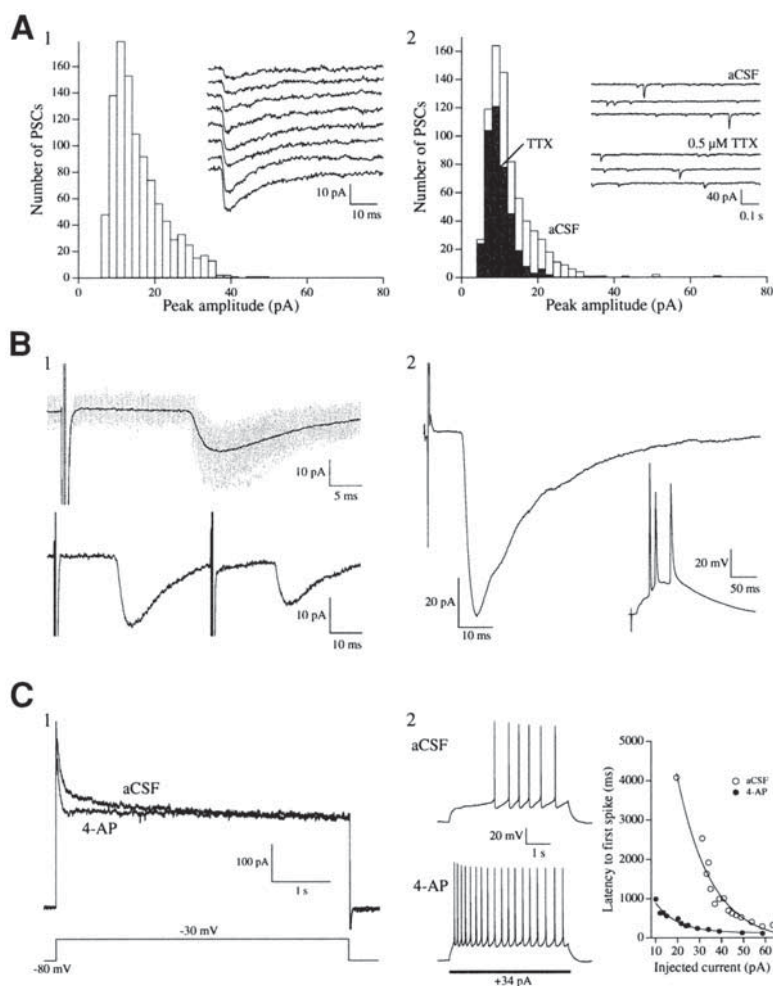


Fig. 10. Voltage-clamp analyses of perirhinal neurons. (**A1**) Spontaneous PSCs of a layer V pyramidal neuron in a brain slice prepared from an aged rat. PSCs were collected for 6 min at a holding potential of -78 mV. A total of 1032 individual PSCs were analyzed (mean amplitude of 15.9 pA). Spontaneous PSCs from this and other layer V pyramidal neurons have a positively skewed amplitude frequency distribution. Inset shows individual examples of spontaneous PSCs. (**A2**) Effects of TTX on spontaneous PSCs. Spontaneous PSCs were collected from a layer V pyramidal neuron in a brain slice prepared from a 3-wk-old rat. Notice that the

for use in brain slices prepared from both adult (Fig. 11) and aged (Fig. 12) rats (*see also* Moyer and Brown, 1998; McGann et al., 2001). Preliminary data indicate that there is little change in the percentages of LS and SS neurons in layer VI of PR between juvenile and adult rats (McGann et al., 2001). Larger-scale comparative studies will ultimately determine whether and how the physiology and morphology of perirhinal cortex changes during the aging process. One thing is certain: PR is very different from other cortical and neocortical brain regions.

3.6. Hardware and Software for Whole-Cell Patch-Clamp Studies

In earlier patch-clamp studies, an inverted microscope was used because the objectives were too large, so it was not feasible to have both the objective and patch electrode approaching the same exposed surface of the slice (Keenan et al., 1988; Dodt and Zieglgänsberger, 1990). Once narrow, high-power objectives with

(*continued*) amplitude frequency distribution was positively skewed before and after bath application of $0.5\ \mu\text{M}$ TTX (holding potential $-87\ \text{mV}$). TTX decreased both the frequency (aCSF $3.1\ \text{Hz}$; TTX $1.7\ \text{Hz}$) and amplitude (aCSF $12.5 \pm 0.2\ \text{pA}$; TTX $9.9 \pm 0.2\ \text{pA}$) of the spontaneous PSCs, by blocking the larger amplitude currents. (**B1**) Stimulation of layer I elicits long latency monosynaptic currents in layer V pyramidal neurons. Top traces are an overlay of 67 consecutive evoked currents and their average (solid current trace) in a layer V pyramidal neuron at $-92\ \text{mV}$. Bottom trace illustrates the paired pulse depression typically seen with stimulation of layer I (average of 14 consecutive evoked PSCs in the same neuron). (**B2**) Monosynaptically-evoked current in a layer V burst spiking neuron voltage-clamped at $-74\ \text{mV}$. Current trace is an average of 58 consecutive PSCs evoked by layer I stimulation. Under current-clamp conditions, the same stimulation elicited a burst of 3 action potentials. (**C1** and **C2**) Voltage- and current-clamp analyses of late spiking. Preliminary data indicate that bath application of $30\ \mu\text{M}$ 4-aminopyridine (4-AP) blocks a slowly-inactivating potassium current in layer VI late spiking cells (C1). This same concentration of 4-AP blocks the delay to first spike in late spiking neurons under current-clamp conditions (C2). The effect of 4-AP is clearly seen by a dramatic leftward and downward compression of the graph of delay to first spike as a function of current injection amplitude (D-I plot, right graph). In late spiking neurons, D-I plots in the presence of 4-AP are similar to those of regular spiking neurons in aCSF.

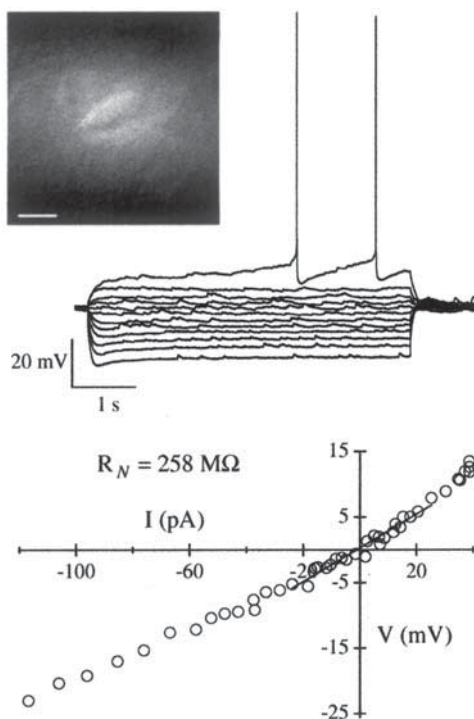


Fig. 11. Visually guided whole-cell recordings from neurons in brain slices prepared from adult rats. IR-DIC videomicrograph and neurophysiology of a layer VI nonpyramidal late spiking neuron in a 3-mo-old rat. The neuron was located $85 \mu\text{m}$ below the slice surface and would not be visible without the benefit of IR-DIC video-enhanced microscopy. This cell had a resting membrane potential of -78 mV and remained stable for 3 h.

ceramic tips and longer working distances were developed, we and others switched over to an upright configuration (Stuart et al., 1993; Brown and Jaffe, 1994; Jaffe et al., 1994). We currently use upright microscopes (Zeiss Axioskop) equipped with a variety of objectives: $2.5\times$, $40\times$ water immersion (0.75 NA), and $63\times$ water immersion (0.9 NA).

A Hamamatsu C2400 video camera with digital enhancement device are used for visualization of individual soma, dendrites,

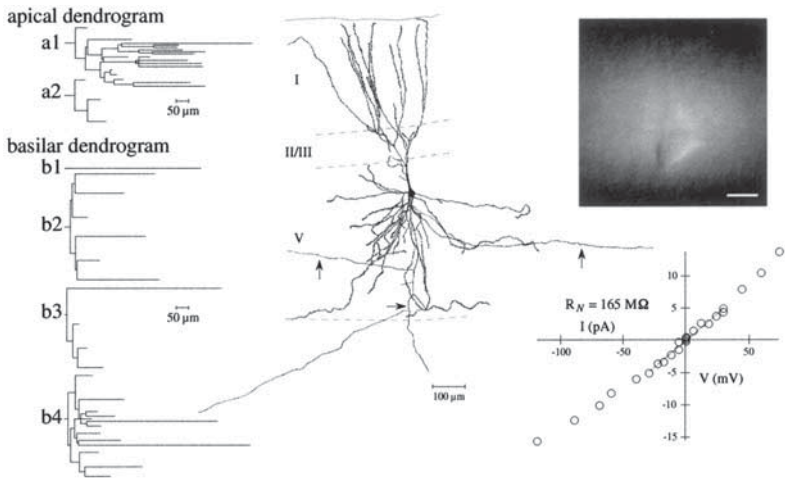


Fig. 12. Morphology and physiology of a layer V pyramidal neuron in perirhinal cortex of a an aged rat. IR-DIC video-enhanced microscopy permitted visualization and subsequent placement of the patch pipet onto the soma of this neuron which was located 76 μm below the surface of a 400 μm thick horizontal brain slice. In aged tissue, a neuron this deep below the slice surface is not visible without IR-DIC video-enhanced microscopy. Inclusion of biocytin in the patch pipet enabled subsequent analysis of neuronal morphology. Shown are the apical and basilar dendrograms obtained using a Neurolucida system (MicroBrightfield, Colchester, VT) along with the camera lucida serial reconstruction. The Neurolucida system readily enables one to obtain three-dimensional drawings of neurons that can be rotated to visualize better the extent of the dendritic and axonal processes. In analyzing morphological data, the Neurolucida system readily enables one to obtain not only dendrograms, which aid in visualizing dendritic branching, but also quantitative estimates of, for example, dendritic length, spine density, branching patterns, and soma size. In addition, morphological data can be exported for compartmental modeling in programs such as NEURON (Hines and Carnevale, 1997). The axon (indicated by arrows) from this cell descended and ramified within layers V and VI en route to the external capsule. This regular spiking neuron had a resting membrane potential of -76 mV and remained stable for 40 min. Scale bar within the IR-DIC videomicrograph is 10 μm.

or axons of neurons using infrared-filtered light (*see* Subheading 3.4.1.). Video images are either captured onto a PC using BioRad's COMOS software in video-capture mode or captured onto a Macintosh using NIH-Image and a frame grabber card. Two of our slice rigs are equipped with a BioRad confocal laser scanning microscope (CLSM). In these cases, the microscope is fixed to maintain alignment with the scanhead and the stage is moveable. Our two standard rigs have the microscope positioned on top of an XY translation device so that the scope is moveable and the stage is fixed. With either microscope configuration, the specimen stage has a circular groove cut out to allow insertion of a recording chamber and platform (Warner Instruments, Hamden, CT). A dual-channel heater controller (Warner Instruments) can be used to automatically maintain the bath temperature during our experiments. We use both hydraulic (Newport MX630, now SD Instruments, Grants Pass, OR) and motorized (MP-225, Sutter Instruments, Novato, CA; Marzhauser-Wetzlar, Germany) micro-manipulators for holding the amplifier headstage and advancing the patch pipet.

A variety of hardware and software packages for acquiring and analyzing patch-clamp data are available from different companies such as Axon Instruments or HEKA. We use IgorPro (WaveMetrics, Lake Oswego, OR) running on Macintosh G4 computers for both on-line data acquisition and off-line analysis. Although we use Macintosh computers, the program is also available for use with Windows-based PCs. We like IgorPro because of its power and flexibility—not only for handling data but also for generating publication quality figures.

Data from our patch-clamp (Axopatch 1D and 200, EPC-7) or current-clamp (Axoclamp 2A) amplifiers are acquired in IgorPro through an Instrutech ITC-16 computer interface using a PCI-16 interface card (Instrutech Corporation, Great Neck, NY). The ITC-16 uses 16 Bit A/D and D/A converters for its analog inputs and outputs with voltage ranges of +10.23 to -10.24 volts. Software drivers for allowing IgorPro to acquire data through the ITC-16 are available through Instrutech. The data are low-pass filtered and acquired at sampling rates greater than 5 times the filtering frequency to minimize distortions due to aliasing (Heinemann, 1995). After completion of an experiment, the data are stored on the hard disk and then transferred either to zip disks, optical disks, or CDs for long-term storage. All electrophysiological data are

simultaneously digitized at 44 kHz using a Neuro-Corder (Neuro Data Instruments, New York, NY) and stored on VCR tape as an additional backup.

Several devices are used to program different paradigms for electrophysiological experiments. One such device that we have been using for years is the Master-8 programmable pulse generator (AMPI, Jerusalem, Israel). It is easy to use and allows storage and rapid retrieval of eight different programs. More recently, we have programmed our IgorPro acquisition software so that it can run pre-defined experimental protocols, including the ability to vary both current injection and voltage step amplitudes. For visualizing both the current and voltage traces simultaneously, we use IgorPro. In addition, we also use either a Tektronix analog storage oscilloscope or a Gould digital oscilloscope. The digital oscilloscope has a printer so current or voltage traces of interest can be printed during an experiment and put into a laboratory notebook for reference. Several excellent reviews on setting up a patch-clamp rig can be found in the literature (e.g., see Levis and Rae, 1992; Heinemann, 1995). The application of IR-DIC video-enhanced microscopy and patch-clamping to brain slices has and is likely to continue to revolutionize studies of in vitro neurophysiology.

Acknowledgments

The authors thank John McGann for critical comments and Dr. John Bekkers for helpful discussion.

References

- Aghajanian, G. K. and Marek, G. J. (1999) Serotonin, via 5-HT_{2A} receptors, increases EPSCs in layer V pyramidal cells of prefrontal cortex by an asynchronous mode of glutamate. *Brain Res.* **825**, 161–171.
- Aghajanian, G. K. and Rasmussen, K. (1989) Intracellular studies in the facial nucleus illustrating a simple new method for obtaining viable motoneurons in adult rat brain slices. *Synapse* **3**, 331–338.
- Aitken, P. G., Breese, G. R., Dudek, F. E., et al. (1995) Preparative methods for brain slices: a discussion. *J. Neurosci. Methods* **59**, 139–149.
- Alger, B. E. and Teyler, T. J. (1976) Long-term and short-term plasticity in the CA1, CA3, and dentate regions of the rat hippocampal slice. *Brain Res.* **110**, 463–480.
- Alvarez-Leefmans, F. J. (1992) Extracellular reference electrodes, in *Practical Electrophysiological Methods: A Guide for In Vitro Studies in Vertebrate Neurobiology* (Kettenmann, H. and Grantyn, R., eds.), Wiley-Liss, New York, pp. 171–182.

- Armstrong, C. M. and Gilly, W. F. (1992) Access resistance and space clamp problems associated with whole-cell patch clamping. *Methods Enzymol.* **207**, 101–122.
- Barrionuevo, G. and Brown, T. H. (1983) Associative long-term potentiation in hippocampal slices. *Proc. Natl. Acad. Sci. USA* **80**, 7347–7351.
- Barry, P. H. (1994) JPCalc, a software package for calculating liquid junction potential corrections in patch-clamp, intracellular, epithelial and bilayer measurements and for correcting junction potential measurements. *J. Neurosci. Methods* **51**, 107–116.
- Barry, P. H. and Diamond, J. M. (1970) Junction potentials, electrode standard potentials, and other problems in interpreting electrical properties of membranes. *J. Membr. Biol.* **3**, 93–122.
- Barry, P. H. and Lynch, J. W. (1991) Liquid junction potentials and small cell effects in patch-clamp analysis. *J. Membr. Biol.* **121**, 101–117.
- Beggs, J. M., Moyer, J. R., Jr., McGann, J. P., and Brown, T. H. (2000) Prolonged synaptic integration in perirhinal cortical neurons. *J. Neurophysiol.* **83**, 3294–3298.
- Bekkers, J. M. (2000) Properties of voltage-gated potassium currents in nucleated patches from large layer 5 cortical pyramidal neurons of the rat. *J. Physiol.* **525**, 593–609.
- Benndorf, K. (1995) Low-noise recording, in *Single-Channel Recording*, 2nd ed. (Sakmann, B. and Neher, E., eds.), Plenum Press, New York, pp. 129–145.
- Berg-Johnsen, J. and Langmoen, I. A. (1992) Temperature sensitivity of thin unmyelinated fibers in rat hippocampal cortex. *Brain Res.* **576**, 319–321.
- Bezanilla, F. and Armstrong, C. M. (1977) Inactivation of the sodium channel. I. Sodium current experiments. *J. Gen. Physiol.* **70**, 549–566.
- Blanton, M. G., LoTurco, J. J., and Kriegstein, A. R. (1989) Whole cell recordings from neurons in slices of reptilian and mammalian cerebral cortex. *J. Neurosci. Methods* **30**, 203–210.
- Borst, J. G. G., Helmchen, F., and Sakmann, B. (1995) Pre- and postsynaptic whole-cell recordings in the medial nucleus of the trapezoid body of the rat. *J. Physiol.* **489**, 825–840.
- Brahma, B., Forman, R. E., Stewart, E. E., Nicholson, C., and Rice, M. E. (2000) Ascorbate inhibits edema in brain slices. *J. Neurochem.* **74**, 1263–1270.
- Brown, T. H. and Jaffe, D. B. (1994) Calcium imaging in hippocampal neurons using confocal microscopy. *Ann. NY Acad. Sci.* **747**, 313–324.
- Brown, T. H. and Keenan, C. L. (1987) Visualization of hippocampal synapses in brain slices using video microscopy. *Soc. Neurosci. Abstr.* **13**, 1515.
- Brown, T. H., Wong, R. K. S., and Prince, D. A. (1979) Spontaneous miniature synaptic potentials in hippocampal neurons. *Brain Res.* **177**, 194–199.
- Cahalan, M. and Neher, E. (1992) Patch clamp techniques: an overview. *Methods Enzymol.* **207**, 3–66.
- Carnevale, N. T., Tsai, K. Y., Claiborne, B. J., and Brown, T. H. (1997) Comparative electrotonic analysis of three classes of rat hippocampal neurons. *J. Neurophysiol.* **78**, 703–720.
- Choi, D. W. (1992) Excitotoxic cell death. *J. Neurobiol.* **23**, 1261–1276.
- Choi, D. W. (1994) Calcium and excitotoxic neuronal injury. *Ann. NY Acad. Sci.* **747**, 162–171.

- Christie, B. R., Eliot, L. S., Ito, K.-I., Miyakawa, H., and Johnston, D. (1995) Different Ca^{2+} channels in soma and dendrites of hippocampal pyramidal neurons mediate spike-induced Ca^{2+} influx. *J. Neurophysiol.* **73**, 2553–2557.
- Coleman, P. A. and Miller, R. F. (1989) Measurement of passive membrane properties with whole-cell recordings from neurons in the intact amphibian retina. *J. Neurophysiol.* **61**, 218–230.
- Davson, H., Welch, K., and Segal, M. B. (1987) *The Physiology and Pathophysiology of the Cerebrospinal Fluid*, Churchill Livingstone, New York, pp. 15–33.
- Desagher, S., Glowinski, J., and Prémont, J. (1997) Pyruvate protects neurons against hydrogen peroxide-induced toxicity. *J. Neurosci.* **17**, 9060–9067.
- Deuchars, J. and Thomson, A. M. (1996) CA1 pyramid-pyramid connections in rat hippocampus in vitro: dual intracellular recordings with biocytin filling. *Neuroscience* **74**, 1009–1018.
- Deuchars, J., West, D. C., and Thomson, A. M. (1994) Relationships between morphology and physiology of pyramid-pyramid single axon connections in rat neocortex in vitro. *J. Physiol.* **478**, 423–435.
- Doty, H.-U. and Zieglgänsberger, W. (1990) Visualizing unstained neurons in living brain slices by infrared DIC-videomicroscopy. *Brain Res.* **537**, 333–336.
- Duffy, C. J. and Teyler, T. J. (1975) A simple tissue slicer. *Physiol. Behav.* **14**, 525–526.
- Edwards, F. A. and Konnerth, A. (1992) Patch-clamping cells in sliced tissue preparations. *Methods Enzymol.* **207**, 208–222.
- Edwards, F. A., Konnerth, A., Sakmann, B., and Takahashi, T. (1989) A thin slice preparation for patch clamp recordings from neurones of the mammalian central nervous system. *Pflügers Arch.* **414**, 600–612.
- Faulkner, B. and Brown, T. H. (1999) Morphology and physiology of neurons in the rat perirhinal-lateral amygdala area. *J. Comp. Neurol.* **411**, 613–642.
- Feig, S. and Lipton, P. (1990) *N*-methyl-D-aspartate receptor activation and Ca^{2+} account for poor pyramidal cell structure in hippocampal slices. *J. Neurochem.* **55**, 473–483.
- Forscher, P. and Oxford, G. S. (1985) Modulation of calcium channels by norepinephrine in internally dialyzed avian sensory neurons. *J. Gen. Physiol.* **85**, 743–763.
- Frazier, D. T., Narahashi, T., and Yamada, M. (1970) The site of action and active form of local anesthetics. *J. Pharmacol. Exp. Therap.* **171**, 45–51.
- Galarreta, M. and Hestrin, S. (1998) Frequency-dependent synaptic depression and the balance of excitation and inhibition in the neocortex. *Nature Neurosci.* **1**, 587–594.
- Geddes, L. A. (1972) *Electrodes and the Measurement of Bioelectric Events*. John Wiley & Sons, New York.
- Gibson, H. L. (1978) *Photography by Infrared*. Wiley, New York, p. 545.
- Gibson, J. R., Beierlein, M., and Connors, B. W. (1999) Two networks of electrically coupled inhibitory neurons in neocortex. *Nature* **402**, 75–79.
- Gupta, A., Wang, Y., and Markram, H. (2000) Organizing principles for a diversity of GABAergic interneurons and synapses in the neocortex. *Science* **287**, 273–278.

- Heinemann, S. H. (1995) Guide to data acquisition and analysis, in *Single-Channel Recording* (Sakmann, B. and Neher, E., eds.), Plenum Press, New York, pp. 53–91.
- Hestrin, S. and Armstrong, W. E. (1996) Morphology and physiology of cortical neurons in layer I. *J. Neurosci.* **16**, 5290–5300.
- Hille, B. (2001) *Ion Channels of Excitable Membranes*, 3rd ed. Sinauer Associates, Sunderland, MA.
- Hines, M. L. and Carnevale, N. T. (1997) The NEURON simulation environment. *Neural. Comput.* **9**, 1179–1209.
- Hoffman, D. A. and Johnston, D. (1998) Downregulation of transient K⁺ channels in dendrites of hippocampal CA1 pyramidal neurons by activation of PKA and PKC. *J. Neurosci.* **18**, 3521–3528.
- Hoffman, D. A., Magee, J. C., Colbert, C. M., and Johnston, D. (1997) K⁺ channel regulation of signal propagation in dendrites of hippocampal pyramidal neurons. *Nature* **387**, 869–875.
- Ives, J. G. D. and Janz, G. J. (1961) *Reference Electrodes. Theory and Practice*. Academic Press, New York.
- Jaffe, D. B. and Brown, T. H. (1994a) Confocal imaging of dendritic Ca²⁺ transients in hippocampal brain slices during simultaneous current- and voltage-clamp recording. *Microsc. Res. Techn.* **29**, 279–289.
- Jaffe, D. B. and Brown, T. H. (1994b) Metabotropic glutamate receptor activation induces calcium waves within hippocampal dendrites. *J. Neurophysiol.* **72**, 471–474.
- Jaffe, D. B. and Brown, T. H. (1997) Calcium dynamics in thorny excrescences of CA3 pyramidal neurons. *J. Neurophysiol.* **78**, 10–18.
- Jaffe, D. B., Fisher, S. A., and Brown, T. H. (1994) Confocal laser scanning microscopy reveals voltage-gated calcium signals within hippocampal dendritic spines. *J. Neurobiol.* **25**, 220–233.
- Jahromi, B. S., Zhang, L., Carlen, P. L., and Pennefather, P. (1999) Differential time-course of slow afterhyperpolarizations and associated Ca²⁺ transients in rat CA1 pyramidal neurons: further dissociation by Ca²⁺ buffer. *Neuroscience* **88**, 719–726.
- Janz, G. J. and Ives, J. G. D. (1968) Silver, silver chloride electrodes. *Ann. NY Acad. Sci.* **148**, 210–221.
- Johnston, D., Hoffman, D. A., Magee, J. C., Poolos, N. P., Watanabe, S., Colbert, C. M., and Migliore, M. (2000) Dendritic potassium channels in hippocampal pyramidal neurons. *J. Physiol.* **525**, 75–81.
- Johnston, D. and Wu, S. M.-S. (1995) *Foundations of Cellular Neurophysiology*, MIT Press, Cambridge, MA.
- Jonas, P., Major, G., and Sakmann, B. (1993) Quantal components of unitary EPSCs at the mossy fibre synapse on CA3 pyramidal cells of rat hippocampus. *J. Physiol.* **472**, 615–663.
- Jung, H.-Y., Mickus, T., and Spruston, N. (1997) Prolonged sodium channel inactivation contributes to dendritic action potential attenuation in hippocampal pyramidal neurons. *J. Neurosci.* **17**, 6639–6646.
- Jung, H.-Y., Staff, N. P., and Spruston, N. (2001) Action potential bursting in subicular pyramidal neurons is driven by a calcium tail current. *J. Neurosci.* **21**, 3312–3321.
- Kay, A. R. (1992) An intracellular medium formulary. *J. Neurosci. Methods* **44**, 91–100.

- Keenan, C. L., Chapman, P. F., Chang, V. C., and Brown, T. H. (1988) Video-microscopy of acute brain slices from amygdala and hippocampus. *Brain Res. Bull.* **21**, 373–383.
- Keller, J. N., et al. (1998) Mitochondrial manganese superoxide dismutase prevents neural apoptosis and reduces ischemic brain injury: suppression of peroxynitrite production, lipid peroxidation, and mitochondrial dysfunction. *J. Neurosci.* **18**, 687–697.
- Kelso, S. R., Ganong, A. H., and Brown, T. H. (1986) Hebbian synapses in hippocampus. *Proc. Natl. Acad. Sci. USA* **83**, 5326–5330.
- Korngreen, A. and Sakmann, B. (2000) Voltage-gated K^+ channels in layer 5 neocortical pyramidal neurons from young rats: subtypes and gradients. *J. Physiol.* **525**, 621–639.
- Kovachich, G. B. and Mishra, O. P. (1980) Lipid peroxidation in rat brain cortical slices as measured by the thiobarbituric acid test. *J. Neurochem.* **35**, 1449–1452.
- Kovachich, G. B. and Mishra, O. P. (1983) The effects of ascorbic acid on malonaldehyde formation, K^+ , Na^+ and water content of brain slices. *Exp. Brain Res.* **50**, 62–68.
- Landfield, P. W. and Pitler, T. A. (1984) Prolonged Ca^{2+} -dependent afterhyperpolarizations in hippocampal neurons of aged rats. *Science* **226**, 1089–1092.
- Levis, R. A. and Rae, J. L. (1992) Constructing a patch clamp setup. *Methods Enzymol.* **207**, 14–66.
- Li, C.-L. and McIlwain, H. (1957) Maintenance of resting membrane potentials in slices of mammalian cerebral cortex and other tissues *in vitro*. *J. Physiol.* **139**, 178–190.
- Lipton, P., et al. (1995) Making the best of brain slices: comparing preparative methods. *J. Neurosci. Methods* **59**, 151–156.
- Llinás, R. and Sugimori, M. (1980) Electrophysiological properties of *in vitro* Purkinje cell somata in mammalian cerebellar slices. *J. Physiol. (London)* **305**, 171–195.
- MacVicar, B. A. (1984) Infrared video microscopy to visualize neurons in the *in vitro* brain slice preparation. *J. Neurosci. Methods* **12**, 133–149.
- Magee, J. C., Avery, R. B., Christie, B. R., and Johnston, D. (1996) Dihydropyridine-sensitive, voltage-gated Ca^{2+} channels contribute to the resting intracellular Ca^{2+} concentration of hippocampal CA1 pyramidal neurons. *J. Neurophysiol.* **76**, 3460–3470.
- Magee, J. C. and Johnston, D. (1995) Synaptic activation of voltage-gated channels in the dendrites of hippocampal pyramidal neurons. *Science* **268**, 301–304.
- Magee, J. C. and Johnston, D. (1997) A synaptically controlled, associative signal for Hebbian plasticity in hippocampal neurons. *Science* **275**, 209–213.
- Magistretti, J., Mantegazza, M., Guatteo, E., and Wanke, E. (1996) Action potentials recorded with patch-clamp amplifiers: are they genuine? *TINS* **19**, 530–534.
- Mainen, Z. F., Carnevale, N. T., Zador, A. M., Claiborne, B. J., and Brown, T. H. (1996) Electrotonic architecture of hippocampal CA1 pyramidal neurons based on three-dimensional reconstructions. *J. Neurophysiol.* **76**, 1904–1923.
- Mainen, Z. F. and Sejnowski, T. J. (1996) Influence of dendritic structure on firing pattern in model neocortical neurons. *Nature* **382**, 363–366.
- Markram, H., Lubke, J., Frotscher, M., Roth, A., and Sakmann, B. (1997a) Physiology and anatomy of synaptic connections between thick tufted pyramidal neurones in the developing rat neocortex. *J. Physiol. (London)* **500**, 409–440.

- Markram, H., Lübke, J., Frotscher, M., and Sakmann, B. (1997b) Regulation of synaptic efficacy by coincidence of postsynaptic APs and EPSPs. *Science* **275**, 213–215.
- Martina, M., Schultz, J. H., Ehmke, H., Monyer, H., and Jonas, P. (1998) Functional and molecular differences between voltage-gated K⁺ channels of fast-spiking interneurons and pyramidal neurons of rat hippocampus. *J. Neurosci.* **18**, 1811–1825.
- Marty A. and Neher, E. (1995) Tight-seal whole-cell recording, in *Single-Channel Recording*, 2nd ed. (Sakmann, B. and Neher, E., eds.), Plenum, New York, pp. 31–52.
- Mattson, M. P. (1998) Modification of ion homeostasis by lipid peroxidation: roles in neuronal degeneration and adaptive plasticity. *TINS* **21**, 53–57.
- McGann, J. P. and Brown, T. H. (2000) Fear conditioning model predicts key temporal aspects of conditioned response production. *Psychobiology* **28**, 303–313.
- McGann, J. P., Moyer, J. R., Jr., and Brown, T. H. (2001) Predominance of late-spiking neurons in layer VI of rat perirhinal cortex. *J. Neurosci.* **21**, 4969–4976.
- McKernan, M. G. and Shinnick-Gallagher, P. (1997) Fear conditioning induces a lasting potentiation of synaptic currents *in vitro*. *Nature* **390**, 607–611.
- Moyer, J. R., Jr. and Brown, T. H. (1998) Methods for whole-cell recording from visually preselected neurons of perirhinal cortex in brain slices from young and aging rats. *J. Neurosci. Methods* **86**, 35–54.
- Moyer, J. R., Jr. and Disterhoft, J. F. (1994) Nimodipine decreases calcium action potentials in an age- and concentration-dependent manner. *Hippocampus* **4**, 11–18.
- Moyer, J. R., Jr., McGann, J. P., and Brown, T. H. (2000a) Analysis of late spiking in rat perirhinal cortex. *Soc. Neurosci. Abstr.* **26**, 1628.
- Moyer, J. R., Jr., McNay, E. C., and Brown, T. H. (2002) Three classes of pyramidal cells in layer V of rat perirhinal cortex. *Hippocampus* **12**, 218–234.
- Moyer, J. R., Jr., Power, J. M., Thompson, L. T., and Disterhoft, J. F. (2000b) Increased excitability of aged rabbit CA1 neurons after trace eyeblink conditioning. *J. Neurosci.* **20**, 5476–5482.
- Moyer, J. R., Jr., Thompson, L. T., Black, J. P., and Disterhoft, J. F. (1992) Nimodipine increases excitability of rabbit CA1 pyramidal neurons in an age- and concentration-dependent manner. *J. Neurophysiol.* **68**, 2100–2109.
- Moyer, J. R., Jr., Thompson, L. T., and Disterhoft, J. F. (1996) Trace eyeblink conditioning increases CA1 excitability in a transient and learning-specific manner. *J. Neurosci.* **16**, 5536–5546.
- Narahashi, T. (1974) Chemicals as tools in the study of excitable membranes. *Physiol. Rev.* **54**, 813–889.
- Narahashi, T., Moore, J. W., and Scott, W. R. (1964) Tetrodotoxin blockage of sodium conductance increase in lobster giant axons. *J. Gen. Physiol.* **47**, 965–974.
- Neher, E. (1992) Correction for liquid junction potentials in patch clamp experiments. *Methods Enzymol.* **207**, 123–131.
- Neher, E. and Sakmann, B. (1976) Single-channel currents recorded from membrane of denervated frog muscle fibres. *Nature* **260**, 799–802.
- Newman, G. C., Qi, H., Hospod, F. E., and Grundmann, K. (1992) Preservation of hippocampal brain slices with *in vivo* or *in vitro* hypothermia. *Brain Res.* **575**, 159–163.

- Ng, B. and Barry, P. H. (1995) The measurement of ionic conductivities and mobilities of certain less common organic ions needed for junction potential corrections in electrophysiology. *J. Neurosci. Methods* **56**, 37–41.
- Nisenbaum, E. S., Xu, Z. C., and Wilson, C. J. (1994) Contribution of a slowly inactivating potassium current to the transition to firing of neostriatal spiny projection neurons. *J. Neurophysiol.* **71**, 1174–1189.
- Okada, Y., Tanimoto, M., and Yoneda, K. (1988) The protective effect of hypothermia on reversibility in the neuronal function of the hippocampal slice during long lasting anoxia. *Neurosci. Lett.* **84**, 277–282.
- Paxinos, G. and Watson, C. (1998) *The Rat Brain in Stereotaxic Coordinates*, 3rd ed. Academic Press, San Diego.
- Penner, R. (1995) A practical guide to patch clamping, in *Single-Channel Recording*, 2nd ed. (Sakmann, B. and Neher, E., eds.), Plenum Press, New York, pp. 3–30.
- Peterlin, Z. A., Kozloski, J., Mao, B.-Q., Tsiola, A., and Yuste, R. (2000) Optical probing of neuronal circuits with calcium indicators. *Proc. Natl. Acad. Sci. USA* **97**, 3619–3624.
- Power, J. M., Oh, M. M., and Disterhoft, J. F. (2001) Metrifonate decreases sI_{AHP} in CA1 pyramidal neurons in vitro. *J. Neurophysiol.* **85**, 319–322.
- Reyes, A., Lujan, R., Rozov, A., Burnashev, N., Somogyi, P., and Sakmann, B. (1998) Target-cell-specific facilitation and depression in neocortical circuits. *Nature Neurosci.* **1**, 279–284.
- Rice, M. E. (1999) Use of ascorbate in the preparation and maintenance of brain slices. *Methods* **18**, 144–149.
- Rice, M. E., Pérez-Pinzón, M. A., and Lee, E. J. K. (1994) Ascorbic acid, but not glutathione, is taken up by brain slices and preserves cell morphology. *J. Neurophysiol.* **71**, 1591–1596.
- Rothman, S. M. (1985) The neurotoxicity of excitatory amino acids is produced by passive chloride influx. *J. Neurosci.* **5**, 1483–1489.
- Saeed, D., Goetzman, B. W., and Gospe, S. M., Jr. (1993) Brain injury and protective effects of hypothermia using triphenyltetrazolium chloride in neonatal rat. *Pediatr. Neurol.* **9**, 263–267.
- Sakmann, B. and Neher, E. (1995) Geometric parameters of pipettes and membrane patches, in *Single-Channel Recording*, 2nd ed. (Sakmann, B. and Neher, E., eds.), Plenum Press, New York, pp. 637–650.
- Sakmann, B. and Stuart, G. (1995) Patch-pipette recordings from the soma, dendrites, and axon of neurons in brain slices, in *Single-Channel Recording*, 2nd ed. (Sakmann, B. and Neher, E., eds.), Plenum Press, New York, pp. 199–211.
- Sather, W., Dieudonne, S., MacDonald, J. F., and Ascher, P. (1992) Activation and desensitization of N-methyl-D-aspartate receptors in nucleated outside-out patches from mouse neurones. *J. Physiol.* **450**, 643–672.
- Scharfman, H. E. (1996) Hyperexcitability of entorhinal cortex and hippocampus after application of aminooxyacetic acid (AOAA) to layer III of the rat medial entorhinal cortex in vitro. *J. Neurophysiol.* **76**, 2986–3001.
- Schurr, A., Payne, R. S., Miller, J. J., and Rigor, B. M. (1997a) Brain lactate is an obligatory aerobic energy substrate for functional recovery after hypoxia: further in vitro validation. *J. Neurochem.* **69**, 423–426.
- Schurr, A., Payne, R. S., Miller, J. J., and Rigor, B. M. (1997b) Brain lactate, not glucose, fuels the recovery of synaptic function from hypoxia upon reoxygenation: an in vitro study. *Brain Res.* **744**, 105–111.

- Schwartzkroin, P. A. (1975) Characteristics of CA1 neurons recorded intracellularly in the hippocampal in vitro slice preparation. *Brain Res.* **85**, 423–436.
- Schwartzkroin, P. A. and Andersen, P. (1975) Glutamic acid sensitivity of dendrites in hippocampal slices *in vitro*, in *Advances in Neurology* (Kreutzberg, G. W., ed.), Raven Press, New York, pp. 45–51.
- Sharp, P. E. and La Regina, M. C. (eds.) (1998) The Laboratory Rat. *The Laboratory Animal Pocket Reference Series* (Suckow, M. A., ed.), CRC Press, New York, p. 13.
- Sherman-Gold, R. (ed.) (1993) *The Axon Guide*. Axon Instruments. Foster City, CA.
- Sigworth, F. J. (1995) Design of the EPC-9, a computer-controlled patch-clamp amplifier. 1. Hardware. *J. Neurosci. Methods* **56**, 195–202.
- Sigworth, F. J., Aftolter, H., and Neher, E. (1995) Design of the EPC-9, a computer-controlled patch-clamp amplifier. 2. Software. *J. Neurosci. Methods* **56**, 203–215.
- Sigworth, F. J. and Zhou, J. (1992) Analysis of nonstationary single-channel currents. *Methods Enzymol.* **207**, 746–762.
- Skrede, K. K. and Westgaard, R. H. (1971) The transverse hippocampal slice: a well-defined cortical structure maintained in vitro. *Brain Res.* **35**, 589–593.
- Spruston, N., Jaffe, D., Williams, S. H., and Johnston, D. (1993) Voltage- and space-clamp errors associated with the measurement of electrotonically remote synaptic events. *J. Neurophysiol.* **70**, 781–802.
- Staley, K. J., Otis, T. S., and Mody, I. (1992) Membrane properties of dentate gyrus granule cells: comparison of sharp microelectrode and whole-cell recordings. *J. Neurophysiol.* **67**, 1346–1358.
- Stuart, G., Schiller, J., and Sakmann, B. (1997a) Action potential initiation and propagation in rat neocortical pyramidal neurons. *J. Physiol. (London)* **505**, 617–632.
- Stuart, G., Spruston, N., Sakmann, B., and Hausser, M. (1997b) Action potential initiation and backpropagation in neurons of the mammalian CNS. *TINS* **20**, 125–131.
- Stuart, G. J., Dodt, H.-U., and Sakmann, B. (1993) Patch clamp recordings from the soma and dendrites of neurons in brain slices using infrared video microscopy. *Pflügers Arch.* **423**, 511–518.
- Stuart, G. J. and Sakmann, B. (1994) Active propagation of somatic action potentials into neocortical pyramidal cell dendrites. *Nature* **367**, 69–72.
- Sucher, N. J., Deitcher, D. L., Baro, D. J., Warrick, R. M. H., and Guenther, E. (2000) Genes and channels: patch/voltage-clamp analysis and single-cell RT-PCR. *Cell Tissue Res.* **302**, 295–307.
- Takahashi, T. (1978) Intracellular recording from visually identified motoneurons in rat spinal cord slices. *Proc. R. Soc. Lond. (B)* **202**, 417–421.
- Tarczy-Hornoch, K., Martin, K. A. C., Jack, J. J. B., and Stratford, K. J. (1998) Synaptic interactions between smooth and spiny neurones in layer 4 of cat visual cortex *in vitro*. *J. Physiol. (London)* **508**, 351–363.
- Thibault, O., Porter, N. M., Chen, K.-C., Blalock, E. M., Kaminker, P. G., Clodfelter, G. V., et al. (1998) Calcium dysregulation in neuronal aging and Alzheimer's disease: history and new directions. *Cell Calc.* **24**, 417–433.
- Thompson, L. T., Moyer, J. R., Jr., and Disterhoft, J. F. (1996) Transient changes in excitability of rabbit CA3 neurons with a time-course appropriate to support memory consolidation. *J. Neurophysiol.* **76**, 1836–1849.

- Thomson, A. M. and Deuchars, J. (1997) Synaptic interactions in neocortical local circuits: dual intracellular recordings *in vitro*. *Cerebr. Cortex* **7**, 510–522.
- Thomson, A. M. and West, D. C. (1993) Fluctuations in pyramid-pyramid excitatory postsynaptic potentials modified by presynaptic firing pattern and postsynaptic membrane potential using paired intracellular recordings in rat neocortex. *Neuroscience* **54**, 329–346.
- Tieu, K. H., Keidel, A. L., McGann, J. P., Faulkner, B., and Brown, T. H. (1999) Perirhinal-amygdala circuit-level computational model of temporal encoding in fear conditioning. *Psychobiology* **27**, 1–25.
- Trussell, L. O. and Jackson, M. B. (1987) Dependence of an adenosine-activated potassium current on a GTP-binding protein in mammalian central neurons. *J. Neurosci.* **7**, 3306–3316.
- Tsien, R. Y. (1980) New calcium indicators and buffers with high selectivity against magnesium and protons: design, synthesis, and properties of prototype structures. *Biochemistry* **19**, 2396–2404.
- Watson, G. B., Lopez, O. T., Charles, V. D., and Lanthorn, T. H. (1994) Assessment of long-term effects of transient anoxia on metabolic activity of rat hippocampal slices using triphenyltetrazolium chloride. *J. Neurosci. Methods* **53**, 203–208.
- White, J. A., Sekar, N. S., and Kay, A. R. (1995) Errors in persistent inward currents generated by space-clamp errors: a modeling study. *J. Neurophysiol.* **73**, 2369–2377.
- Williams, S. and Johnston, D. (1988) Muscarinic depression of long-term potentiation in CA3 hippocampal neurons. *Science* **242**, 84–87.
- Xiang, Z. and Brown, T. H. (1998) Complex synaptic current waveforms evoked in hippocampal pyramidal neurons by extracellular stimulation of dentate gyrus. *J. Neurophysiol.* **79**, 2475–2484.
- Xiang, Z., Greenwood, A. C., Kairiss, E. W., and Brown, T. H. (1994) Quantal mechanism of long-term potentiation in hippocampal mossy-fiber synapses. *J. Neurophysiol.* **71**, 2552–2556.
- Yamamoto, C. (1975) Recording of electrical activity from microscopically identified neurons of the mammalian brain. *Experientia* **31**, 309–311.
- Yamamoto, C. and Chujo, T. (1978) Visualization of central neurons and recording of action potentials. *Exp. Brain Res.* **31**, 299–301.
- Yamamoto, C. and McIlwain, H. (1966) Electrical activities in thin sections from the mammalian brain maintained in chemically-defined media *in vitro*. *J. Neurochem.* **13**, 1333–1343.
- Yeckel, M. F., Kapur, A., and Johnston, D. (1999) Multiple forms of LTP in hippocampal CA3 neurons use a common postsynaptic mechanism. *Nature Neurosci.* **2**, 625–633.
- Yuste, R. and Denk, W. (1995) Dendritic spines as basic functional units of neuronal integration. *Nature* **375**, 682–684.
- Zhang, L., Weiner, J. L., Valiante, T. A., Velumian, A. A., Watson, P. L., Jahromi, S. S., et al. (1994) Whole-cell recording of the Ca^{2+} -dependent slow afterhyperpolarization in hippocampal neurones: effects of internally applied anions. *Pflügers Arch.* **426**, 247–253.
- Zilles, K. and Wree, A. (1995) Cortex: Areal and laminar structure, in *The Rat Nervous System*, 2nd ed. (Paxinos, G., ed.), Academic Press, San Diego, pp. 649–685.

6

Perforated Patch-Clamp Technique

Raimondo D'Ambrosio

1. Introduction

The great advantage of patch clamp in cellular physiology is that it allows sensitive and reliable analysis of the electrical activity of cell membranes at the molecular level. Whole cell is the most popular variant of the patch-clamp technique. It is easy to obtain and it allows the use of intra- and extra-cellular recording solutions particularly devised to isolate the ionic membrane conductance of interest, or to intracellularly apply modulators or drugs. Patch clamp is therefore a very powerful technique, but the study of intracellular signaling—and the assessment of its impact on cellular electricity—requires the experimenter to perform recordings from virtually intact cells.

Unfortunately, classical whole-cell patch clamp significantly affects recorded cells and has, thus, several drawbacks that often bear consequences in certain type of experiments. One of the major problems is that the rupture of the membrane patch under the pipet's tip leads to the dialysis of the intracellular compartment. The pipet solution has a volume much greater than the one of the patched cell, therefore it may wash out known and unknown cytoplasmic components that may be required for signaling and ion-channel activity and modulation. The progressive wash-out of necessary intracellular components has been considered responsible for the time-dependent changes in electrophysiological responses of cellular responses that has been typically associated with classical whole cell recordings. The time-dependency decay of a variety of physiological cellular responses and membrane ionic currents have been

From: *Neuromethods*, Vol. 35: *Patch-Clamp Analysis: Advanced Techniques*
Edited by: W. Walz, A. A. Boulton, and G. B. Baker @ Humana Press Inc., Totowa, NJ

termed "run down." Not uncommon is also the opposite phenomenon: a progressive increase in the electrophysiological parameter studied, termed "run up" (i.e., Duchatelle-Gourdon et al., 1991).

Another problem also is related to the virtually infinite volume of the pipet solution in respect to the cellular volume, and is intrinsic to the classic ruptured patch whole-cell recordings. Trans-membrane ionic fluxes cannot change the intracellular ionic concentrations as they would do under physiological conditions, and that would otherwise affect the recorded current itself.

Another drawback of the classical patch-clamp technique is often overlooked. The suction applied to the interior of the pipet in order to break the membrane patch stretches the underlying cytoskeleton anchored to it. Since ion-channel activity has been shown to depend on their interaction with the cytoskeleton (Johnson and Byerly, 1993, 1994; Mazzanti et al., 1996), this stretch may alter ion channel kinetics, as well as the activity of other membrane proteins anchored to it.

2. Perforated Patch Principles

The necessity to preserve cellular integrity during whole cell recordings prompted the development of a less invasive version of the patch clamp technique: the perforated patch recording (Fig. 1). The invention of the perforated patch may be ascribed to Lindau and Fernandez (1986). When studying the electrophysiological properties of degranulating mast cells, these investigators found that patch-clamped mast cells rapidly lost the capability to respond to external stimuli, and concluded that essential cytoplasmic components were being washed out. They developed a new approach in which the membrane patch under the pipet was not disrupted by suction but permeabilized so as to prevent the diffusion of large molecules out of the cell. ATP, which causes an increase in conductance of mast cells, was used to render the patch membrane permeable to ions. However, in contrast to standard whole-cell recording where the access resistance between pipet and cell is 1–10 M Ω , ATP only reduced the access resistance to 100–5,000 M Ω . For this reason the technique was named "slow-whole cell." An improvement of the slow whole-cell technique was brought about by the use of specific perforating antibiotics, such as nystatin, that allow electrical continuity between cell cytoplasm and electrode, while

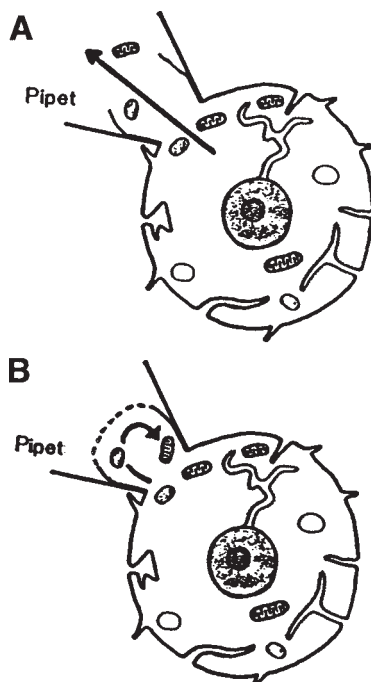


Fig. 1. Schematic representation of the fast and slow whole-cell configurations. (A) During standard whole cell recordings, the patch under the pipet is ruptured, and diffusion of cytoplasmic constituents out of the cell volume (<1 pL) into the large volume of the pipet (~ 25 μ L) occurs. (B) In the slow whole-cell configuration, the membrane patch under the pipet is not ruptured but permeabilized by ATP, therefore preventing the dialysis of the cell cytoplasm. Reproduced with permission from Lindau and Fernandez (1986).

blocking the dialysis of the cellular compartment (Horn and Marty, 1988; Korn and Horn, 1989; Fig. 2). Antibiotics such as nystatin or amphotericin B form ion channels in cell membranes that are permeable to monovalent ions, while cations such as Mg^{2+} or Ca^{2+} do not permeate (Horn and Marty, 1988; Rae et al., 1991). Furthermore, no large molecules can permeate through these channels, therefore no wash out of cellular components occurs. Nystatin has negligible

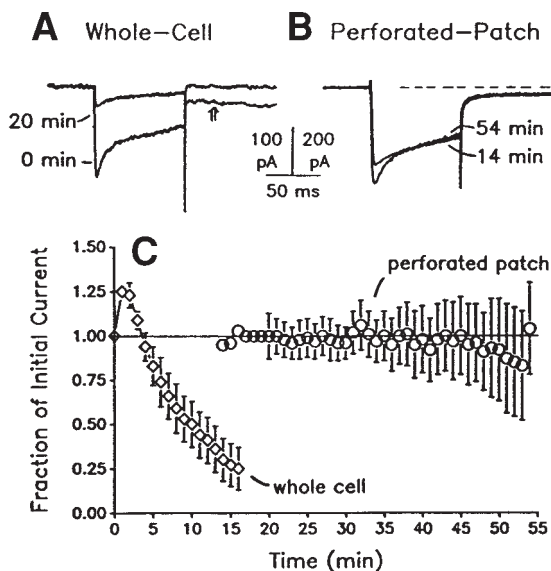


Fig. 2. Perforated patch recordings prevent run-down of membrane Calcium currents (Korn and Horn, 1989). High voltage-activated (HVA) Ca^{2+} -currents were recorded from GH_3 pituitary cells using standard whole-cell and perforated patch techniques. Ca^{2+} currents were elicited every 15 s by 100-ms voltage steps to 0 mV from a holding potential of -70 mV. (A) Standard whole-cell recordings of HVA Ca^{2+} currents elicited 15 s and 20 min after rupture of the membrane patch. (B) Perforated patch-clamp recordings of HVA Ca^{2+} currents elicited 14 and 54 min after gaining electrical access to cell. The dashed line indicates zero current level. (C) Time course of the Ca^{2+} current run-down in a population of cells recorded with each method. Amplitudes in each cell were normalized to the first current recorded. Whole-cell currents declined to $25 \pm 13\%$ (mean \pm SEM, $n = 8$) of the initial current at $t = 10$ min. Perforated patch data represent mean \pm SEM for four to five cells at $t = 23$ – 53 min, one to four cells at other times. Mean $R_s = 2.18 \pm 0.22 \text{ M}\Omega$ in whole-cell recordings, $14.9 \pm 2.1 \text{ M}\Omega$ in perforated patch recordings. Reproduced with permission from Korn and Horn (1989).

lateral diffusion away from the membrane patch, through the rim of the interface between cell membrane and pipet's glass (Horn, 1991). Thus, little or no contamination of cell membrane beyond the patch seal is expected. In addition, the perforated patch pre-

sents reasonably a low-access resistance thus allowing good voltage-clamp recordings in spite of the integrity of the membrane patch under the pipet (Horn and Marty, 1988).

2.1. Polyene Antibiotics

The polyene antibiotics are a group of antibiotics produced by *Streptomyces* bacteria (Vandeputte et al., 1956). Their activity against fungi derives from their ability to perforate cell membranes, thus making the fungi permeable to water and electrolytes. These compounds appear to be active predominantly on sterol-containing membranes and little on cholesterol-containing membranes (Lampen, 1966). This unique property of polyene antibiotics may explain why they can be effective therapeutically also in the treatment of internal fungal infections. There is a concentration range within which polyene antibiotics do not kill cholesterol-containing mammalian cells, but are fatal to ergosterol-containing fungi (Cass et al., 1970). The polyene antibiotics contain a large polyhydrophylic lactone ring, and are amphipathic which allows them to form aqueous pores embedded in the cell membrane. Nystatin and amphotericin-B have similar molecular structure, and are the polyene antibiotics most commonly used in perforated patch recordings. Nystatin was first used to perforate the patch of membrane obtain electrical continuity between cell cytoplasm and pipet solution while blocking the dialysis of the cellular compartment by the pipet (Horn and Marty, 1988). Nystatin diffuses in the lipidic bilayer in a receptor-independent manner, and forms small pores that are permeable to monovalent ions, water and small hydrophylic solutes, but impermeable to larger molecule. Cass and Dalmark (1973) described the ion permeability of nystatin-perforated human erythrocytes being as Li^+ , Na^+ , K^+ , choline, H_3O^+ , and Cl^- , but no permeability was found for Mg^{2+} , Ca^{2+} , and SO_4^{2-} . Also larger molecules like NADP^+ , glucose, sucrose, or enzymes do not permeate. With large tip electrodes, the access resistance can be made as low as 5–10 M Ω . This access resistance is low enough to allow for voltage clamp as well as current clamp experiments. It has been demonstrated that polyene antibiotics do not diffuse laterally from the patch under the pipet to the rest of the cell membrane (Horn, 1991). Rae and colleagues introduced the use of amphotericin B, as an alternative to nystatin for perforated patch (Rae et al., 1991). Although amphotericin B is similar to nystatin, they

showed that lower access resistance was achievable by using Amphotericin B. In fact, amphotericin B forms cation conductances at a lower concentration (Marty and Finkestein, 1975). It appears that amphotericin B form an aqueous pore that is larger than the one formed by nystatin. In fact, glucose permeates through amphotericin B permeabilized membranes.

2.2. Gramicidin

Since the polyene antibiotics are permeable to both monovalent cations and anions their use in perforated patch results in the equilibrium of such ions between the intracellular and pipet compartments. This results in the disruption of the physiological electrochemical gradient for Cl^- . The equilibrium of intracellular $[\text{Cl}^-]$ with the pipet's electrolytic solution is not ideal since many cellular physiological phenomena depend on a proper electrochemical gradient for Cl^- , including GABA_A -mediated inhibition. In addition it has been shown that $[\text{Cl}^-]$ directly modulates the activity of ion channels, such as outward K^+ currents in glial cells (Bekar et al., 1999; Bekar and Walz, 1999), and GABA_B currents in neurons (Lopantsev and Schwartzkroin, 1999). An additional problem associated with the disruption of the electrochemical gradient for Cl^- during perforated patch based on polyene antibiotics is the development of Donnan forces. Since Cl^- can freely diffuse in both directions across the polyene-formed channels while larger cellular anions cannot, Donnan forces may arise when $[\text{Cl}^-]$ pipet is different from the intracellular $[\text{Cl}^-]$. The consequent movement of ions and water may damage the cell, alter its electrophysiological response, or simply introduce a junctional potential across pipet and cell that can be of several millivolts, depending on the recording conditions, and hinder the voltage-clamp analysis (Horn and Marty, 1988; Akaike and Harata, 1994). Because Cl^- has such a complex impact in cellular physiology, the need to study cellular electrophysiology with intact $[\text{Cl}^-]$ in arose. This became possible thanks to the development of a new approach to perforated patch that exploited the antibiotic gramicidin (Abe et al., 1994; Rhee et al., 1994; Kyrozis and Reichling 1995).

Gramicidin exerts its antibiotic action by forming pores in the cell membrane. Gramicidin molecules are linear pentadecapeptides that have the sequence $\text{HCO-L-Xxx-Gly-L-Ala-D-Leu-L-Ala-D-Val-L-Val-D-Val-L-Trp-D-Leu-L-Yyy-D-Leu-L-Trp-D-Leu-L-Trp-}$

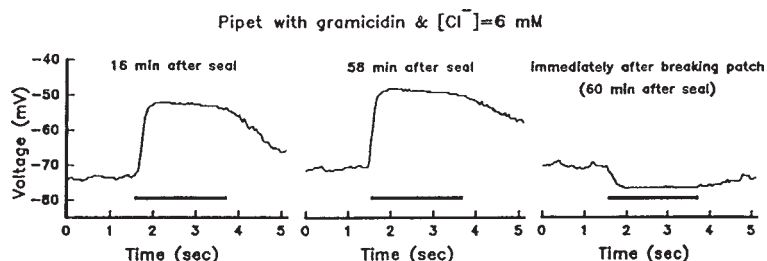


Fig. 3. Responses to glycine of a neuron recorded with gramicidin-perforated patch and 6 mM chloride in the electrode. Bars represent the application of 100 μM glycine. Breaking the patch to establish conventional whole-cell recordings caused an immediate shift of response to values close to the calculated chloride reversal potential. Reprinted with permission from Kyrozis and Richling (1995).

$\text{NHCH}_2\text{CH}_2\text{OH}$, where Xxx can be Ile or Val and Yyy can be Trp (gramicidin A), Phe (gramicidin B), or Tyr (gramicidin C). These polipeptides are hydrophobic, and in lipid bi-layers they form helical dimers that act as cation-selective ion channel. In fact, the gramicidin-formed ion channel is the most studied ion channel ever (Andersen et al., 1988; Sawyer et al., 1989; Hille, 1992). Gramicidin-formed ion channels are only permeable to monovalent cations. The channels are not voltage-dependent, and small cations—such as K^+ , Na^+ and Cs^+ —permeate equally well from both sides of the patch, thus allowing for good voltage clamp of both inward and outward currents (Sawyer et al., 1989; Tajima et al., 1996).

Because of the selectivity for cations of gramicidin-formed channels, intracellular $[\text{Cl}^-]$ is not disrupted (Fig. 3), and no Donnan forces develop between pipet's interior and cytosol for imbalances in anion concentrations. An additional advantage of a Cl^- -impermeable perforating molecule such as gramicidine is found when studying the impact on cell membrane potential of transmembrane ionic fluxes through carriers. An example of this problem is the nonphysiological persistent membrane hyperpolarization of cultured astrocytes caused by extracellular application of HCO_3^- , when no HCO_3^- is introduced in the pipet solution during ruptured-patch whole-cell recordings (McKhann et al., 1997; Fig. 4).

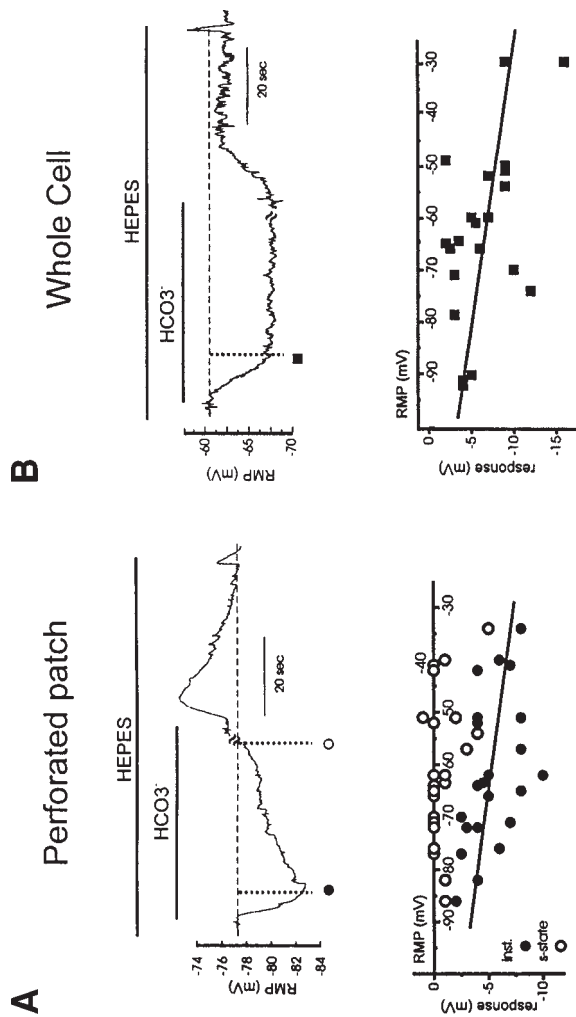


Fig. 4. $\text{Na}^+/\text{2HCO}_3^-$ co-transporter activity affects cell-resting membrane potential during whole-cell recordings but not in cells with intact anion gradients. (A) Perforated patch-clamp recordings from a cultured neocortical astrocyte under current-clamp conditions ($I_{\text{pipet}} = 0$). Application of HCO_3^- caused a transient hyperpolarization followed by a prompt return to a pre- HCO_3^- value. The peak of the hyperpolarizing response is marked by a filled circle, whereas the steady state is indicated by an open circle. The bottom graphs illustrate the cumulative results from these experiments. During perforated-patch recording, the hyperpolarization seen at the peak had recovered to baseline at steady state. (B) In contrast, during whole-cell recordings, no difference between steady-state and peak response was seen. Reproduced with permission from McKhann et al. (1997).

2.3. β -Escin

It has been recently shown that molecules other than channel-forming antibiotics can be effectively employed for perforated patch. In an attempt to reduce the waiting times and inconvenience sometimes experienced with nystatin, amphotericin-B, or gramicidin, Fan and Palade (1998) used β -escin, a saponin, to permeabilize the patch for perforate patch recordings. β -Escin was initially employed as tensioactive to permeabilize muscle cells (Kobayashi et al., 1989; Konishi and Watanabe, 1995). Palade and coworkers found no obvious effect of β -escin on the kinetics of Ca^{2+} currents as compared to whole-cell recordings (Palade PT, personal communication to the author). However, caution should be exercised in its use in physiological studies until it can be demonstrated that there is no lateral or cytoplasmic diffusion of β -escin. In fact, it has been demonstrated that detergents at very low concentrations can affect ion channel gating (Sawyer et al., 1989). It has been also demonstrated that commonly used antibiotics do not diffuse in the cytoplasm, and do not diffuse laterally, that is across the rim between cell membrane and pipet to the rest of the cell membrane (Horn, 1991).

The finding that β -escin works well in preventing calcium current run-down in spite of the large pores formed (Fan and Palade, 1998) suggests that run-down may be often times caused by the simultaneous disorganization of the cytoskeleton and the rupturing of the membrane patch. This could lead to the loss of compartmentalization of specific enzymatic and co-enzymatic activities anchored to the cytoskeleton that are required for channel activity or transduction signaling.

3. The Perforated Vesicle Patch-Clamp

One of the advantages of patch-clamp is the outside-out patch recording. Such patch-clamp configuration allows one to record the activity of ion channels embedded in the patch membrane while the pipet's interior replaces the intracellular compartment, and the bath solution as extracellular space. The disadvantage of a classic outside-out recording is that the pipet's solution dialyze the submembrane environment and therefore may alter the signal transduction mechanisms or modulation of the ion channel's properties. Levitan and Kramer developed a hybrid configuration of the outside-out and perforated patch recordings: the perforated

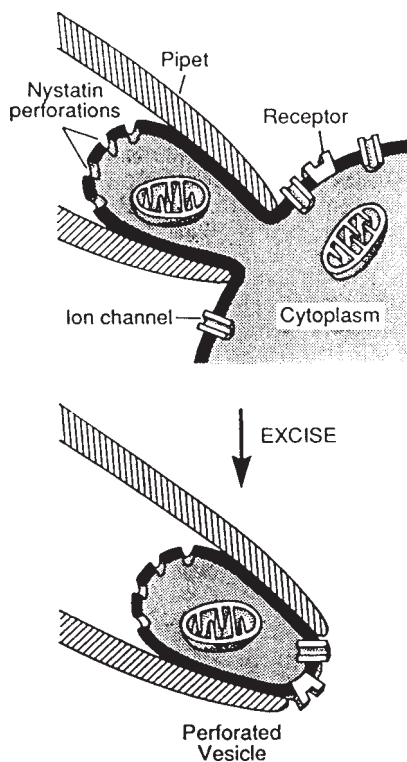


Fig. 5. Schematic of the perforated vesicle configuration. A perforated patch is obtained with a pipet containing nystatin (top panel). The pipet is then withdrawn to form a perforated vesicle (bottom panel). The patch of cell membrane facing the bath contains receptors and ion channels with an out-side out orientation. The vesicle maintains the submembrane cytoplasm. Reproduced with permission from Levitan and Kramer (1990).

vesicle (Levitan and Kramer, 1990; Fig. 5). This technique entails in first establishing the cell-attached configuration on a cell with a pipet containing a perforating antibiotic. The antibiotic enters the membrane and forms ion channels establishing the perforated whole-cell recording. Once the perforated patch configuration is achieved, the pipet is withdrawn as is done to establish an outside out patch configuration. However, because of the previous

establishment of the perforated patch this procedure ends with the formation of a vesicle that contains ion channels in the outside out configuration and the cytoplasmic submembrane matrix. Levitan and Kramer loaded cells with a fluorescent dye, rhodamine 123, that is sequestered in mitochondria, to test whether cytoplasm was retained in the vesicles at the tip of the pipets. The vesicles present ion channels in the outside-out configuration. Levitan and Kramer used nystatin as perforating antibiotic, rhodamine 123 to stain live mitochondria. Extracellular medium (in mM): NaCl 150, KCl 5.4, CaCl_2 2, MgCl_2 , glucose 20, Na-HEPES 10, pH 7.5. The tip of the pipet was filled with solution I (in mM): KCl 150, MgCl_2 5, K-HEPES, pH 7.1, or solution II (in mM): K_2SO_4 120, KCl 16, MgSO_4 5, Na-HEPES 10, pH 7.1. The remainder of the pipet was backfilled with nystatin 100 $\mu\text{g}/\text{mL}$ (stock solution of 25 mg/mL in DMSO). After formation of the gigaseal the patch perforation was monitored by measuring the pipet-to-cell access resistance. When the access resistance became $<50\text{ M}\Omega$, the recording was switched to current clamp while the pipet was withdrawn and a vesicle excised. Rae et al. (1991) were able to perform perforated vesicle patch using amphotericin B and hold the recording from the vesicles for 30 min or longer.

4. Pipet Filling Solutions

Electrode filling solutions used for ruptured-patch whole-cell recordings may be used with perforated patch as well. Such pipet solutions are recommended when the experimenter wants to compare cell's responses in perforated patch against response in whole cell. In fact, if the pipet-filling solution is appropriate, following the perforated-patch recording, the experimenter has the option to break the membrane patch and quickly perform recordings in a ruptured patch configuration. The time available for such a test is however limited since the antibiotic will diffuse to the rest of the cell and create channels that will deteriorate the recording and kill the cell. However, the existence of an intact patch of membrane between the cytoplasm and the pipet solution can be advantageous, because it allows for the use of specific filling solutions that may facilitate the experimenter under certain conditions, or disadvantageous, because may lead to junction potential. We will discuss these advantages and disadvantages.

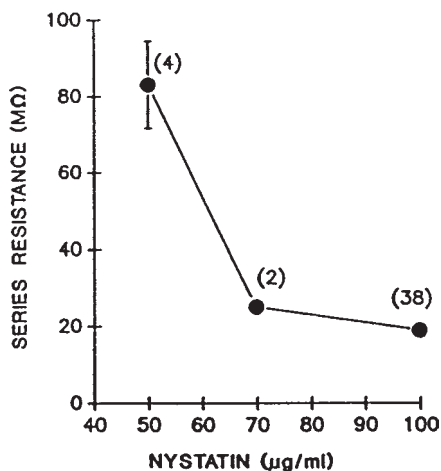


Fig. 6. Concentration dependence of the steady-state pipet-to-cell access resistance on nystatin concentration. Data points represent the mean \pm SEM. The number above the points represent the number of cells included in the mean. Reproduced with permission from Korn and Horn (1989).

4.1. Nystatin

Dissolve 5–30 mg of nystatin (Sigma, N5303) in 100 μL DMSO (Sigma, S8779), using a vortex. The solvation of nystatin is facilitated by sonication 1–3 min. The pH of this stock solution can be lowered to 2.0 by HCl under constant stirring to increase solvation, and then elevated to 7.2 with KOH (Akaike and Harata, 1994). Alternatively, the stock solution may be prepared by dissolving nystatin in methanol at 5–10 mg/mL (Horn and Marty, 1988). The stock solution (50–300 mg/mL) should be prepared freshly daily because the antibiotic loses its pore-forming activity rather quickly. However, there are reports it can be stored in a freezer (-20°C) for up to a month. An alternative procedure is to put 5 mg of nystatin into Eppendorf tubes, and stored desiccated under liquid nitrogen until usage. Just before use, add 100 μL of DMSO to the Eppendorf tube containing nystatin. Bath sonicate for at least 30 s. At room temperature nystatin is active for about 2 h. After this time, it is better to prepare a fresh solution. The final pipet solution should contain nystatin 70–100 $\mu\text{g/mL}$ (Fig. 6).

4.2. Amphotericin B

Rae et al. (1991) dissolved 6 mg amphotericin B in 100 μ L DMSO. The solution was vortexed for 5 s. This stock solution was then diluted in pipet solution to a final concentration of amphotericin B equal to 240 μ g/mL. The pipet solution was then filtered with 0.2 μ m Nalgene syringe filters. Rae and colleagues did not apply the amphotericin-containing pipet solution at the tip of their pipets, but rather filled the initial 500 μ m with antibiotic-free pipet solution. The pipet was then back filled with antibiotic-containing pipet solution. These electrodes allowed a good perforation within 5–10 min. It is worth mentioning that there are reports on the difficulty to obtain good gigaseals or healthy cells when the antibiotic is placed at the very tip of the pipet and recordings are performed *in situ*. Dean and colleagues have reported successful gigaseal formation if the cell soma is first cleaned and exposed (Dean et al., 1997). Such procedure leads to a fast perforated patch with perforation obtain in 1 min. They also used amphotericin-B in DMSO at 60 mg/mL, then diluted it in the pipet solution to a final concentration of 240 μ g/mL. The solution is filtered (0.2 μ m pore-size, Nalgene) and used to fill the entire pipet including the tip.

4.3. Gramicidin

Commercially available gramicidin is usually a mixture of gramicidin A, B, and C, which is termed gramicidin D (Sigma G5002). The pipet solution is usually prepared by first dissolving gramicidin D either in methanol at 10 mg/mL, or in DMSO at 1–5 mg/mL. The stock solution is sonicated for a few seconds before being diluted, without pH adjustments, in the pipet solution to reach a final concentration of gramicidin of 20–100 μ g/mL. For perforated patch *in situ*, we routinely use gramicidin 20–25 μ g/mL, but higher concentration should be used whenever possible to accelerate perforation. With gramicidin 20 μ g/mL perforation occurs in 40 min, while gramicidin 100 μ g/mL fully perforates in 20 min or less. Gramicidin in solution loses its activity in a few hours, therefore we freshly prepare a gramicidin stock solution on each experiment, and a gramicidin-containing pipet solution every 2 h. It is convenient to keep the gramicidin stock on ice throughout the experiment to preserve the antibiotic's activity for longer time. A simple pipet solution based on KCl is (in mM): KCl 140, NaCl 10, HEPES

10, pH adjusted to 7.2 with KOH. Since anions do not permeate through gramicidin-formed channels, the ionic composition of the pipet solution can be easily modified without generating large junction potentials.

Perforated patch recordings present the experimenter with a new challenge: to guarantee that the membrane patch sealed by the pipet did not break, and that the data have not been obtained from a cell unintentionally dialyzed by the pipet filling solution. With a standard pipet solution for ruptured patch recordings, the experimenter will observe a progressive deterioration of the cell-membrane potential, and ultimately its death when the membrane patch breaks and the antibiotics diffuse into the cytoplasm. However, this disruption can take even up to 10 min and is not a clear-cut phenomenon. Thus, different pipet solutions have been used. We commonly use a potassium fluoride-based pipet solution. Fluoride is not permeable through gramicidin-formed channels, and it is a potent nonspecific ion-channel blocker. Therefore, when KF is included in the pipet solution, breakage of the membrane patch is accompanied by a rapid depolarization of cell membrane. We routinely use the following fluoride-based pipet solution for both neurons and glial cells in brain slices (in mM): KF 70, KCl 70, NaCl 10, HEPES 35, EGTA 1, pH 7.2 with KOH. When recording from *in situ* or cultured astrocytes we observed stable recordings for up to 1 h. Since Cl^- is not permeable through gramicidin-formed ion channels, and therefore no Donnan forces are expected to develop, we prefer to have a rather elevated $[\text{Cl}^-]_{\text{pipet}}$ so to improve the performance of the Ag/AgCl electrode. In addition, the inclusion of F^- allows us to recognize a sudden cell depolarization due to unintentional rupture of the membrane patch.

4.4. β -Escin

The use of β -escin in perforated patch is new. Fan and Palade reported that they obtained the best results in ventricular cardiocytes when the internal solution of the pipet had β -escin 30–50 μM , which is higher than that usually employed for open-cell-attached patch clamp (Muraki et al., 1992; Ahn et al., 2001). β -Escin was prepared daily or as a 50 mM stock solution in water and stored up to one week at -20°C (Fan and Palade, 1998). In our laboratory the same procedure was effective to establish perforated patch from *in situ* glial cells.

5. Electrode Construction for Perforated Patch

Patch pipets are fabricated by pulling borosilicate glass capillaries. We use glass by Sutter with 1.5 mm outer diameter, and 0.86 mm inner diameter (B150-86-10), and a horizontal puller (Sutter, P97). Tip diameter being equal, we want the lowest possible access resistance, thus we make short tapered pipets' tips. We use a tip diameter of $\sim 3\ \mu\text{m}$ when patch clamping from neurons. However, we use a tip diameter of about $1\text{--}2\ \mu\text{m}$ to obtain reliably the cell-attached configuration in *in situ* glial cells. In fact, their cell diameter is often equal or less than $10\ \mu\text{m}$. Patch clamping from these cells in culture is facilitated by their flatter geometry and increase in surface accessibility to the pipet. Some investigator reports that firepolishing the pipet tip improves seal resistance in certain studies. However we did not find differences between polished and unpolished pipets for both ruptured and perforated patch, so we generally use unpolished electrodes.

Patch-clamp recording from cultured cells is always easier where cells are clearly visible, their surface easily accessible, and the pipet cannot get plugged with tissue debris. Conversely, patch-clamp recordings from *in situ* cells are more difficult because the experimenter needs to maneuver the pipet in the tissue, while applying a positive pressure to free the space surrounding the tip itself. This procedure, which is essential for a good success rate of recordings in brain slices, may create difficulties when one attempts the perforated patch configuration. In fact, since positive pressure has to be applied to free the way to the pipet, a constant outflow of pipet filling solution occurs. If the antibiotic flows out of the pipet it may perforate the cells, in particular the one from where one is attempting to record. To prevent this problem, one may use an antibiotic-free pipet-filling solution at the tip of the electrode when recording from cells *in situ*. The amount of the antibiotic-free solution that has to be placed at the tip depends on how long it will take to obtain a cell-attached configuration and on the pressure applied to set the outflow of the pipet-filling solution. Some laboratories fill the whole pipet with antibiotic-containing solution and find no deleterious effect of the antibiotic on the gigaseal formation or on the health of the cell. We found that this procedure prevents good seal-formation when recording from glial cells in the slice preparation. This possibly happens because the gigaseal formation requires more time when performed in the slice,

and also requires the application of a positive pressure to the pipet solution to prevent clogging of the pipet's tip by tissue debris. Therefore gramicidin may significantly flow out of the pipet and damage the cell. Therefore, we fill the first 300–500 μm of the pipet tip with antibiotic-free pipet solution when attempting a recording from *in situ* cells. This is easily achieved by simply dipping the pipet in such solution for a few seconds, and then back filling the rest of the pipet with gramicidin-containing solution. One does not want to fill too much of the tip with antibiotic-free solution because the perforation time may be excruciatingly prolonged for the time it takes for the antibiotic to reach the patch membrane at a significant concentration. It is worth mentioning that Dean and colleagues have reported that amphotericin-B does not flow out of the tip when co-applied with lucifer yellow (0.15–0.5%; Dean et al., 1997). Thus, under certain circumstances it may be worthwhile to first clean and expose the soma of an *in situ* cell, and then approach it with a pipet for rapid perforated patch recordings. In our experience this procedure is advantageous for big *in situ* neurons, but small *in situ* cells, such as glial cells, are not easy to expose and clean from debris. We therefore fill the pipet tip with antibiotic-free solution.

6. Detailed Protocol for Perforated Patch Recording

1. Fill the very tip of the patch pipet with an antibiotic-free pipet-filling solution by dipping the electrode's tip in a Eppendorf tube full of pipet filling solution for few seconds. The portion of the pipet's tip that is filled also depends on the shank of the electrodes. The experimenter should determine with a microscope the amount of the tip that is actually filled. Too much tip filling will cause significant delays in the time the antibiotic will take to diffuse to the tip and perforate the membrane patch. For *in situ* recordings we fill 300–500 μm ; for culture we fill about 100–200 μm of the tip.
2. Back-fill the rest of the barrel with antibiotic-containing filling solution. We use a syringe with a very fine needle of plastic and silica (Microfil, WPI). The use of metal needle is not recommended since interactions between metal and ions are possible. The formation of small air bubbles at the interface between the two solutions interferes with the diffusion of the antibiotic to the membrane patch, and should be considered an advantage.

- Diffusion of the antibiotic to the tip initiates only following tapping the electrode to remove any air bubble.
3. Once the pipet is immersed in the bathing media, approach the cell of the slice. Then apply a small positive pressure (with a syringe or with your mouth), and apply a negative voltage close to the resting membrane potential the type of cells we want to record from. We usually use -60 mV when approaching neurons, and -70 for glial cells. The positive pressure applied to the pipet's interior result is a slow outflow of solution that prevent the pipet from clogging and, in brain slices, clear the way to the cell membrane. A voltage command of ± 5 mV, 20 ms, is applied at 50 Hz superimposed to the holding potential. The current evoked is used to monitor the resistance across the pipet's tip. This allows the experimenter to determine the contact of the pipet's tip with the cell membrane. Gigaseals are obtained by placing the pipet tip onto the cell under visual control. We gradually push the tip against the membrane while decreasing the pressure applied to the pipet filling solution. This process allows for cleaning the surface of the cell membrane that need to be patched first, and then attach the pipet tip to the cell without pushing it away or damaging. In addition the pipet tip is left free from tissue debris. When the resistance across the pipet's tip is about double of the one of the pipet in the free bath, we consider the pipet in sufficient contact with the cell membrane. We zero the tip-potential (offset) and reverse the pressure inside the pipet.
 4. When recording from cultured cells we often times obtain gigaseals without reverting the pressure, but in our experience this does not happen in brain slices. To obtain a good gigaseal ($>2\text{G}\Omega$) we hyperpolarize the membrane patch by bringing the holding potential to about -90 mV. Often times this simple procedure forces the formation of excellent gigaseals. Once the gigaseal ($\geq 2\text{G}\Omega$) is obtained, the pressure inside the pipet is removed, and the holding potential is immediately brought back to about -70 mV.
 5. Once the Gigaseal is formed, it is the time to quickly compensate for the pipet capacitance till its transients are zeroed. We suggest this compensation be performed within few seconds before the perforation is significant. For ruptured patch recording, this is the time to brake the membrane patch. For perforated patch the experimenter just needs to wait for the antibiotic

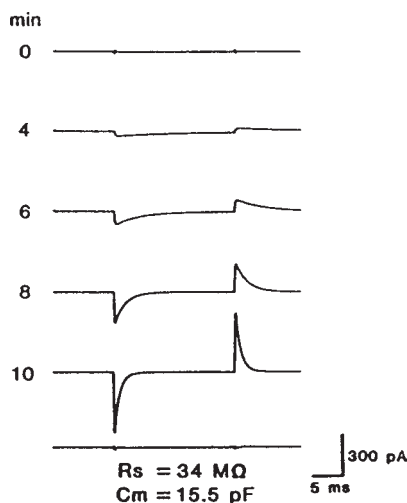


Fig. 7. Time course of electrical access formation to the cell interior during perforated patch recordings. Traces represent membrane currents responses to a 20-ms, -10 mV voltage pulse from a holding potential of -60 mV. Numbers to the left of each trace indicate the time (in minutes) after the formation of the gigaseal patch. In the bottom trace the capacitive current was compensated. Reproduced with permission from Korn and Horn (1989).

to perforate the membrane patch. Usually within 1 min one observes the appearance of a small resistive current and a small capacitive transient due to the fact that the antibiotic begins to perforate the membrane patch. If one does not see the appearance of small capacitive and resistive currents within 5 min the perforation is not ideal. Either the antibiotic has to diffuse too much of a distance to reach the membrane patch, or its effective concentration is too small. After few attempts, one can adjust the tip filling and/or the antibiotic concentration to observe the initial perforation within a minute. Depending on the antibiotic and concentration used, the perforation may proceed for the following 30 min. If one observed increase in capacitive currents overtime after that time, the antibiotics is acting too slowly (Fig. 7). Once the resistive and capacitive currents reach their steady-state, it is time to compensate for cell-membrane capacitance and series resistance and proceed with the experiment.

7. Problems Associated with Perforated Patch Recordings

7.1. High Series Resistance

Perforated patch clamp is intrinsically associated with high pipet-to-cell access (series) resistance. When recording from *in situ* cells by perforated patch clamp, a series resistance of about 20 M Ω is generally regarded as low. Yet, this resistance is much higher than what can be obtained with standard ruptured-patch whole cell. Such an elevated series resistance results in at least two problems. First, it prevents the use of the perforated patch technique in association with standard patch-clamp amplifiers in studies of action potentials. Second, it may introduce significant errors when recording from cells with low membrane resistance or highly coupled cells. Therefore, one should always try minimize the resistance of the pipet used, either by increasing the diameter (as much as it is allowed by the dimension of the cell) or by fabricating pipets with large shanks. In first approximation a nystatin or amphotericin B-based perforated patch will result in a series resistance five times larger than the resistance of the pipet used. Therefore, when recording from small cells, and using pipets of 5–6 M Ω , we get a perforated patch of 25–30 M Ω : much higher than what can be obtained with ruptured patch.

It has been demonstrated that standard patch clamp amplifiers are not suitable to perform accurate studies in current clamp (CC) mode to investigate cell excitability. The measurements of action potentials are distorted when access resistance is elevated because of intrinsic current absorption—and consequent alteration of the recorded voltage—by the patch-clamp amplifier input section (Magistretti et al., 1996). It has been also shown that the smaller the cell-membrane capacitance, the greater the errors introduced will be (Magistretti et al., 1996). Therefore, standard patch-clamp amplifiers cannot be reliably used to measure action potentials during perforated patch recordings in the current clamp configuration. The problem becomes more severe if one considers that perforated patch is often times used to record from small cells—that have small membrane capacitance—which would otherwise be injured by standard whole-cell recordings. Several solutions have been adopted. Patch pipet are sometimes used to perform perforated patch CC recordings using microelectrode bridge amplifiers

rather than patch-clamp amplifiers. This is an excellent solution for current clamp recordings, but the performance of the voltage clamp offered by classical microelectrode amplifiers does not match the one offered by patch-clamp amplifiers. An alternative solution is to use advanced patch-clamp amplifiers that are specifically designed to handle an higher pipet-to-cell resistance. One of such amplifiers is the Axopatch 200A that offers the fast CC (I fast), which does not introduce the voltage distortions typical of the standard slow CC. The drawback is that the fast CC mode is stable only with pipet-to-cell access resistance greater than 10M Ω . New patch clamp amplifiers have been developed (Wanke et al., 1987; Magistretti et al., 1996) that combine the advantages of the voltage-clamp typical of patch amplifiers with the superior CC of microelectrode bridge amplifiers (MultiClamp 700A by Axon Instruments).

7.2. Significant Junction Potentials

Nystatin and amphotericin B are permeable to small cations and anions, such as Cl^- , but not to larger anions such as SO_4^- or cellular proteins. If the intracellular $[\text{Cl}^-]_i$ is significantly smaller than $[\text{Cl}^-]_{\text{pipet}}$, and the predominant intracellular anions are not permeable through the antibiotic-formed pores, then Donnan forces develop across the perforated patch. Because common pipet solutions contain Cl^- in excess than its intracellular concentration, Cl^- will flow into the cell till a Donnan equilibrium is established. This movement of ions and water may alter the cell's electrophysiological properties, or simply introduce a junctional potential across pipet and cell that may hinder voltage-clamp analysis (Horn and Marty, 1988). One way to minimize the problem is to replace part of the Cl^- in the pipet with a nonpermeating anion, to approximately match $[\text{Cl}^-]_{\text{pipet}}$ with the intracellular $[\text{Cl}^-]_i$. For instance the pipet solution may be based on K^+ -methanesulfonate or KSO_4 (130 mM), and NaCl (10 mM). In case $[\text{Cl}^-]_i$ is not known, or when it may change during the experiment, the antibiotic gramicidin, which is not permeable to Cl^- , is preferred.

Acknowledgments

The author gratefully acknowledges the support of the Epilepsy Foundation of America and the National Institutes of Health (NS 40823).

References

- Abe, Y., Furukawa, K., Itoyama, Y., and Akaike, N. (1994) Glycine response in acutely dissociated ventromedial hypothalamic neuron of the rat: new approach with gramicidin perforated patch-clamp technique. *J. Neurophysiol.* **72**, 1530–1537.
- Ahn, S. C., Lee, S. J., Goo, Y. S., Sim, J. H., So, I., and Kim, K. W. (2001) Protein kinase C suppresses spontaneous, transient, outwards K^+ currents through modulation of the Na/Ca exchanger in guinea-pig gastric myocytes. *Pflügers Arch.* **441**(4), 417–424.
- Akaike, N. and Harata, N. (1994) Nystatin perforated patch recording and its applications to analyses of intracellular mechanisms. *Japn. J. Physiol.* **44**, 433–473.
- Andersen, O. S., Durkin, J. T., and Koeppe, R. E. II. (1988) Transport through membranes: carriers, channels, and pumps (Pullman, A., et al., eds.), Kluwer Academic Publishers, Dordrecht, The Netherlands, pp. 115–132.
- Bekar, L. K., Jabs, R., and Walz, W. (1999) GABAA receptor agonists modulate K^+ currents in adult hippocampal glial cells in situ. *Glia* **26**(2), 129–138.
- Bekar, L. K. and Walz, W. (1999) Evidence for chloride ions as intracellular messenger substances in astrocytes. *J. Neurophysiol.* **82**(1), 248–254.
- Cass, A., Finkelstein, A., and Krespi, V. (1970) The ion permeability induced in thin lipid membranes by the polyene antibiotics nystatin and amphotericin B. *J. Gen. Physiol.* **56**, 100–124.
- Cass, A. and Dalmark, M. (1973) Equilibrium dialysis of ions in nystatin-treated red cells. *Nature* **244**, 47–49.
- Dean, J. B., Huang, R.-Q., Erlichman, J. S., Southard, T. L., and Hellard, D. T. (1997) Cell-cell coupling occurs in dorsal medullary neurons after minimizing anatomical-coupling artifacts. *Neuroscience* **80**(1), 21–40.
- Duchatelle-Gourdon, I., Lagrutta, A. A., and Hartzell, H. C. (1991) Effects of Mg^{2+} on basal and beta-adrenergic-stimulated delayed rectifier potassium current in frog atrial myocytes. *J. Physiol.* **435**, 333–347.
- Fan, J. S. and Palade, P. (1998) Perforated patch recordings with β -escin. *Pflügers Arch.* **436**, 1021–1023.
- Hille, B. (1992) *Ionic Channels of Excitable Membranes*, 2nd ed. Sinauer, Sunderland, MA.
- Horn, R. and Marty, A. (1988) Muscarinic activation of ionic currents measured by a new whole-cell recording method. *J. Gen. Physiol.* **92**, 145–159.
- Horn, R. (1991) Diffusion of nystatin in plasma membrane is inhibited by a glass-membrane seal. *Biophys. J.* **60**, 329–333.
- Johnson, B. D. and Byerly, L. (1993) A cytoskeletal mechanism for Ca^{2+} channel metabolic dependence and inactivation by intracellular Ca^{2+} . *Neuron* **10**(5), 797–804.
- Johnson, B. D. and Byerly, L. (1994) Ca^{2+} channel Ca^{2+} -dependent inactivation in a mammalian central neuron involves the cytoskeleton. *Pflügers Arch.* **429**(1), 14–21.
- Kobayashi, S., Kitazawa, T., Somlyo, A. V., and Somlyo, A. P. (1989) Cytosolic heparin inhibits muscarinic and β -adrenergic Ca^{2+} release in smooth muscle. *J. Biol. Chem.* **264**, 17,997–18,004.
- Konishi, M. and Watanabe, M. (1995) Molecular size-dependent leakage of intracellular molecules from frog skeletal muscle fiber permeabilized with β -escin. *Pflügers Arch.* **429**, 598–600.

- Korn, S. J. and Horn, R. (1989) Influence of sodium-calcium exchange on calcium currents rundown and the duration of calcium-dependent chloride currents in pituitary cells, studies with whole cell and perforated patch recording. *J. Gen. Physiol.* **94**, 789–812.
- Kyrozis, A. and Reichling, D. B. (1995) Perforated-patch recording with gramicidin avoids artifactual changes in intracellular chloride concentration. *J. Neurosci. Methods* **57**, 27–35.
- Lampen, J. O. (1966) Interference of polyenic antifungal antibiotics (especially nystatin and filipin) with specific membrane function, in *Biochemical Studies of Antimicrobial Drugs* (Newton, B. A. and Reynolds, P. E., eds.), The Society for General Microbiology, Cambridge, MA, p. 111.
- Levitan, E. S. and Kramer, R. H. (1990) Neuropeptide modulation of single calcium and potassium channels detected with a new patch clamp configuration. *Nature* **348**, 545–547.
- Lindau, M. and Fernandez, J. M. (1986) IgE-mediated degranulation of mast cells does not require opening of ion channels. *Nature* **319**(6049), 150–153.
- Lopantsev, V. and Schwartzkroin, P. A. (1999) GABAA-Dependent chloride influx modulates GABAB-mediated IPSPs in hippocampal pyramidal cells. *J. Neurophysiol.* **82**(3), 1218–1223.
- Magistretti, J., Mantegazza, M., Guatteo, E., and Wanke, E. (1996) Action potentials recorded with patch-clamp amplifiers: are they genuine? *Trends Neurosci.* **19**(12), 530–534.
- Marty, A. and Finkelstein, A. (1975) Pores formed in lipid bilayer membranes by nystatin. *J. Gen. Physiol.* **65**, 515–526.
- Mazzanti, M., Assandri, R., Ferroni, A., and DiFrancesco, D. (1996) Cytoskeletal control of rectification and expression of four substates in cardiac inward rectifier K⁺ channels. *FASEB J.* **10**(2), 357–361.
- McKhann, G. M. II, D'Ambrosio, R., and Janigro, D. (1997) Heterogeneity of astrocyte resting membrane potentials and intercellular coupling revealed by whole-cell and gramicidin-perforated patch recordings from cultured neocortical and hippocampal slice astrocytes. *J. Neurosci.* **17**(18), 6850–6863.
- Muraki, K., Imaizumi, Y., and Watanabe, M. (1992) Ca-dependent K channels in smooth muscle cells permeabilized by beta-escin recorded using the cell-attached patch-clamp technique. *Pflugers Arch.* **420**(5-6), 461–469.
- Rae, J., Cooper, K., Gates, P., and Watsky, M. (1991) Low access resistance perforated patch recordings using amphotericin B. *J. Neurosci. Methods* **37**, 15–26.
- Rhee, J.-S., Ebihara, S., and Akaike, N. (1994) Gramicidin perforated patch-clamp technique reveals glycine-gated outward chloride current in dissociated nucleus solitarii neurons of the rat. *J. Neurophysiol.* **72**, 1103–1108.
- Sawyer, D. B., Koeppe, R. E., and Andersen, O. S. (1989) Induction of conductance heterogeneity in gramicidin channels. *Biochemistry* **28**, 6571–6583.
- Tajima, Y., Ono, K., and Akaike, N. (1996) Perforated patch-clamp recording in cardiac myocytes using cation-selective ionophore gramicidin. *Am. J. Physiol.* **271**(2 Pt 1), C524–C532.
- Vandeputte, J., Wachtel, J. L., and Stiller, E. T. (1956) Amphotericins A and B, antifungal antibiotics produced by streptomycetes. II. The isolation and properties of the crystalline amphotericins, in *Antibiotics Annual, 1955–1956*. Medical Encyclopedia, Inc., New York, pp. 587–591.
- Wanke, E., Ferroni, A., Malgaroli, A., Ambrosini, A., Pozzan, T., and Meldolesi, J. (1987) Activation of a muscarinic receptor selectively inhibits a rapidly inactivated Ca²⁺ current in rat sympathetic neurons. *Proc. Natl. Acad. Sci. USA* **84**(12), 4313–4317.

Fast-Drug Application

Manfred Heckmann and Christian Pawlu

1. What Do We Gain from Fast Drug Application?

“...The determination of the three-dimensional structures of protein molecules showed for the first time in detail the construction of the molecular ‘machines’ of the life cycle. If we want to learn how these ‘machines’ work it is not sufficient only to know their construction. We actually have to see them at work, and this requires dynamical studies, i.e. penetration into the dimension of time.” (Eigen, 1968).

The dimension of time is of particular relevance at synapses. Synaptic events are usually short, in the order of milliseconds, and their exact duration and timing are of prime relevance. “For many synaptic receptors/channels, the ‘natural’ mode of transmitter application is a short, steep pulse, and many of these systems show rapid desensitization.” (Dudel et al., 1992). The last quote is from the first review of a technique that allows very fast application of drugs to receptor channels in out-side-out patches. The purpose of this chapter is to provide practical tips and additional information for setting up a fast drug application system. Scientists interested in this technique should in addition study the book chapter by Jonas (1995) and the article by Sachs (1999).

2. Material and Equipment

For general information regarding patch-clamp equipment *see* Chapters 1–5. In the following we focus on the aspects that are relevant for fast drug application. We describe our system consisting of a piezo, a monoluminal application pipet, and an application chamber.

From: *Neuromethods*, Vol. 35: *Patch-Clamp Analysis: Advanced Techniques*
 Edited by: W. Walz, A. A. Boulton, and G. B. Baker @ Humana Press Inc., Totowa, NJ

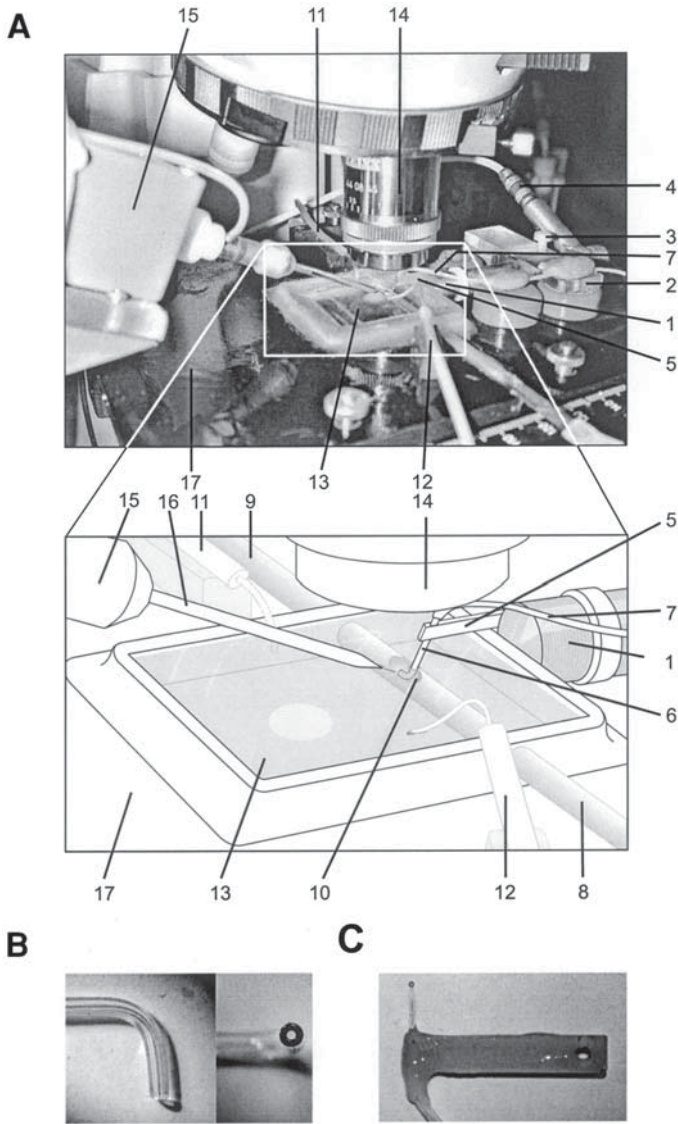
2.1. The Microscope

In principle the technique of fast drug application does not require a microscope. However, a microscope is helpful for patch-clamping in most preparations. We tried different types of microscopes and found upright microscopes more convenient than inverted microscopes. DIC optics allow one to visualize the liquid filament, and a video camera with a monitor is also useful. We use upright microscopes with a fixed stage (Fig. 1A). The micromanipulator is mounted on the table. If, instead, a microscope with a mobile stage is used, the micromanipulator should be mounted on the stage. With respect to the micromanipulator, it is important to realize that one needs to cover relatively long distances (up to 10 mm) with the electrode during an experiment with fast drug application. Because electrodes need to be replaced frequently, mounting the head-stage or the whole micromanipulator on a hinge might help. In the course of an experiment, a patch electrode is lowered onto the preparation, an out-side-out patch is excised (Hamill et al., 1981) and, with a fixed stage and the micromanipulator mounted on the table (Fig. 1A), the stage is moved relative to the electrode to reach the application chamber. Thereby the electrode tip remains in the optical field.

2.2. The Piezo

The piezo (1 in Fig. 1A) is contained in a metal tube and prestressed by a spring. We use the low-voltage minitranslator P810.30 element

Fig. 1. A piezo-driven application system on the stage of an upright microscope. (A) The photograph and the schematic drawing show components of the system: the piezo device (1), which can be fixed in its frame (2) with a screw (3), and its power supply (4); a platelet (5) to hold the application pipet (6) connected to a tube (7); in- (8) and out-flow (9) of the application chamber (10); in- (11) and out-flow (12) of the bath (13); objective (14); head-stage of an Axopatch 200A amplifier (15); patch-clamp electrode (16); fixed stage (17) of an upright microscope. (B) The application pipet is made from borosilicate glass with an outer diameter of 0.5 mm and an inner diameter of about 0.3 mm. To obtain the desired angle, a longer piece of glass (5–10 cm long) is heated in the flame of a common lighter. A scratch with a diamond knife on the convex side of the bend allows to break the glass as close to the bend as desired. The open end of the application pipet can then be firepolished in the lighter flame. (C) The application pipet is



(continued) glued into a fiber-glass platelet. A tube whose inner diameter fits tightly the outer diameter of the pipet is then put over the other end. Finally, the tool is mounted to the piezo with a screw.

from Physik Instrumente (Waldbronn, Germany). It lengthens by 45 μm on application of 100 V. It needs to be driven with sufficient power to overcome its capacitive load. Suitable power supplies for this piezo element are available from Physik Instrumente. To fix the piezo device on the stage, we use a frame (2 in Fig. 1A), held by strong magnets. The piezo can be rotated within the frame to allow easy access to the application pipet. A plastic screw (3 in Fig. 1A) allows one to fix the position of the piezo.

2.3. Application Pipets and Tubing

Our application pipets are made from glass tubes. We found borosilicate glass from Hilgenberg (Malsfeld, Germany) with an outer diameter of 0.5 mm and an inner diameter of about 0.3 mm suitable. An important constraint is that the opening of the application pipet needs to fit under the objective of the microscope. Usually we work with a 20 \times LD Zeiss objective (14 in Fig. 1A). Therefore the application pipet needs to be bent to fit below the objective (Fig. 1B). To obtain the desired angle, we heat a longer piece of glass (5–10 cm long) in the flame of a common lighter. A scratch with a diamond knife on the convex side of the bend allows to break the glass as close to the bend as desired. The one end of the application pipet is then firepolished in the lighter flame and the application pipet is glued into a fiberglass platelet. A tube whose inner diameter fits tightly the outer diameter of the pipet is put over its other end. Silicon might help to seal this connection. Finally, the platelet is mounted to the piezo with a screw. The tube is connected to a 6-port valve (HVX 86915 Hamilton, Darmstadt, Germany) that allows to change the solution flowing to the application pipet rapidly. Syringes are used as solution reservoirs. The syringes are sealed airtight and connected to compressed air with a pressure regulator.

2.4. Application Chamber

The tip of the application pipet is placed in an application chamber (10 in Fig. 1A) that is separated from the rest of the bath. We make our application chamber from Kimax glass tube (outer diameter 3 mm). An opening of about 120 degrees and about 1 cm length is filed into the tube. This opening is the access to the chamber for both the application pipet and the patch electrode. The application chamber is glued into the bath chamber. The ends of the glass

tube, i.e., the application chamber, are then connected to a solution reservoir and a pump. It is important to obtain a very steady flow of the solution in the application chamber. We use the hydrostatic pressure (height of the solution reservoir) and an adjustable pump to fine-tune the flow as precisely as possible. If the pump is not ideal, an air-chamber (i.e., a large syringe, half full with water and connected parallel to the tube) may help to steady the flow. We adjust the pump so that a little solution is always sucked from the bath to avoid contamination of the bath with the solution in the application chamber.

2.5. Patch Electrodes

Many electrodes are used in experiments with out-side-out patches and a rapid application system. We like electrodes with a resistance of about 10 M Ω when filled with a standard intracellular saline. We produce these electrodes “online” during the experiments. This has the advantage that the tip size and the geometry of the electrode can always be fine-tuned as desired. For example by adjusting the tip diameter, one can try to increase or decrease the numbers of channels in a patch. We found the DMZ Universal Puller by Zeitz Instruments (Munich, Germany), suitable, but other commercial pullers may also be appropriate. Zeitz Instruments also offers a quartz-glass puller for low-noise recordings (Dudel et al., 2000).

2.5. Hard- and Software

We use commercially available computers and software for the recording and evaluation of our data. A pulse generator like the Master8 from AMPI (Jerusalem, Israel), or the Max21 from Zeitz Instruments are useful to control the piezo device. Usually, the recording software triggers the pulse generator. Short current traces (100–300 ms) are recorded at intervals of 1–5 s directly onto the hard disk of the computer. To make sure that periodic noise sources are likely to be out of phase, we use an interval of, say, 1.001 s instead of exactly 1 s. The most important functions of the data-analysis program are averaging, subtracting, and fitting current traces. Jitter or imprecise timing of the traces (inevitable in earlier times with videotapes or dat-recorders) precludes precise subtraction. On good days up to 2000 sweeps have to be processed per patch, which can be a cumbersome procedure with some programs.

We found for this purpose the ISO2 software (MFK, Taunusstein, Germany) more useful than PClamp6 from Axon or PulseFit from HEKA. However, using ISO2 is more and more difficult on new computers due to outdated hardware requirements. For comfortable data evaluation high performance of the processor hardware is recommended.

3. Procedures, Applications, and Results

3.1. Testing the System

After the equipment has been set up, it needs to be tuned. The first step is to optimize the solution flow from the pipet. One needs a steady stream with a sharp interface (Fig. 2A). One can judge this easily with the microscope and the video monitor if there is a difference in osmolarity between the solutions. Turn on the solution flow, focus on the liquid filament, and check that it remains steadily in focus for, say, half an hour or the period you want to record from a patch. To measure the time course of the solution exchange, monitor the liquid junction potential. A reasonable exchange rate is shown in Fig. 2C and D. Keep in mind that inevitably the exchange at an intact patch is somewhat slower than at an open pipet.

The position of the patch electrode relative to the liquid filament is relevant for the solution exchange (Fig. 2E and F). It is important to map out the best position and to practice how to find it. With a real patch, there is on the one hand no time for searching, and on the other hand it is more difficult than with an open pipet. It is advisable to control the performance of the system routinely after experiments (use pressure to blow away the patch).

3.2. Working with Real Patches

Artefacts that superimpose with the currents of interest arise when the piezo is turned on and off. To illustrate the problem, we picked an extreme example for Fig. 3. We cannot give precise advice how to reduce these artefacts; you have to try around. Small changes in the setup often have large effects. Particularly important are: the mounting of the piezo on the stage, the size of the application pipet, its fixation to the piezo, and finally the electrode glass. We have the impression that quartz glass electrodes, which have otherwise superior noise performances, tend to ring

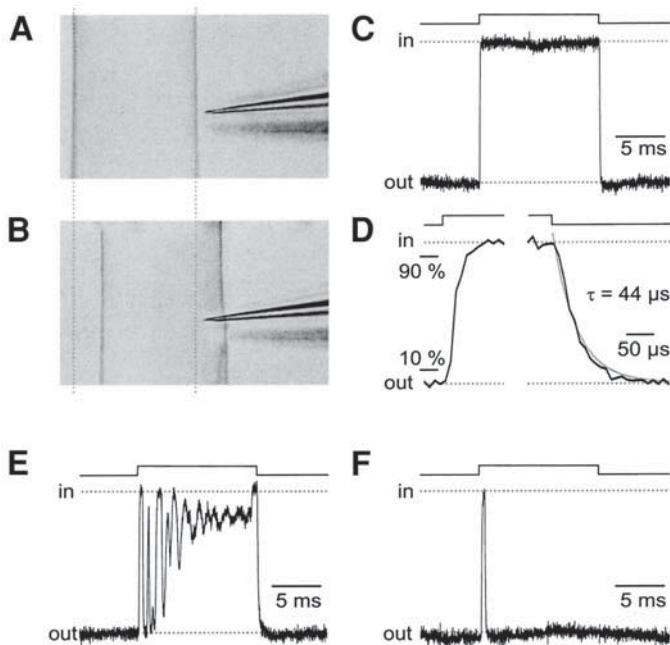


Fig. 2. Testing the performance of the system. (A) The liquid filament with reduced osmolarity close to a patch-clamp electrode is visible in differential interference contrast. (B) In response to a voltage pulse (thin lines above the current traces) the liquid filament moves $45 \mu\text{m}$ towards the electrode. After the pulse, the liquid filament returns to its initial position (dotted lines). Recording the liquid junction current during such a movement with an open patch electrode allows to measure the speed of the solution exchange (C). In this case a 12.5 ms pulse was applied to the piezo. (D) The rise and decay phase of the trace shown in (C) are shown on an expended time scale. The 10–90% rise time is about $30 \mu\text{s}$, and the decay of the current is fitted with a monoexponential function with a time constant of $44 \mu\text{s}$. (E, F) Effects with less favourable positions of the same patch-clamp electrode. Due to unavoidable vibrations of the system the tip is not necessarily always immersed for the whole-pulse duration.

more than usual borosilicate electrodes in our rapid application system. Some artefact will always remain, which can be eliminated by subtraction of blank traces (Fig. 3C). Usually it is possible to start off with a much smaller vibration artefact than the one shown

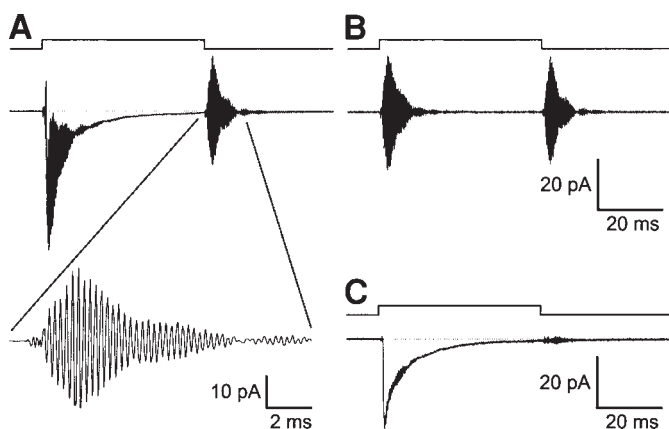


Fig. 3. Vibration artefacts. (A) Average current response from an out-side-out patch from a CA3 pyramidal neuron of a rat hippocampal slice. The patch was held at -80 mV, and 10 mM glutamate was applied for 50 ms. Large artefacts occur at the beginning and the end of the pulse (thin lines above the current traces). This is a common problem, but an extreme example is shown here. (B) Average current response from the same out-side-out patch recorded a few seconds earlier without glutamate flowing through the application pipet. (C) Subtraction of the trace shown in (B) from the one in (A) purges the current.

in Fig. 3 in a real recording, and it is then often possible to obtain clean average currents even at a very high gain (*see* for example the trace with 0.2 mM glutamate in Fig. 4 of Heckmann and Dudel, 1997).

3.3. Data Analysis

In the following we review some data for one particular receptor channel (Heckmann et al., 1996). The purpose of this section is to briefly illustrate how we obtain kinetic information from average current responses with a fast drug application system. The interested reader should also turn to the following papers: Dilger and Brett (1990), Dudel et al. (1990), Franke et al. (1991), and Colquhoun et al. (1992).

Figure 4A shows data from a recording with an out-side-out patch. In this case recombinant kainate receptors were exposed to various glutamate concentrations. A first step might be to measure

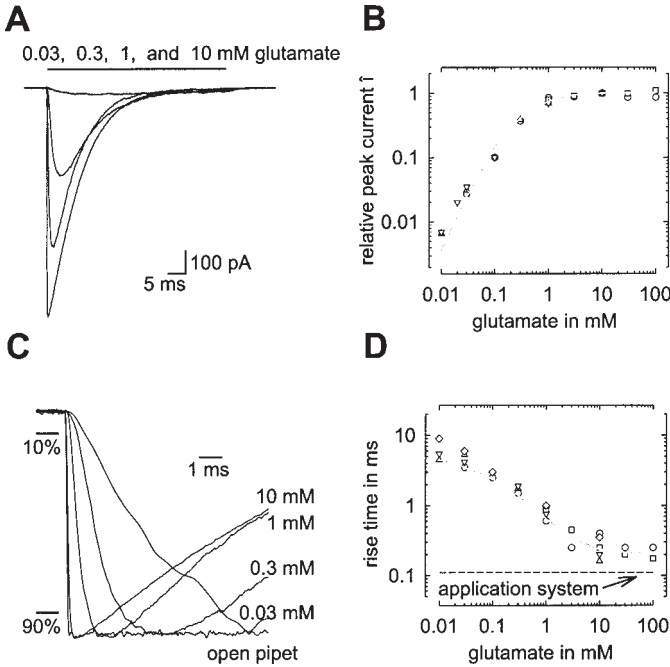


Fig. 4. From current traces to the rate constants of channel activation. The data shown here and in Fig. 6 are from out-side-out patches with recombinant, homomeric kainate receptors (GluR6), expressed in HEK 293 cells. (A) Averaged current traces from a patch, which was held at -60 mV, are shown superimposed. The peak current amplitude depends on the glutamate concentration. Each trace is the average of three to seven single responses to 0.03, 0.3, 1, or 10 mM glutamate. The horizontal bar above the traces indicates the application (pulse duration 50 ms; interval 5 s). (B) Double logarithmic plot of the peak current \hat{i} vs the glutamate concentration. \hat{i} was normalized to the \hat{i} value with 10 mM glutamate. The data from five patches are marked by different symbols. The grey line is a fit of the data with the kinetic mechanism and the rate constants given in Fig. 5. The peak current amplitude is half-maximal with about 0.5 mM (ratio of k_-/k_+). For glutamate concentrations $\ll K_m$, the slope is about 1.3, giving a lower limit of 2 for the number of binding steps. (C) Dependence of current rise time on glutamate concentration. The rising phase of the traces in (A) are shown normalized. In addition, the response of the open electrode recorded at the end of the experiment is shown. (D) Double logarithmic plot of the rise time (10–90%) vs the glutamate concentration. The data from five patches are shown. The grey line is a fit of the data with the kinetic mechanism.

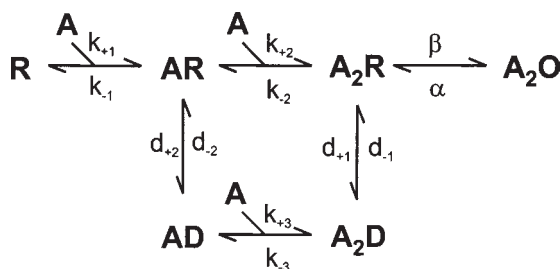


Fig. 5. Kinetic reaction scheme. R represents a closed channel, A agonist molecules and AR , A_2R , and A_2O a closed and an open channel with one or two agonist molecules bound. D represents desensitized states. For the computer simulations, the following rate constants were chosen: k_{+1} 7.2×10^6 , k_{-1} 1000, k_{+2} $3.6 \cdot 10^6$, k_{-2} 2000, k_{+3} $3.6 \cdot 10^6$, k_{-3} 80, α 1500, β 7000, d_{+1} 800, d_{-1} 0.08, d_{+2} 400, d_{-2} 1 (units: s^{-1} and $M^{-1}s^{-1}$ for k_{+n}).

the affinity of the receptors. High densities of receptors are nice in these experiments because one needs to measure current responses also at low agonist concentrations. Dose-response curves for the peak current amplitude and the current rise times are shown in Fig. 4B and D. The half-maximal activating concentration (K_m) is about 0.5 mM (Fig. 4B). For glutamate concentrations well below the K_m , the logarithmic slope is above 1.3 for these receptors. This provides a lower limit of 2 for the number of agonist binding steps (Fig. 5). To estimate the k_+ and k_- rate constants and the channel opening (β) and closing rate constants (α) we fitted the scheme (Fig. 5) to the two dose-response curves. Commercial programs like ChannelLab from Synaptosoft Inc. or the Berkeley Madonna are user-friendly environments to do these simulations. More information about the shape of the rise time curves is found in Franke et al. (1991), von Beckerath et al. (1995), and Heckmann et al. (1996).

As is obvious in Fig. 4A, the current decays in the presence of glutamate. This is due to desensitization of the receptors and demands at least one desensitized state (A_2D in Fig. 5) that is reached either from A_2R or A_2O . Experiments like the ones shown in Fig. 6C and D provide more information about the kinetics of desensitization. The experiments shown in Fig. 6A and B measure recovery from desensitization. Simulations allow one to estimate the relevant rate constants.

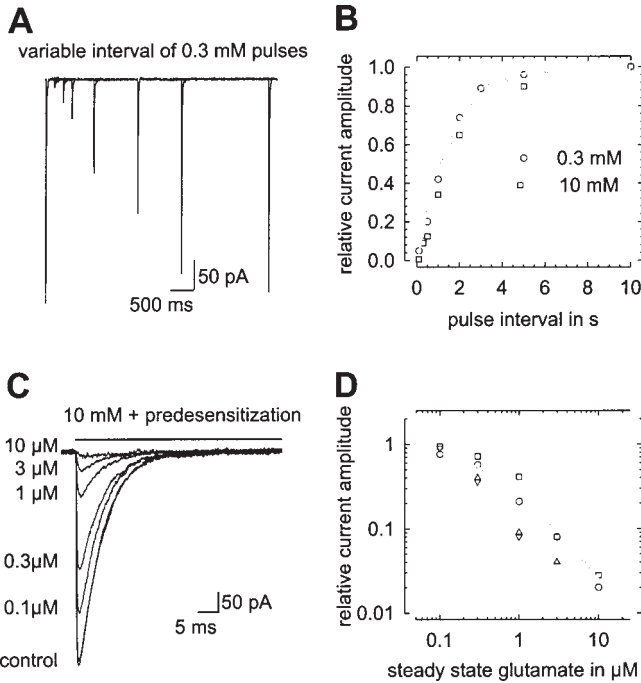


Fig. 6. Measuring desensitization. (A) Time course of recovery from desensitization. As shown in Fig. 4A, the currents desensitize. To measure the recovery from desensitization, here a control pulse was followed by a test pulse after 0.1, 0.3, 0.5, 1, 2, 3, and 5 s. Averaged currents of 3–5 single responses are shown. (B) Plot of the relative current amplitudes with 0.3 and 10 mM glutamate vs pulse interval. The solid and dashed grey lines are the results of computer simulations of these experiments for the two concentrations. (C) To quantify steady-state desensitization by low glutamate concentrations, responses to test pulses with a saturating glutamate concentration were recorded as controls. The other responses were recorded in the presence of 0.1–10 μ M glutamate, as indicated on the left side of the traces. The traces are averages of four to seven single responses from one patch. (D) Double logarithmic plot of the relative peak current vs steady-state glutamate concentration. The data from four patches are shown. The gray line is the result of a computer simulation of this experiment with the model given in Fig. 5.

In addition to the purely agonist elicited responses, the technique of fast drug application can be used to study the mechanism of competitive inhibition, ion-channel block, and allosteric modification.

4. Perspectives

Fast drug application allows one to obtain information about many aspects of receptor channel function that cannot be studied in the steady-state. We are convinced that the technique described here is very useful. With the modification described by Tour et al. (1995), even more complex pulse protocols are possible. The main limitation in experiments with fast drug application is the stability and quality of the recording, which requires training. The challenge for the future is to advance with fast drug application from average current traces to low-noise single-channel recordings.

Acknowledgments

Supported by the Deutsche Forschungsgemeinschaft SFB 391.

References

- Colquhoun, D., Jonas, P., and Sakmann, B. (1992) Action of brief pulses of glutamate on AMPA/kainate receptors in patches from different neurones of rat hippocampal slices. *J. Physiol.* **458**, 261–287.
- Dilger, J. P. and Brett, R. S. (1990) Direct measurement of the concentration- and time-dependent open probability of the nicotinic acetylcholine receptor channel. *Biophys. J.* **57**, 723–731.
- Dudel, J., Franke, C., and Hatt, H. (1990) Rapid activation, desensitization, and resensitization of synaptic channels of crayfish muscle after glutamate pulses. *Biophys. J.* **57**, 533–545.
- Dudel, J., Franke, C., and Hatt, H. (1992) High-speed application of drugs with a piezo drive, in *Practical Electrophysiological Methods* (Kettenmann, H. and Grantyn, R., eds.), Wiley-Liss, New York, pp. 141–145.
- Dudel, J., Hallermann, S., and Heckmann, M. (2000) Quartz glass pipette puller operating with a regulated oxy-hydrogen burner. *Pflügers Arch.* **441**, 175–180.
- Eigen, M. (1968) New looks and outlooks on physical enzymology. *Q. Rev. Biophys.* **1**, 3–33.
- Franke, C., Hatt, H., Parnas, H., and Dudel, J. (1991) Kinetic constants of the acetylcholine (ACh) receptor reaction deduced from the rise in open probability after steps in ACh concentration. *Biophys. J.* **60**, 1008–1016.
- Hamill, O. P., Marty, A., Neher, E., Sakmann, B., and Sigworth, F. J. (1981) Improved patch-clamp techniques for high-resolution current recording from cells and cell-free membrane patches. *Pflügers Arch.* **391**, 85–100.

- Heckmann, M., Bufler, J., Franke, C., and Dudel, J. (1996) Kinetics of homomeric GluR6 glutamate receptor channels. *Biophys. J.* **71**, 1743–1750.
- Heckmann, M. and Dudel, J. (1997) Desensitization and resensitization kinetics of glutamate receptor channels from *Drosophila* larval muscle. *Biophys. J.* **72**, 2160–2169.
- Jonas, P. (1995) Fast application of agonists to isolated membrane patches, in *Single-Channel Recording*, 2nd ed. (Sakmann, B. and Neher, E., eds.), Plenum, New York, pp. 231–243.
- Sachs, F. (1999) Practical limits on the maximal speed of solution exchange for patch-clamp experiments. *Biophys. J.* **77**, 682–690.
- Tour, O., Parnas, H., and Parnas, I. (1995) The double-ticker: an improved fast drug-application system reveals desensitization of the glutamate channel from a closed state. *Eur. J. Neurosci.* **7**, 2093–2100.
- von Beckerath, N., Adelsberger, H., Parzefall, F., Franke, C., and Dudel, J. (1995) GABAergic inhibition of crayfish deep extensor abdominal muscle exhibits a steep dose-response relationship and a high degree of cooperativity. *Pflügers Arch.* **429**, 781–788.

8

Pipet Perfusion Methods

Techniques and Applications

Gea-Ny Tseng and Minoru Horie

1. Introduction

The patch-clamp method was introduced in 1976 (Hamill et al., 1981; Neher and Sakmann, 1976). It has been widely used to study whole-cell and single-channel currents. In many cases, the experimenter needs to test how changing the pipet solution composition can affect membrane-channel function (*see* Subheading 2. Applications of the Pipet Perfusion Technique). This can be accomplished by applying pipets containing different solutions to different cells or to different membrane patches. The effects are inferred by comparing the properties of currents recorded under these different conditions. Problems in data interpretation may arise because of cell-to-cell variations in cell membrane-channel properties. This is especially the case for heterogeneous systems such as the central nervous system (CNS). An alternative approach is to excise the membrane patch to form inside-out or outside-out patch recording configuration. In this way, the experimenter can perfuse the bath with various solutions, thus controlling the milieu facing the intracellular (inside-out patch) or extracellular (outside-out patch) surface of the cell membrane. Potential problems here are channel density (should be high enough to allow a reasonable chance of recording channel currents from a patch), and the stability of channel function in cell-free patches. A further consideration is the large volume of solutions needed to perfuse the bath, that may become a limiting factor when studying expensive or precious substances of limited supply.

From: *Neuromethods*, Vol. 35: *Patch-Clamp Analysis: Advanced Techniques*
Edited by: W. Walz, A. A. Boulton, and G. B. Baker @ Humana Press Inc., Totowa, NJ

A direct method is to perfuse the pipet interior with different solutions during the course of an experiment, the pipet perfusion technique. This technique can avoid or reduce problems arising from: 1) cell-to-cell variations in channel properties (because each cell or patch serves as its own control), 2) issues of channel density or run-down in cell-free patches, and 3) cost of substance under study. Attempts to make user-friendly pipet perfusion devices began shortly after the patch-clamp method was introduced (Cull-Candy et al., 1980; Lee et al., 1980). Various designs have been described over the last two decades, each with advantages and disadvantages (Alpert et al., 1989; Byerly and Yazejian, 1986; Hattori et al., 1984; Lapointe and Szabo, 1987; Soejima and Noma, 1984; Tang et al., 1990; Velumian et al., 1993). In this chapter, we will begin by discussing the most notable applications of the pipet perfusion technique. We will then briefly describe the representative designs of pipet perfusion device available in the literature. This is followed by a discussion of key factors one needs to consider when constructing a pipet perfusion device. Finally, we will describe the pipet perfusion device used in our laboratories with particular emphasis on how to assemble the pipet and accessories.

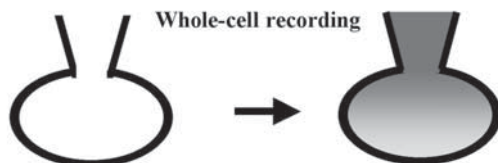
2. Applications of the Pipet Perfusion Technique

Figure 1 depicts different patch-clamp recording configurations and several key questions one can address using the pipet perfusion technique.

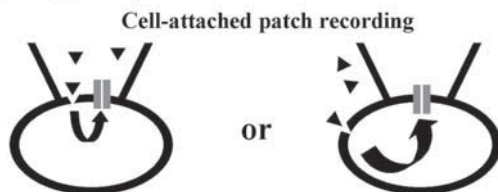
The most common question is how changing the intracellular milieu can alter the membrane currents. Therefore, the pipet perfusion technique has been used to study how changes in the intracellular ionic composition (e.g., Ca^{2+} , Na^+ , K^+ , H^+), or application of small molecules or second messengers (e.g., ATP, cAMP, cGMP), peptides (e.g., Na-Ca exchanger peptide inhibitor), or proteins (catalytic subunit of protein kinase A or C, ≥ 40 kDa) can affect membrane-channel function (Fischmeister and Hartzell, 1987; Horie and Irisawa, 1989; Horie et al., 1987; Kameyama et al., 1985; Kameyama et al., 1984; Ono and Trautwein, 1991; Saxena et al., 1997; Tseng and Boyden, 1991; Verrecchia et al., 1999).

Another question that can be well-addressed by the pipet perfusion technique is the mechanism of signal transduction following membrane receptor activation by an extracellular ligand. For example, activation of G-protein coupled receptors leads to a release of

What are the effects of changing intracellular milieu on membrane currents?



Does a ligand-activated receptor induce changes in membrane currents by a membrane-delimited or diffusible signaling pathway?



What is the sidedness of a drug (from which side of the cell membrane does it work)?

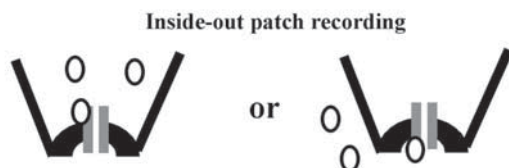


Fig. 1. Schematic diagrams of different patch-clamp configurations and key questions one can address using the pipet perfusion technique. More details in text.

G-protein α and $\beta\gamma$ subunits, that can induce changes in channel (effector) function by a membrane-delimited pathway (e.g., $\beta\gamma$ subunits activate muscarinic-receptor K channels, Clapham, 1794) and/or generating second messengers (e.g., α_s subunits activate adenylate cyclase, leading to cAMP production) that diffuse through the cytoplasm and affect channels on other parts of the cell membrane. These two possibilities can be distinguished by using a patch pipet to record the basal channel activity from cell-attached patches, and applying the ligand through the pipet using a pipet

perfusion device or through the bath solution (Fig. 1, middle panel). In the first case, the ligand can only activate receptors encompassed by the patch pipet. Therefore, one will see a change in channel activity due to receptor activation only if the signaling is through a membrane-delimited pathway. In the second case, the ligand activates receptors outside the patch membrane. Thus, a change in channel activity associated with ligand application indicates that a diffusible signaling pathway is involved. The best example of this application is the landmark paper published by Dr. Akinori Noma and his colleague in 1984, studying the mechanism of muscarinic activation of K channels in rabbit atrial cells (Soejima and Noma, 1984).

In studies of sites and mechanisms of drug actions on membrane channels, an important question is the sidedness of drug actions: from which side of the cell membrane does the drug work? This question can be best addressed using a pipet perfusion device in any of three patch-clamp configurations: whole cell, cell-attached, and inside-out patch recordings (Fig. 1, bottom panel, shows a diagram of inside-out patch recording). If the drug works from the cytoplasmic side of the membrane, it should affect channel function when applied to the pipet (whole-cell recording) or to the bath (cell-attached or inside-out patch recording). On the other hand, if the drug works from outside the cell membrane, its effects will be seen when applied to the bath (whole-cell recording), or to the pipet (cell-attached or inside-out patch recording). An example of this application is the study of lidocaine binding sites in cardiac Na channels (Alpert et al., 1989). An important consideration for data interpretation here is the membrane permeability of drug molecules (*see* Subheading 3. Consideration for Constructing a Pipet Perfusion Device), that can significantly affect the effective drug concentration on the side of the membrane to which the drug is applied.

3. Representative Designs of Pipet Perfusion Device

3.1. Cull-Candy, Miledi, and Parker (1980)

Cull-Candy et al. inserted a multibarrel pipet down the inside of a patch electrode. The patch electrode and perfusion pipet were held on the two arms of a Zeiss double-tool holder. The fine control of the arm on which the perfusion pipet was mounted was then used to position the tip of the perfusion system within 100 μm

of the patch electrode tip, under visual control using a microscope (100 \times). Air pressure could then be applied to one of the hypodermic needles that were cemented into the back of the perfusion pipet. Test pipet solution was thereby released from the desired barrel to produce an excess in the patch electrode tip.

3.2. Soejima and Noma (1984)

The device described by Soejima and Noma (1984) has been widely copied by many other laboratories, including ours, often with some minor modifications. In its original design, the 3 M KCl salt-bridge/Ag-AgCl half-cell, suction port, and the pipet solution waste chamber were all built-in features of the pipet holder. This shortened the fluid path length, reducing the stray capacitance and noise (see Subheading 3. Consideration for Constructing a Pipet Perfusion Device). The pipet solution reservoirs were separately mounted on a manipulator, which allowed multiple solution switches during the course of an experiment. The "inner tubing" was made from polyethylene tubing (PE 10, Clay Adams) drawn out over a heated tungsten filament to a desired size (diameter 40–70 μm) at the tapered end.

3.3. Lapointe and Szabo (1987)

These authors improved upon the design of Soejima and Noma with the following changes. First, the pipet solution reservoir was mounted to the pipet holder, thus reducing the fluid path length and accompanying stray capacitance and noise. Second, the driving force for solution flow from the reservoir to the patch pipet was provided by either suction applied to the back of the patch pipet, or by pressure applied to a closed system of reservoir. The latter method could provide a fast delivery (<2 min) of large protein molecules (e.g., catalytic subunit of protein kinase A, 40 kDa) to the patch-pipet tip. This is a significant advantage when working with channels that tend to run-down with time in the whole cell-recording mode. Third, a polymer-coated quartz capillary (Polymicro Technologies, Phoenix, AZ) was used instead of a polyethylene tubing as the conduit of pipet solution from reservoir to patch pipet tip. The polymer coating provided mechanical resistance and flexibility while the quartz interior provided excellent chemical resistance.

This excellent design is somewhat limited in the following aspects. First, the operation of the reservoir (closing the reservoir valve when forming a seal or between solution changes) can cause mechanical vibrations. Thus, after forming a giga-seal between the patch pipet and a cell it is necessary to lift the cell from the bottom of the chamber. Second, the pressure system allows only one solution change during an experiment. Finally, it requires fairly sophisticated machine shop work to construct the pipet holder, which may not be always available.

3.4. Tang, Wang, Quandt, and Eisenberg (1990)

Similar to the design of Lapointe and Szabo, these authors used a polymer-coated quartz capillary as the conduit of pipet solution. An Ag/AgCl wire was inserted into the patch pipet to provide electrical contact between the pipet solution and the amplifier headstage. The test pipet solution flew from the nearby reservoir through a PE tubing (threaded through a hole drilled in the pipet holder between the suction port and the headstage connector) into the capillary tip, which is positioned close to the patch-pipet tip under a microscope. One can buy this type of pipet holder from several commercial sources (E. W. Wright Microelectrode Holders and Accessories, Warner Instrument Corporation, and World Precision Instruments). This design has the minimum fluid path length and thus a low noise level. However, this advantage also imposes a serious limitation: only a small amount of test pipet solution can be introduced into the pipet to avoid an outflow of solution from the suction port, which can cause a significant increase in the noise level.

3.5. Pipet Perfusion Device Using θ (Double-Barreled) Glass

Alpert et al. (Makielski et al., 1987) used a 2 mm od borosilicate θ -glass (R & D Scientific Glass, Spencerville, MD) to construct their pipet perfusion device in their study of the sidedness of lidocaine binding to Na channels of single canine Purkinje myocytes. A piece of θ glass with the septum partially removed was pulled on a puller. The tip was fractured with a diamond-tipped pencil and fire-polished to give pores with diameters of 20–30 μ m. A Purkinje myocyte was drawn into the pipet pore by application of negative pressure and allowed to seal to the glass leaving only a part

of the cell extending into the bath. The part of the cell membrane inside the pipet was disrupted by a 25- μm diameter platinum wire advanced down the outflow barrel of the pipet. Electrical contact was made by a 3 M KCl salt-bridge/Ag-AgCl half cell connected to a side port of the θ glass tube. Pipet perfusion with different solutions was accomplished by introducing new pipet solution into one barrel, and the other barrel provided the outflow track. Davis and Gore described a method to create a side port in one of the barrels to allow electrical contact with Ag/AgCl pellet via a 3 M KCl agar salt bridge (Davis and Gore, 1987). This design has not been widely used, probably because of difficulty in removing the septum in a controlled manner, and the large bore of the tip that makes giga-seal difficult.

4. Considerations for Constructing a Pipet Perfusion Device

An ideal pipet perfusion device should meet the following criteria: ready availability and low cost of materials needed, easy to assemble, achieving low-noise recording with fast exchange of pipet solution multiple times during the course of a single-cell/patch experiment. There is probably no single “best” design of a pipet perfusion device that suits all needs. Here we provide some general principles and tips that will be of help when one designs one’s own pipet perfusion device. Figure 2 illustrates the key components of such a device, and important questions one needs to consider. This figure also lists key questions important for experimental design and data interpretation when using a pipet perfusion device.

As shown in Fig. 2, the device begins with a reservoir containing the test pipet solution. At a desired time during an experiment, the test pipet solution is allowed to flow from the reservoir to the patch pipet via an “inlet” tube (polyethylene or polymer-coated quartz capillary pulled to a tapered end of 40–70 μm diameter). This pipet solution exits from the opening of the inlet tube inside the patch pipet, and diffuses toward the pipet tip. If suction is applied to the back of the patch pipet, the displaced pipet solution will be also drawn toward to suction port into a waste chamber (if provided). After the new pipet solution reaches the tip of the patch pipet, it will diffuse into the cell (whole-cell recording) or affect the membrane channels encompassed by the pipet tip

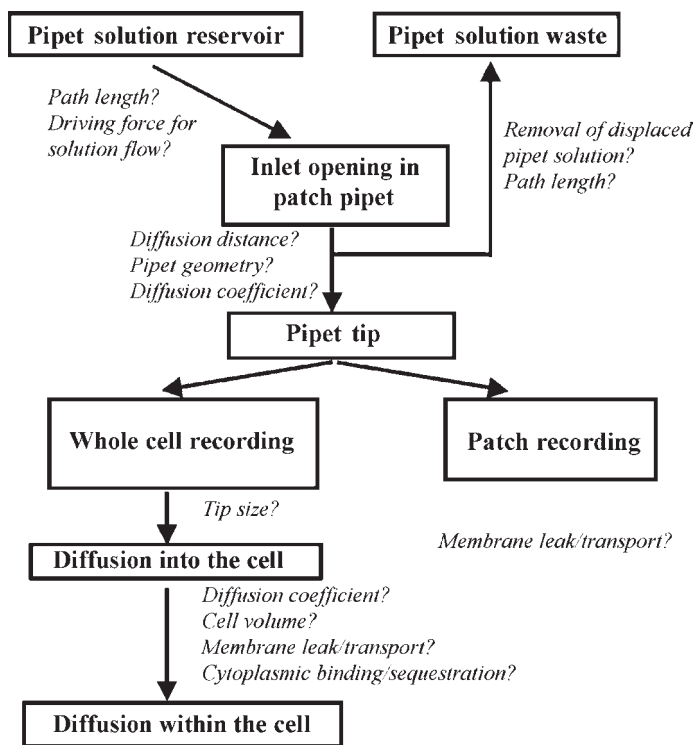


Fig. 2. Components of a pipet perfusion device and key questions one needs to consider when constructing such a device and during experimental design and data interpretation.

(patch recording in one of three configurations: cell-attached, inside-out, and outside-out).

The following points require careful consideration when designing a pipet perfusion device:

1. Fluid path length of the whole system. Electrolyte solution occupies the space from the reservoir to the patch pipet and to the waste chamber (if provided). A longer fluid path length will increase the stray capacitance and electrical noise of the system, causing a deterioration of the voltage-clamp quality. Therefore, it is desirable to machine these components into one

- piece (a compound pipet holder) or mount them very close to each other and make connections using tubings of the shortest possible lengths. Another advantage of shortening the path length between the reservoir and the pipet is a decrease in time needed for the new solution to reach the tip.
2. Driving force for solution flow. This is usually provided by suction applied to the back of the patch pipet. Thus solution is drawn from the reservoir through the inlet tube into the pipet. In this way, an open reservoir can be used, allowing multiple changes of pipet solution during the course of an experiment. To avoid a sudden change in suction at the pipet tip that may destroy the giga-seal, a low level of suction should be maintained during the recording. The amount of suction should be controlled and monitored all the time. Another way to move the pipet solution from the reservoir to the pipet tip is by applying pressure to the reservoir (Lapointe and Szabo, 1987). This requires a closed reservoir and makes multiple switches of pipet solution during a single experiment more difficult.
 3. Mounting and manipulating the reservoir. If the reservoir is separated from the pipet holder, it should be mounted on a manipulator and positioned very close to the patch pipet (to shorten fluid path length). The manipulator can move the reservoir from one to the other, while the inlet tube is kept stationary to minimize mechanical vibrations transmitted to the pipet tip. If there is a maintained suction during recording (see above), one needs to control the solution flow from the reservoir to the pipet using a constriction device (see an example in Fig. 3). Since there will be some motions when manipulating the reservoir, the manipulator ideally should be mounted on a rod or platform separated from the microscope stage. It is also a good idea to screw the pipet securely to a holder (see a simple design in Fig. 3). This will provide support to the pipet and avoid movement of the pipet tip when manipulating the reservoir that may transmit some movements to the inlet tube. To avoid large capacitance surges when switching the reservoir, the reservoirs should be kept isopotential by connecting them with Ag-AgCl wires.
 4. Diffusion distance from the opening of inlet tube to the pipet tip. The positioning of the inlet tubing inside the patch pipet is a crucial step in assembling the pipet perfusion device. The distance should as short as possible. Otherwise, the new pipet

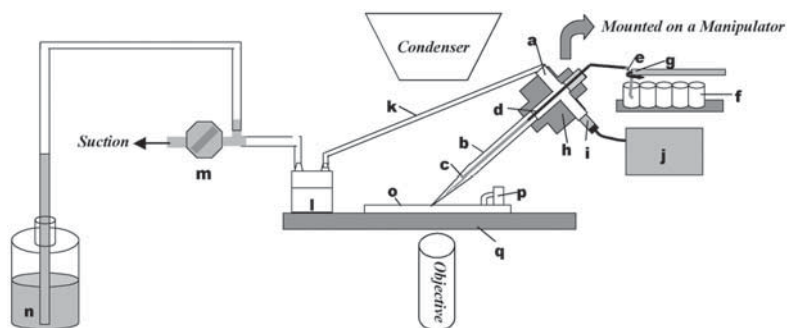


Fig. 3. A schematic diagram of the pipette perfusion device. Drawing is not to the scale. Keys: (a) Cross connector with one arm filled with silicon rubber (dotted area). (b) Patch pipette. (c) Inner tubing. (d) Stainless tubing connecting the inner tubing to the silastic tubing (e) whose free end is immersed in one of the pipette solution reservoirs (f) through a constriction device (g). The pipette solution reservoirs are mounted on a manipulator that allows switching of the solution perfusing the patch pipette. (h) Holder plate machined to have grooves accommodating the cross-connector and the patch pipette. The cross-connector is screwed to this holder plate securely. The whole assembly is mounted on a manipulator to allow positioning of the tip of patch pipette in the cell bath (o) monitored through a Nikon inverted microscope (shown here are microscope stage, (q) condenser and objective). (i) Ag-AgCl pellet half-cell connected to the pipette interior through a 3 M KCl/agar salt bridge and the cross-connector filled with the pipette solution. The other end of the Ag-AgCl pellet is connected to the headstage (j) through a short flexible wire. (k) Silastic tubing (~5 cm in length) connecting the pipette interior (via the cross-connector) to the waste chamber (l). The waste chamber is insulated from the metal surface, and is air-tight with two connectors. One is connected to the pipette interior through k. The other is connected to the room suction through a multi-turn valve (m). The valve controls the degree of suction applied to the pipette, monitored by the height of a water column (n). (p) Ag/AgCl pellet connecting the bath solution to ground via a 3 M KCl/agar salt bridge.

solution exiting from the inlet tube opening will be drawn to the suction port more than diffusing toward the pipet tip. This will delay the time needed for a total exchange of the solutions at the pipet tip. On the other hand, if the inlet tube is

pushed against the pipet tip and obstruct the pipet lumen, suction can not reach the pipet tip. A rule of thumb is to make the inlet tube opening at a diameter of 40–70 μm , and position the inlet tube inside the pipet under a microscope in such a way that the inlet tube opening occupies about half of the lumen of the pipet (Lapointe and Szabo, 1987). Another factor is the geometry of the patch pipet. Making a steep tapering will reduce the resistance to solution diffusion inside the pipet and allow a closer proximity of the opening of inlet tube to the tip, accelerating the solution exchange here.

5. Kinetics of solution change within the cell. The most important rate-limiting factor for solution change within the cell is the pipet tip: the larger the tip, the faster the diffusion of a new pipet solution into the cell. Other important factors include: cell volume (larger cells requires more time to reach an equilibrium within the cell) and the diffusion coefficient of newly introduced molecules (protein molecules require more time to reach an equilibrium than small molecules). As to how closely the intracellular milieu can be controlled by the content the of pipet solution, one needs to consider whether there is binding of ions or molecules under investigation to intracellular molecules or organelles (e.g., Ca buffer and stores, pH buffer), whether the substance can leak out or be transported out of the cell (e.g., Na transport out of the cell by Na/Ca exchange, Na pump, and Na/H exchange, lipid-soluble molecules leak out through the membrane). Two papers have provided very useful discussion of these issues (Kameyama et al., 1985; Oliva et al., 1988).

5. Detailed Description of a Pipet Perfusion Device and Assembly of Pipet with Accessories

Figure 3 depicts a schematic diagram of the pipet perfusion device used in our laboratory. This is based on the design of Soejima and Noma, with the modifications that the pipet holder is fabricated from a simple cross-connector and the waste chamber is separated from the pipet holder (but mounted very closely). This is a very practical design, with inexpensive and readily available materials and only minimal amount of machine shop work.

Following is a detailed description of how to assemble the pipet and accessories:

1. Fill one arm of the cross connector (Cole Palmer, Cat. #P-06297-10) with silicone rubber (Toshiba TSE3500). A stainless tubing (od 1 mm, Cole Palmer Cat. #P-03300-03) is inserted as shown in Fig. 3. The inlet tube (drawn out PE tubing, see above) is connected to one end of the stainless tubing and a fine silastic tubing (id 1 mm) is connected to the other end. Both should fit the stainless tubing snugly.
2. Connect a ~5 cm outlet silastic tubing (id 1.5 mm) to one arm of the cross-connector. This will be used to connect the cross connector to the waste chamber/suction (Fig. 3). Epoxy this junction if necessary to prevent air leak.
3. Connect the fine silastic tubing via a needle to a syringe filled with the control pipet solution. Fill all the tubing space with the control pipet solution.
4. Connect the 3 M KCl salt bridge/Ag-AgCl half-cell to the cross-connector as shown in Fig. 3. Make sure that the half-cell fits tightly.
5. Fill the space inside the cross-connector and the outlet silastic tubing with the control pipet solution. Use an alligator clip to clamp off the outlet tubing.
6. Heat-polish the patch pipet to make the tip of the desired size. Put a small piece of silastic tubing at the rear end of the patch pipet as a "sleeve". Fill the patch pipet with the control pipet solution (first capillary action to fill the tip and then back fill). Make sure there is no air bubble in the pipet.
7. Connect the patch pipet to the solution-filled cross connector. Use the "sleeve" to fit the pipet snugly into the connector (Fig. 3). At this time, check to make sure that there is no air bubble trapped in any part of the assembly.
8. Under a microscope (40 \times) move the stainless tubing back and forth in the silicone rubber so that the opening of the inlet tube is positioned at a desired location (100–300 μ m from the tip of the patch pipet). Before mounting the assembly to the holder plate, it is a good idea to check whether the inlet tube is still open or whether this opening is pushed against the patch pipet tip. This can be done by removing the alligator clamp from the outlet tubing and push the plunger of the syringe connected to the inlet tube. Solution should flow out from the outlet tubing without much resistance. The whole assembly is now ready for mounting to the holder plate. With practice, this assembling procedure can be routinely done in 5–10 min.

6. Concluding Remarks

The pipet perfusion technique has been used successfully to address many important scientific questions. Some degree of effort is needed to construct and maintain a pipet perfusion device, and it takes more time to assemble the pipet with accessories than a conventional pipet. However, the benefits provided by this technique (discussed in Subheading 1. Introduction) make the efforts all very worthwhile. It is anticipated that the pipet perfusion technique will find more applications in the era of molecular cloning and functional expression, when the constraint of channel expression density can be overcome in heterologous systems and a wide range of molecular tools are available to tackle important questions in the areas of physiology, pathology, and pharmacology.

References

- Alpert, L. A., Fozzard, H. A., Hanck, D. A., and Makielski, J. C. (1989) Is there a second external lidocaine binding site on mammalian cardiac cells? *Am. J. Physiol.* **257**, H79–H84.
- Byerly, L. and Yazejian, B. (1986) Intracellular factors for the maintenance of calcium currents in perfused neurones from the snail, *Lymnaea stagnalis*. *J. Physiol.* **370**, 631–650.
- Clapham, D. E. (1994) Direct G protein activation of ion channels? *Annu. Rev. Neurosci.* **41**, 464.
- Cull-Candy, S. G., Miledi, R., and Parker, I. (1980) Single glutamate-activated channels recorded from locust muscle fibers with perfused patch-clamp electrodes. *J. Physiol.* **321**, 195–210.
- Davis, M. J. and Gore, R. W. (1987) Double-barrel pipette system for microinjection. *Am. J. Physiol.* **253**, H965–H967.
- Fischmeister, R. and Hartzell, H. C. (1987) Cyclic guanosine 3',5'-monophosphate regulates the calcium current in single cells from frog ventricle. *J. Physiol.* **387**, 453–472.
- Hamill, O. P., Marty, A., Neher, E., Sakmann, B., and Sigworth, F. J. (1981) Improved patch clamp techniques for high resolution current recordings from cells and cell-free membrane patches. *Pflugers Arch.* **391**, 85–100.
- Hattori, K., Akaike, N., Oomura, Y., and Kuraoka, S. (1984) Internal perfusion studies demonstrating GABA-induced chloride responses in frog primary afferent neurons. *Am. J. Physiol.* **246**, C259–C265.
- Horie, M. and Irisawa, H. (1989) Dual effects of intracellular magnesium on muscarinic potassium channel current in single guinea-pig atrial cells. *J. Physiol.* **408**, 313–332.
- Horie, M., Irisawa, H., and Noma, A. (1987) Voltage-dependent magnesium block of adenosine-triphosphate-sensitive potassium channel in guinea-pig ventricular cells. *J. Physiol.* **387**, 251–272.

- Kameyama, M., Hofmann, F., and Trautwein, W. (1985) On the mechanism of β -adrenergic regulation of the Ca channel in the guinea-pig heart. *Pflugers Arch.* **405**, 285–293.
- Kameyama, M., Kakei, M., Sato, R., Shibasaki, T., Matsuda, H., and Irisawa, H. (1984) Intracellular Na^+ activates a K^+ channel in mammalian cardiac cells. *Nature* **309**, 354–356.
- Lapointe, J.-Y. and Szabo, G. (1987) A novel holder allowing internal perfusion of patch-clamp pipettes. *Pflugers Arch.* **410**, 212–216.
- Lee, K. S., Akaike, N., and Brown, A. M. (1980) The suction pipette method for internal perfusion and voltage clamp of small excitable cells. *J. Neurosci. Methods* **2**, 51–78.
- Makielski, J. C., Sheets, M. F., Hanck, D. A., January, C. T., and Fozzard, H. A. (1987) Sodium current in voltage clamped internally perfused canine cardiac Purkinje cells. *Biophys. J.* **52**, 1–11.
- Neher, E. and Eckert, R. (1988) Fast patch-pipette internal perfusion with minimum solution flow, in *Calcium and Ion Channel Modulation* (Grinell, A. D., Armstrong, D., and Jackson, M. B., eds.), Plenum, New York, pp. 371–377.
- Neher, E. and Sakmann, B. (1976) Single channel currents recorded from membrane of denervated frog muscle. *Nature* **260**, 799–802.
- Oliva, C., Cohen, I. S., and Mathias, R. T. (1988) Calculation of time constant for intracellular diffusion in whole cell patch clamp configuration. *Biophys. J.* **54**, 791–799.
- Oono, K. and Trautwein, W. (1991) Potentiation by cyclic GMP of β -adrenergic effect on Ca^{2+} current in guinea-pig ventricular cells. *J. Physiol.* **443**, 387–404.
- Saxena, N. C., Fan, J.-S., and Tseng, G.-N. (1997) Effects of elevating $[\text{Na}]$ on membrane currents of canine ventricular myocytes: role of intracellular Ca ions. *Cardiovas. Res.* **33**, 548–560.
- Soejima, M. and Noma, A. (1984) Mode of regulation of the ACh-sensitive K -channel by the muscarinic receptor in rabbit atrial cells. *Pflugers Arch.* **400**, 424–431.
- Tang, J. M., Wang, J., Quandt, F. N., and Eisenberg, R. S. (1990) Perfusing pipettes. *Pflugers Arch.* **416**, 347–350.
- Tseng, G.-N. and Boyden, P. A. (1991) Different effects of intracellular Ca^{2+} and protein kinase C on the cardiac T and L Ca^{2+} currents. *Am. J. Physiol.* **261**, H364–H379.
- Velumian, A. A., Zhang, L., and Carlen, P. L. (1993) A simple method for internal perfusion of mammalian central nervous system neurones in brain slices with multiple solution changes. *J. Neurosci. Methods* **48**, 131–139.
- Verrecchia, F., Duthe, F., Duval, S., Duchatelle, I., Sarrouilhe, D., and Herve, J. C. (1999) ATP counteracts the rundown of gap junctional channels of rat ventricular myocytes by promoting protein phosphorylation. *J. Physiol.* **516**, 447–459.

9

Patch-Clamp Detection of Cyclic GMP in Intact Cells

Richard H. Kramer

1. Introduction

Information is transmitted throughout the nervous system by chemical and electrical signals. The cacophony of neuronal signals does not end at the cell surface, but continues deep into cells via diffusible intracellular messenger molecules. The list of molecules that serve as intracellular messengers continues to expand, but several stand out as very common examples, including Ca^{2+} , cyclic nucleotides (cAMP and cGMP), and inositol phospholipids and their metabolites (IP_3 , diacylglycerol, etc.). Cellular responses to extracellular neurotransmitters are often mediated by one or more of these intracellular messengers, affording several functional advantages. Intracellular messengers allow spatial spread of signals within cells, contribute to amplification of signals, and allow responses to persist even after the neurotransmitter is gone from outside the cell. Intracellular messenger systems are also advantageous because they participate in a great degree of “cross-talk,” increasing the repertoire of responses to a given external stimulus and allowing for biochemical computation at the level of an individual cell.

To understand the functions of intracellular messengers such as cAMP and cGMP, it is important to know something about the kinetics and spatial distribution of these molecules in the cytoplasm. We have focussed our attention on monitoring cGMP, both for technical reasons, and because cGMP is a fascinating and important intracellular messenger. Several physiological stimuli can

From: *Neuromethods*, Vol. 35: *Patch-Clamp Analysis: Advanced Techniques*
Edited by: W. Walz, A. A. Boulton, and G. B. Baker @ Humana Press Inc., Totowa, NJ

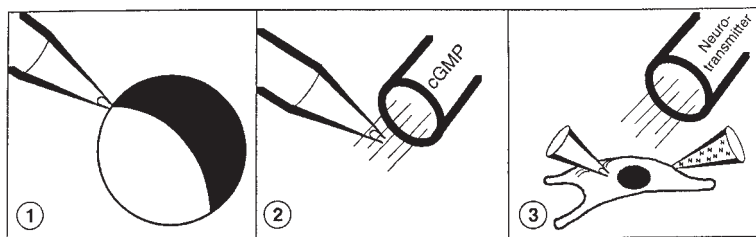


Fig. 1. The patch-cramming method. (A) Step 1: A glass patch pipet is used to obtain a detector inside-out patch from a *Xenopus* oocyte expressing CNG channels. (B) Step 2: The detector patch is calibrated with various concentrations of cGMP. (C) Step 3: The detector patch is "crammed" into a recipient cell to monitor intracellular cGMP in response to applied neurotransmitters, hormones, or drugs. A nystatin-containing pipet is used to voltage-clamp the cell using the perforated patch technique.

elevate cGMP in cells. Nitric oxide (NO), an intriguing and elusive intercellular messenger important for regulation of vascular tone and a putative retrograde messenger in the nervous system, signals primarily by activating soluble guanylate cyclase (GC), which synthesizes cGMP (for review, *see* Garthwaite, 1991; Moncada and Higgs, 1995; Hobbs et al., 1997). Receptors for atrial natriuretic factor and related brain natriuretic factors possess intrinsic guanylate cyclase activity and therefore also signal through cGMP (for review, *see* Garbers, 1991). Cyclic GMP exerts its physiological effects by binding to and activating several proteins including cGMP-dependent protein kinase (PKG), cGMP-activated cAMP phosphodiesterase, and cyclic nucleotide-gated (CNG) cation channels. Strategies for detecting cGMP depend on using these effectors as biosensors, because the effector proteins have evolved over eons to be highly sensitive and selective for cGMP over other intracellular molecules.

2. Patch-Cramming

The patch-cramming method utilizes ion channels that are directly sensitive to a given intracellular messenger as biosensors for monitoring the cytoplasmic concentration of that molecule in an intact cell in real-time. As illustrated in Fig. 1, an excised inside-out patch of membrane is obtained from a cell expressing a high density of

the desired detector ion channel, for example a *Xenopus* oocyte. After calibrating the response of the detector channels to known concentrations of the second messenger in a cell-free environment, the detector patch electrode is inserted, or "crammed," into a recipient cell in which the intracellular messenger is to be monitored. Since the sensitive portion of the detector ion channels is exposed in an inside-out patch, after the detector patch is crammed into the recipient cell, the activity of the channels should reflect the cytoplasmic concentration of the intracellular messenger of interest. Using the patch-cramming method, one may examine continuous, real-time changes in the level of intracellular messengers in response to application of neurotransmitters, drugs, or other stimuli. A second pipet containing nystatin or amphotericin B can be used to simultaneously voltage-clamp the recipient cell, using the perforated patch method (Horn and Marty, 1988; Korn and Horn, 1992).

3. Detector Ion Channels

In theory, any ion channel directly gated by an intracellular messenger could be used as a patch-cram detector. This includes Ca^{2+} -activated channels, cyclic nucleotide-gated channels, and intracellular IP_3 receptors. In practice, we have used detector channels to monitor Ca^{2+} (Kramer, 1990) and cGMP (Trivedi and Kramer, 1998), although this chapter will concentrate only on cGMP. For the patch-cramming technique to be valid and effective in monitoring cGMP, several criteria must be met. First, the detector channels must be appropriately sensitive and selective for cGMP over other intracellular messengers and metabolites. To specifically sense cGMP, we have used a CNG channel specially engineered to reduce cAMP sensitivity and eliminate sensitivity to Ca^{2+} /calmodulin (for review, *see* Molday, 1996) and NO (Broillet and Firestein, 1996), which also directly affect some CNG channels. The detector channel that has proven to be optimal for cGMP detection is a chimeric construction between the bovine rod photoreceptor CNG channel, which is highly selective for cGMP over cAMP, and the catfish olfactory CNG channel, which is nonselective between cAMP and cGMP, but which has a high apparent affinity to both. The resulting chimeric channel (Fig. 2A), named RON-S2 (Goulding et al., 1994), is highly sensitive and selective for cGMP ($K_{1/2}$ for activation = 2–5 μM), with cAMP eliciting responses only above 1 mM

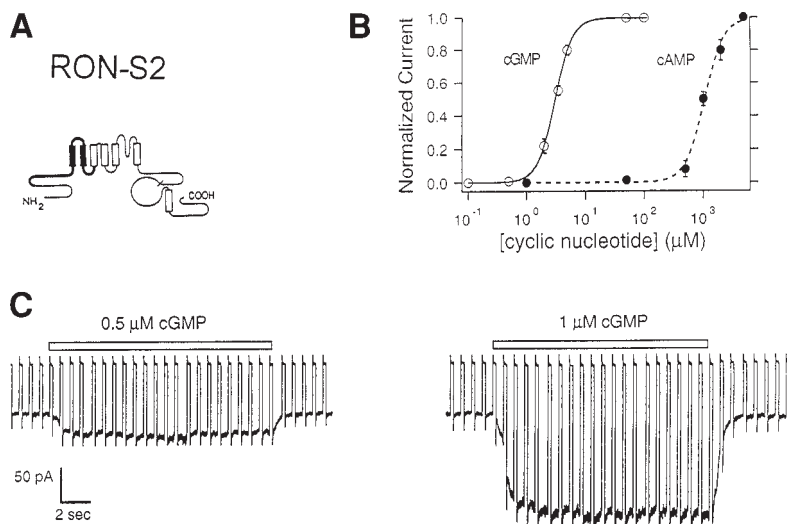


Fig. 2. Properties of detector ion channels. (A) The transmembrane topology of RON-S2, the cGMP detector channel. RON-S2 is a chimeric CNG channel with bold drawn domains (cytoplasmic region near the N-terminus and S1-S2 transmembrane domains) originating from the catfish olfactory CNG channel α subunit (Goulding et al., 1992) and lightly drawn domains originating from the bovine rod CNG channel α subunit (Kaupp et al., 1989). (B) Dose-response curves of RON-S2 channel activation by cGMP and cAMP. (C) Detector patch calibration responses to cGMP. Current transients were induced by repeated voltage pulses from -75 to 0 mV. Note that less than $1 \mu\text{M}$ cGMP can be clearly detected with high temporal resolution.

(Fig. 2B), outside the physiological range found in most cells. Unfortunately, it has been much more difficult to engineer a detector CNG channel for cAMP. All known natural or mutant CNG channels that are activated by cAMP are also at least as sensitive to cGMP (Zagotta and Siegelbaum, 1996). Therefore, at least for the time being, we have focused our attention on using the patch clamp technique for cGMP rather than cAMP.

The RON-S2 appears to be insensitive to other intracellular messengers. While it is impossible to screen every chemical constituent of cytoplasm on these channels, we have tested a wide variety of molecules, including amino acids, nucleotides, and cyclic nucleo-

tides, nitric oxide donors, phosphodiesterase inhibitors, and several other drugs, and none of these has any measurable ability to directly activate the channels or affect their sensitivity to cGMP. RON-S2 channels can express very effectively in *Xenopus* oocytes, at a level of several hundred per μm^2 of plasma membrane. Hence, even with very low concentrations of cGMP ($<1 \mu\text{M}$), which activate $<1\%$ of the channels, the combination of high channel density and high sensitivity insures relatively large responses with high signal-to-noise characteristics (Fig. 2C). The expression level varies between oocytes. As a rule of thumb, patches generating more than 1 nA (driving force = 75 mV) of current in response to saturating (i.e., 1 mM) cGMP have a sufficient number of channels to accurately report 1 μM cGMP.

Like most CNG channels, the detector RON-S2 channels are voltage-insensitive and have rapid activation and deactivation kinetics (rise and fall times <100 ms) upon application and removal of cGMP. Moreover, the channels exhibit no desensitization to prolonged (>10 min) applications of cGMP. All of these properties are highly desirable characteristics for quick and accurate monitoring of cGMP.

CNG channels, like most ion channels, are subject to modulation by protein phosphorylation. In particular, *Xenopus* oocyte membranes contain constitutively active protein tyrosine kinases (PTKs) and phosphatases (PTPs) that act to phosphorylate and dephosphorylate the channels, respectively (Molokanova et al., 1997; 1999). When a patch is excised in the absence of ATP, the PTP effectively dephosphorylates the channel, rendering it more sensitive to cGMP by two- to threefold. Addition of ATP allows the PTK to partly reverse the process, lowering cGMP sensitivity. An effective way to prevent CNG channel phosphorylation from confounding cGMP measurement is to remove the crucial tyrosine phosphorylation site (Y498) from the channel protein by mutating it to a phenylalanine (Molokanova et al., 1999).

4. The Patch-Cramming Procedure

The patch-cramming procedure itself is rather simple. First, the detector patch is excised from the oocyte and calibrated with different concentrations of cGMP. Repeated voltage pulses (10 mV, 100 ms) are applied to elicit currents, allowing measurement of the conductance of the detector patch. Because the gating of CNG

channels is largely voltage-insensitive, patch conductance is independent of the holding potential, but is a reliable indicator of cGMP concentration. After calibration is complete, the pipet is moved away from the oocyte and toward a glass cover slip, upon which recipient cells are attached. In most studies to date, we have used a rat neuroblastoma cell line, N1E-115 cells, as the recipient cell. These cells can be induced to differentiate into neuronal-like cells by repeated exposure to DMSO (Kimhi et al., 1976). Differentiated N1E-115 cells can reach 50–100 μm in diameter and are easy targets for patch cramming. The detector pipet is brought into close proximity to the recipient cell and a motorized or piezoelectric-driven micromanipulator is used to provide 2–5 μm steps to insert the pipet into the recipient cell. Often, considerable “dimpling” of the recipient cell occurs before impalement is successful. To ascertain that successful impalement has occurred, the following procedure is used. Before patch insertion, a bolus of cGMP (5–10 μM) is applied in the vicinity of the recipient cell to activate channels in the detector patch. This extracellular concentration is much higher than in cytoplasm, so successful impalement is accompanied by a decrease in the patch conductance, reflecting the decrease in cGMP detected by the channels. If the cramming procedure is performed on a cell that has been voltage-clamped (i.e., by the perforated patch method), changing the intracellular voltage will shift the basal current in the detector patch, without changing the conductance measurements.

In our hands, the patch cramming procedure is successful in 25–50% of attempts on appropriate recipient cells. In cases where the procedure is not successful, the main problem is damage or explosion of the recipient cell. With conventional patch electrodes (1–2 μm tip diameter) we have had success on cells with diameters of 30 μm or greater, with higher success rates in larger cells. In preliminary studies, we successfully inserted detector patches into primary cultured rat dorsal-root ganglion (DRG) neurons, with diameters of about 40 μm . We were unsuccessful in cramming cultured hippocampal pyramidal cells, with somatal diameters of about 15 μm . However, we did succeed with rat ventricular myocytes, which were “rounded-up” after 5–6 d in culture. In DRG cells and myocytes, 100 μM IBMX led to an increase in detector patch conductance, indicating an increase in cGMP. In future studies, we will attempt to use the patch-cram technique on Purkinje neurons in cerebellar slices and horizontal and ganglion cells from

retina. These cells not only may be sufficiently large, but they exhibit interesting and important forms of functional modulation and/or plasticity possibly mediated by cGMP. Various other cells may be suitable targets, including oocytes, invertebrate neurons, and skeletal muscle fibers.

It is possible that smaller pipets will allow patch cramming of smaller cells. However there is a trade-off; as small pipets usually result in excision of smaller excised patches containing fewer detector ion channels. In culture, some cell types "flatten-out" to a great extent, which can also lower the success rate. The detector patch is rarely disrupted upon insertion into the recipient cell, presumably because excised inside-out patches are recessed into the lumen of the pipet, and therefore protected by the walls of the pipet tip. Likewise, it is very unlikely for the pipet to "pick up" an additional patch of membrane originating from the recipient cell upon insertion, because the pipet tip has already contacted the donor cell (the oocyte) and the pipet tip is no longer sufficiently clean for additional seal formation.

It should be noted that patch cramming has been used not only as a method for tracking intracellular messengers such as cGMP, but also to study ion-channel modulation itself. Thus, once ion channels are removed from their normal cytoplasmic environment by excising a membrane patch, soluble biochemical systems that modulate or maintain channel activity may be lost, resulting in changes in gating or "run-down" of activity. By cramming the patch electrode back into the cell of origin, various investigators (Catarsi and Drapeau, 1996; Tang and Hoshi, 1999; Costantin et al., 1999) have convincingly demonstrated that cytoplasmic constituents, such as protein kinases, are necessary for maintaining activity of certain ion channels.

5. The Patch-Cram Set-Up

Little specialized equipment is needed for patch-cram measurements. We have used a simple inverted compound microscope (Nikon TMS) for visualizing both the source of the detector patch (a *Xenopus* oocyte) and the recipient cells (neuroblastoma cells grown on a polylysine coated glass cover slip). The oocyte is opaque, so it appears dark when viewed through the inverted scope. Therefore, patches must be obtained while blindly approaching the "dark side of the oocyte" with the patch pipet. After forming a

seal and excising an inside-out patch, we use a gravity-fed 8-channel superfusion manifold to apply various cGMP concentrations for patch calibration. Two patch-clamp amplifiers are required; one for amplifying signals from the detector patch and one for voltage-clamping the recipient cell. Our microscope is mounted on a motorized X-Y translation stage, so the microscope is moved under the preparation while the electrodes and the cells are kept in place. This allows visualization of either the oocyte or the target recipient cell without the need to reposition either the detector patch or recipient cell electrodes. Both data streams (detector patch current and recipient cell current) are digitized, stored, and analyzed using a Pentium III computer equipped with Axon Instruments pClamp 8.0 software.

We have recently assembled a new patch-cram set-up that will allow patch-cram recording from appropriately large neurons in tissue slices. The components of the set-up are nearly identical to those described earlier, except for the presence of an upright water-immersion microscope (Olympus BX51) instead of the inverted scope. Initial experiments will utilize Purkinje neurons in rat cerebellar slices and horizontal and ganglion cells from salamander retinal slices as the recipient cells.

Like other CNG channels (Zagotta and Seigelbaum, 1996), the detector CNG channel exhibits voltage-dependent block in the presence of sufficiently high concentrations of Ca^{2+} or Mg^{2+} . To maximize the detector patch signal, both the pipet solution, bathing the extracellular surface of the channels, and the cGMP-containing calibration solutions, applied on the intracellular surface of the channels, are kept essentially devoid of Ca^{2+} or Mg^{2+} by including EGTA and EDTA. Except for the lack of Mg^{2+} , the calibration solution approximate the conditions the patch will experience after cramming into cytoplasm, where free Ca^{2+} is $<1 \mu\text{M}$ and free Mg^{2+} is $\sim 1 \text{ mM}$. We hold the detector patch at -75 mV both during calibration and after insertion into the cell. Internal Mg^{2+} blocks outward currents elicited at positive membrane potentials, but it does not block inward currents elicited at negative potentials, so the presence or absence of Mg^{2+} is without consequence.

One problem that arises in the patch-cram procedure regards differences in the nature of the calibration solutions and the physiological solution used to bathe the recipient cells. Whereas removing Ca^{2+} or Mg^{2+} is useful for patch calibration, exposing recipient cells to divalent cation-free solution may not be desirable. In neu-

roblastoma cells, cGMP responses seem to be unaffected by exposure to calibration solutions, but there could be more serious problems with other recipient cells or tissue slices. To avoid potential problems associated with contaminating the recipient cells with calibration solutions, we are now using a 3-compartment chamber, with one compartment for the oocyte, one compartment for the recipient cell or slice, and an intermediate compartment that acts as a dam/reservoir for transferring the detector patch from the calibration solution to the solution bathing the recipient cells. A commercial source for such a chamber is Warner Instruments (catalog number RC-28).

6. Real-Time Measurement of cGMP in Intact Neuroblastoma Cells

To illustrate the utility of patch cramming, I will describe studies in which we have monitored cGMP in N1E-115 neuroblastoma cells (Trivedi and Kramer, 1998). After insertion of a detector patch into a recipient cell, application of a muscarinic agonist (oxotremorine-M, or oxo-M) cause constant amplitude voltage pulses to generate larger current responses (Fig. 3A), indicating an increase in conductance. To relate the conductance change to the cGMP calibration, conductance is plotted with respect to time (Fig. 3B), with the pre-calibration responses indicated with arrowheads on the left x-axis. The detector patch usually survives for many minutes, so it can be removed from the recipient cell and recalibrated at the end of the experiment. The postcalibration response is indicated with arrowheads on the right x-axis. The observation that the pre- and postcalibrations are nearly identical indicates that the detector channels are not affected in a long-term manner by exposure to the recipient cell's cytoplasm. Rather, the conductance increase reflects a transient increase in cGMP. Judging from the calibrations, resting cGMP was $<1 \mu\text{M}$ and reversibly increased to near $5 \mu\text{M}$ at the peak of the oxo-M response.

Previous biochemical measurements (radio- or enzyme-immunoassays) from populations of homogenized cells showed that activation of muscarinic receptors leads to a rise in cGMP. This is true both for these cells (Hu and el-Fakahany, 1993; Mathes et al., 1996) and for sympathetic neurons (Ando et al., 1994), which are developmentally, biochemically and physiologically similar to N1E-115 cells (Kimhi et al., 1976). Studies utilizing Ca^{2+} indicator dyes,

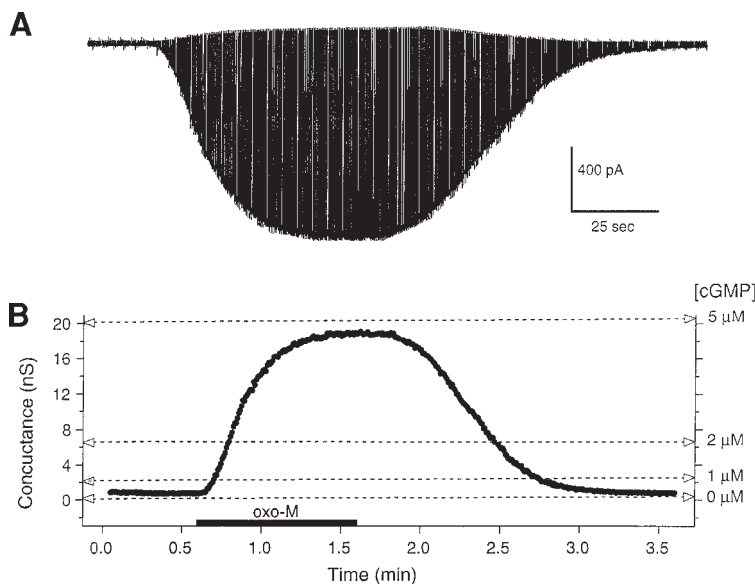


Fig. 3. Response of the detector patch to cGMP generated in the recipient cell in response to transmitter. (A) Application of a muscarinic agonist (10 μ M oxotremorine-M) elicits a reversible increase in currents elicited by constant amplitude voltage pulses. (B) Conductance values calculated from the currents in (A). The triangles on the left ordinate represent precalibration responses (before cramming) and those on the right ordinate represent postcalibration responses (after removal of the detector patch from the cell) to the indicated concentrations of cGMP.

pharmacological blockers, and biochemical assays, have led to a widely accepted model (Fig. 4) of how muscarinic activation leads to cGMP elevation (Briggs et al., 1985; Fostermann, et al., 1990; Thompson et al., 1995; Watta et al., 1998), which is also supported by many of our experiments. Binding of muscarinic agonists to surface M1 receptors leads to G-protein-mediated activation of phospholipase C (PLC), leading to hydrolysis of phosphatidyl inositol and production of diacylglycerol (DAG) and IP₃. IP₃ binds to its receptor, causing release of Ca²⁺ from intracellular stores, which results in an increase in cytoplasmic Ca²⁺. Ca²⁺, via calmodulin, activates nitric oxide synthase (NOS), producing NO, which goes on to activate soluble guanylate cyclase (GC). Activation of GC

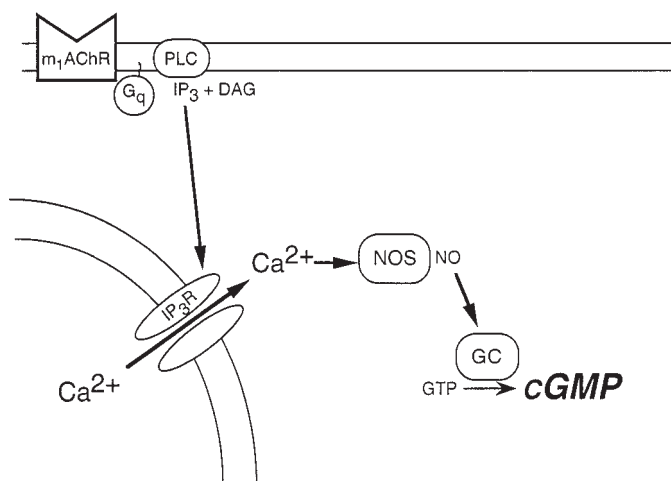


Fig. 4. Cellular signaling cascade linking activation of M1 muscarinic acetylcholine receptor to elevation of cGMP. See text for further details.

leads to production and elevation of cGMP. cGMP is eventually degraded by phosphodiesterase, terminating the response.

A major advantage of patch cramming for monitoring cGMP is the excellent time resolution possible with the technique. The rising kinetics of the cGMP response are nearly identical (time constants of about 40 s in each case) if the cascade is activated at the beginning (activation of the muscarinic receptor with oxo-M) or near the end (activation of GC by an NO-donor, NOR-4) (Fig. 5A). This observation suggests that the rate-limiting step in muscarinic elevation of cGMP is synthesis by GC, rather than more proximal steps, such as Ca²⁺ mobilization or NO production. Close inspection of cGMP transients elicited by oxo-M and NO reveals that while cGMP rises at the same rates, there is an approx 3 s longer delay when oxo-M is applied (Fig. 5B), consistent with the involvement of more steps than for NO. Activation of the detector patches either by directly applying cGMP before the patch is inserted (see Fig. 2C), or by photolysis of "caged cGMP" after the patch is inside the recipient cell, is very rapid (<1 s), indicating that the slow activation of the detector patch reflects the slow kinetics of cGMP elevation in the neuroblastoma cell, rather than a kinetic limitation of the detector.

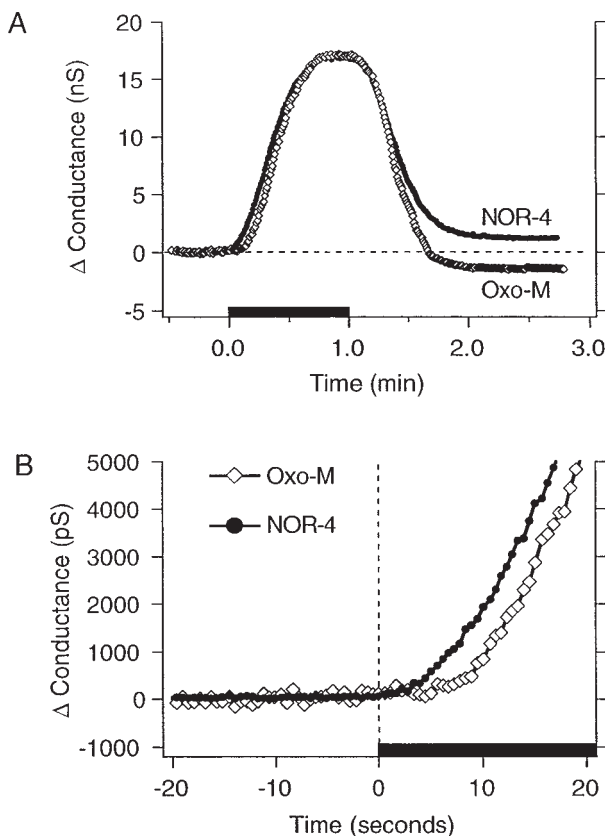


Fig. 5. Kinetics of cGMP responses. (A) The rising kinetics of cGMP elevation is very similar whether elicited by muscarinic activation (oxo-M) or downstream, using an NO donor (NOR-4). (B) The onset of the oxo-M response has a longer delay, probably because of the additional biochemical steps leading to activation of soluble guanylate cyclase.

The most surprising finding revealed with the patch-clamp techniques is that muscarinic agonists not only elevate cGMP, but also trigger a profound suppression of cGMP that can persist for hours after a brief agonist (1 min) application. Repeated or prolonged oxo-M exposures elicit decrementing cGMP responses (Fig. 6A), along with a pronounced “undershoot” in which the cGMP concentration after agonist exposure is lower than the basal cGMP

concentration before agonist exposure. In contrast, NO application elicits nondecrementing cGMP responses without an undershoot (Fig. 6B). Muscarinic receptors, like many G-protein coupled receptors, are known to desensitize in response to prolonged agonist exposure, whereas direct activation of GC by NO does not exhibit desensitization. However, we have observed that muscarinic activation not only causes suppression of cGMP responses elicited by muscarinic agonists, but also suppresses responses elicited by NO itself (Fig. 6C). The suppression persists for up to 2 h, and can also be elicited by activation of other G-protein coupled receptors (e.g., receptors for angiotensin, neurotensin, bradykinin) that act through a biochemical cascade similar or identical to the muscarinic system. Biochemical measurements of cGMP in populations of sympathetic neurons (superior cervical ganglia) in primary culture show that muscarinic agonists also suppress cGMP responses in *bona fide* mammalian neurons.

How does muscarinic activation cause this "long-term suppression" (LTS) of cGMP? Experiments in which cGMP was directly pressure injected into patch-clammed neuroblastoma cells show a dramatic decrease in cGMP transients, consistent with an increase in the activity of phosphodiesterase (PDE), the degradative enzyme of cGMP metabolism (Trivedi and Kramer, unpublished results). How does muscarinic stimulation lead to a rise in PDE activity? Some component of the muscarinic signaling pathway must feed-forward to regulate PDE activity. Experiments with ionomycin, a Ca^{2+} ionophore, and thapsigargin, which depletes internal Ca^{2+} stores, suggest that Ca^{2+} mobilization is necessary and sufficient for LTS induction. Additional experiments involving intracellular injection of the Ca^{2+} chelator BAPTA, indicate that while induction of LTS is Ca^{2+} -dependent, once initiated, maintenance of LTS is Ca^{2+} -independent. The Ca^{2+} -dependent "switch" that maintains LTS appears to be the enzyme Ca^{2+} -calmodulin dependent protein kinase II (CaMKII), which is famous for its role in mediating other forms of neuronal plasticity, such as long-term facilitation of synaptic transmission in the hippocampus (Malinow et al., 1988; Barria et al., 1997). CaMKII presumably phosphorylates PDE or an associated regulatory protein, increasing the enzymatic activity of PDE and suppressing cGMP signaling in the cell. The net effect is that muscarinic activation causes a single brief rise in cGMP, followed by silencing of cyclic nucleotide signaling that persists for several hours.

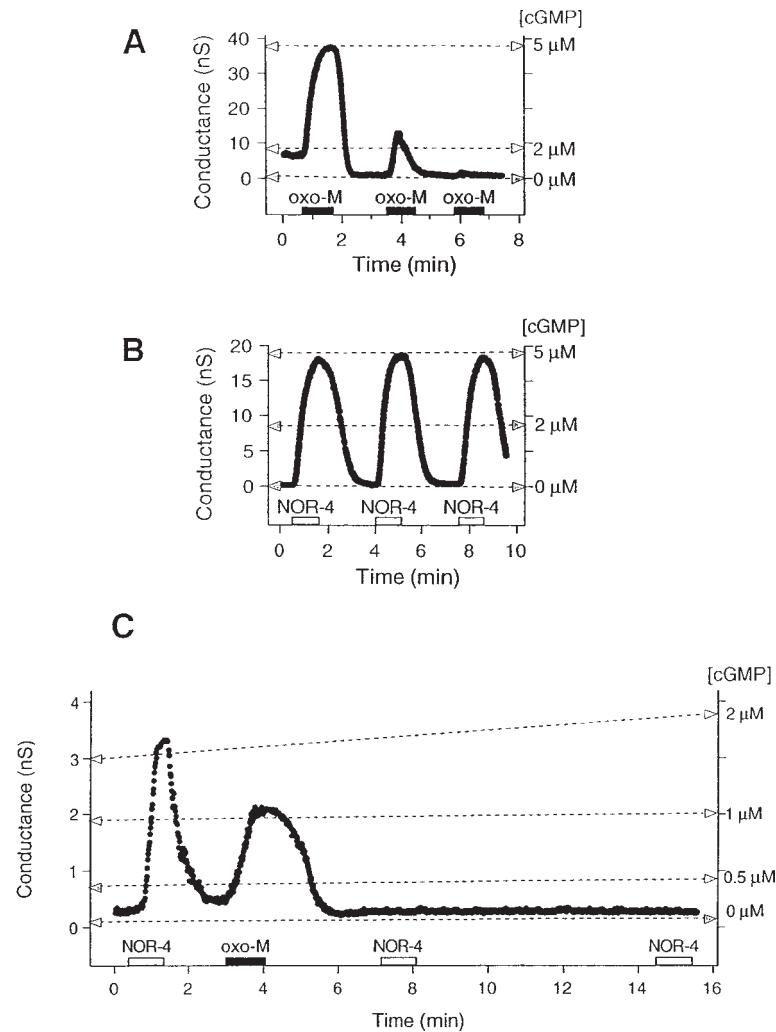


Fig. 6. Long-term plasticity of cGMP responses revealed with the patch-clamp method. (A) Repeated application of muscarinic agonist elicits decrements in cGMP responses. (B) Repeated application of NO donor elicits nondecrementing responses. (C) Muscarinic agonist induces long-term suppression (LTS) of cGMP responses elicited by NO.

7. Other Methods for Real-Time Monitoring of Intracellular Cyclic Nucleotides

Levels of total cAMP and cGMP in cells have been determined for many years using biochemical assays on extracts from populations of cells, using immunological methods such as radio- or enzyme- immunoassays. These methods require large numbers of cells and have minimal temporal resolution, since each time point requires a different sample. Moreover, these methods do not distinguish free vs bound cyclic nucleotides.

To improve temporal and spatial resolution and allow measurement from individual cells, fluorescent indicators have been developed. Cyclic AMP indicators have been derived from PKA, which consisting of 2 regulatory (R) subunits and 2 catalytic (C) subunits (holoenzyme: = R_2C_2). Binding of AMP to the R subunits results in dissociation of the disulfide-bonded R subunits (R_2) from the C-subunits. Roger Tsien and colleagues have attached fluorescent groups to the R and C subunits, allowing their dissociation to be monitored. The detector molecule consists of Fluorescein conjugated on the C subunit and Rhodamine conjugated on the R subunit, hence the name FICRhR (pronounced "flicker") (Adams et al., 1991). In the absence of cAMP the holoenzyme is intact and the fluorophores are in sufficiently close proximity to insure fluorescence resonance energy transfer (FRET). FRET occurs when excitation of a donor dye (fluorescein) triggers emission from a nearby longer-wavelength acceptor dye (rhodamine). Binding of cAMP induces dissociation of the R subunits, lowering rhodamine emission, because FRET drops off steeply with the distance between fluorophores.

FICRhR has been used on cells lines derived from tumors of smooth muscle, fibroblasts (Adams et al., 1991), and osteoblasts (Civitelli et al., 1994), in addition to native neuronal cells from *Aplysia* (Bacskai et al., 1993), and crustaceans (Hembel et al., 1996). FICRhR must be injected, so large cells make an easier target for its use than do small cells. This limitation has driven the development of a genetically-encoded cAMP indicator, which instead of being injected, can be transfected and expressed in cells of interest (Zacollo et al., 1999). Instead of fluorescein and rhodamine, two different mutants of green fluorescent protein (GFP) are used as the FRET donor and acceptor fluorophores. Changes in FRET, can be detected within tens

of seconds after application of neurotransmitters, forskolin, or non-hydrolyzable cAMP derivatives, confirming its usefulness for detecting cAMP in intact cells.

In addition to detecting cAMP, these fluorescent molecules have helped elucidate subcellular movements of PKA itself. Thus, after activation by cAMP, the C subunit enters the nucleus, whereas the R subunit does not (Bacskai et al., 1993; Zoccolo et al., 2000). While this finding is intrinsically interesting, the differential compartmentalization of R and C subunits poses a problem for using FICRhR as a reliable indicator of cAMP, especially when cAMP is repeatedly elevated. Since the intracellular concentration of cAMP is deduced from the extent of holoenzyme dissociation, processes that interfere with re-association of R and C subunits, such as differential subcellular compartmentalization, will seriously distort the cAMP signal. In addition, cells have endogenous PKA, and the labeled R and C subunits introduced by injection or exogenous expression will mix and match with the native R and C subunits, further distorting and diluting the FRET signal over time.

Very recently, Tsein and colleagues have introduced a genetically encoded fluorescent indicator that detects cGMP (Honda et al., 2001). The indicator, named "cygnet" (for cyclic GMP indicator using energy transfer), consists of 2 mutant GFP-based fluorophores coupled to cGMP-dependent protein kinase (PKG). Like PKA, PKG has regulatory and catalytic domains, but in PKG these domains are part of the same polypeptide, with the R domain near the amino terminus and the C domain near the carboxyl terminus. Binding of cGMP to sites on the regulatory domains causes a large conformational change that essentially unfolds the protein, resulting in an increase in the distance between fluorophores spliced onto the amino and carboxyl termini. The net result is a measurable change in FRET. Cygnet has an apparent affinity of about 1.5 μ M for cGMP. The fluorescent change induced by cGMP is small, but responses to IBMX, NO donors, and natriuretic peptides have been observed with lag times of hundreds of seconds.

8. Monitoring cGMP with Patch-Cramming or Fluorescent Indicators?

Both the patch-cram technique and the fluorescent indicator technique have advantages and drawbacks. Patch cramming can provide high temporal resolution measurement of cGMP, but since

the tip of the pipet is only at one cellular location, gives very little spatial information. At best, agonists can be applied locally on a cell at increasing distances away from the site where the detector patch is inserted into the recipient cell, potentially providing a rough profile of the spread of cGMP. In contrast, a fluorescent intracellular cGMP indicator may allow visualization of cGMP throughout the cell, giving a two- or even three-dimensional view of cGMP diffusion. To get an accurate picture of intracellular cGMP, it would be advantageous if the indicator were evenly distributed in the cytoplasm and not compartmentalized as previously shown for FICRhR. Further studies are needed to determine if this is the case. While there are obvious spatial advantages, the temporal resolution of the fluorescent indicators is not nearly as good as for detection with CNG channels, in part because the intrinsic responses of PKA and PKG to cyclic nucleotides are slower.

Detector CNG channels greatly amplify the effect of cGMP, whereas fluorescent derivatives of PKA or PKG do so to much lesser extent. Each time a CNG channel opens, millions of ions flow, such that the behavior of individual channels can be measured. A typical detector patch contains several hundred CNG channels, whose presence should have a negligible effect on intracellular cGMP. In contrast, in order to detect cGMP with fluorescent indicators, a much greater concentration of detectors must be introduced into the recipient cell, raising the possibility that the detector itself will alter cGMP levels by acting as a buffer. Moreover, kinase-based detectors are active enzymes, and the over-expression of these enzymes could potentially alter cellular behaviors.

Technically, methods using either detector are feasible, but in both cases the detectors are difficult to introduce into adult neurons. Patch clamping is restricted to rather large cells, presently limiting its use to only a handful of neuronal types. Fluorescent indicators must be injected, or expressed via transfection or infection of genes encoding the detector proteins. Theoretically, fluorescent detectors can be used in many more types of neurons, but in practice, it may be difficult to induce cells to express a sufficiently high fluorescent detector concentration to give FRET signals with high signal-to-noise characteristics. Despite these difficulties, both techniques hold out considerable promise for answering basic questions about cyclic nucleotide signaling in intact cells. Future technological advances will undoubtedly improve the sensitivity, temporal resolution, and ease of use of both techniques.

References

- Adams, S. R., Harootunian, A. T., Buechler, Y. J., et al. (1991) Fluorescence ratio imaging of cyclic AMP in single cells. *Nature* **349**, 694–697.
- Ando, M., Tatematsu, T., Kunii, S., and Nagata, Y. (1994) The intercellular communication via nitric oxide and its regulation in coupling of cyclic GMP synthesis upon stimulation of muscarinic cholinergic receptors in rat superior cervical sympathetic ganglia. *Brain Res.* **650**, 283–288.
- Backsaw, B. J., Hochner, B., Mahaut-Smith, M., Adams, S. R., Kaang, B. K., Kandel, E. R., and Tsien, R. Y. (1993) Spatially resolved dynamics of cAMP and protein kinase A subunits in Aplysia sensory neurons. *Science* **260**, 222–226.
- Barria, A., Muller, D., Derkach, V., Griffith, L. C., and Soderling, T. R. (1997) Regulatory phosphorylation of AMPA-type glutamate receptors by CaMKII during long-term potentiation. *Science* **276**, 2042–2045.
- Briggs, C. A., Horwitz, J., McAfee, D. A., Tsymbalov, S., and Perlman, R. L. (1985) Effects of neuronal activity on inositol phospholipid metabolism in the rat autonomic nervous system. *J. Neurochem.* **44**, 731–739.
- Broillet, M. C. and Firestein, S. (1996) Direct activation of the olfactory cyclic nucleotide-gated channel through modification of sulphydryl groups by NO compounds. *Neuron* **16**, 377–385.
- Catarsi, S. and Drapeau, P. (1996) Modulation and selection of neurotransmitter responses during synapse formation between identified leech neurons. *Cell. Mol. Neurobiol.* **16**, 699–713.
- Civitelli, R., Bacskaï, B. J., Mahaut-Smith, M. P., Adams, S. R., Avioli, L. V., and Tsien, R. Y. (1994) Single-cell analysis of cyclic AMP response to parathyroid hormone in osteoblastic cells. *J. Bone Miner. Res.* **9**, 1407–1417.
- Costantin, J. L., Qin, N., Waxham, M. N., Birnbaumer, L., and Stefani, E. (1999) Complete reversal of run-down in rabbit cardiac Ca^{2+} channels by patch-clamping in *Xenopus* oocytes; partial reversal by protein kinase A. *Pflügers Arch.* **437**, 888–894.
- Dhallan, R. S., Yau, K. W., Schrader, K. A., and Reed, R. R. (1990) Primary structure and functional expression of a cyclic nucleotide-activated channel from olfactory neurons. *Nature* **347**, 184–187.
- Horn, R. and Marty, A. (1988) Muscarinic activation of ionic currents measured by a new whole-cell recording method. *J. Gen. Physiol.* **92**, 145–159.
- Forstermann, U., Gorsky, L. D., Pollock, J. S., et al. (1990) Hormone-induced biosynthesis of endothelium-derived relaxing factor/nitric oxide-like material in N1E-115 neuroblastoma cells requires calcium and calmodulin. *Mol. Pharmacol.* **38**, 7–13.
- Garbers, D. L. (1981) Guanylyl cyclase-linked receptors. *Pharmacol. Ther.* **50**, 337–345.
- Garthwaite, J. (1991) Glutamate, nitric oxide and cell-cell signalling in the nervous system. *Trends Neurosci.* **14**, 60–67.
- Garthwaite, J., Southam, E., Boulton, C. L., Nielsen, E. B., Schmidt, K., and Mayer, B. (1995) Potent and selective inhibition of nitric oxide-sensitive guanylyl cyclase by 1H-[1,2,4]oxadiazolo[4,3-a]quinoxalin-1-one. *Mol. Pharmacol.* **48**, 184–188.
- Goulding, E. H., Tibbs, G. R., and Siegelbaum, S. A. (1994) Molecular mechanism of cyclic-nucleotide-gated channel activation. *Nature* **372**, 369–374.
- Hempel, C. M., Vincent, P., Adams, S. R., Tsien, R. Y., and Sclerston, A. I. (1996) Spatio-temporal dynamics of cyclic AMP signals in an intact neural circuit. *Nature* **384**, 166–169.

- Hobbs, A. J. (1997) Soluble guanylate cyclase: the forgotten sibling. *Trends Pharmacol. Sci.* **18**, 484–491.
- Horn, R. and Marty, A. (1988) Muscarinic activation of ionic currents measured by a new whole-cell recording method. *J. Gen. Physiol.* **92**, 145–159.
- Honda, A., Adams, S. R., Sawyer, C. L., Lev-Ram, V. V., Tsien, R. Y., and Dostmann, W. R. (2001) Spatiotemporal dynamics of guanosine 3',5'-cyclic monophosphate revealed by a genetically encoded, fluorescent indicator. *Proc. Natl. Acad. Sci. USA* **98**, 2437–2442.
- Horn, R. and Korn, S. J. (1992) Prevention of rundown in electrophysiological recording. *Methods Enzymol.* **207**, 149–155.
- Hu, J. and el-Fakahany, E. E. (1993) Role of intercellular and intracellular communication by nitric oxide in coupling of muscarinic receptors to activation of guanylate cyclase in neuronal cells. *J. Neurochem.* **61**, 578–585.
- Kimhi, Y., Palfrey, C., Spector, I., Barak, Y., and Littauer, U. Z. (1976) Maturation of neuroblastoma cells in the presence of dimethylsulfoxide. *Proc. Natl. Acad. Sci. USA* **73**, 462–466.
- Kramer, R. H. (1990) Patch cramming: monitoring intracellular messengers in intact cells with membrane patches containing detector ion channels. *Neuron* **4**, 335–341.
- Lev-Ram, V., Jiang, T., Wood, J., Lawrence, D. S., and Tsein, R. Y. (1997) Synergies and coincidence requirements between NO, cGMP, and Ca^{2+} in the induction of cerebellar long-term depression. *Neuron* **18**, 1025–1038.
- Malinow, R., Madison, D. V., and Tsein, R. W. (1988) Persistent protein kinase activity underlying long-term potentiation. *Nature* **335**, 820–824.
- Mathes, C. and Thompson, S. H. (1996) The nitric oxide/cGMP pathway couples muscarinic receptors to the activation of Ca^{2+} influx. *J. Neurosci.* **16**, 1702–1709.
- Molokanova, E., Maddox, F., Luetje, C. W., and Kramer, R. H. (1999) Activity-dependent modulation of rod photoreceptor cyclic nucleotide-gated channels mediated by phosphorylation of a specific tyrosine residue. *J. Neurosci.* **19**, 4786–4795.
- Molokanova, E., Trivedi, B., Savchenko, A., and Kramer, R. H. (1997) Modulation of rod photoreceptor cyclic nucleotide-gated channels by tyrosine phosphorylation. *J. Neurosci.* **17**, 9068–9076.
- Moncada, S. and Higgs, E. A. (1995) Molecular mechanisms and therapeutic strategies related to nitric oxide. *FASEB J.* **9**, 1319–1330.
- Tang, X. D. and Hoshi, T. (1999) Rundown of the hyperpolarization-activated KAT1 channel involves slowing of the opening transitions regulated by phosphorylation. *Biophys. J.* **76**, 3089–3098.
- Thompson, S. H., Mathes, C., and Alousi, A. A. (1995) Calcium requirement for cGMP production during muscarinic activation of N1E-115 neuroblastoma cells. *Am. J. Physiol.* **269**, C979–C985.
- Wotta, D. R., Parsons, A. M., Hu, J., Grande, A. W., and El-Fakahany, E. E. (1998) M1 muscarinic receptors stimulate rapid and prolonged phases of neuronal nitric oxide synthase activity: involvement of different calcium pools. *J. Neurochem.* **71**, 487–497.
- Zaccolo, M., De Giorgi, F., Cho, C. Y., Feng, L., Knapp, T., Negulescu, P. A., et al. (2000) A genetically encoded, fluorescent indicator for cyclic AMP in living cells. *Nat. Cell Biol.* **2**, 25–29.
- Zagotta, W. N. and Siegelbaum, S. A. (1996) Structure and function of cyclic nucleotide-gated channels. *Annu. Rev. Neurosci.* **19**, 235–263.

10

Loose-Patch Voltage-Clamp Technique

Blake D. Anson and William M. Roberts

1. Introduction

As mentioned by Cole (1968) the connections between life and electricity have long held the attention of investigators, with observations dating from ancient examinations of the electric catfish *Malapterurus* in 2600 B.C to modern examinations of the structure/function relationships within individual electrically active proteins. Patch techniques use pipets with a smooth bore of less than one micron to 100 microns in diameter fashioned from capillary tubing. With this method, discrete areas of membrane can be sampled by pressing the rim of the patch pipet against the cell membrane to electrically isolate it from the external saline. Early experiments focally stimulated discrete areas of nerves or muscle fibers with capillary pipets to substantiate the all-or-none principle for skeletal muscle-fiber contraction (Lucas, 1909; Pratt and Eisenberger, 1919). Later investigations used single patch pipets to both elicit and record ionic currents from the same area of membrane (Strickholm, 1961). Currently, patch clamp techniques can be broken down into two broad categories based on the electrical resistance of the seal between the cell membrane and the rim of the pipet. "Tight-seal" techniques are associated with high seal resistances (>1 gigohm) while "loose-seal" techniques employ smaller seal resistances (kilo- to megohm range). The magnitude of the seal resistance is directly related to the resolution of the patch clamp. Initial tight-seal resistances were on the order of tens of megohms and enabled the first recordings of current flow through single channels (Neher and Sakmann, 1976; Neher et al., 1978).

From: *Neuromethods*, Vol. 35: *Patch-Clamp Analysis: Advanced Techniques*
Edited by: W. Walz, A. A. Boulton, and G. B. Baker @ Humana Press Inc., Totowa, NJ

Subsequent investigations found that seal resistances could be increased to the gigaohm range if particular care was taken to keep the cell membrane and patch pipet extremely clean (Hamill et al., 1981). The advent of tight-seal patch pipet technology spawned a plethora of high-resolution voltage-clamp experiments that has resulted in much of our current knowledge of ion-channel function and modulation.

The requirements of tight-seal recording technology limit its uses. For example, the small size and single use nature of tight seal pipets introduce sampling difficulties when gathering information on ion-channel distribution. The close proximity (<1 nm; Corey and Stevens, 1983) of pipet bore and cell membrane required for tight seal formation and subsequent low-noise recording precludes recordings from cells with thick extracellular sheaths or protective layers. Also, the physical distortion resulting from tight seal formation (Sakmann and Neher, 1983; Milton and Caldwell, 1990) may alter the underlying cytoskeleton as evidenced by Brownian motion within the bleb (Roberts et al., 1990), and increased lateral diffusion of membrane proteins (Tank et al., 1982), and even alter channel properties (Eickhorn et al., 1994). Loose-seal (also commonly referred to as "loose-patch") recordings, on the other hand, circumvent sampling difficulties by employing larger-bore pipets to record from multiple areas within and/or between cells. The low seal resistance allows for greater distance between cell membrane and pipet (20–100 nm; Stuhmer and Almers, 1982), thus allowing recording from "dirty" or covered cells. Formation of the loose-seal minimally perturbs the membrane and allows for long-term stable recordings. It is important to note that with both techniques, the requirements of the technology limit their usefulness; if one wishes to attain high resolution of relatively few or single channels, then the tight-seal patch clamp is the appropriate choice. However, if an investigator is examining channel distribution, needs to sample from the same population of channels multiple times, wishes to avoid generating "clean" cells, and keep the cytoskeleton relatively intact, then the loose-seal patch clamp is the appropriate choice. This chapter deals with the latter technology and its most recent modification, the whole-cell/loose-patch clamp (Anson and Roberts, 1998, Anson and Roberts, 2001). Previous reviews have also dealt with the basic loose-seal voltage clamp and the reader is encouraged to refer to them (Stuhmer et al., 1983, Roberts and Almers, 1992).

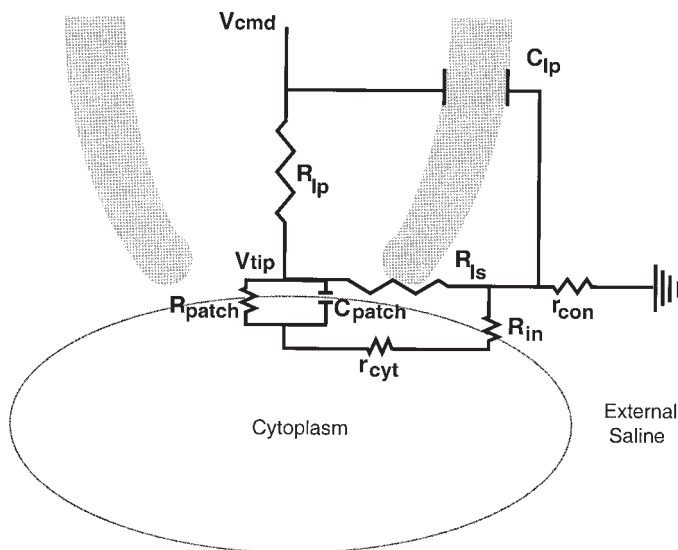


Fig. 1. Schematic of the loose-seal pipet and membrane interface. The primary electrical components at the pipet/membrane interface in loose-patch recording are the potentials of the voltage-clamp command (V_{cmd}) and the tip of the pipet (V_{tip}), the resistances of the pipet (R_{ip}), seal (R_{ls}), patch (R_{patch}), membrane outside of the patch (R_{in}), internal (r_{cyt}) and external (r_{con}) salines, and the capacitances of the loose-seal pipet (C_{ip}) and patch (C_{patch}).

2. The Loose-Seal Patch-Clamp Technique

The loose-seal patch-clamp typically uses large bore (5–20 μm diameter), low resistance (0.1–1 megohm) capillary pipets to electrically insulate a patch of membrane within the pipet bore from the external saline with a low-resistance seal. Figure 1 is a schematic illustrating the primary electrical components of the loose-seal setup at the pipet/membrane interface. The advantages of this technique arise from the gentle nature of the seal present between the pipet and cell membrane. The low resistance of the loose-patch seal does not require extremely close apposition of pipet and membrane and does not generally generate an omega figure with the membrane, thus leaving the membrane and associated proteins in a more physiological state. Also, the requirements for clean

pipets are not nearly as rigid in loose-seal formation as they are for tight-seal formation and a single large-bore pipet can record from many patches within or between cells. The ability to record from "messy" preps also allows the loose-seal technique to be used on cells with thick basal lamina or protective coverings as well as avoiding cell-isolation techniques that could result in altered channel properties (Eickhorn, 1994; Armstrong and Roberts, 1998). Ironically, the primary disadvantages of the loose-seal patch clamp also stem from the mild interaction between the pipet and cell membrane. The low seal resistance of the loose patch technique allows a large "leak current" to flow across the seal, thus a greater proportion of the total voltage drop to ground occurs over the resistance of the pipet. In order to maintain the tip of the pipet at the desired potential the voltage clamp must therefore supply greater amounts of current, which can ultimately mask ionic patch currents. The low resistance of the seal also adds significant amounts of noise due to the random movements of ions through the seal, and also provides a significant shunt to ground for active patch currents. This section examines pipet fabrication, the loose-seal voltage clamp, consequences of low-seal resistances, uncertainties in patch potential, and compensation techniques.

2.1. Pipet Fabrication

Loose-seal pipets are generated in the same basic manner as tight-seal pipets with a few slight modifications (Roberts and Almers, 1992). Pipets can be pulled on vertical or horizontal pullers, but must be done so with at least two heating stages. The first stage is used to draw out the capillary tubing until it is approx 250 μm in diameter. The hourglass portion of the drawn out tubing is then centered within the heating coil and heated until the two ends separate. The heat and force of the second and subsequent pulls are the primary determinants of tip shape and size, with greater heat and force producing longer and narrower tips. Most horizontal pullers have multiple parameters for adjusting the heat, strength, and duration of the pull that can be adjusted to achieve the desired tip size and shape. The tip shaping characteristics of passive vertical pullers are limited to the heat of the coil and pull of gravity. However, it is possible to lessen the force of the passive puller by simply tilting the puller away from the long axis of the pulled capillary tubing. It should be noted that the larger the bore

size one wishes to attain, the greater the proportion of pipets that are pulled with ragged and/or hanging rims. Sometimes these defects can be corrected through extensive firepolishing (which has its own caveats; *see* section on Uncertainties in Patch Potential), or by removing the hanging portion of the rim by gently touching it to another solid surface (the firepolishing filament is a handy surface).

Another method for pulling large pipets is the procedure used for pulling tight-seal macropatch pipets (Hilgemann, 1995). In this method, the patch pipet is pulled to a small diameter opening and mounted in a standard microforge equipped with a filament that has a bead of glass with a lower melting point than that of the pipet deposited on it. Just enough current is passed through the filament to heat it to the melting point of the glass bead without melting the pipet. The pipet is then pushed into the molten bead, the current through the filament is turned off, and the bead is allowed to solidify. The pipet is then backed away from the filament and (if all goes well) will break off at its junction with the bead. By varying the depth to which the pipet is inserted into the molten bead, one can vary the diameter of the pipet bore. It is has been our experience that fabricating loose-seal pipets is much more time-consuming and variable than pulling tight-seal pipets, with the majority of pipets pulled going straight into the waste container. In this aspect patience is indeed a virtue!

Regardless of the method chosen to fabricate the loose-seal pipet, heat polishing is required to smooth and shape the rim. Specialized microforges are available, or homemade devices can be fabricated within the lab. Typically the pipet and a platinum or nichrome wire heating filament are held by micromanipulators on opposite sides of a microscope equipped with a 20× or greater objective. Alternatively, a single manipulator can be used to hold either the filament or pipet while the other is held by the microscope's slide holder, or the filament can be attached to the condenser of the forge microscope and the pipet to the slide holder. When preparing to polish pipets, it is helpful to first focus on the filament, then move it well out of the way along a single axis, maneuver the pipet tip into the field of view, and subsequently bring back the filament. This method minimizes the number of tips inadvertently broken against the filament. Once pipet and filament are in position, apply current to the filament to heat it and polish the glass until the desired pipet tip shape is obtained. It is recommended to start with a tip that is approx twice the desired diameter. Extensive

heat polishing will then collapse and smooth the tip down to the appropriate size (although *see* Uncertainties in Patch Potential section).

To protect delicate cells and prevent the membrane from creeping up the interior of the pipet (and thus avoid introducing errors in seal-resistance compensation) the pipet bore can be filled with a collagen plug. The plug is generated by drawing several μL of 1 mg/mL collagen in acetic acid into the pipet tip and allowing the solution to evaporate thus leaving a collagen meshwork. The collagen plug does not appreciably increase the pipet resistance and will also prevent excessively high resistance seals from forming (Roberts et al., 1990; Roberts and Almers, 1992).

2.2. The Loose-Seal Voltage Clamp

The basic patch-clamp design of a tight-seal patch clamp can be used for loose-seal recordings with a lower feedback resistor in the headstage and modifications for complete pipet and seal-resistance compensations. Most commercial amplifiers do not provide these modifications, however the Axopatch 300B (Axon Instruments) and the EPC-9 (HEKA Elektronik) voltage clamps can be used for loose-patch experiments. Stuhmer et al. (1983) and Roberts and Almers (1992) also provide descriptions of their home-made amplifiers.

2.3. Pipets, Seals, and Controlling Patch Potential

The ultimate goal of the patch clamp is to precisely control the potential and accurately record current flow across a patch of cell membrane. Inaccuracies in patch control and current recording are caused by the large voltage drop inside the pipet associated with current flowing through the pipet resistance. This resistance, and the accompanying voltage drop, are concentrated in the tapered region near the tip. The deviation between the potential at the tip of the pipet (V_{tip}) and the desired command voltage (V_{cmd}) is proportional to the internal resistance of the pipet (R_{lp}):

$$V_{\text{tip}} = V_{\text{cmd}} - (I - C_{\text{lp}} (dV_{\text{cmd}} / dt)) R_{\text{lp}} \quad (1)$$

where I is the current entering at the back of the pipet and $I - C_{\text{lp}} (dV_{\text{cmd}} / dt)$ is the current exiting at the tip. The difference between these currents, $C_{\text{lp}} (dV_{\text{cmd}} / dt)$, is the current that crosses the pipet

wall through the pipet capacitance (C_{lp}). The pipet capacitance is distributed uniformly along the submerged length of glass, so the capacitive current does not contribute significantly to the voltage drop because it escapes before encountering a significant part of R_{lp} . This capacitive current occurs only at the onset and offset of the voltage step, when dV_{cmd}/dt is large, and can be minimized by coating the pipet with Sylgaard™ to increase the distance between the conducting salines and prevent creep of external saline up the outside of the pipet.

If not properly compensated, the resistances of the loose-patch pipet (R_{lp}) and seal (R_{ls}) introduce serious errors in the potential at the tip of the pipet (V_{tip}) and the measured patch current (I_{patch} ; Fig. 1). First, during steps of V_{cmd} , the similar magnitude of R_{lp} and R_{ls} cause a significant proportion of V_{cmd} to drop across R_{lp} causing V_{tip} to deviate from V_{cmd} . Second, V_{tip} also changes as a function of active currents flowing across the patch (I_{patch}). Third, there is a significant shunt to ground through R_{ls} for I_{patch} . Last but not least, during steps of V_{cmd} , the large current flowing through the series combination of R_{lp} and R_{ls} can obscure the much smaller and more interesting I_{patch} . Ignoring for the moment r_{con} , the equivalent circuit in Fig. 1 shows R_{lp} in series with the parallel combination of $R_{ls} \parallel R_x$, where R_x is the series combination of R_{patch} , r_{cyt} , and R_{in} . R_{patch} is the largest component of R_x and, except when large patch currents are activated, orders of magnitude greater than R_{ls} . Thus during step commands of V_{cmd} ,

$$V_{tip} \cong V_{cmd} \cdot \frac{R_{ls}}{R_{lp} + R_{ls}}. \quad (2)$$

If $R_{lp} = R_{ls}$, then $V_{tip} = V_{cmd}/2$. Smaller values of R_{ls} cause even larger errors.

Series resistance typically refers to any resistance existing in series with the resistance of the membrane under voltage control. In patch-clamp experiments, this includes the resistances of the pipet, cytoplasm, cell membrane, and the bath outside the pipet tip. In tight-seal patch-clamp experiments, the seal resistance is assumed to be infinite, and thus ignored, while the internal and external saline resistivities are considered relatively small, leaving the pipet resistance as the vast majority of the series resistance. Readers are strongly encouraged to read the excellent treatment of this topic and its consequences in patch-clamp recordings by

Armstrong and Gilly (1992). In loose-seal experiments, the seal resistance is of the same magnitude as the pipet resistance and must therefore be taken into consideration during experiments.

A series resistance error (V_{series}) occurs when active patch currents flow across the series resistance, thereby changing the tip potential: $V_{tip} = V_{cmd} - V_{series}$. Thus large I_{patch} can cause significant deviations in V_{tip} . In tight seal recordings where the seal resistance is assumed to be essentially infinite V_{series} is easy to calculate as $I_{patch}R_{pip}$. The situation is more complex in loose patch-clamp experiments because R_{lp} and R_{ls} are of similar magnitude and I_{patch} flows through their parallel combination thus,

$$V_{series} = I_{patch} \cdot R_{lp} \left(\frac{R_{ls}}{R_{ls} + R_{lp}} \right). \quad (3)$$

Combining Eqs. 2 and 3 shows V_{tip} as a function of V_{cmd} during the step command

$$V_{tip} = V_{cmd} \cdot \frac{R_{ls}}{R_{lp} + R_{ls}} + I_{patch} \cdot R_{lp} \left(\frac{R_{ls}}{R_{ls} + R_{lp}} \right). \quad (4)$$

Equation 4 demonstrates that for tight seal experiments where the seal resistance is much greater than the pipet resistance, V_{tip} approaches V_{cmd} during the step and in the presence of active currents the series resistance error is equivalent to the patch current flowing across the pipet resistance, while during loose-seal recordings where the seal resistance approaches the pipet resistance, the deviation of V_{tip} from V_{cmd} increases and the series resistance error decreases due to shunting of I_{patch} to ground. Equation 4 also shows that compensation must both increase V_{cmd} and scale I_{patch} by the same ratio, $(R_{lp} + R_{ls})/R_{ls}$.

In loose-seal recordings I_{patch} is a small fraction of the total pipet current (I_p), usually less than 10%. For example, ohm's law shows that a 100 mV step at V_{tip} across a R_{lp} of 500 kohm requires 200nA of current. Typical Na^+ currents from skeletal muscle fibers are <20nA and thus <10% of the total pipet current. Therefore the uninteresting "leak" current (so called because it leaks to ground through R_{ls}) must be subtracted from I_{patch} . Because I_{patch} is such a small component of the total pipet current, leak subtraction must

be very precise and typically involves both analog and digital subtraction procedures (Roberts and Almers, 1992).

2.4. Uncertainties in Patch Potential

The potential across the patch (V_{patch}) is determined by V_{tip} and the intracellular potential (V_{int}), $V_{patch} = V_{int} - V_{tip}$. Thus the error in V_{patch} is at least as large as the uncertainty in V_{int} . V_{int} can be determined with an intracellular or whole-cell pipet, estimated using assumed channel properties (such reversal potentials), or set to a particular potential via ionic substitution of the salines (V_{int} for *Xenopus* oocytes is close to 0 mV in 100 mM external K^+). The intracellular voltage will also change as a result of active currents flowing through the patch. The magnitude of the change depends upon the passive properties of the cell membrane and the size and duration of the active current. For a given rectangular current waveform of duration t

$$\Delta V = I_{patch} \cdot R_{in} \quad \text{for } t \gg \tau_m \quad (5)$$

$$\Delta V = I_{patch} R_{in} \cdot t / \tau_m \quad \text{for } t \ll \tau_m \quad (6)$$

where R_{in} is the input resistance of the cell and τ_m is the time constant of the cell membrane (Roberts and Almers, 1992). Thus brief transient currents can be (τ_m/t) -fold larger than sustained currents and still cause the same ΔV . This voltage error has typically limited the use of the loose-seal patch clamp to the study of transient currents from large cells with low R_{in} .

The final uncertainty in absolute patch potential is a form of "space clamp" error arising from nonisopotentiality of the membrane underneath the pipet annulus (Roberts and Almers, 1992). Channels located beneath the rim of the pipet experience a voltage between V_{tip} and 0 and thus behave differently than channels encompassed within the bore of the pipet. Previous reports have shown practical and theoretical interference by "rim currents" mediated by these channels while measuring Na^+ reversal potentials, but not peak current flow (Stuhmer et al., 1983; Almers et al., 1983). The probability of rim current artifacts impinging upon data increases with pipet annulus thickness and channel density. Thus one is left to empirically match pipet fabrication to the particular preparation under study.

2.5. Sealing and Recording Patch Currents

The first step in recording loose-patch currents is to determine R_{ip} and R_{is} and engage compensation. Once the pipet is in the bath, current offsets are nulled, small test voltage steps (V_{step}) < 5 mV are continually applied, and R_{ip} is calculated as V_{step}/I_{step} . This calculation overestimates R_{ip} by approx 10% due to r_{con} outside of the pipet (the exact value depending upon tip geometry; Roberts and Almers, 1992; Strickholm, 1961; Roberts, 1987). The pipet is then advanced until it makes contact with the cell and a seal begins to form as evidenced by decreases in I_{step} . Seal formation usually works best if the pipet bore can be positioned somewhat perpendicular to the cell membrane. For flat or cultured cell, it may be necessary to bend the shank of the pipet (Anson and Roberts, 2001). Once a seal has been made, R_{ip} compensation is engaged to 90% of the previously calculated R_{ip} . R_{is} compensation is now engaged and increased until I_{step} equals the baseline current level. If R_{is} is adjusted correctly, there should be minimal deflection of I_{step} from the baseline level for a series of V_{step} depolarizations within the linear range of the membrane. Depending on the voltage clamp, R_{is} can now be read from the setting on the leak compensation dial or a digital read-out. The track command of the screen driven Pulse software for the EPC-9 patch clamp is especially useful because it tracks R_{is} and adjusts compensation during the course of the stimulation. If necessary, R_{is} can be increased by pushing the pipet further into the cell or by applying slight suction to the back of the pipet. The analog circuitry described by Stuhmer et al. (1983) and Roberts and Almers (1992) enable 100% compensation for seal and pipet resistances. Most commercial patch-clamp amplifiers will allow full compensation for the seal resistance (leak subtraction), but they typically do not allow for full compensation of R_{ip} . Any errors in V_{tip} resulting from inaccurate estimation of R_{ip} or inability for full compensation, will be smaller by the ratio of R_{ip}/R_{is} . A rule of thumb for loose-seal recordings is that in order for the voltage clamp to maintain adequate control of V_{tip} , $R_{is} \geq 2 R_{ip}$ (Roberts and Almers, 1992).

Since I_{patch} is typically $\leq 10\%$ of the total pipet current, leak subtraction methods need to be accurate to 1% to give 10% or less error in measured I_{patch} . The R_{is} compensation described earlier is usually not adequate by itself, and must be augmented by digital leak subtraction. P/N leak subtraction is most commonly used. In

this method, small control voltage steps within the linear range of the membrane are averaged, scaled, and subtracted from a test pulse N times as large. P/N leak subtraction adds substantial amounts of noise to the signal and to minimize this contribution to less than that present in the test signal, at least N^2 control pulses should be used for each test pulse. Noise can also be minimized by making the control pulses as large as possible without leaving the linear range of the cell membrane. Additionally, control pulses should be delivered as temporally close to the test pulse as possible to minimize the effects of fluctuations in R_{ls} . The combination of analog and digital R_{ls} compensation can be quite accurate, but the investigator should be aware that I_{patch} is not entirely separated from the leak current. The remaining artifact appears to arise from intrinsic nonlinearity in the seal resistance.

2.6. Loose-Patch Recording Applications

The relatively high levels of noise (including the leak subtraction artifact) inherent to the loose-patch clamp technique when the pipet is used as a stimulating and recording electrode has traditionally limited its use to cells with fairly high channel densities, which give rise to large patch currents that would substantially change the membrane potential of high impedance cells under physiological conditions. Thus a primary objective for stimulating and recording with the loose patch-clamp technique has been to map and/or characterize relatively high densities of ion channels on low-impedance cells such as skeletal muscle fibers (Korper et al., 1998; Matavel et al., 1998; Ruff, 1996a, 1996b, 1999; Milton and Behforouz, 1995; Lupa et al., 1993, 1995; Wolters et al., 1994; Lupa and Caldwell, 1994; Girod, et al., 1993; Ruff and Whittlesey, 1992, 1993a, 1993b; Araujo et al., 1993; Roberts and Almers, 1992), invertebrate muscle cells (Schwartz and Stuhmer, 1984; Zucker and Lando, 1986), cardiac myocytes (Kirstein et al., 1996a, 1996b; Kirstein et al., 1994; Eickhorn et al., 1994; Antoni et al., 1988), large neurons (Hong and Lnenicka, 1997; Cooper et al., 1992; Roberts and Almers, 1992), and glia (Marrero and Orkand, 1993; Blanco et al., 1993; Marrero et al., 1989). Artifacts are much smaller when the loose-patch pipet is simply used to record activity and not stimulate membrane. Under these conditions the loose-patch technique has been used to monitor electrical activity within neurons (Brodie et al., 1999), examine responses to olfactory (Dubin and Harris, 1997) and

gustatory (Varkevisser and Kinnamon, 2000) stimuli, and monitor synaptic activity by recording postsynaptic currents (Bennet et al., 1997; Correges and Dunant, 1996; Warren et al., 1995) even to the resolution of single quanta released from individual boutons (Forti et al., 1997). When the intracellular voltage must be determined or held at particular levels, a second whole-cell clamp can be used (Roberts and Almers, 1992). The second voltage clamp can also be used for stimulating the membrane while the loose-seal clamp records patch responses. This technique has enabled measurement of the leak conductance and mapping of ion channels on saccular hair cells (Roberts et al., 1990) and taste cells (Kinnamon 1988). However, to accurately map conductances under these conditions, the membrane beneath the loose-patch pipet must be well controlled by the second voltage clamp. If maintaining adequate voltage control is not possible, then one can switch the roles of the clamps and use the whole-cell clamp to record currents elicited through loose-patch stimulation. In theory, this technique affords even greater sensitivity. We have developed this technique (Anson and Roberts, 1998), which we call the whole-cell/loose-patch clamp, and used it to study the low-density distribution of Na^+ channels on skeletal myotubes as they develop in vitro (Anson and Roberts, 2001).

3. The Whole-Cell/Loose-Patch Voltage Clamp

As discussed above, the drawbacks of the traditional loose-seal patch clamp has typically limited its use to examining large cells designed to support fast action potentials (i.e., cells with high channel densities and low input resistances). Lupa and Caldwell (1990) have estimated the lower resolution of the loose patch clamp to be 1 mA/cm^2 of membrane, or approx the peak current through 10 Na^+ channels/ μm^2 . Loose patch recordings suggest that Na^+ current densities on fast-twitch vertebrate skeletal muscle fibers are present at of 15–30 mA/cm^2 at the end-plate and 2–5 mA/cm^2 within extrajunctional areas (Almers et al., 1983; Beam et al., 1985; Roberts, 1987). Thus the loose-patch technique has been an excellent method for mapping ion channels within mature skeletal muscle cells.

We wished to map the density of Na^+ channels on embryonic myotubes, where tight-seal cell attached patch recordings suggested channel densities of 1 channel/ μm^2 , an order of magnitude lower

than the resolving power of the traditional loose-patch clamp (Anson and Roberts, unpublished observations). As discussed previously, the resolution of the loose-seal patch clamp is much greater when it is used purely as a recording electrode. For mapping purposes, this would require a second stimulating clamp to be employed to accurately control the membrane potential. In the case of embryonic myotubes the second clamp (a tight-seal whole-cell voltage clamp) was unable to adequately control the myotube membrane potential. Therefore we used the tight-seal whole-cell pipet to record patch currents elicited through loose-patch stimulation (WCLP recording), hoping to use the advantages of one technique to overcome the disadvantages of the other technique. This section describes the theory, artifacts, and current recovery techniques of WCLP recording.

3.1. WCLP Theory

Figure 2 is a schematic detailing the WCLP setup at the cell membrane. In this technique, voltage steps are applied to the discrete patch of membrane contained within the bore of the loose-patch pipet. Current flow through the patch is then recorded by the whole-cell voltage clamp. In the ideal setting with no uncompensated whole-cell pipet resistance (R_{series}), an infinite membrane space constant, and no bath resistivity, whole-cell current would be equivalent to elicited patch current and faithfully recorded by the whole-cell voltage clamp. In the actual setting, however, the nonideal characteristics of the whole-cell voltage clamp and non-isopotentiality of the cell, introduces uncertainties in the whole-cell holding potential (and thus in patch potential as well) and grossly filters patch currents. Both uncertainties, but primarily filtering, vary as a function of distance between the stimulating and recording pipets. Therefore, if left in their raw form, recorded patch currents would inaccurately reflect channel densities within and between individual myotubes.

3.2. Estimating Patch Potential

In WCLP recordings, patch potential (V_{patch}) depends on the intracellular potential (V_{int}) and the potential at the tip of the loose-patch pipet (V_{tip}),

$$V_{patch} = V_{int} + V_{tip} \quad (7)$$

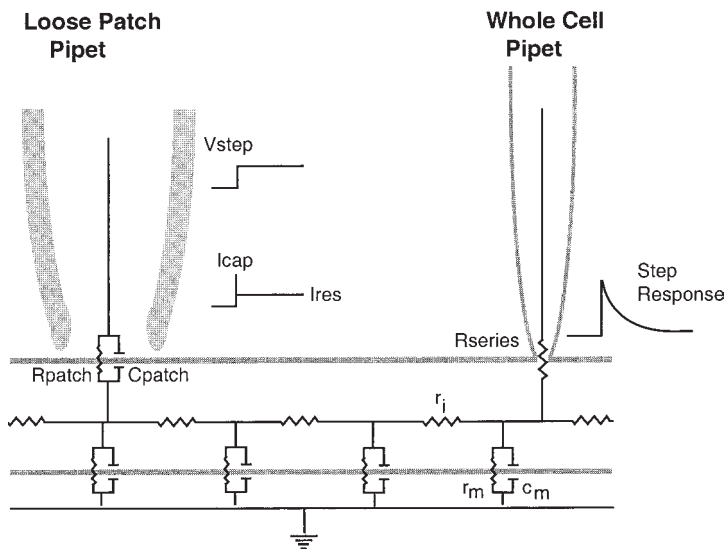


Fig. 2. Schematic of the primary filtering components of the WCLP recording arrangement. A rectangular voltage step (V_{step}) within the linear range of the cell applied by the loose-seal patch clamp generates a transient capacitive current (I_{cap}) that flows through the patch capacitance (C_{patch}) and a sustained resistive current (I_{res}) flowing through the patch resistance (R_{patch}). These currents are then filtered by the cable properties of the myotube (i.e., the internal resistance (r_i), membrane capacitance (c_m) and membrane resistance (r_m)) and the uncompensated series resistance of the whole-cell recording pipet (R_{series}). Thus the step response recorded by the whole-cell pipet is the sum of the filtered resistive and capacitive currents. Calculation of the filtered I_{cap} characterizes the filtering components of the set-up and allows recovery of unfiltered active patch currents.

In the absence of uncompensated R_{series} , V_{int} equals the whole-cell clamp command (V_c). However, uncompensated R_{series} is always present and the input resistance of the cell (R_{input}) is finite. Thus V_{int} near the whole-cell pipet is

$$V_{int} = \frac{V_c \cdot R_{input} + V_{rest} \cdot R_{series}}{R_{input} + R_{series}} \quad (8)$$

where V_{rest} is the resting membrane potential. For a non-isopotential cell, V_{int} will approach V_{rest} as a function of the cell's space constant (λ) with increased distance between the whole-cell and loose-patch pipets.

3.3. Recovery of Low-Frequency Patch-Current Components

In typical whole-cell tight-seal recordings where the cell is isopotential and $R_{input} \gg R_{series}$, whole cell currents are filtered by a one-pole RC filter (Levis and Rae, 1992), where R is the uncompensated R_{series} and C is the membrane capacitance. This is also the case when the WCLP clamp is applied to high-resistance isopotential cells. However, in WCLP recordings of nonisopotential cells where $R_{input} \approx R_{series}$ the effective RC filter is the $R_{series} \parallel R_X C$, where R_X represents cable properties of the cell; r_m, r_i, c_m . The whole-cell pipet will therefore only collect a fraction of the low-frequency patch-current components and a smaller fraction still of high-frequency components. The similar magnitudes of R_{series} and R_{input} present a situation identical to R_{ip} and R_{is} in loose-seal recordings (see above). Thus, currents collected during WCLP recordings must be scaled by the factor $(R_{input} + R_{series})/R_{input}$. R_{series} is calculated as V_{step}/I_0 , where I_0 is the whole-cell current extrapolated to time 0 and V_{step} is a small whole-cell voltage step. R_{input} is then calculated as $V_{step}/I_{ss} - R_{series}$, where I_{ss} is the steady-state level of whole-cell current in response to V_{step} . In our WCLP recordings from embryonic myotubes (Anson and Roberts, 2001), R_{input} was 10 to 100% of R_{series} , thus the whole-cell pipet only collected 90 to 50% of the patch current.

3.4. Recovery of High-Frequency Components

Recovery of the original current waveform is necessary for accurate determination of peak current values and channel density. The recovery process assumes that the cable properties of the cell and R_{series} are passive and temporally constant and therefore constitute a linear filter. Linear filters can be characterized by their impulse response, i.e., the manner in which they filter a spike of infinite amplitude and infinitesimal duration. Any time varying waveform can be approximated by a series of closely spaced finite impulses of different amplitudes (Jack et al., 1983). Therefore the output of

a linear filter is simply the superposition of the impulse responses of the impulses comprising the unfiltered waveform. The mathematical equivalent of such a superposition is convolution: the output of a linear filter is the convolution of the input with the filter's impulse response. Convolution, and its inverse deconvolution, is most easily handled in the frequency domain as simple multiplication (McGillem and Cooper, 1991). If $I_{unfiltered}$ is the true waveform of the patch current, then

$$F[I_{filtered}] = F[I_{unfiltered}] \cdot F[I_{impulse}] \quad (9)$$

where $F[]$ represents the Fourier transform operation, $I_{filtered}$ is the filtered current recorded by the whole cell electrode, and $I_{impulse}$ is the impulse response of the recording set-up for that particular patch. The inverse of convolution is deconvolution and in the frequency domain deconvolution is simply division. Thus rearranging Eq. 9 as

$$F[I_{unfiltered}] = F[I_{filtered}] / F[I_{impulse}] \quad (10)$$

shows that $I_{unfiltered}$ is the inverse Fourier transform of the ratio of the Fourier transform of the filtered patch current over the Fourier transform of the impulse response of the filter. The filtering characteristics of the myotube and R_{series} vary as function of distance between the two pipets, thus for each patch $I_{filtered}$ is measured, $I_{impulse}$ is derived, and $I_{unfiltered}$ calculated using Eq. 10.

Small voltage steps delivered by the loose-patch clamp result in a decaying transient current recorded by the whole-cell voltage clamp (Fig 2, step response). The loose-seal clamp is able to change the patch potential in nearly a stepwise fashion resulting in an instantaneous capacitive transient (I_{cap}) and single amplitude resistive current (I_{res}). The step response recorded by the whole-cell electrode is therefore the sum of filtered I_{cap} and filtered I_{res} . Thus I_{cap} is an impulse, and the portion of the step response comprised of the filtered I_{cap} is the impulse response of the filter. Note, in order for the capacitive transient to be considered an impulse, the voltage step creating the capacitive transient must charge the membrane in one-tenth or less of the time constant of the filter (McGillem and Cooper, 1991).

In theory, the primary factor in deconvolution of filtered patch currents is calculating the capacitive portion of the step response. This calculation relies upon two important properties of I_{cap} and

I_{res} . First, filtered I_{cap} can be represented by Green's function for the cable equation (Rall, 1977)

$$G(X, T) = T^{-1/2} \exp(-X^2 / 4T - T) \quad (11)$$

$G(X, T)$ specifies the filtering of the signal along a cable in terms of normalized time, ($T = t/\tau$) and electrotonic distance ($X = x/\lambda$) where τ is the membrane time constant, γ is the cable space constant and x is the distance between the pipets. Second, I_{res} is the time integral of I_{cap} . Therefore one must find the best I_{cap} waveform through Eq. 11 that when summed with its own time integral most closely approximated the step response.

In our practical experience with WCLP recording from skeletal myotubes (Anson and Roberts, 1998; 2001) two additional factors influenced I_{cap} . First, a stimulus artifact comprised of current flow through the nonzero resistance of the bath ground, capacitive coupling between the pipets, and a field potential around the tip of the loose-patch pipet. The stimulus artifact was proportional to the loose patch-clamp current and was thus removed from the signal by appropriately scaling and subtracting whole-cell currents recorded in response to loose-patch stimulations on and off the myotube. The second factor was filtering of the impulse by the whole-cell patch-clamp filter. As with typical whole-cell recordings, the whole-cell voltage clamp's filter was applied to remove very high-frequency noise. Although this filter setting did not appreciably filter active patch currents, it did affect the impulse. To account for this filtering, I_{cap} derived from Eq. 11 was convoluted with a Gaussian function ($B(t)$) that approximated the whole cell clamp's Bessel filter to generate a filtered waveform (I_c) of the capacitive transient,

$$I_c = G(X, T) * B(t), \quad (12)$$

where $B(t) = \exp(-(t - d)^2 / \sigma^2)$, d is the Bessel filter's time delay and σ specifies the -3dB cutoff frequency. The convolution generates a normalized I_c waveform, which must be scaled to the individual step response such that

$$I_{cap} = A_{cap} I_c. \quad (13)$$

The goal of the fitting procedure was thus to find values of X , T , A_{cap} , and A_{res} that generated capacitive and resistive waveforms

that summed to replicate the step response. We chose to minimize the mean squared error for this procedure:

$$\left| I_r A_{res} + I_c A_{cap} - I_{step} \right|^2 = \min. \quad (14)$$

For the actual digital computation, Eq. 14 was reformulated as a single matrix equation:

$$\left| M \cdot A - I_{step} \right|^2 = \min. \quad (15)$$

where M is a 512×2 matrix in which the columns are I_c and I_r , and A is a 2×1 matrix in which the elements are A_{cap} and A_{res} . The values of A_{cap} and A_{res} that minimize Eq. 15 are given by

$$A = (M^T M)^{-1} M^T I_{step}, \quad (16)$$

where M^T is the transpose of M .

Typical WCLP recordings were performed as follows. The whole-cell and loose-patch pipets were positioned over the myotube of interest. Tight-seal whole-cell recording configuration was obtained and a small whole-cell linear current was averaged and stored for subsequent calculation of R_{series} , R_{input} , and recovery of current lost to ground. The loose-patch pipet was then positioned just above the myotube surface and with R_{lp} and R_{ls} compensation off delivered a small voltage step. The loose-patch pipet was then sealed onto the membrane, R_{lp} and R_{ls} compensation was engaged as described in the previous sections, and another voltage step was applied. The small voltage steps applied off and on the cell were of the same magnitude and the current responses from each were averaged and stored for later calculation of the stimulus artifact. The loose-patch clamp then delivered the stimulation protocol for examining Na^+ current. The loose-patch pipet was then repositioned at a new location on the myotube, small current responses were obtained from off and on the cell-voltage steps, and the Na^+ current protocol was delivered. The process was repeated until the myotube was completely mapped or tight-seal whole-cell recording configuration was lost. All analysis was post-hoc, using macros within Clampfit 6 (Axon Instruments) to calculate R_{series} , R_{input} , and the whole-cell scalar. The data was then transferred to Microsoft Excel spreadsheets where macros carried out the deconvolution process. For each patch the fitting process began with initial estimates of X and T from which I_c was calculated though Eq. 12–14. I_r was then derived as the time integral of

I_c and A_{cap} and A_{res} found through Eq. 16. New best fit values of X and T were then found using the algorithm within EXCEL until the derived waveform closely matched the step response. Deconvolution of filtered patch currents generated current waveforms that were greater in magnitude and had kinetics resembling Na^+ currents recorded from small isopotential cells (Anson and Roberts, 1998).

4. Summary

Loose-seal patch-recording technique is one of many techniques available for functionally assaying ion-channel physiology and cellular electrical activity. The advantage of this technique is that it is gentle, does not require excessively clean cells, and is relatively simple to implement (as long as one realizes the technical pitfalls). Data collected through loose-patch and tight-seal recording complement each other well. The low-resistance nature of the seal between the pipet and cell membrane has limited the traditional loose patch-clamp to use on large cells with high channel densities. However, modifications are possible that enable the basic technique to be used on many other cell types as well. Thus, we anticipate that the loose-seal patch clamp and its derivatives will continue to increase our understanding of ion channels and the basic physiology of electrically excitable cells.

References

- Almers, W., Stanfield, P. R., and Stuhmer, W. (1983) Lateral distribution of sodium and potassium channels in frog skeletal muscle: measurements with a patch-clamp technique. *J. Physiol.* **336**, 261–284.
- Anson, B. D. and Roberts, W. M. (1998) A novel voltage clamp technique for mapping ionic currents from cultured skeletal myotubes. *Biophys. J.* **74**, 2963–2972.
- Anson, B. D. and Roberts, W. M. (2001) Sodium channel distribution on uninervated and innervated embryonic myotubes. *J. Neurobiol.* **48**(1), 42–57.
- Antoni, H., Bocker, D., and Eickhorn, R. (1988) Sodium current kinetics in intact rat papillary muscle: measurements with the loose-patch-clamp technique. *J. Physiol.* **406**, 199–213.
- Araujo, D. A., Cordeiro, M. N., Diniz, C. R., and Beiro, P. S. (1993) Effects of a toxic fraction, PhTx2, from the spider *Phoneutria nigriventer* on the sodium current. *Naunyn-Schmiedeberg's Arch. Pharmacol.* **347**, 205–208.
- Armstrong, C. E. and Roberts, W. M. (1998) Electrical properties of frog saccular hair cells: distortion by enzymatic dissociation. *J. Neurosci.* **18**, 2962–2973.
- Armstrong, C. M. and Gilly, W. F. (1992) Access resistance and space clamp problems associated with whole-cell patch clamping, in *Methods in Enzymology* (Rudy, B. and Iverson, L., eds.), Academic Press, New York, NY, pp. 100–122.

- Beam, K. G., Caldwell, J. H., and Campbell, D. T. (1985) Na channels in skeletal muscle concentrated near the neuromuscular junction. *Nature* **313**, 588–590.
- Bennet, M. R., Farnell, L., Gibson, W. G., and Lavidis, N. A. (1997) Synaptic transmission at visualized boutons: stochastic interaction between acetylcholine and its receptors. *Biophys. J.* **72**, 1595–1606.
- Blanco, R. E., Marrero, H., Orkand, P. M., and Orkand R. K. (1993) Changes in ultrastructure and voltage-dependent currents at the glia limitans of the frog optic nerve following retinal ablation. *GLIA* **8**, 97–105.
- Brodie, M. S., Pesold, C., and Appel S. B. (1999) Ethanol directly excites dopaminergic ventral tegmental area reward neurons. *Alcohol. Clin. Exp. Res.* **23**, 1848–1852.
- Cooper, R. L., Fernandez-de-Miguel, F., Adams, W. B., and Nicholls J. G. (1992) Anterograde and retrograde effects of synapse formation on calcium currents and neurite outgrowth in cultured leech neurons. *Proc. R. Soc. Lond. B.* **249**, 217–222.
- Corey, D. P. and Stevens, C. F. (1983) Science and technology of patch-recording electrodes, in *Single Channel Recording*, 1st ed. (Sakmann, B. and Neher, E., eds.), Plenum Press, New York, NY, pp. 53–68.
- Correges, P. and Dunant, Y. (1996) Disorganisation of quantal acetylcholine release by zinc at the Torpedo nerve-electroplate junction. *Pflugers Arch.* **432**, 859–866.
- Dubin, A. E. and Harris, G. L. (1997) Voltage-activated and odor-modulated conductances in olfactory neurons of *Drosophila melanogaster*. *J. Neurobiol.* **32**, 123–137.
- Eickhorn, R., Dragert, C., and Antoni, H. (1994) Influence of cell isolation and recording technique on the voltage dependence of the fast cardiac sodium channel of the rat. *J. Mol. Cell. Cardiol.* **26**, 1095–1108.
- Girod, R., Correges, P., Jacquet, J., and Dunant, Y. (1993) Space and time characteristics of transmitter release at the nerve-electroplaque junction of Torpedo. *J. Physiol.* **471**, 129–157.
- Hamill, O. P., Marty, E., Neher, E., Sakmann, B., and Sigworth, F. J. (1981) Improved patch-clamp techniques for high-resolution current recording from cells and cell-free membrane patches. *Pflugers Arch.* **391**, 85–100.
- Hilgemann, D. W. (1995) The giant membrane patch, in *Single Channel Recording*, 2nd ed. (Sakmann, B. and Neher, E., eds.), Plenum Press, New York, NY, pp. 307–328.
- Hong, S. J. and Lnenicka G. A. (1997) Characterization of a P-type calcium current in a crayfish motoneuron and its selective modulation by impulse activity. *J. Neurophys.* **77**, 76–85.
- Jack, J. J., Noble, D., and Tsien, R. W. (1983) *Electric Current Flow in Excitable Cells*. Oxford University Press, Oxford, UK.
- James, J. F. (1995) *A Student's Guide to Fourier Transforms*. Cambridge University Press, Cambridge, UK.
- Kinnamon, S. C., Dionne, V. E., and Beam, K. G. (1988) Apical localization of K⁺ channels in taste cells provides the basis for sour taste transduction. *Proc. Natl. Acad. Sci. USA* **85**, 7023–7027.
- Kirstein, M., Eickhorn, R., Kochsiek, K., and Langenfeld, H. (1996b) Dose-dependent alteration of rat cardiac sodium current by isoproterenol: results from direct measurements on multicellular preparations. *Pflugers Arch.* **431**, 395–401.

- Kirstein, M., Katzer, A., Hu, K., Gaudron, P., Ertl, G., Langenfeld, H., and Kochsiek, K. (1996a) Influence of cariac dysfunction on fast sodium current regulation by forskolin. *Pacing Clin. Electrophysiol.* **19**, 2018–2022.
- Kirstein, M., Langenfeld, H., Katzer, A., and Kochsiek, K. (1994) Dissimilar action of two cyclic adenosine-monophosphate analogues on the sodium current in intact rat papillary muscle. *Pacing Clin. Electrophysiol.* **17**, 2068–2073.
- Korper, S., Wink, M., and Fink, R. H. (1998) Differential effects of alkaloids on sodium currents of isolated single skeletal muscle fibers. *FEBS Lett.* **436**, 251–255.
- Levis, R. A. and Rae, J. L. (1992) Constructing a patch clamp setup, in *Methods in Enzymology* (Rudy, B. and Iverson, L., eds.), Academic Press, New York, NY, pp. 14–66.
- Lucas, K. (1909) The “all-or-none” contraction of the amphibian skeletal muscle fiber. *J. Physiol.* **38**, 113–133.
- Lupa, M. T., Krzemien, D. M., Schaller, K. L., and Caldwell, J. H. (1993) Aggregation of sodium channels during development and maturation of the neuromuscular junction. *J. Neurosci.* **13**, 1326–1336.
- Lupa, M. T. and Caldwell, J. H. (1994) Sodium channels aggregate at former synaptic sites in innervated and denervated regenerating muscles. *J. Cell Biol.* **124**, 139–147.
- Lupa, M. T., Krzemien, D. M., Schaller, K. L., and Caldwell, J. H. (1995) Expression and distribution of sodium channels in short- and long-term denervated rodent skeletal muscles. *J. Physiol.* **483**, 109–118.
- Marrero, H. and Orkand, R. K. (1993) Facilitation of sodium currents in frog neuroglia by nerve impulses: dependence on external calcium. *Proc. R. Soc. Lond. B.* **253**, 219–224.
- Marrero, H., Astion, M. L., Coles, J. A., and Orkand, R. K. (1989) Facilitation of voltage-gated ion channels in frog neuroglia by nerve impulses. *Nature* **339**, 378–380.
- Matavel, A. C., Ferreira-Alves, D. L., Beirao, P. S., and Cruz, J. S. (1998) Tension generation and increase in voltage-activated Na⁺ current by crotamine. *Eur. J. Pharm.* **348**, 167–173.
- McGillem, C. D. and Cooper, G. R. (1991) *Continuous and Discrete Signal and System Analysis*. Oxford University Press, New York, NY.
- Milton, R. L. and Behforouz, M. A. (1995) Na channel density in extrajunctional sarcolemma of fast and slow twitch mouse skeletal muscle fibers: functional implications and plasticity after fast motoneuron transplantation onto a slow muscle. *J. Musc. Res. Cell Motil.* **16**, 430–439.
- Milton, R. L. and Caldwell, J. H. (1990) How do patch clamp seals form? A lipid bleb model. *Pflugers Arch. Eur. J. Phys.* **416**, 758–762.
- Neher, E. and Sakmann, B. (1976) Single-channel currents recorded from membrane of denervated frog muscle fibres. *Nature* **260**, 799–801.
- Neher, E., Sakmann, B., and Steinbach, J. H. (1978) The extracellular patch clamp: a method for resolving currents through individual open channels in biological membranes. *Pflugers Arch.* **375**, 219–228.
- Pratt, F. H. and Eisenberger, J.P. (1919) the quantal phenomena in muscle: methods, with further evidence of the all-or-none principle for the skeletal fiber. *Am. J. Physiol.* **49**, 1–54.

- Rall, W. (1977) Core conductor theory and cable properties of neurons, in *The Nervous System: Handbook of Physiology* (Brookhart, J. M. and Mountcastle, V. B., eds.), American Physiological Society, Bethesda, MD, pp. 39–97.
- Roberts, W. M. (1987) Sodium channels near end-plates and nuclei of snake skeletal muscle. *J. Physiol.* **388**, 213–232.
- Roberts, W. M. and Almers, W. (1992) Patch voltage clamping with low-resistance seals: loose patch clamp, in *Methods in Enzymology* (Rudy, B. and Iverson, L., eds.), Academic Press, New York, NY, pp. 155–176.
- Roberts, W. M., Jacobs, R. A., and Hudspeth, A. J. (1990) Colocalization of ion channels involved in frequency selectivity and synaptic transmission at presynaptic active zones of hair cells. *J. Neurosci.* **10**, 3664–3684.
- Ruff, R. L. (1996a) Single-channel basis of slow inactivation of Na⁺ channels in rat skeletal muscle. *Am. J. Physiol.* **271**, C971–C981.
- Ruff, R. L. (1996b) Sodium channel inactivation and the distribution of sodium channels on skeletal muscle fibres enable the performance of properties of different skeletal muscle fibre types. *Acta Phys. Scand.* **156**, 159–168.
- Ruff, R. L. (1999) Effects of temperature on slow and fast inactivation of rat skeletal muscle Na⁺ channels. *Am. J. Physiol.* **277**, C937–C947.
- Ruff, R. L. and Whittlesey, D. (1992) Na⁺ current densities and voltage dependence in human intercostal muscle fibers. *J. Physiol.* **458**, 85–97.
- Ruff, R. L. and Whittlesey, D. (1993a) Na⁺ currents near and away from endplates on human fast and slow twitch muscle fibers. *Muscle Nerve* **16**, 922–929.
- Ruff, R. L. and Whittlesey, D. (1993b) Comparison of Na⁺ currents from type IIa and IIb human intercostal muscle fibers. *Am. J. Physiol.* **265**, C171–C177.
- Sakmann, B. and Neher, E. (1983) Geometric parameters of pipettes and membrane patches, in *Single Channel Recording*, 1st ed. (Sakmann, B. and Neher, E., eds.), Plenum Press, New York, NY, pp. 53–68.
- Schwartz, L. and Stuhmer, W. (1984) Voltage-dependent sodium channels in an invertebrate striated muscle. *Science* **225**, 523–525.
- Strickholm, A. (1961) Impedance of a small electrically isolated area of the muscle cell surface. *J. Gen. Physiol.* **44**, 1073–1088.
- Stuhmer, W. and Almers, W. (1982) Photobleaching through glass micropipettes: sodium channels without lateral mobility in the sarcolemma of frog skeletal muscle. *Proc. Natl. Acad. Sci. USA* **79**, 946–950.
- Stuhmer, W., Roberts, W. M., and Almers, W. (1983) The loose patch clamp, in *Single Channel Recording*, 1st ed. (Sakmann, B. and Neher, E., eds.), Plenum Press, New York, NY, pp. 123–132.
- Tank, D. W., Wu, E. S., and Webb, W. W. (1982) Enhanced molecular diffusibility in muscle membrane blebs: release of lateral constraints. *J. Cell Biol.* **92**, 207–212.
- Varkevisser, B. and Kinnamon, S. C. (2000) Sweet taste transduction in hamster: role of protein kinases. *J. Neurophysiol.* **83**, 2526–2532.
- Warren, D., Lavidis, N. A., and Bennett, M. R. (1995) Quantal secretion recorded from visualized boutons. *Neurosci. Lett.* **192**, 205–208.
- Wolters, H., Wallinga, W., Ypey, D. L., and Boom, H. B. (1994) Ionic currents during action potentials in mammalian skeletal muscle fibers analyzed with loose patch clamp. *Am. J. Physiol.* **267**, C1699–C1706.
- Zucker, R. S. and Lando, L. (1986) Mechanism of transmitter release: voltage hypothesis and calcium hypothesis. *Science* **231**, 574–579.

Recording from Macropatches

Frances Moody-Corbett and Mark Fry

1. Introduction

The purpose of this chapter is to describe the procedures used to record macroscopic currents from patches of biological membranes. Several variations of the classic patch-clamp recording procedure are available and described in other chapters of this book, however the procedure reported here is unique from single-channel recording, loose patch-clamp recording, and giant-patch recording. Like single-channel recording and giant-patch recording, macropatch recording requires the formation of a tight seal between the recording pipet and the membrane. However, the size of the pipet tip used for macropatch recording is typically larger than that used in single-channel recording and considerably smaller than the pipets used for giant-patch recording (*see* Subheading 3.2.3.). It is possible using macropatch recording to determine both the identity of currents as well as their spatial distribution in biological membranes.

2. Biological Application

Historically, it has been known for several decades that ion channels are not uniformly distributed in biological membranes. For example, Langley in 1907 used a delicately constructed “paint brush” to estimate the distribution of acetylcholine (ACh) responses on skeletal muscle and predicted both the occurrence of receptors to ACh as well as a crude description of the unique spatial distribution of these channels (Langley, 1907). Today, a variety of techniques are available to identify and determine the spatial distribution of

membrane channels including the use of labeled-toxins and antibodies and variations on electrophysiological techniques.

Electrophysiological techniques offer the advantage of providing both functional information as well as spatial information. Tight-seal, single-channel, patch-clamp recording is one such technique, which has been used to examine the properties of a variety of chemical, mechanical, and voltage-operated channels. Recently, several laboratories have taken advantage of the tight-seal patch-clamp technique to record from slightly larger areas of membrane (macropatches) and examine both the characteristics and distribution of ion channels in specialized areas of membrane such as the synapse (Fry and Moody-Corbett, 2000; Hoffman et al., 1997; Rashid et al., 2001; Sakmann and Stuart, 1995). The focus of this chapter is to describe the technique used to record from such macropatches.

3. Technique

The basic technique for macropatch recording is similar to tight-seal single-channel recording. The electrodes are pulled to larger tip diameters than would be used for single-channel recording (*see* Subheading 3.2.3.); however, as with single-channel recording, following initial contact with the membrane, suction is applied to form an electrically and mechanically tight seal in the gigohm range. Recordings can be obtained in the cell-attached configuration or from inside-out or outside-out membrane patches. The electronics of the recording procedure are the same as that described for single-channel recordings and will not be repeated here. Several references are available that describe the single-channel recording technique in detail (Cahalan and Neher, 1992; Hamill et al., 1981; Penner, 1995).

3.1. Membranes

3.1.1. Preparation

Macropatch recording does not require any novel preparation of membranes different from that described for normal tight-seal patch-clamp recording. In embryonic tissue the membranes do not need to be cleaned chemically. Enzymatic treatment may be used to expose cleaner areas of membrane in more mature preparations, such as adult muscle (Hamill et al., 1981), however other methods, such as the spread-print technique (Kotecha et al., 1997;

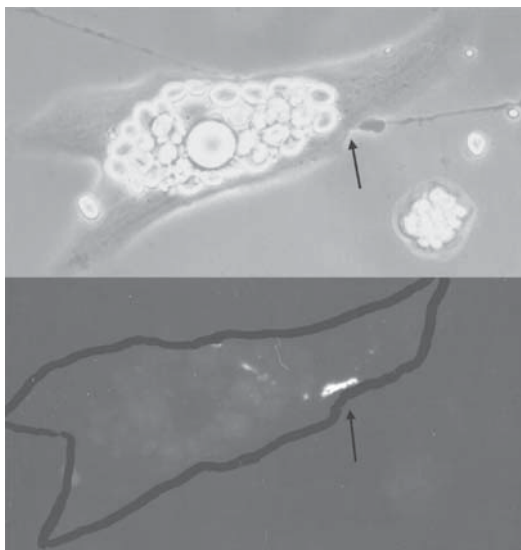


Fig. 1. Phase (upper) and fluorescence (lower) micrographs of a nerve-contacted *Xenopus* muscle cell grown in culture. Rhodamine-labeled α -bungarotoxin is used to identify AChRs, which aggregate along the path of nerve contact (arrow). A macropatch electrode can be placed relative to these nerve-contact sites and the distribution of voltage-activated ion channels determined.

Rashid et al., 2001), have been described to expose neuronal specializations for recording.

3.1.2. Visualization

The objective, for many laboratories using this technique, is to record from specific areas of the membrane relative to known specializations, for example, the distribution of ion channels in the pre- or postsynaptic membrane, dendritic vs somatic membranes. Therefore, it is important to be able to visualize the area of membrane to be patched. In this laboratory, labeling postsynaptic ACh receptors with rhodamine- α -bungarotoxin is used to identify neuromuscular junctions. Using 400 \times magnification and phase and fluorescence microscopy it is then possible to identify a patch of ACh receptors and position a macropatch recording electrode relative to this area (Fig. 1). The macropatch electrode can

then be used to determine the voltage-regulated ion channels that are associated with these postsynaptic sites (Fry and Moody-Corbett, 2000). Other laboratories have taken advantage of differential interference contrast and infrared optics to visualize details of the neuronal architecture in brain slices and record preferentially from dendrites or soma (Sakmann and Stuart, 1995). The choice of microscope, therefore, will vary accordingly.

3.2. Pipets

3.2.1. Type of Glass

Several glasses are commercially available for recording electrodes and the properties of a number of these glasses have been reviewed (Rae and Levis, 1992; Sakmann and Neher, 1995). There are two major considerations in choosing the appropriate glass: noise and seal formation. As with single-channel recording, it is important to utilize a glass that has low noise properties. In general, hard glasses (alumino- or borosilicate) have better noise properties than soft glasses (soda-glass) and thick-walled glasses have better noise properties than thin-walled glasses. In addition to noise considerations, forming a tight-seal on the membrane relies on a smooth contact between the glass of the electrode and the cell membrane, therefore it is important that the tip of the electrode does not present a jagged edge. Firepolishing is used to smooth the electrode tip. Soft or thin-walled glasses are more easily firepolished than hard or thick-walled glasses. Choosing the appropriate electrode glass will be a balance between the best glass for the lowest noise performance and the glass that easily forms a tight-seal with the membrane under study. For tight-seal macropatch recordings from embryonic skeletal muscle we have used a thin-walled borosilicate glass.

3.2.2. Fabrication

As with the single-channel electrode, electrodes used for macropatch recording are pulled using a double-pull technique. The first pull thins the capillary tubing and will effect the characteristics of the shaft of the electrode and together with the second pull determines the tip diameter. Slowing the second pull using a low heat can vary the size of the electrode tip. As described below, tip diameters larger than 1 μm and smaller than 10 μm are typically used. Several models of electrode puller are available. In this lab

we have used a Narishige model PP-83 (Narishige Scientific Instrument Lab., Tokyo, Japan) for several years and have obtained electrodes of consistent size over the course of an experiment. Several laboratories take advantage of the programmable features of the Sutter P-87 electrode puller (Sutter Instruments Co., Novato, CA).

3.2.3. Size

Typically in electronic recordings the electrode tip diameter is estimated based on the resistance of the electrode. This is done, with the tip immersed in the recording solution, by applying a short (10 ms), low voltage step (10 mV) to the pipet and measuring the resultant current. The electrode resistance can be calculated using Ohm's law. Electrodes used for single-channel recording experiments are usually in the range of 4–10 M Ω and are in the order of 1 μ m in diameter (Sakmann and Neher, 1995). Depending on the density of channels in the patch of membrane, electrodes of this size may be used to record macroscopic currents (e.g., Rashid et al., 2001). However, typically electrodes to be used for macroscopic current recording are pulled to slightly larger diameters than a single-channel electrode (e.g., Fry and Moody-Corbett, 2000; Stuhmer et al., 1989; Stuhmer and Parekh, 1995). Macropatch electrodes have resistances in the range of 0.5–3 M Ω and are in the order of 2–8 μ m diameter. Choosing the appropriately sized electrode depends on the experiment and biological preparation under study. For example, electrodes to be used to sample the population of ion channels near synaptic sites, which occupy a small surface area, will have a small diameter. On the other hand, measuring the biophysical properties of a class of ion channels expressed in *Xenopus* oocytes may be best accomplished with a larger diameter electrode and the technique of giant-patch recording (Hilgemann, 1995).

3.2.4. Bending, Coating, and Polishing

In typical recording setups, the electrode holder is mounted such that the approach to the membrane is at an angle of approx 45°. However, depending on the architecture of the membrane, it is often desirable to approach the membrane at a more vertical angle, in which case the electrode will need to be bent. In this laboratory using an inverted microscope, 40 \times objective and a long working-distance condenser, a bend along the shaft of the electrode will allow a near-vertical approach to the membrane (Fig. 2A). In other

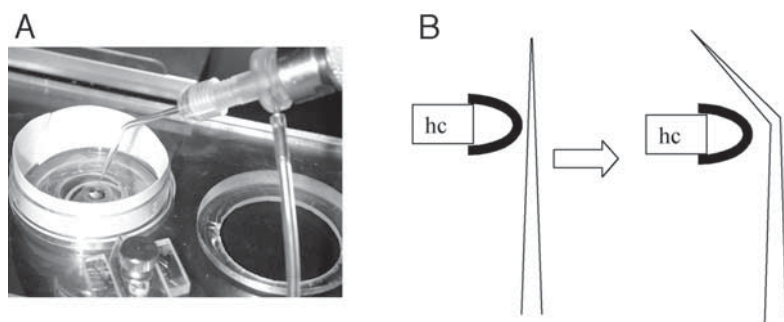


Fig. 2. Method used to make a vertical approach to cells in culture. (A) Photograph demonstrating an approx 45° bend in the shaft of the macropatch electrode. (B) Schematic diagram demonstrating the technique used to bend the electrode near the tip. Visualized under low-power magnification, a heating coil (hc) is placed near the electrode tip and the tip gently bent to provide an approx 45° angle.

instances, where the working distance is much more restricted (e.g., short working-distance condenser or an upright microscope), the electrode can be bent close to the tip. Bending is accomplished by visualizing the electrode with low-power objectives and the tip is positioned near a small heating coil. Using a simple tool, such as a stainless-steel probe, it is possible to gently bend the tip to the desired angle (Fig. 2B).

In order to ensure low noise recording it is necessary to coat the electrode near the tip with a layer of insulating material such as Sylgard 184 (Dow Corning, Midland, MI) (Rae and Levis, 1992; Penner, 1995). Under low magnification, the Sylgard is applied within a few microns of the tip and then rapidly cured using a localized heating source. The Sylgard can be pre-mixed and stored in small aliquots in the freezer for several weeks before use. The aliquot is brought to room temperature before use and should be used within the day.

Following the Sylgard treatment and before filling, the electrode tip should be firepolished. Polishing needs to be done under high magnification so both the electrode tip and the heating coil can be visualized. Microforges are commercially available however a setup for firepolishing can also be constructed, as described by Rae and Levis (1992). Typically, the diameter of the macropatch

electrode tip is larger than that used for single-channel recording and so the tip should be easily visualized during firepolishing.

3.2.5. Storage

Electrodes can be pulled and stored for a few hours before use. It is important to keep the tips covered and free of debris. The process of Sylgard coating and final firepolishing should be done immediately before use.

3.2.6. Ground Electrode

Ground electrodes are similar to that used for single-channel recording. In our laboratory the connection is formed using a silver pellet electrode holder (MEH1S, World Precision Instruments, Sarasota, FL) filled with extracellular recording solution and a glass capillary tube to form the connection to the bath. In this case the capillary tubing is filled with a 2–3% agar-extracellular recording solution. Using the same extracellular recording solution as in the patch electrode eliminates additional junction potentials due to solution differences. Using an agar salt-bridge reduces the potential problem of membrane sensitivity to silver ions. The ground electrodes can be made and stored in the refrigerator for several weeks before use.

3.3. Solutions

The macropatch recording technique can be used in several configurations (cell-attached, inside-out, or outside-out) and as such the filling solution will vary. Whether an intracellular or extracellular solution is used the solution should be filtered with a 0.22 μm filter immediately before use. The electrodes can be easily back-filled. Generally air bubbles are not present but these can be removed by gentle tapping.

3.4. Recording

Macropatch-recording experiments provide a method to estimate channel density in membrane regions. The amplifier to be used should be sensitive enough to have a very low noise window and a range of gains to record currents up to several hundred picoamperes. As with single-channel recording, the noise window should be as low as possible to confirm the absence of channel activity. Several patch-clamp amplifiers are commercially available with

these capabilities and low noise-recording techniques have been reviewed elsewhere (Benndorf, 1995; Levis and Rae, 1992).

3.4.1. *Forming Seals*

Formation of a seal is monitored electrically by measuring the resistance of the electrode before and during seal formation. The electrode is advanced slowly until an increase in resistance is observed, after which time slight suction is applied. Seal formation can occur almost immediately, or may take up to a few minutes. This often appears to correlate with the density of channels in the membrane patch (unpublished observations). Intense or prolonged suction should be avoided, as this may draw large amounts of membrane into the tip of the electrode, which may result in blebbing or distortion of the membrane (Milton and Caldwell, 1990). Several factors will affect the degree of deformation, including the size of the electrode opening, amount of suction applied (Sakmann and Neher, 1995), and enzymatic treatment of the membrane (Hilgemann, 1995; Milton and Caldwell, 1990).

3.4.2. *Membrane Potential*

In macropatch recording, as in the single-channel recording method, the membrane patch is under the control of the voltage applied to the pipet. In the cell-attached configuration with the same solution in the electrode as in the bath and no applied potential the membrane patch is assumed to be near resting membrane potential. Depolarizing steps from this potential can be obtained by applying negative voltage steps to the pipet and conversely hyperpolarization will be obtained by applying positive potentials to the electrode. The software used to set the potential of the membrane in the macropatch must be programmed to assure that the voltages applied at the membrane are correct. Similarly, the software must correctly describe inward and outward currents. This information is clearly denoted in the manuals available with commercial amplifiers. *The Axon Guide* book available with pClamp software (Axon Instruments, Foster City, CA), also details the software programming.

The resting membrane potential of the cell can be determined using standard intracellular recording techniques, however because of the configuration of the membrane in the macropatch electrode tip it is possible that the true potential at the patch may vary from rest.

3.4.3. Membrane Current

The conventions used for single-channel recording apply in macropatch recording. In the cell-attached configuration outward current will appear as a negative signal at the current monitor outputs. Therefore in order to display an outward current as a positive signal, the current monitor output is inverted. Most software used to program the stimulus output and record current input can be programmed to provide such an inversion and therefore have voltages and currents conform to standard electrophysiological practice.

The amplitude of current in a macropatch recording should not exceed the capabilities of conventional patch-clamp amplifiers. However, unlike single-channel recording the amplitude of current recorded from one patch to the next may vary by up to two orders of magnitude. As a result during a recording session it will be necessary to adjust the gain accordingly. The Axopatch amplifiers with pClamp software have the advantage that a change in the gain of the amplifier automatically adjusts the software to accurately record the current amplitude. However, not all amplifiers have this capability and therefore a change in amplifier gain may require re-programming the software during the experiment.

3.4.4. Leak Subtraction

Most leak currents, due to uncompensated capacitances and stray leakage, are effectively removed using an online P/N procedure (Dempster, 1993). N-test pulses, each of which is $1/N^{\text{th}}$ the size of the voltage step to be applied to the membrane patch, are applied to the membrane before or after the voltage step of interest. The N-test currents are then summed and subtracted from the current generated by the voltage step of interest. This procedure is effective so long as the test pulses do not activate a current. Leak subtraction is often necessary in order to visualize small activated currents.

3.5. Membrane Surface Area

A major purpose of macropatch recording is to compare channel or current densities in identified membrane regions, in which case it is important to be able to establish a method of comparing the amount of membrane in the electrode tip. In general, there are three methods.

Membrane area can be estimated by measuring the amount of membrane visualized in the electrode tip. With a macropatch electrode it is often possible to visualize the membrane in the electrode tip. In many cases, it will approximate a hemisphere (Fry and Moody-Corbett, 2000; Matsuda and Stanfield, 1989) and the surface area of the hemisphere can be calculated based on the measured diameter. In other cases the membrane may appear flat at the electrode tip and the surface area can be calculated as the area of a circular patch of membrane (Lin et al., 1999).

The area of the membrane in the electrode tip can also be estimated from the capacitance transient (Sakmann and Neher, 1995). The capacitance of most biological membranes (excluding adult skeletal muscle) is estimated to be $1 \mu\text{F}/\text{cm}^2$ (Cole, 1968; Fenwick et al., 1982), therefore by measuring the membrane capacitance in the electrode patch it is possible to calculate an estimate of membrane area. Following seal formation, the capacitive current during a short, low-voltage step is recorded. This capacitive current can be determined using the capacitance compensation circuitry of most amplifiers. Alternatively, capacitance can be measured by integration of the current during the transient following the voltage step. A more accurate measure of just the membrane capacitance can be obtained by comparing capacitance measured from the membrane and that recorded from sealing on a bubble of Sylgard (Sakmann and Neher, 1995).

In some cases comparisons of channel density are made not from a calculated surface area but by comparing the current per patch using electrodes with very similar electrode size (Hoffman et al., 1997). In this situation channel density is estimated per patch as opposed to per μm^2 . This method allows estimates of current density within the parameters of the experiment; however, it is not possible to compare current or channel densities with other studies.

3.6. Analysis

Current data should be stored on-line using a software acquisition package such as the Clampex programs from pClamp (Axon Instruments). The currents recorded from macropatches will vary in amplitude from a few picoamperes to hundreds of picoamperes (Fig. 3 A–C). Peak or steady-state current can be measured and the current density can be calculated based on capacitance or membrane area (*see* Subheading 3.5.) and used to plot current density-

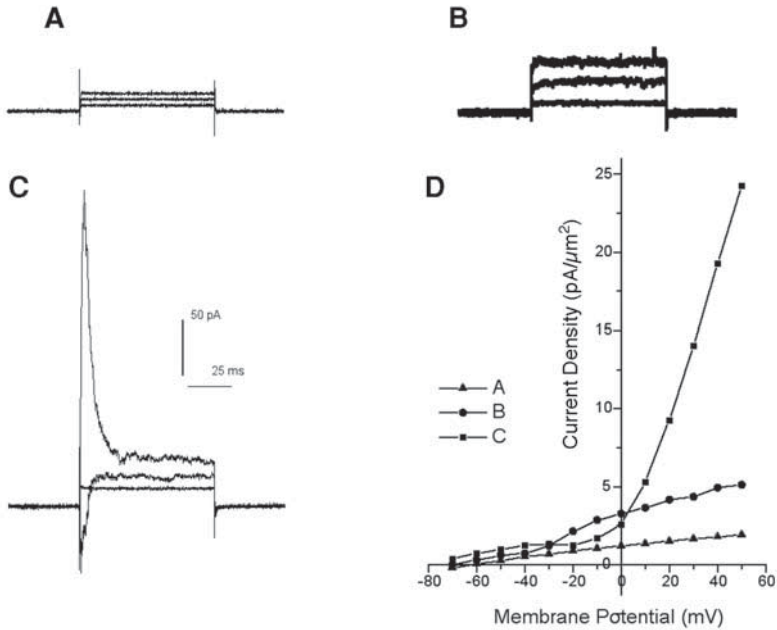


Fig. 3. (A–C) Currents were recorded from three cell-attached macropatches on nerve-contacted *Xenopus* muscle cells grown in culture. Each patch was stepped to three membrane potentials (-50 mV, -10 mV, $+40$ mV) and the current traces are superimposed. (A) The membrane patch showed no voltage-activated currents. (B) The membrane patch showed a small noninactivating outward potassium current. (C) The membrane patch showed a large inactivating outward potassium current and an inward sodium current. The scale bars apply to all current traces. (D) Current density-voltage plots for the outward potassium currents shown in (A–C).

voltage relationships (Fig. 3D). As with whole-cell currents, the time course of activation and inactivation of macroscopic currents can be measured by using the fitting routines of an appropriate software package.

4. Advantages and Disadvantages

The formation of tight-seals on the membrane offers the advantage of low-noise recordings. It is possible, therefore, to record

the full range of currents from small currents, or single-channel currents, in some patches, to macroscopic currents produced by an aggregation of channels. Unlike the loose-patch-clamp technique, rim currents and the related space-clamp problems are not an issue in macropatch recordings (Roberts and Almers, 1993).

On the other hand, tight-seal recordings have the disadvantage that repeated recordings from several different areas of the membrane of the same cell are not possible. Unlike the loose patch-clamp electrode, removal of a macropatch electrode that has formed a tight seal usually results in damage to the membrane and the cell. In addition, because of debris left on the tip of the electrode reformation of a tight seal is prevented. Determining the unique distribution of ion channels across a membrane must rely on sampling several cells with similar topology or specific cell landmarks (Fry and Moody-Corbett, 2000).

A further disadvantage of this technique, common also to single-channel recording is the uncertainty of the actual membrane potential in the patch. In the cell-attached configuration of these recording techniques the membrane potential can be estimated by simultaneous recording using a standard intracellular electrode. However, it is not clear to what extent the distortion of the membrane patch in the electrode will alter the membrane potential. Furthermore, the ionic composition of the solution in the patch electrode during a recording will have a local effect on the membrane potential that will not be "seen" by an intracellular electrode.

However, given these limitations, the macropatch recording technique provides a method to estimate channel distribution on cells and to study the unique characteristics of channel aggregations.

References

- Benndorf, K. (1995) Low-noise recording, in *Single-Channel Recording*, 2nd ed. (Sakmann, B. and Neher, E., eds.), Plenum Press, NY, pp. 129–145.
- Cahalan, M. and Neher, E. (1992) Patch-clamp techniques: an overview, in *Ion Channels: Methods in Enzymology*, vol. 207 (Rudy, B. and Iverson, L. E., eds.), Academic Press, NY, pp. 3–14.
- Cole, C. (1968) *Membranes, Ions and Impulses*. University of California Press, CA.
- Dempster, J. (1993) *Computer Analysis of Electrophysiological Signals*. Academic Press, NY.
- Fenwick, E., Marty, A., and Neher, E. (1982) A patch clamp study of bovine chromaffin cells and of their sensitivity to acetylcholine. *J. Physiol.* **331**, 577–597.
- Fry, M. and Moody-Corbett, F. (2000) Localization of sodium and potassium currents at sites of nerve-muscle contact in embryonic *Xenopus* muscle cells in culture. *Pflugers Arch.* **437**, 895–902.

- Hamill, O. P., Marty, A., Neher, E., Sakmann, B., and Sigworth, F. J. (1981) Improved patch-clamp techniques for high-resolution current recording from cells and cell-free membrane patches. *Pflugers Arch.* **391**, 85–100.
- Hilgemann, D. W. (1995) The giant membrane patch, in *Single-Channel Recording*, 2nd ed. (Sakmann, B. and Neher, E., eds.), Plenum Press, NY, pp. 307–327.
- Hoffman, D. A., Magee, J. C., Colbert, C. M., and Johnston, D. (1997) K⁺ channel regulation of signal propagation in dendrites of hippocampal pyramidal neurons. *Nature* **387**(6636), 851–853.
- Kotecha, S. A., Eley, D. W., and Turner, R. W. (1997) Tissue printed cells from telodendrosensory and cerebellar structures. *J. Comp. Neurol.* **386**, 277–292.
- Langley, J. N. (1907) On the contraction of muscle, chiefly in relation to the presence of 'receptive' substances. Part I. *J. Physiol.* **36**, 347–384.
- Levis, R. A. and Rae, J. L. (1992) Constructing a patch clamp setup, in *Ion Channels: Methods in Enzymology*, vol. 207 (Rudy, B. and Iverson, L. E., eds.), Academic Press, NY, pp. 14–66.
- Lin, J.-H., Sand, P., and Rydqvist, B. (1999) Macrocurrents of voltage gated Na⁺ and K⁺ channels from the crayfish stretch receptor neuronal soma. *Neuro-Report* **10**, 2503–2507.
- Matsuda, H. and Stanfield, P. R. (1989) Single inwardly rectifying potassium channels in cultured muscle cells from rat and mouse. *J. Physiol.* **414**, 111–124.
- Milton, R. L. and Caldwell, J. H. (1990) How do patch clamp seals form? A lipid bleb model. *Pflugers Arch.* **416**, 758–762.
- Penner, R. (1995) A practical guide to patch clamping, in *Single-Channel Recording*, 2nd ed. (Sakmann, B. and Neher, E., eds.), Plenum Press, NY, pp. 3–30.
- Rae, J. L. and Levis, R. A. (1992) Glass technology for patch clamp electrodes, in *Ion Channels: Methods in Enzymology*, vol. 207 (Rudy, B. and Iverson, L. E., eds.), Academic Press, NY, pp. 66–92.
- Rashid, A. J., Morales, E., Turner, R. W., and Dunn, R. J. (2001) The contribution of dendritic Kv3 K⁺ channels to burst threshold in a sensory neuron. *J. Neurosci.* **21**(1), 125–135.
- Roberts, W. M. and Almers, W. (1993) Patch voltage clamping with low-resistance seals: Loose patch clamp, in *Ion Channels: Methods in Enzymology*, vol. 207 (Rudy, B. and Iverson, L. E., eds.), Academic Press, NY, pp. 155–176.
- Sakmann, B. and Neher, E. (1995) Geometric parameters of pipettes and membrane patches, in *Single-Channel Recording*, 2nd ed. (Sakmann, B. and Neher, E., eds.), Plenum Press, NY, pp. 637–650.
- Sakmann, B. and Stuart, G. (1995) Patch pipette recordings from the soma, dendrites, and axon of neurons in brain slices, in *Single-Channel Recording*, 2nd ed. (Sakmann, B. and Neher, E., eds.), Plenum Press, NY, pp. 199–212.
- Stuhmer, W., Ruppersberg, J. P., Schroter, K. H., Giese, K. P., Perschke, A., Baumann, A., and Pongs, O. (1989) Molecular basis of functional diversity of voltage-gated potassium channels in mammalian brain. *EMBO J.* **8**, 3235–3244.
- Stuhmer, W. and Parekh, A. B. (1995) Electrophysiological recordings from *Xenopus* oocytes, in *Single-Channel Recording*, 2nd ed. (Sakmann, B. and Neher, E., eds.), Plenum Press, NY, pp. 341–356.

12

Combining Patch-Clamp Techniques with RT-PCR

*Gerald Seifert, Albert Becker,
and Christian Steinhäuser*

1. Introduction

One of the main challenges for a better understanding of signaling mechanisms in the normal and diseased central nervous system (CNS) is to unravel the molecular basics of function on the cellular and systemic levels. Several important cellular processes, such as proliferation, differentiation, and cell death, are directly or indirectly influenced or even controlled by the activity of ion channels and receptors. The patch-clamp technique has been proven a powerful method for studying functional peculiarities of such channels, which considerably improved our knowledge of mechanisms underlying neuronal excitation and inhibition.

Besides discriminating ion channels according to their biophysical and pharmacological profile, molecular-cloning technologies have been developed over the past two decades, enabling the identification of a wealth of structurally distinct subunits. These subunits comprise a number of ion-channel families and heterologous expression experiments in combination with electrophysiology has shown that the assembly of different subunits can cause distinct channel functioning. However, these studies have also demonstrated that in most cases, it is not possible to identify subunit combinations or even single subunits from functional studies alone. Native cells usually possess very complex expression patterns and so far our knowledge about their subunit assemblies and receptor stoichiometry is very limited.

From: *Neuromethods*, Vol. 35: *Patch-Clamp Analysis: Advanced Techniques*
Edited by: W. Walz, A. A. Boulton, and G. B. Baker @ Humana Press Inc., Totowa, NJ

The introduction of the single-cell reverse transcription-polymerase chain reaction (RT-PCR) (Lamboleze et al., 1992) and its combination with the patch-clamp method and fast application techniques makes now possible to identify gene transcripts and to correlate them with functional data in the same individual cell.

2. Optimizing the RT-PCR

Procedure Using mRNA from Brain Tissue

2.1. General Laboratory Practice

To avoid degradation of cellular RNAs and to maintain a RNase-free environment in the lab, all pipets, tubes, glass, and plasticware have to be autoclaved with gas (ethylene oxide) sterilization. The surface of the worktops and all used pipets and tweezers must be frequently cleaned with RNase AWAY™ (Molecular BioProducts, San Diego, CA) to remove RNases and DNA contamination. Gloves should always be worn during the experiments. Only aerosol resistant filter tips are recommended for the preparation of RT and PCR. RNAs should be processed on a laminar flow box to avoid any contamination of the samples by lab personnel.

Contamination with cDNAs, which are easily amplified by PCR and produce false-positive results, is of particular risk for transcript analysis. Therefore, RNA processing and PCR should be performed in separate rooms. Similarly all pipets, equipment, and reagents should be separated to avoid cDNA transfer to reagents used for cell harvesting and first-strand synthesis. For the same reason, amplified cDNAs must always be handled with care. These precautions have absolutely to be accompanied by appropriate negative control experiments to identify and prevent potential contamination (Dragon, 1993).

When performing semiquantitative real-time RT-PCR, all fluorescent probes must be accurately handled to prevent contamination of tubes, reagents and samples to avoid false-positive fluorescence. For each PCR run, background fluorescence must be carefully checked with appropriate controls, e.g., by omitting the template (RNA, cDNA) while leaving all other reagents unchanged, or by performing the reaction without DNA polymerase. Under these conditions, consecutive PCR cycles must necessarily fail to produce any increase in fluorescence intensity. In addition, fluorescence dyes are added to buffers of numerous commercial RT-PCR

Kits to overcome the background fluorescence problem (passive references).

2.2. Design of PCR Primers

To investigate the expression profile in single cells, the subunits of the corresponding gene family as well as closely related genes should be aligned to identify homologous and diverse nucleotide sequences. Primer design particularly has to consider all the putative insertions or alternatively spliced exons, editing, and mutation sites which might be of relevance for the subsequent analysis. A two-round PCR is recommended to increase yield and specificity using nested primers in the second amplification round. For qualitative approaches it is favorable to place the “outer” primers for the first PCR in conserved regions while at least one of the second round, “nested” primers should be located in a subunit-specific region of the nucleotide sequence. Synthesis of long products is less efficient and hence the fragments to be amplified should not exceed 800 base pairs (bp). In order to avoid amplification of genomic DNA, ideal primers should be located on different exons separated by introns. The use of computer programs is recommended for the design of effective primers. These commercially available computer programs help to avoid primer pair dimers, primer self dimers, hairpins, or misannealing of primers. Primers can also be defined empirically, but the reaction conditions for optimal gene detection must always be optimized. The recommended G/C content of the primers should exceed 50%.

2.3. mRNA Isolation and Reverse Transcription

To test and optimize the RT-PCR procedure, we prepare total RNA from freshly isolated rodent brain using guanidinium isothiocyanate and phenol (Trizol™, Life Technologies, Gaithersburg, MD) (Chomczynski and Sacchi, 1987). The RNA pellet is dissolved in water and stored at -80°C . To estimate the RNA concentration, the optical absorbency of the solution is determined at 260 nm (OD_{260}). In order to remove residual genomic DNA, we incubate 4 μg total RNA in PCR buffer, add 10 mM dithiothreitol (DTT), 10 mM MgCl_2 , 40 U RNase inhibitor (RNasin™, Promega, Madison, WI), and 40 U RNase-free DNaseI (Roche, Mannheim, Germany; reaction volume 20 μL). After incubation in a bloc thermostat (37°C , 30 min), the reaction is stopped with EDTA (2.5 mM), RNA extraction is repeated

with phenol/chloroform/isoamyl alcohol, RNA is precipitated with isopropanol, and the RNA pellet is redissolved in water. The final concentration of the yielded RNA can be determined with absorption spectrometry (OD_{260}) and the solution should be stored at -80°C (see Ausubel et al., 1996).

Alternatively, mRNA can be isolated immediately after DNase treatment. Therefore, 50 μL of deoxythymidine oligonucleotide [oligo (dT)₂₅] linked Dynabeads™ (Dynal, Oslo, Norway) are used to segregate and purify mRNA from total RNA, the latter containing only about 3% of cytoplasmic mRNA. This method is based on the binding of polyadenylated mRNA tails to oligo (dT)₂₅, covalently linked to monodisperse polymer spheres that are coated with magnetic iron oxide. mRNA then can be separated from total RNA by means of a permanent magnet. The mRNA bound to the beads has to be washed and suspended in water, frozen, and stored at -80°C . Removal of mRNA from the Dynabeads™ is realized by heating to 90°C (2 min). The beads are separated from the target-containing supernatant when the reaction tube is placed in a magnet stand, although the presence of the beads does not affect the RT-PCR. Subsequently, a fourth of the isolated mRNA amount (corresponding to 1 μg of the original total RNA) is transcribed into cDNA using the following mix: RT buffer, 0.1 mM DTT, $4 \times 125 \mu\text{M}$ deoxyribonucleotide triphosphates (dNTPs), 50 μM random hexanucleotide primers (Roche), 40 U RNase inhibitor, 200 U Superscript II-RT (Life Technologies), reaction volume 20 μL , incubation for 1 h at 37°C .

To adapt the procedure to single-cell conditions 1 ng of DNA-free, total RNA is transcribed using an alternative RT protocol as described in Subheading 3.3.

2.4. Two-Round PCR

For further PCR optimization, a two-round RT-PCR should be performed with 1/10 of the cDNA amount resulting from the reverse transcription. In the first PCR round, we usually perform a multiplex PCR for parallel detection of different genes, including a house-keeping gene as an internal positive control. This internal control is of particular relevance in the case of single-cell RT-PCR. However, different primer pairs sometimes interact with each other, which may reduce the yield of the PCR. It is, therefore, always recommended to compare the results obtained with primers for the tar-

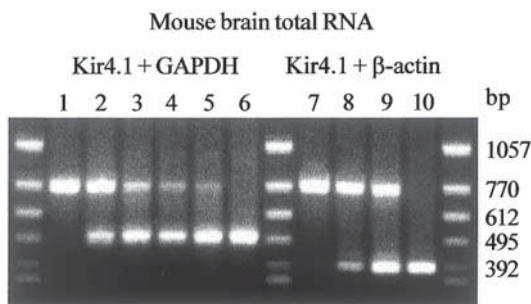


Fig. 1. Sensitivity and specificity of multiplex RT-PCR. Mouse brain total RNA (DNA-free, 1 μ g) was reverse transcribed into cDNA as described in Subheading 2.3. This cDNA (2 μ L) served as a template for PCR (35 cycles). PCR was run with Kir4.1 primers (concentration always 200 nM; lanes 1–5, 7–9) together with increasing concentrations of GAPDH (0, 50, 100, 150, and 200 nM; lanes 1–5) or β -actin primers (0, 100, and 200 nM; lanes 7–9). Lanes 6 and 10 represent respective PCR products using either GAPDH or β -actin primers alone (200 nM each). Agarose gel electrophoresis (1.5%, stained with ethidium bromide) confirmed the expected sizes of the amplified cDNAs (Kir4.1, 767 bp; GAPDH, 504 bp; β -actin, 387 bp). The molecular-length marker was Φ X-174-RF DNA *HincII* digest.

get gene alone and those obtained together with the housekeeping gene primers. Such type of analysis is shown in Fig. 1. In this example, increasing amounts of primers for glyceraldehyde-3-phosphate dehydrogenase (GAPDH) suppressed the amplification of cDNA encoding the K⁺ inward rectifier (Kir) channel, Kir4.1, while the housekeeping gene β -actin did not. Obviously, in this case, GAPDH should not be used as an internal control because it can produce false-negative results.

After the first-round PCR using multiplex primers, the PCR product has to be cleaned with commercial cleaning kits (e.g., UltraClean[™] PCR Clean-up[™] Kit, Mobio, Solana Beach, CA). Therefore, we resolve 50 μ L of the PCR product in 40 μ L water. An aliquot of this solution (2 μ L) is used as a target for the subsequent parallel PCR runs. This second PCR usually runs with a reduced number of cycles (20–35; depending on the amount of existing gene copies).

PCR is followed by ethidium bromide agarose gel electrophoresis (1.5%) to identify the lengths of the cDNAs. Ideally, only one band of the expected length should appear in each lane for the respective subunit. If an additional, weaker band of a putative by-product appears in the gel, the second PCR round has to be repeated. First, annealing temperature and Mg^{2+} concentration should be empirically modified to find optimal conditions that result in specific PCR products. If this does not help, alternative primer pairs must be tested.

The first- and the second-round PCR each is performed in a reaction volume of 50 μ L, containing PCR buffer, 2.5 mM $MgCl_2$, $4 \times 50 \mu$ M dNTPs, and 200 nM of the respective primer.

Our standard PCR protocol starts with initial denaturation at 95°C (4 min), then the temperature is held at 85°C until *Taq* DNA polymerase (2.5–5 U; Life Technologies) is added to all tubes in the bloc (hot-start PCR). Five PCR cycles are performed, each of them with three temperature steps: denaturation at 94°C (25 s), primer annealing at 43–65°C (2 min), and primer extension at 72°C (30 s). The next 20–40 cycles use the same temperatures except the duration of primer annealing, which is shortened to 45 s. Final elongation runs at 72°C (7 min). The annealing temperature matches the melting temperature of the primers.

2.5. Restriction Analysis

Independent methods, such as nucleotide sequencing, sequence-specific probe hybridization (Southern blotting), and restriction analysis have to be performed to verify the identity of the PCR products. Restriction analysis offers a fast and convenient possibility to confirm cDNA specificity. Here, cDNA double strands are cleaved by bacterial-restriction endonucleases recognizing a defined nucleotide sequence. An advantage of this method is the almost 100% effectiveness of digestion. As a prerequisite for this type of analysis, the second-round PCR must be repeated to produce a sufficient amount of cDNA copies, and the PCR product has to be cleaned from buffers and salts. Restriction endonucleases need specific reaction conditions to reach maximal activity. We perform digestion in a small volume (15 μ L), and add buffer and 10–20 U restriction enzyme to the PCR product, which is dissolved in water. Incubation takes at least 3 h. The cDNA fragments are analyzed in agarose gels with high band resolution designed to

detect even tiny lengths differences between double-stranded cDNAs (Separide™ gel matrix; 2%; Life Technologies).

Figure 2 shows cDNAs encoding Kir2.0 and Kir4.1 subunits, amplified from mouse brain total RNA, together with the respective fragments after restriction analysis. The PCR products were completely digested and the resulting cDNA fragments were of the expected lengths, demonstrating the specificity of the procedure.

Suitable restriction endonucleases can be selected with computer programs. The enzyme should recognize a specific nucleotide sequence occurring in only one of the subunits to be analyzed, and should not cut related sequences. In addition, for easy detection the enzyme of choice should cut the cDNA only once or twice, to produce no more than three fragments.

3. Peculiarities of Single-Cell RT-PCR Techniques

3.1. Harvesting of Cellular RNA from Brain Slices

Patch-clamp analysis of voltage and ligand-gated ion channels in single neural cells and the subsequent identification of gene transcripts in the same cell requires some attention to avoid degradation of RNA during recording. To reduce contamination with RNases and nucleotides other than from the tissue to be analyzed, solutions necessary for electrophysiological recording should be prepared in a room separated from that where PCRs are performed, and a sterile laboratory practice must be followed. Gloves should always be worn for the preparation of solutions and when performing electrophysiological recordings, particularly when touching the recording pipet. The surface of pipet puller and recording setup have to be disinfected with propanol or ethanol, and the Ag/AgCl electrode must be cleaned prior to recording. The recording chamber should daily be thoroughly washed with distilled water.

Filtrated millipore water should be used to prepare bath solutions perfusing the brain slice in the recording chamber. Reagents specifically prepared for the use in RT-PCR should be utilized as far as possible, and the solutions have to be stored in sterilized glassware. Pipet solutions are prepared from aliquots of pyrogene-free water. Separate salt aliquots are added and the pH can only be adjusted after cleaning the pH-electrode with water and ethanol. Pipet solutions are immediately aliquoted on a sterile bench

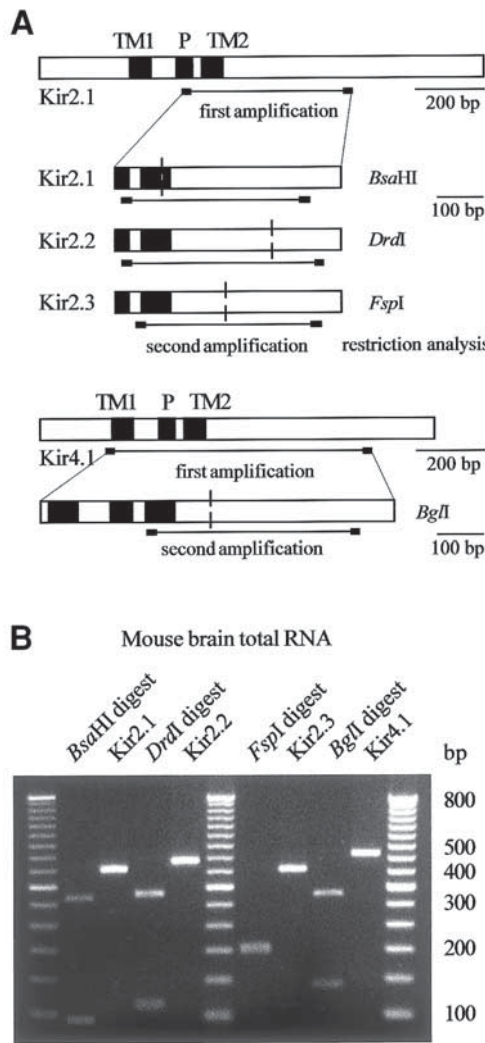


Fig. 2. PCR procedure and analysis of amplified cDNA products. (A) Scheme of the nucleotide sequences of the coding region of mouse Kir2.1 and Kir4.1 subunits (5' left). Full boxes represent transmembrane regions (TM1, TM2) and pore region (P) of the corresponding protein. For the first amplification of Kir2.x subunits, the upstream (sense) primer was located in the pore-coding region and the downstream (antisense) primer was set into the C-terminus (primer location is indicated by horizontal bars).

and frozen. We observed a reduced success rate of transcript analysis when the preceding electrophysiological analysis took more than 15 min, probably due to wash-out and dilution of cytoplasmic RNA in the pipet and/or its deletion by ubiquitously existing RNases. The latter can be counteracted by adding RNase inhibitor to the pipet solution (0.5 U/ μ L pipet solution; stock of 40 U/ μ L RNasin[™]; Promega), which should be prepared fresh daily. This precaution enabled successful mRNA identification even after prolonged electrophysiological analysis.

Our recording pipets are fabricated from borosilicate capillaries and we fill them with 6 μ L of pipet solution using long polyethylene microloaders (Eppendorf, Hamburg, Germany), which restricts filling to the tip of the pipet. This tip can be considered "sterile" since it was heated during the pulling step. We refrain from adding buffers or dNTPs to the pipet solution to avoid changes of the ionic composition of pipet solution. The resistance of the recording pipets is 4–6 M Ω , which allows both stable whole-cell recordings and subsequent aspiration of cytoplasm into the patch pipet. The cell content is harvested by applying negative pressure to the pipet interior while retaining the gigaohm seal resistance between pipet tip and membrane. It is advantageous to follow the flow of the cytoplasm into the pipet, preferably via a monitor

(continued) In the case of Kir4.1, the sense primer was located in the TM1 region. The lower panels represent gene fragments resulting from the first amplification. The sizes of the PCR products were 491 bp (Kir2.1, Kir2.2, and Kir2.3) and 767 bp (Kir4.1). For the second amplification, upstream primers were located in the P (Kir2.1 and Kir2.2) and TM2 region (Kir2.3 and Kir4.1) while the nested downstream primers all were set in the C-terminus. At least one primer of each pair was subunit-specific. Vertical dashes indicate restriction sites of the respective cDNA. Kir2.1 was cut by *Bsa*HI (position 516), Kir2.2 by *Drd*I (755), Kir2.3 by *Fsp*I (626), and Kir4.1 by *Bgl*II (426). (B) Total RNA from mouse brain (1 ng) was used to test for specificity of the RT-PCR. After performing a two round RT-PCR according to the single-cell protocol, the agarose gel (Separide[™], 2%) revealed cDNAs (Kir2.1: 408 bp; Kir2.2: 437 bp; Kir3.3: 401 bp; Kir4.1: 461 bp), which were subsequently digested by specific restriction enzymes, yielding fragments of the expected lengths: 318 bp and 90 bp for Kir2.1 (*Bsa*HI), 326 bp and 111 bp for Kir2.2 (*Drd*I), 204 bp and 197 bp for Kir2.3 (*Fsp*I), and 329 bp and 132 bp for Kir4.1 (*Bgl*II). A 50 bp ladder was used as a molecular-weight marker.

connected to a CCD camera (e.g., C5405; Hamamatsu Photonics, Hamamatsu, Japan) (Jonas et al., 1994; Monyer and Jonas 1995). This helps to avoid the aspiration of neighboring tissue. After sucking about half the cell content, we often lift the cell on top of the pipet above the slice and complete harvesting in the flow of the bath solution under visual control. Only single cells without any adhered other cells or tissue debris are selected for RT-PCR analysis (Fig. 3).

After aspiration of the cytoplasm, the pipet is transferred into a thin-walled reaction tube filled with 3 μ L of DEPC-treated water. The tip of the pipet is broken at the bottom and only part of the pipet solution (about 3 μ L) is expelled into the water with positive pressure. Thus, the cytoplasm is released into the water and the reaction tube is frozen in liquid nitrogen and stored at -80°C until the RT reaction is carried out (von Eggeling and Ballhausen, 1995).

3.2. Harvesting of Acutely Isolated Cells

Brain-slice recordings offer the great advantage of analyzing membrane properties with the cellular environment left largely intact. However voltage-clamp control is often limited under these conditions, particularly in cells with extensive branching. Also, the analysis of receptor currents with fast time constants of activation or inactivation is compromised by the relatively slow speed of agonist application due to diffusion barriers *in situ*. One possibility to overcome such limitations is the use of freshly isolated cells. Basically, RNA harvesting from isolated cells requires the same precautions as described earlier for the slice preparation. We use a combination of enzymatic and mechanical treatments to acutely isolate viable cells from the tissue. Brain slices are prepared (thickness 300–450 μm) and incubated in a protease (e.g., papain, trypsin, or pronase) containing solution. The duration of enzymatic incubation depends on various parameters (e.g., age of the animal, cell type, enzyme concentration, temperature) and usually varies between 10 and 60 min (Seifert et al., 2000; Seifert et al., 1997b). After thorough wash and recovery from protease incubation, the region of interest is carefully dissected with a scalpel. The cells are then disaggregated under microscopic control using fire polished Pasteur pipets (tip diameter 100–200 μm) or tungsten needles. Process bearing cells without indications of osmotic swelling are selected and proved suitable for patch-clamp analy-

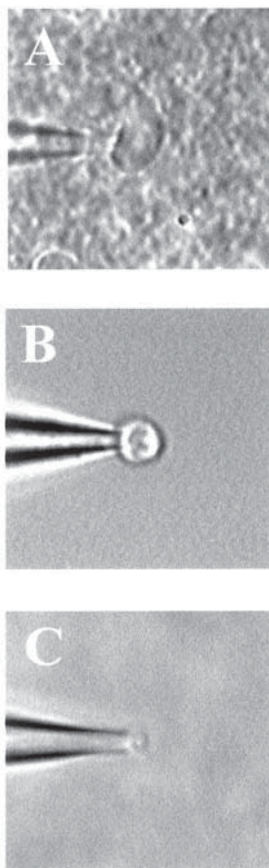


Fig. 3. Harvesting of cytoplasm from glial cells. After recording *in situ* (brain slice, 150 μm thick, CA1 stratum radiatum) (A), the cell on top of the patch pipet was lifted out of the tissue (B), and subsequently was aspirated into the pipet (C). Cell harvesting was observed with IR-DIC optics and videomicroscopy.

sis and subsequent transcript investigation with RT-PCR. Careful comparison with recordings obtained *in situ* from the same cell type confirmed that characteristic electrophysiological parameters remain unchanged after the isolation procedure (Steinhäuser et al., 1994). Recording pipets are filled with 6 μL of pipet solution. After recording, the cell at the tip of the pipet has to be transferred

to a separate dish to be washed with fresh bath solution, and then is sucked into the recording pipet. The cell content and about 3 μL of the pipet solution is expelled into a reaction tube containing 3 μL DEPC-treated water. Alternatively, the whole cell can be harvested with a second pipet (diameter 10–20 μm) under microscopic control. The cell is easily removed from the tip of the recording pipet and sucked into the harvesting pipet, whereby one has to be cautious and avoid aspiration of too much bath solution. The tip of the harvesting pipet is broken and about 3 μL of its content is expelled into a water-filled reaction tube (Seifert et al., 1997a). Harvesting with a second pipet can also be performed *in situ* if the cell is drawn out of the tissue after electrophysiological analysis (Seifert et al., 1999). The reaction tubes are frozen in liquid nitrogen and stored at -80°C . We always perform negative controls in parallel, by using cell-free bath solution for RT-PCR.

3.3. Preventing Contamination with Genomic DNA, Reverse Transcription of RNA

The nucleus is often aspirated into the pipet in our experiments and the harvested material therefore contains mRNA as well as genomic DNA. PCR approaches may use primers that do not span intron regions. In these cases, to prevent amplification of genomic DNA (Li et al., 1988), which would result in PCR products of the same length as the corresponding mRNA, RT-PCR has to be preceded by DNase treatment. To decide whether DNA digestion is necessary, e.g., if the exon-intron structure of the gene to be analyzed is unknown, one should first determine the DNA size by amplifying genomic DNA (200 ng). In the case the amplicon spans introns, this yields a larger PCR product than that of the corresponding cDNA. If the intron is too long, DNA amplification will fail completely.

DNase mastermix is added to the frozen cell content in the reaction tube. This mastermix contains all reagents necessary for the RT reaction, except reverse transcriptase: first-strand buffer; $4 \times 250 \mu\text{M}$ dNTPs, 20 U RNasin[™] (Promega); 50 μM random hexamer primers (Roche); and 5 U RNase-free DNaseI (Roche) (reaction volume 10 μL) (Dilworth and McCarrey, 1992; Gurantz et al., 1996). The reaction mix has to be covered with freshly aliquoted paraffin oil, incubated at 37°C (30 min), and afterwards DNaseI is heat-inactivated at 95°C (5 min). We observed a dramatic drop of PCR

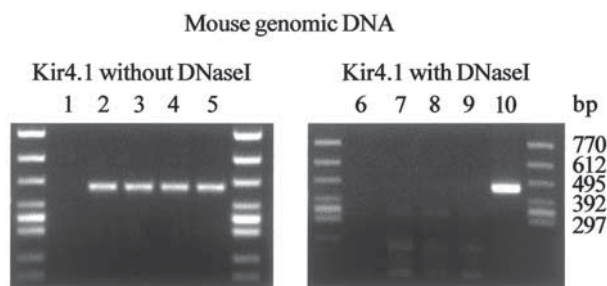


Fig. 4. Mouse genomic DNA (0, 50, 100, 250, and 500 ng; lanes 1–5, and 6–10, respectively) was used as a template for a two-round nested PCR with outer and inner Kir4.1 specific primers. A two-round PCR was performed according to the single-cell protocol (Subheading 4.3.2.). Amplification yielded Kir4.1 cDNAs of the expected length (461 bp; lanes 2–5). No reaction products were observed when treating up to 250 ng genomic DNA with 5 U DNaseI (Roche) prior to the two-round PCR (lanes 7–9). The length marker was Φ X-174-RF DNA *HincII* digest.

success rate when trace amounts of active DNaseI remained during the RT reaction. Covering of the DNaseI reaction volume seems to be necessary to prevent evaporation. Subsequently, reverse transcriptase (0.5 μ L) and RNase inhibitor (20 U) are added to the reaction volume, and the RT reaction is started at 37°C.

As a negative control for RT and verification of complete DNA degradation, the reverse transcriptase should be omitted. Prior to its application to single cells, the effectiveness of DNA digestion should be tested under the same conditions (buffers, reagents, volume) by adding increasing amounts of genomic DNA (10, 50, 100, 250, 500 ng; Promega) to water, treating with DNaseI, and amplifying the mixture in a two-round PCR. These experiments confirmed a reliable and complete digestion of up to 250 ng genomic DNA (Fig. 4), which by far exceeds the DNA content of a single cell.

Efficient reverse transcription of RNA into cDNA is a prerequisite for the success of the subsequent PCR. Single-cell RT is performed in a small volume (about 10 μ L) (Lambolez et al., 1992; Brenner et al., 1989). We use random hexamer nucleotide primers that bind to all possible matching sites and can transcribe even pieces of mRNA. Thus, the probability of receiving the first cDNA

strand is greater compared to corresponding experiments with oligo (dT)₂₅ primers. For semiquantitative single-cell transcript analysis the use of gene-specific antisense primers can be recommended (Subheading 4.4.1.). We use reverse transcriptase from Moloney murine leukemia virus (MMLV) carrying a RNase H deletion (RNase H⁻; Superscript II[™]; Life Technologies) or an enzyme from a new retroviral source, especially designed for the transcription of small RNA amounts (Sensiscript[™]; Hilden, Germany).

3.4. Multiplex and Nested PCR

Single-cell RT-PCR provides the opportunity to detect several genes, including cell type-specific markers or even a whole gene family in individual, electrophysiologically characterized cells and thus enables investigation of structure/function relationships. Such an approach can be realized with a multiplex PCR using more than one primer pair for the first PCR round (Ruano et al., 1995). Careful optimization of primers and PCR conditions is strictly required, as illustrated in the example given in Fig. 1.

For a simultaneous detection of several subunits of a gene family, we use nonspecific primer pairs and locate them in a conserved region of the gene that is common to all those subunits. Up- and downstream primers are designed to allow up to two mismatches while the last 6 bp of the primer's 3' end should fully match. In the case of more than two mismatches, degenerated primers should be used. Partition of cDNA after the RT should be avoided in the case of single cells because this often reduces the success rate of subsequent PCR amplification. Instead, we utilize the whole cDNA as a template in the first-round PCR. The annealing temperature should always be set below the melting temperature of the primers (Lambolez et al., 1992). The separation of the initially co-amplified gene fragments is implemented in a second-round PCR using nested primers. The first PCR round consists of about 45 cycles, with primer annealing being prolonged to 2 min for the first 5 rounds and lasting 45 s in the following cycles. A hot-start PCR should be performed by adding *Taq* polymerase directly to the denaturated reaction mix at 85°C, rather than by using hot-start polymerase that requires pre-heating at 95°C (10–15 min). In single-cell approaches the PCR should be performed in reaction volumes of about 50 µL. After RT, mastermix containing PCR buffer, 2.5 mM MgCl₂, and 10 pmol of each primer is added to

the cDNA. dNTPs are not added (present at a concentration of $4 \times 50 \mu\text{M}$ due to dilution of the RT mix). *Taq* polymerase (4 U, Life Technologies) is added at 85°C . We use a PCR cycler (e.g., MJ Research, Madison, WI) that permits very rapid temperature ramps, reducing the overall reaction time and limiting polymerase inactivation.

The second PCR runs with an aliquot ($2 \mu\text{L}$) of the cleaned PCR product resulting from the first round and uses either one (heminested) or two (nested) new primers. Both specificity and sensitivity of the PCR are improved with nested primers, which have to be set into the pre-amplified cDNA obtained from the first round. In the second round, sense or antisense primer must be gene specific to prevent amplification of related subunits. To meet this postulation the primers of the first round should span a heterologous region, which is the target of the specific primers used in the second PCR.

Optimal conditions for the second PCR have to be found empirically whereby the variation of Mg^{2+} concentration and annealing temperature is of particular relevance. Annealing temperatures should roughly match the melting temperatures of the respective primers. The number of cycles should be reduced as compared to the first round and range between 20 and 35. Again, the PCR should be performed in a reaction volume of $50 \mu\text{L}$, adding mastermix containing PCR buffer, 2.5 mM MgCl_2 , 10 pmol of each primer, and $4 \times 50 \mu\text{M}$ dNTPs to the pre-amplified product. *Taq* polymerase (2.5 U, Life Technologies) is added at 85°C . The PCR product then can be analyzed in a 1.5–2% ethidium bromide-labeled agarose gel.

As a negative control, we run the PCR with water instead of cDNA. Further controls concern the cell harvesting/RT-step (replacement of cell content by recording solution) and omission of reverse transcriptase in the RT-reaction (cf. Subheading 3.3.).

3.5. Real-Time RT-PCR for Semiquantitative Single-Cell Transcript Analysis

3.5.1. Introduction to mRNA Quantification

An ABI PRISM™ 7700 Sequence Detection System (PE Applied Biosystems, Foster City, CA) can be used for mRNA quantification in a one-round, single-tube, single-enzyme RT-PCR amplification. This system permits a quantitative detection of PCR product accumulation during each cycle by using the fluorogenic 5'-nuclease

assay (Holland et al., 1991). Thereby the real-time RT-PCR approach takes advantage of the 5'-nuclease activity of the DNA polymerase for cleavage of a dual-labeled fluorogenic hybridization probe (TaqMan™ probe). The TaqMan™ probe hybridizes between the forward and reverse primers on the complementary DNA strand. This probe consists of an oligonucleotide of about 25–35 bp length labeled on the 5' end with a fluorescent reporter dye. The 3' end of the TaqMan™ probe is labeled with a second fluorescent dye, which absorbs the emitted light of the reporter dye by fluorescent energy transfer (fluorescence quencher) when both dyes are attached to the oligonucleotide probe, as long as the probe is not digested. The DNA polymerase cleaves the TaqMan™ probe and separates reporter dye and fluorescence quencher, resulting in an interruption of fluorescent energy transfer and light emission by the reporter dye (Livak et al., 1995). Emission increase at dye-specific wavelengths during each PCR cycle is consecutively monitored. After normalization of emission intensity to an internal reference, the threshold cycle (C_T value) is determined in the exponential phase of the PCR. The C_T value is used for quantification of the input copy number of target mRNA normalized to a reference gene (Fink et al., 1998).

3.5.2. Cell Harvesting and mRNA Isolation

Application of this quantitative method to single cells requires the same precautions with respect to contamination with RNases and preamplified cDNAs, as mentioned earlier. Harvesting of cytoplasm from single cells *in situ* should follow the instructions given in Subheading 3.1., with an alteration in the last step. Since this method lacks an initial cDNA amplification round, and the cell content usually has to be split into several portions to enable parallel amplification of target and reference genes (*see below*), the success rate of single-cell analysis is lower for certain low copy genes as compared with two-round, qualitative PCR approaches. We circumvent this problem by pooling cells with similar electrophysiological properties. To limit the liquid volume for the subsequent reactions, recording pipets should be filled with 6 μ L and the cell contents should be harvested into an empty reaction tube. After breaking the tip of the pipet, about 2 μ L of the pipet content are expelled under positive pressure, collected at the bottom by quick centrifugation and immediately frozen in liquid nitrogen. In this way, 4–6 cells should be consecutively collected in the same tube

(final volume about 10 μ L). Oligo (dT)₂₅ linked Dynabeads™ can be used to separate mRNA from genomic DNA. Lysis buffer (20 μ L) and Dynabeads™ suspended in lysis buffer (10 μ L) are added to the reaction tube. After wash (50 μ L) the beads with the adhered mRNA are suspended in water (20 μ L), frozen, and stored at -80°C until amplification.

3.5.3. Primer and Probe Design

TaqMan™ probes and primers should be designed using commercial software (e.g., Primer Express, PE Applied Biosystems). As opposed to the first round of nested PCR approaches, primers must be used that are specific to the mRNAs to be detected. The usage of the TaqMan™ fluorescent probes additionally ensures specificity of the amplified products since the probe must be sequence-specific. Accordingly, increasing fluorescence intensity during consecutive PCR cycles is only observed if the probe is complementary to the target gene, but not during the formation of putative nonspecific amplicons. On the other hand, confirmation of the resulting cDNAs with restriction analysis is not feasible. The design of primers and probe is not independent of each other. As a general rule, the melting temperature of the probe should be $5\text{--}10^{\circ}\text{C}$ higher than that of the primers. The 5' end of the probe should not contain any 'G' and should immediately follow the 3' end of the respective primer.

3.5.4. Optimization of Quantitative Transcript Analysis in Single Cells

The RT-PCR is performed as a single-step, single-enzyme procedure using rTth DNA polymerase (PE Applied Biosystems). In a single-buffer system, this enzyme possesses efficient RT activity at 60°C and acts as a DNA polymerase at temperatures $>60^{\circ}\text{C}$. To reach high amplification efficiency, primers should be designed so that the size of the resulting amplicons do not exceed 150 bp. Generally, longer cDNA fragments are amplified with lower and more variable efficiency, which may hinder semiquantitative analysis relative to a reference gene.

Optimization of the PCR conditions should start with varying the concentration of primers, probe, and the Mn^{2+} content using DNA-free mRNA. Next, since the different target and housekeeping genes to be compared are simultaneously run in separate tubes, it is very important to ensure that the respective cDNAs are amplified with

the same efficiency, which is illustrated in the example of Subheading 4.4.2.

4. Examples: Functional and Molecular Analysis of Kir Channels in Individual Glial Cells

4.1. Introduction

Kir channels constitute a large family, which by now comprises seven subfamilies (Kir1.x–Kir7.x). These channels are present in many different tissues and cell types (Reimann and Ashcroft, 1999). Kir channels form homomeric or heteromeric tetramers and each subunit has two transmembrane domains connected by a pore-forming loop. Since these channels are selectively permeable for K^+ and have a high open probability at rest, they largely determine the resting membrane potential and stabilize it near the K^+ equilibrium potential (E_K). Unlike voltage-gated K^+ channels they lack an intrinsic voltage sensor. The inward rectifying property results from positively charged cytoplasmic polyamines and Mg^{2+} , which plug the channel pore from the intracellular side in a voltage-dependent manner. Pharmacologically, they are characterized by their sensitivity to sub-mM concentrations of Ba^{2+} (Fakler and Ruppersberg, 1996; Reimann and Ashcroft, 1999).

Kir channels are abundantly expressed in astrocytes in the CNS and were implicated to play a major role for K^+ homeostasis. The pivotal role of Kir channels for K^+ buffering was demonstrated in retinal astrocytes (Newman, 1986). Spatial K^+ buffering by Kir channels, rather than by Na^+/K^+ ATPases and $Na^+-K^+-2Cl^-$ transporters (Jauch et al., 1999) was also suggested to occur in the hippocampus. Moreover, recent data suggested that alterations in astroglial Kir channel function might be involved in seizure generation or seizure spread in human epilepsy (Schröder et al., 2000; Hinterkeuser et al., 2000; Bordey and Sontheimer, 1998). Immunohistochemistry suggested a presence of the subunit Kir4.1 and/or members of the Kir2.x family in hippocampal astrocytes (Poopalasundaram et al., 2000; Stonehouse et al., 1999).

In the examples presented here we use single-cell RT-PCR subsequent to functional analysis: 1) to investigate the Kir channel expression pattern in mouse hippocampal astrocytes (Subheading 4.3.) and 2) to find out which astroglial Kir subunits might be affected in the hippocampus of epilepsy patients (Subheading 4.4.).

4.2. Functional Properties of Kir Currents in Hippocampal Astrocytes In Situ

Recordings were obtained from astrocytes in the CA1 stratum radiatum area of mouse or human hippocampus as previously described (Steinhäuser et al., 1992; Kressin et al., 1995; Schröder et al., 2000; Hinterkeuser et al., 2000) (*see also* Chapters 2 and 5 in this book). Inward currents were activated when applying hyperpolarizing voltage steps in the voltage clamp mode (holding potential -70 mV). In most cells, these currents showed voltage-dependent inactivation negative to -130 mV (Figs. 5A, 6A). To test for the K^+ sensitivity of inward currents, the reversal potential was determined in bath solutions containing 5 and 50 mM $[K^+]_o$. Voltage ramps were applied which continuously changed the membrane potential between -140 and $+90$ mV within 1 s. To reduce the contribution of voltage-gated Na^+ and K^+ currents, recordings were taken in solutions containing TEA and 4-AP. Two important changes were observed as $[K^+]_o$ was increased. First, the zero-current potential shifted by about 50 mV towards positive membrane potential and this shift was very close to that predicted by the Nernst equation for a K^+ -selective membrane, indicating that the channels were predominantly permeable to K^+ ions. Second, the conductance was significantly increased in high K^+ solutions, which is also typical of inward rectifying K^+ channels (Fig. 5B). Moreover, inward currents were significantly reduced when adding low concentration of Ba^{2+} (50–100 μM) to the bath solution. The I/V relation of the Ba^{2+} sensitive currents showed a change in slope conductance at about -70 mV, i.e., near E_K , indicating inward rectification (Fig. 6B,C). Taken together, these data strongly suggested that the inward currents in astrocytes were mainly carried by K^+ ions (Kir currents).

4.3. Molecular Identity of Kir Subunits in Astrocytes of Mouse Hippocampus

4.3.1. Methodical Considerations: Harvesting, DNA Removal, and Reverse Transcription

Single-cell RT-PCR followed the strategy described in Subheadings 3.1., 3.3., and 3.4. (Seifert et al., 1999). The pipet solution (6 μL) was supplemented with RNasinTM (3U, Promega) and harvesting of

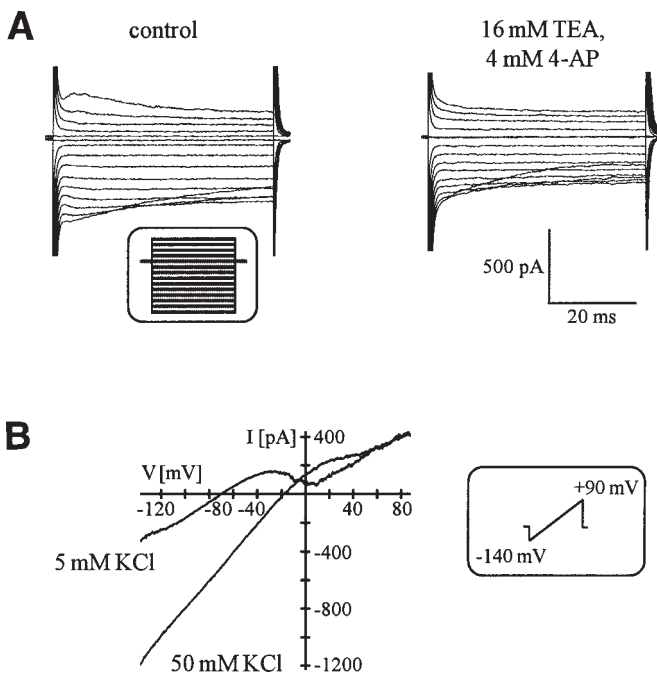


Fig. 5. Astroglial inward rectifier currents are mainly carried by K^+ (A) Starting from a holding potential of -70 mV, outward and inward currents were activated in a hippocampal astrocyte *in situ* by stepping the membrane between -160 and -20 mV (inset, left panel). To separate inward rectifier currents, voltage-dependent outward K^+ currents were reduced by adding tetraethyl ammonium chloride (TEA) and 4-aminopyridine (4-AP) to the bath solution (right). (B) Voltage ramps were applied to the same cell in normal (5 mM) or elevated K^+ concentrations, which continuously changed the membrane potential between -140 mV and $+90$ mV within 1 s (see inset). Both solutions contained TEA and 4-AP. Changing the bath K^+ concentration from 5 mM to 50 mM shifted the zero-current potential by 51.6 mV, indicating that the currents were predominantly carried by K^+ . The initial resting potential of the cell was -75 mV. Modified with permission from Kressin et al. (1995). Copyright © 1995, Wiley-Liss, Inc., a subsidiary of John Wiley & Sons, Inc.

the cell content was monitored with a CCD camera (C5405, Hamamatsu Photonics) using IR-DIC optics. Part of the pipet content (3 μ L) was transferred into a tube filled with DEPC-treated water (3 μ L)

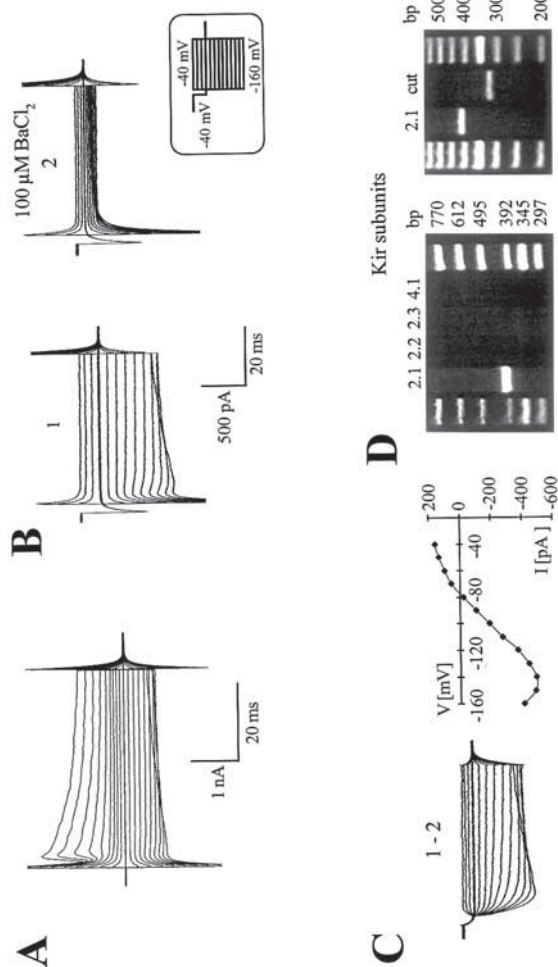


Fig. 6. Kir subunit expression by an individual glial cell. (A) Membrane currents were activated in response to de- and hyperpolarizing voltage steps between -160 mV and +20 mV (10 mV increments, holding potential -70 mV). (B) In BaCl_2 solution (2), the cell's resting potential shifted from -72 to -53 mV. (C) gives the Ba^{2+} sensitive current (1-2) with its I/V relation. (D) After recording, the cytoplasm was harvested for RT-PCR analysis. In this cell, gel electrophoresis detected only Kir2.1 cDNA (408 bp; left panel). The second round of Kir2.1 PCR was repeated and the resulting PCR product was cut by *Bsa*HI (318 bp; right panel).

by expelling under positive pressure. The tube was stored at -80°C until the RT reaction was carried out.

To prevent amplification of genomic DNA, RT was preceded by a DNase step. Therefore, $3.5\ \mu\text{L}$ of DNase reaction mix was added to the tubes (final volume about $10\ \mu\text{L}$) containing SensiscriptTM Buffer (Qiagen, Hilden, Germany), dNTPs (final concentration $4 \times 250\ \mu\text{M}$; PE Applied Biosystems), random hexanucleotide primer (final concentration $50\ \mu\text{M}$; Roche), $20\ \text{U}$ RNasinTM (Promega) and $5\ \text{U}$ RNase-free DNaseI (Roche). The mixture was covered with paraffin oil, incubated at 37°C (30 min) and denatured at 95°C (5 min). Immediately after denaturation, the reaction mixture was chilled, and $0.5\ \mu\text{L}$ ($20\ \text{U}$) RNasinTM (Promega) and $0.5\ \mu\text{L}$ SensiscriptTM reverse transcriptase (Qiagen) were added to the tubes. Single-strand cDNA synthesis was performed at 37°C (1 h).

4.3.2. Methodical Considerations:

PCR Amplification of Mouse Kir2.x and Kir4.1 Subunits

A two-round PCR was performed, using the PCR product obtained after the first round as a template for the second round. The single-cell multiplex PCR approach used primer pairs for Kir2.x and Kir4.1 together with primers for β -actin as a positive control. The sense and antisense Kir4.1 primers were 5'-GGCGCTACAAGCTT CTGCTC (position 191, position 1 being the first base of the initiation codon; gene bank accession number AB039879) and 5'-GGCT GACAGTGAGATCGCAG (position 938). The sense and antisense β -actin primers were 5'-GATATCGCTGCGCTGGTCGTC (position 10, X03672) and 5'-CATGGCTGGGGTGTGAAGGTC (position 375). The Kir2.x primer pair, designed to amplify cDNAs of mouse Kir2.1, Kir2.2 and Kir2.3 simultaneously, was located in a homologous region of the corresponding protein (pore region downstream to the second transmembrane region). The sense primer was 5'-GAG ACCCAGACCACCATT (position 412, Kir2.1, NM008425; position 415, Kir2.2, NM010603; position 385, Kir2.3, U11075), having one mismatch with each of the individual subunits. The antisense primer 5'-ATGCCTTCCAGGATGAC(A/C)ACAA had one mismatch with Kir2.1 and Kir2.2, and two mismatches with Kir2.3. The position of the antisense primers were 881, 884, and 854 for Kir2.1, Kir2.2, and Kir2.3, respectively; the expected fragment lengths were 491bp for each subunit.

The first-round PCR was performed after adding PCR buffer, MgCl_2 (final concentration 2.5 mM), and the corresponding primers (final concentration 200 nM each) to the RT product (final volume 50 μL). After denaturation (94°C, 4 min), 3.5 U *Taq* polymerase (Life Technologies) was added at 85°C. Forty-five PCR cycles were performed (denaturation at 94°C, 30 s; annealing at 49°C, 2 min for the first 5 cycles, and 45 s for the remaining cycles; extension at 72°C, 25 s; final elongation at 72°C, 7 min) using a thermocycler (MJ Research).

The PCR product was purified with a gene clean spin kit (Bio101, La Jolla, CA), and resolved in water (40 μL). An aliquot (3 μL) of the product was used as template for the second PCR (35 cycles; annealing at 54°C, first 5 cycles: 2 min, remaining cycles: 45 s) using the following nested primers: Kir2.1: sense 5'-CATTGGCTATGGTTTCAGGTGTG, position 426; antisense 5'-GGGCTGTCTTCATCTATTCGTGA, position 810; Kir2.2: sense 5'-CATTGGCTACGGGCTACGCTGTG, position 429; antisense 5'-CAAGGTCTTGACGGCTAAT, position 847; Kir2.3: sense 5'-GGAGTGCCCGTTGGCGGTCATT, position 429; antisense 5'-CCTCCTTGCCCATGCCGTA GAGTG, position 806; Kir4.1: sense 5'-CCCACTGGCCATCGTGCTTCTTA, position 420; antisense 5'-AGGTGGCACTGGTGGACTC, position 862; β -actin: sense 5'-CGTGGGCGCCCTAGGCACCA, position 102; antisense 5'-CTTAGGGTTCAGGGGGG, position 323. The PCR conditions were the same as described for the first round, but dNTPs (final concentration $4 \times 50 \mu\text{M}$) were added to each sample. The PCR products were identified by agarose gel electrophoresis (1.5%; stained with ethidium bromide) using a molecular-weight marker (ΦX174 *HincII* digest, Eurogentec, Seraing, Belgium).

For restriction analysis, the second PCR has been repeated. The product was purified as described, and redissolved in water (25 μL). The cDNAs of Kir2.1, Kir2.2, and Kir2.3 subunits were digested by the isoform-specific restriction endonucleases *Bsa*HI (cut at position 516), *Drd*I (position 755), and *Fsp*I (position 626; all from New England Biolabs, Frankfurt, Germany), respectively. Each product contained one recognition site yielding two cDNA fragments. Kir4.1 cDNA was digested by *Bgl*II (position 426; New England Biolabs), which did not cut the most related subunit, Kir4.2. Seven μL of the respective PCR product were incubated in 10 U restriction enzyme (3 h, 37°C). The cDNA fragments were analyzed by

electrophoresis (2% Separide™ gel matrix, Life Technologies) using a 50 bp ladder molecular weight marker (Life Technologies).

4.3.3. Single-Cell RT-PCR Analysis

of Kir Subunits in Mouse Hippocampal Astrocytes

After functional analysis single-cell RT-PCR (Schröder et al., 2000) was performed to investigate which Kir subunits were expressed by the astrocytes. A total of 26 glial cells with prominent Kir currents were tested for Kir4.1 transcripts. Only two of them contained Kir4.1 although in all those cells the housekeeping gene β -actin was identified, which served as a positive control. Kir2.x transcript analysis after functional characterization was performed in 13 cells. Kir2.1 mRNA was found in 10 cells while the subunits Kir2.2 and Kir 2.3 were only half as prevalent. The Kir2.1 subunit either occurred solely (39%) or was co-expressed with Kir2.2 (15%), with Kir2.3 (8%), or with both subunits (15%). Another three cells were devoid of Kir2.1 but contained either Kir 2.2 or Kir2.3 mRNAs.

Figure 6 gives an examples of this combined analysis. After characterizing the Ba²⁺ sensitivity of Kir currents (Fig. 6B) the cytoplasm was harvested and tested for the presence of Kir2.x and Kir4.1 transcripts. In this cell, RT-PCR detected Kir2.1 mRNA (Fig. 6D, left) and the specificity of the product was confirmed with restriction analysis (Fig. 6D, right).

4.4. Quantitative Kir Transcript Analysis and Correlation with Functional Data in Astrocytes Obtained from Epilepsy Patients

4.4.1. Methodical Considerations:

Real Time, Single-Cell RT-PCR

Analysis in the human tissue basically followed the strategies described in Subheading 3.5. The TaqMan™ EZ RT-PCR Kit (PE Applied Biosystems) was used to investigate human Kir4.1 and GAPDH transcripts with real-time RT-PCR. The reaction volume was 12.5 μ L. DNA-free mRNA was isolated with Dynabeads™ (Dyna) and used as a template for the following reactions (aliquots of 4.9 μ L). RT-PCRs for hKir4.1 and hGAPDH were run in parallel for each of the samples to be analyzed. The optimized reaction mixture contained TaqMan™ EZ buffer, 3 \times 300 μ M dNTP (dATP, dCTP, dGTP), 600 μ M dUTP, 3 mM Mn(OAc)₂, 1.25 U rTth DNA polymerase, 0.125 U uracil-N-glycosylase (UNG), 100 nM fluoro-

genic TaqMan[™] probe, and 50 nM of each primer. hGAPDH primers and TaqMan[™] probes were commercially available (5' labeled with JOE as a reporter dye; PE Applied Biosystems, Foster City, CA) and were used at the same concentrations as for hKir4.1. The following hKir4.1 specific TaqMan[™] oligonucleotides were used: sense primer, 5'-GCGCAAAAGCCTCCTCATT, position 609; anti-sense primer, 5'-CCTTCCTTGGTTTGGTGGG, position 659; probe FAM-5'-TGCCAGGTGACAGGAAACTGCTTCAG-TAMRA, position 631, gene bank accession number U52155. During the first step (50°C, 2 min), UNG hydrolyzes dU-containing DNA to prevent carryover contamination during the following PCR. Subsequent first-strand synthesis was performed at 60°C (20 min). The antisense primers also served as primers for the reverse transcriptase. UNG was denaturated at 95°C (5 min), followed by 60 PCR cycles (denaturation at 94°C, 15 s; primer annealing and extension at 59°C, 60 s). The fluorescence intensity was readout during each annealing/extension step. RT-PCR was performed in special optical tubes (PE Applied Biosystems) covered with optical caps for optimal fluorescence excitation and detection of emitted light.

4.4.2. Correlation of Kir Current Density and Kir4.1 Transcript Expression in Human Astrocytes

We have previously reported that astrocytes in the hippocampus of patients with Ammon's horn sclerosis possess a reduced Kir current density as compared to cells from nonsclerotic epilepsy patients (Hinterkeuser et al., 2000). Moreover, subsequent single-cell RT-PCR identified Kir4.1 transcripts in about 44% of the cells analyzed (Schröder et al., 2000). Here we performed real-time RT-PCR to figure out whether the reduction of Kir currents in the sclerotic tissue was due to diminished expression of Kir4.1 channels.

Because analysis of hKir4.1 and hGAPDH was simultaneously run in separate tubes, first we checked whether the corresponding cDNAs were amplified with the same efficiency. Figure 7 illustrates that increasing amounts of respective mouse brain mRNAs (7.4 pg to 1.9 ng) resulted in a continuous decrease of the C_T values whereby doubling the concentration required one cycle less to reach the same threshold. The threshold cycles were plotted against the logarithmic mRNA concentration. The resulting lines for the target and the housekeeping gene displayed the same slope (Fig. 7A), indicating similar amplification efficiency (Halford, 1999; Medhurst et al., 2000).

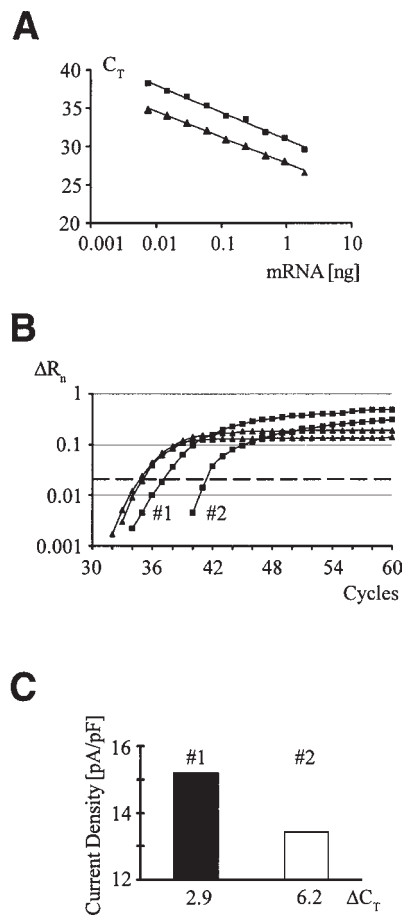


Fig. 7. Semiquantitative transcript analysis of hKir4.1 in single astrocytes of epilepsy patients. (A) Threshold cycles, C_T , for hKir4.1 (squares) and hGAPDH (triangles) were plotted against mRNA concentration prepared from human hippocampus. Note that doubling the amount of input mRNA led to a decrease in C_T by one cycle, indicating high efficiency for both reactions. (B) Amplification plot of two samples of pooled astrocytes from different patients. While hGAPDH (triangles) expression was identical in both cell pools, hKir4.1 transcript amount of sample #2 ($\Delta C_T = 6.2$) was lower than that of cell pool #1 ($\Delta C_T = 2.9$). (C) The respective averaged Kir current densities ($V = -130$ mV) were 13.4 pA/pF (sample #2) and 15.2 pA/pF (sample #1), suggesting that at least part of the reduced currents in astrocytes of cell pool #2 was due to lower abundance of Kir4.1 expression.

In a next step real-time RT-PCR was applied to two samples of pooled, electrophysiologically characterized human hippocampal astrocytes (Fig. 7B,C). Kir current densities were determined at -130 mV by dividing steady-state amplitudes by the respective membrane capacitance, as described elsewhere (e.g., Hinterkeuser et al., 2000). Cell pool #1 contained cytoplasm of 6 cells, and its mean current density amounted to 15.2 ± 4.2 pA/pF. Cell pool #2 was collected from another epilepsy patient, and these cells possessed a lower Kir current density (13.4 ± 6.5 pA/pF; $n = 7$). After TaqMan™ analysis ΔR_n , the fluorescence intensity normalized to a passive fluorescent reference, was plotted against the PCR cycles (Fig. 7B). Threshold for detection was set at $\Delta R_n = 0.02$ (indicated by the dashed line). While the C_T values for hGAPDH were almost the same in the two cell pools, the mRNA levels for hKir4.1 were clearly different, with the difference $\Delta C_T = C_{T, \text{Kir4.1}} - C_{T, \text{GAPDH}}$ of sample #2 being significantly higher than that of sample #1 (6.2 vs 2.9). These ΔC_T values now allowed to compare the relative amount of hKir4.1 transcripts in the respective cell pools ($\Delta \Delta C_T$ -method; cf. Fink et al., 1998) (Fig. 7C). Thus, cells with a larger Kir current density also possessed a higher hKir4.1 mRNA level, suggesting that downregulation of Kir4.1 expression might underlie insufficient functioning of hippocampal astrocytes in epilepsy patients with Ammon's horn sclerosis.

5. Conclusions

The combination of the patch-clamp method with single-cell RT-PCR has proven to be a powerful approach to identify the molecules underlying biophysical properties of individual cells. Moreover, this technique simultaneously allows detection of transcripts encoding proteins other than transmembrane channels, e.g., cell type-specific markers. However, because the presence of transcripts does not necessarily entail the presence of the corresponding proteins and their incorporation into the plasma membrane, such investigations should always be flanked by other, independent methods, such as immunocytochemistry or electron microscopy. The detailed analysis of structure-function relations in single native cells is now within reach and this information will be important in exploring mechanisms that govern changes in cell-cell signaling during normal development and in pathogenesis.

Acknowledgments

The authors' work was supported by the Bundesministerium für Bildung und Forschung, Fonds der Chemischen Industrie, and the Deutsche Forschungsgemeinschaft. We thank Dr. S. Hinterkeuser, who provided the photographs shown in Fig. 3.

References

- Ausubel, F. M., Brent, R., Kingston, R. E., Moore, D. D., Seidman, J. G., Smith, J. A., and Struhl, K. (eds.) (1996) *Current Protocols in Molecular Biology*. John Wiley & Sons, New York, NY.
- Bordey, A. and Sontheimer, H. (1998) Properties of human glial cells associated with epileptic seizure foci. *Epilepsy Res.* **32**, 286–303.
- Brenner, C. A., Tam, A. W., Nelson, P. A., Engleman, E. G., Suzuki, N., Fry, K. E., and Larrick, J. W. (1989) Message amplification phenotyping (MAPPING): a technique to simultaneously measure multiple mRNAs from small numbers of cells. *BioTechniques* **7**, 1096–1103.
- Chomczynski, P. and Sacchi, N. (1987) Single-step method of RNA isolation by acid guanidinium thiocyanate-phenol-chloroform extraction. *Anal. Biochem.* **162**, 156–159.
- Dilworth, D. D. and McCarrey, J. R. (1992) Single-step elimination of contaminating DNA prior to reverse transcriptase PCR. *PCR Methods Appl.* **1**, 279–282.
- Dragon, E. A. (1993) Handling reagents in the PCR laboratory. *PCR Methods Appl.* **3**, S8–S9.
- Fakler, B. and Ruppersberg, J. P. (1996) Functional and molecular diversity classifies the family of inward-rectifier K⁺ channels. *Cell. Physiol. Biochem.* **6**, 195–209.
- Fink, L., Seeger, W., Ermert, L., Hänze, J., Stahl, U., Grimminger, F., et al. (1998) Real-time quantitative RT-PCR after laser-assisted cell picking. *Nature Med.* **4**, 1329–1333.
- Gurantz, D., Ribera, A. B., and Spitzer, N. C. (1996) Temporal regulation of *Shaker*- and *Shab*-like potassium channel gene expression in single embryonic spinal neurons during K⁺ current development. *J. Neurosci.* **16**, 3287–3295.
- Halford, W. P. (1999) The essential prerequisites for quantitative RT-PCR. *Nat. Biotechnol.* **17**, 835.
- Hinterkeuser, S., Schröder, W., Hager, G., Seifert, G., Blümcke, I., Elger, C. E., et al. (2000) Astrocytes in the hippocampus of patients with temporal lobe epilepsy display changes in potassium conductances. *Eur. J. Neurosci.* **12**, 2087–2096.
- Holland, P. M., Abramson, R. D., Watson, R., and Gelfand, D. H. (1991) Detection of specific polymerase chain reaction product by utilizing the 5'–3' exonuclease activity of *Thermus aquaticus* DNA polymerase. *Proc. Natl. Acad. Sci. USA* **88**, 7276–7280.
- Jauch, R., Gabriel, S., Kivi, A., and Heinemann, U. (1999) Spatial buffering of iontophoretically applied K⁺ in rat hippocampal CA1. *Pflugers Arch.* **437**, R121.

- Jonas, P., Racca, C., Sakmann, B., Seeburg, P. H., and Monyer, H. (1994) Differences in Ca^{2+} permeability of AMPA-type glutamate receptor channels in neocortical neurons caused by differential GluR-B subunit expression. *Neuron* **12**, 1281–1289.
- Kressin, K., Kuprijanova, E., Jabs, R., Seifert, G., and Steinhäuser, C. (1995) Developmental regulation of Na^+ and K^+ conductances in glial cells of mouse hippocampal brain slices. *Glia* **15**, 173–187.
- Lamboleze, B., Audinat, E., Bochet, P., Crépel, F., and Rossier, J. (1992) AMPA receptor subunits expressed by single Purkinje cells. *Neuron* **9**, 247–258.
- Li, H. H., Gyllenstein, U. B., Cui, X. F., Saiki, R. K., Erlich, H. A., and Arnheim, N. (1988) Amplification and analysis of DNA sequences in single human sperm and diploid cells. *Nature* **335**, 414–417.
- Livak, K. J., Flood, S. J., Marmaro, J., Giusti, W., and Deetz, K. (1995) Oligonucleotides with fluorescent dyes at opposite ends provide a quenched probe system useful for detecting PCR product and nucleic acid hybridization. *PCR Methods Appl.* **4**, 357–362.
- Medhurst, A. D., Harrison, D. C., Read, S. J., Campbell, C. A., Robbins, M. J., and Pangalos, M. N. (2000) The use of TaqMan RT-PCR assays for semi-quantitative analysis of gene expression in CNS tissues and disease models. *J. Neurosci. Methods* **98**, 9–20.
- Monyer, H. and Jonas, P. (1995) Polymerase chain reaction analysis of ion channel expression in single neurons of brain slices, in *Single-Channel Recording*, 2nd ed. (Sakmann, B. and Neher, E., eds.), Plenum Press, New York, NY, pp. 357–373.
- Newman, E. A. (1986) High potassium conductance in astrocyte endfeet. *Science* **233**, 453–454.
- Poopalasundaram, S., Knott, C., Shamotienko, O. G., Foran, P. G., Dolly, J. O., Ghiani, C. A., et al. (2000) Glial heterogeneity in expression of the inwardly rectifying K^+ channel, Kir4.1, in adult rat CNS. *Glia* **30**, 362–372.
- Reimann, F. and Ashcroft, F. M. (1999) Inwardly rectifying potassium channels. *Curr. Opin. Cell. Biol.* **11**, 503–508.
- Ruano, D., Lamboleze, B., Rossier, J., Paternain, A. V., and Lerma, J. (1995) Kainate receptor subunits expressed in single cultured hippocampal neurons: molecular and functional variants by RNA editing. *Neuron* **14**, 1009–1017.
- Schröder, W., Hinterkeuser, S., Seifert, G., Schramm, J., Jabs, R., Wilkin, G. P., and Steinhäuser, C. (2000) Functional and molecular properties of human astrocytes in acute hippocampal slices obtained from patients with temporal lobe epilepsy. *Epilepsia* **41**, S181–S184.
- Seifert, G., Rehn, L., Weber, M., and Steinhäuser, C. (1997a) AMPA receptor subunits expressed by single astrocytes in the juvenile mouse hippocampus. *Mol. Brain Res.* **47**, 286–294.
- Seifert, G., Zhou, M., and Steinhäuser, C. (1997b) Analysis of AMPA receptor properties during postnatal development of mouse hippocampal astrocytes. *J. Neurophysiol.* **78**, 2916–2923.
- Seifert, G., Kuprijanova, E., Zhou, M., and Steinhäuser, C. (1999) Developmental changes in the expression of *Shaker*- and *Shab*-related K^+ channels in neurons of the rat trigeminal ganglion. *Mol. Brain Res.* **74**, 55–68.
- Seifert, G., Zhou, M., Dietrich, D., Schumacher, T. B., Dybek, A., Weiser, T., et al. (2000) Developmental regulation of AMPA-receptor properties in CA1 pyramidal neurons of rat hippocampus. *Neuropharmacology* **39**, 931–942.

- Steinhäuser, C., Berger, T., Frotscher, M., and Kettenmann, H. (1992) Heterogeneity in the membrane current pattern of identified glial cells in the hippocampal slice. *Eur. J. Neurosci.* **4**, 472–484.
- Steinhäuser, C., Kressin, K., Kuprijanova, E., Weber, M., and Seifert, G. (1994) Properties of voltage-activated sodium and potassium currents in mouse hippocampal glial cells in situ and after acute isolation from tissue slices. *Pflügers Arch.* **428**, 610–620.
- Stonehouse, A. H., Pringle, J. H., Norman, R. I., Stanfield, P. R., Conley, E. C., and Brammar, W. J. (1999) Characterisation of Kir2.0 proteins in the rat cerebellum and hippocampus by polyclonal antibodies. *Histochem. Cell Biol.* **112**, 457–465.
- von Eggeling, F. and Ballhausen, W. (1995) Freezing of isolated cells provides free mRNA for RT-PCR amplification. *BioTechniques* **18**, 408–410.

Index

A

ABI PRISM 7700 Sequence Detection System, 315–316
Acquisitions software
 supplier, 131
aCSF, 136
Action potential, 176
Algorithms
 Levenberg-Marquard, 58
 Simplex, 58
Aliasing
 whole-cell patch clamp recordings, 45–46
Aluminosilicates, 4
Amino acids, 69
Amphotericin B, 197, 199–200
 pipet filling solutions, 207
Amplified cDNA products
 PCR, 308f
Amplifier, 123
Amplitudes
 single-channel recording, 87–88
Antibiotics
 polyene
 perforated patch clamp technique, 199–200
Application chamber
 fast drug application, 220–221
Artificial CSF (aCSF), 136
Astrocytes
 Kir currents, 319
 Kir subunits
 hippocampus, 324
 single-cell RT-PCR, 324
 Kir transcript analysis
 quantitative, 324–327, 326f

ATP regenerative system, 159
Axoclamp 2A, 184
Axopatch 200B, 72
Axopatch 1 D, 39, 184

B

β -escin, 203
 pipet filling solutions, 208
Bessel filters, 44
 frequency response, 45f
 4 pole, 39
BK channels
 inside-out patch recording, 82f
Boltzman's constant, 22–25, 70
Borosilicate glasses
 noise, 15–16
Brain
 removal, 145
Brain slices
 cutting, 143–144
 oxygenation, 141–142
 preparation, 135–152
 adult and aged animals, 148–152
 juvenile animals, 144–148
 recording and cutting solutions, 136–137, 136–139
 whole-cell recordings, 160f, 165–175
Bursts
 single-channel recording, 102–108
 spiking cells, 176, 178f

C

Calcium transients
 line-scan recordings, 116f–117f
Calibration solutions, 252

- cAMP, 259
- Capacitive transients
 - minimize, 167–168
- Carolina Biological Supply
 - website, 131
- cDNA products
 - amplified
 - PCR, 308f
- Cell-attached patch, 77–79
 - schematic diagram, 233f
- Cell capacitance
 - whole-cell patch clamp recordings, 47–49, 48f
- Cell-resting membrane potential
 - whole-cell recording, 202f
- Cellular signaling cascade
 - cGMP, 255f
- cGMP
 - cellular signaling cascade, 255f
 - FRET, 259
 - kinetics, 256f
 - long-term plasticity, 258f
 - long-term suppression, 257
 - neuroblastoma cells
 - real-time measurements, 253–258
 - patch-clamping *vs* fluorescent indicators, 260–261
- Channel. *See also* Single-channel activity, 35–36
 - BK
 - inside-out patch recording, 82f
 - CNG, 252
 - detector ion, 247–249, 248f
 - dwell times, 94
 - Kir analysis
 - glial cells, 318–327
 - NMDA receptor, 86f, 106f
 - NMDA single
 - one-channel patch, 107f
 - open times, 98–100
 - shut times, 100–102
 - single analysis, 90
- Chemical constituents
 - glass, 5
- Chloride intracellular pipet
 - solution, 159
- Chris Patton
 - website, 131
- Clamp
 - I-V plots, 63–65, 64f
- CLSM, 121, 124, 184
- CNG channels, 252
- Coarse fritted glass bubblers, 141
- COMO software, 184
- Computer, 38
- Concentration jump
 - outside-out patch, 85f
- Conductance
 - single-channel recording, 85–87
- Conductance-voltage curves, 55–56
- Confocal laser-scanning microscopy (CLSM), 121, 124, 184
- Continuous quasi steady-state I-V curves, 53–55
- Corning 080, 5
- Corning 7052, 9
- Corning 7056, 6
- Corning 7740, 6, 9
- Cross connector
 - pipet perfusion, 242
- Cull-Candy, Miledi, Parker design
 - pipet perfusion, 234–235
- Current-clamp recordings, 169–171
- Currents
 - isolation
 - pharmacology, 51–52, 52f
 - kinetic dissection, 49
 - subtraction
 - vs.* stimulus protocols, 49
 - traces
 - least squared fit, 59f
- Current-to-voltage converter
 - scheme, 38f
- Current-voltage (I-V) relationships, 53–56

- Cutting solutions
 - brain slices, 136–139
 - composition, 138–139
 - sodium chloride
 - brain slices, 138–139
 - sucrose
 - brain slices, 138–139, 150
- Cyanoacrylate, 140
- Cyclic GMP
 - patch-cram, 245–261
 - response time, 254f
- Cyclic GMP indicator using energy transfer (cygnet), 254–255
- D**
- DAG, 254
- Data
 - acquisition
 - fluorometric and electro-physiological recordings, 127–128
 - analysis
 - fast drug application, 224–228, 225f–227f
 - single-channel recording, 88–108
 - filtering
 - whole-cell patch clamp recordings, 43–44
 - presentation
 - whole-cell patch clamp recordings, 58–60
 - storage
 - whole-cell patch clamp recordings, 46
- Deactivation I-V curves, 56
- Del Castillo-Katz reaction scheme
 - single-channel data, 97f
- Densitization
 - measuring, 227f
- Detector ion channels
 - patch-cram, 247–249, 248f
- Diacylglycerol (DAG), 254
- DIC microscopy
 - with videomicroscopy
 - development, 154
- Dielectric constant, 16
- Dielectric noise, 19f
 - patch pipet, 22–25
- Die throwing distribution, 93f
- Differential interference contrast (DIC) microscopy
 - with videomicroscopy
 - development, 154
- Digital audio tape, 88–89
- Digital oscilloscope, 185
- Dimple
 - whole-cell patch pipet, 167f
- Dissection time sheet
 - sample, 146f
- Dissipation factor, 16
 - elastomer, 24
 - quartz, 16
- Distributed RC noise
 - patch pipet, 18–22
 - PSD, 21
- DMZ Universal Puller, 221
- DNA
 - genomic
 - patch-clamp with RT-PCR, 312–314
 - hippocampal astrocytes
 - Kir currents, 319–322
- Dodt gradient-contrast illumination
 - supplier, 131
- Double-barreled glass
 - pipet perfusion, 236–237
- Double impalement, 36
- Dwell times, 88–89
- E**
- Elastomer
 - coating
 - dip method, 23–24
 - single-channel pipet, 10–12
 - whole-cell electrodes, 7

- dissipation factor, 24
- pipet
 - dielectric noise, 22–23
- Electrical properties
 - glasses, 3, 16
 - pipet glass, 4
- Electrodes
 - construction
 - perforated patch clamp technique, 209–210
 - glass
 - construction, 2–3
 - ground
 - macropatch recording, 293
 - multiple
 - simultaneous recordings, 174–175
 - patch. *See* Patch electrodes
 - patch-clamp
 - recent developments, 32–33
 - technology, 1–33
 - planar, 32
 - resistance, 60–61
 - single-channel
 - pulling, 10
 - whole-cell, 6–8
- Electronic components
 - whole-cell patch clamp recordings, 38–39
- Electrophysiological recordings, 111–131
- Electrophysiological setups
 - grounding, 123
- Epilepsy astrocytes
 - quantitative Kir transcript analysis, 324–327, 326f
- Equipment
 - shielding, 71
- Exponential distribution, 93f
- External signal filter, 38
- F**
- Fast drug application, 217–228
 - data analysis, 224–228, 225f–227f
 - material and equipment, 217–222
 - real patches, 222–224
 - system testing, 222, 223f
- Fast spiking cells, 176, 178f
- Fast whole-cell configurations
 - schematic representation, 197f
- Fiber optics
 - supplier, 131
- Firepolishing
 - single-channel pipet, 12
 - whole-cell electrodes, 7–8
- Flag inserter, 119f, 123
- Flaming/Brown micropipet puller, 166
- Fluid path length
 - pipet perfusion, 238–239
- Fluorescence calcium indicators, 124–125
- Fluorescence detection unit
 - alignment, 123
- Fluorescence markers, 65
- Fluorescence resonance energy transfer (FRET), 111
 - cGMP, 259
- Fluorescent indicators
 - vs.* patch-clamp
 - cyclic GMP, 254–255
- Fluorescent probes
 - supplier, 131
- Fluorescent transients
 - algorithm, 118f
- Fluorometric and electrophysiological recordings, 111–131
 - analysis, 129–131
 - recording setup, 112–131
 - imaging system, 115–123
 - microscope, 113–115
 - schematic drawing, 113f
 - suppliers, 131
 - vibration control, 112–113
- Fourier transform, 280
- FRET, 111

- cGMP, 259
- Fura-2, 125, 130
- Fura Red, 130
- G**
- GABA-induced current
 - stimulus protocols, 54f
- Gaussian distribution, 87–88, 93f
- Genomic DNA
 - patch-clamp with RT-PCR, 312–314
 - two-round nested PCR, 313f
- Geometric distribution, 93f
- GFP, 111, 259
- Gigaohm seals, 7, 17, 71
 - inhibition, 171
 - obtaining, 165–166
- Gigaseals
 - obtaining, 211
- Glass
 - borosilicate
 - noise, 15–16
 - chemical constituents, 5
 - electrodes
 - construction, 2–3
 - high lead, 6
 - pipet
 - general properties, 4–5
 - macropatch recording, 290
 - properties, 2–3
 - soda lime, 5
 - sonicating, 10
 - tubing, 9
- Glial cells
 - cytoplasm harvesting, 311f
 - Kir channel analysis, 318–327
 - Kir subunit expression, 321f
- Goldman-Hodgkin-Katz equation, 78
- Gould digital oscilloscope, 185
- Gramicidin, 200–201
 - pipet filling solutions, 207–208
- Gramicidin-perforated patch
 - glycine, 201f
- Graphing and analysis software
 - supplier, 131
- Green fluorescent proteins (GFP), 111, 259
- Green's function, 281
- Ground electrodes
 - pipet
 - macropatch recording, 293
- Grounding
 - neurons, 161–162
- Guanylate cyclase, 254–255
- H**
- Halothane, 144
- Hamamatsu C2400 video camera, 182
- Hardware
 - fast drug application, 221–222
 - whole-cell patch-clamp studies, 181–185
- Harvesting
 - hippocampal astrocytes
 - Kir currents, 319–322
- Headstage input
 - capacitance, 17
- Henderson Liquid Junction
 - Potential Equation, 164
- High-frequency patch-current
 - component recovery
 - whole-cell loose-patch voltage clamp, 279–283
- High lead glasses, 6
- High-resistance seal, 71
- High series resistance
 - perforated patch-clamp technique, 213–214
- Hippocampus
 - astrocytes
 - Kir currents, 319
 - Kir subunits, 324
 - Kir molecular identity, 319–324
- Hoffman modulation microscopy, 153

I

- IgorPro, 184, 185
- Image analysis software
 - supplier, 131
- Imaging system, 115–123
 - fluorometric and electrophysiological recordings
 - excitation light, 121–122
 - focusing, 114
 - hardware, 122–123
 - software, 122
 - spatial resolution, 116–117
 - temporal resolution, 116
- Immersed pipet
 - capacitance, 17
- Incubation chambers
 - patch-clamp techniques, 140–143
 - assembling, 140–141
 - brain slice oxygenation, 141–142
 - design, 142f
- Indo-1, 125, 130
- Infrared differential interference contrast (IR-DIC), 114
 - benefits, 153–154
 - neuron visualization, 152–158
 - video-enhanced microscopy, 149f
- Inlet tube
 - pipet perfusion, 237, 239–241
- Inside-out patch, 81–83
 - BK channels, 82f
 - schematic diagram, 233f
- Intracardiac perfusions
 - brain slices, 151–152
- Inverted microscope, 154
- Ion-channel blockers, 51f
- Ion dependence, 49–50
- IR-DIC, 114
 - benefits, 153–154
 - neuron visualization, 152–158
 - video-enhanced microscopy, 149f

Isofluorane, 144

I-V curves

- continuous quasi steady-state, 53–55
- deactivation, 56
- whole-cell patch clamp recordings, 53–56

J**Junction potentials**

- perforated patch clamp technique, 214

K**Ka current**

- subtraction, 50f

Kimax, 6, 9

Kimble R-6, 5

Kinetic reaction scheme, 226f

Kir channel analysis

- glial cells, 318–327

Kir currents

- density, 325–327
- hippocampal astrocytes, 319

Kir molecular identity

- hippocampus, 319–324

K-methylsulfate intracellular pipet

- solution, 159

Kohler illumination

- alignment, 165–166

L**Lapointe and Szabo design**

- pipet perfusion, 235–236

Late spiking cells, 176, 178f

Leak current, 172–173

Leak subtraction, 173

- macropatch recording, 295
- whole-cell patch clamp recordings, 46–47

Least squared fit

- current traces, 59f

Levenberg-Marquard algorithm,

58

- Life-times distribution
 - single-channel recording, 92–95
- Liquid-liquid junction potentials
 - calculating, 164
 - measuring, 163–164
 - neurons, 163–164
- Loose patch voltage-clamp,
 - 265–283
 - applications, 275–276
 - loose seal, 270
 - patch current sealing and recording, 274–275
 - pipet, 270–271
 - pipet fabrication, 268–270
 - schematic, 267f
 - seals, 270–273
 - uncertainties, 273
- Loose seal
 - loose patch voltage-clamp, 270
- Low-frequency patch-current
 - component recovery
 - whole-cell loose-patch voltage clamp, 279
- Low input resistance, 61–62
- Low noise, 14
 - recording, 13–15
- Low-resistance pipet, 126
- Luigs & Neumann
 - website, 131
- LY, 65–66
- M**
- Macropatch recording, 287–298
 - advantages and disadvantages, 297–298
 - analysis, 296–297
 - biological application, 287–288
 - leak subtraction, 295
 - membrane current, 295
 - membrane potential, 294, 297f
 - membranes, 288–290
 - membrane surface area, 295–296
 - pipet, 290–293
 - recording, 293–295
 - seals, 294
 - solutions, 293
 - technique, 288
- Magnesium Green, 125–126
- Markov processes, 94
- Master8, 221
 - programmable pulse generator, 185
- Max21, 221
- MaxChelator
 - supplier, 131
- Melles Griot
 - website, 131
- Membrane potential
 - cell-resting
 - whole-cell recording, 202f
 - conductance, 36
 - macropatch recording, 288–290, 294, 297f
 - current, 295
 - surface area, 295–296
 - perforated patch recordings, 198f
- Messenger RNA. *See* mRNA
- Methylsulfate intracellular pipet
 - solution, 159
- Micromanipulator
 - fast drug application, 218
- Microscope
 - confocal laser-scanning, 121, 124, 184
 - differential interference contrast
 - with videomicroscopy, 154
 - fast drug application, 218
 - fluorometric and electrophysiological recordings, 113–115
 - numerical aperture, 115
 - transmittance, 115
 - Hoffman modulation, 153
 - two-photon, 121
- Mineral oil, 14
- Molecular Probes
 - website, 131

- Mouse hippocampal astrocytes
 - Kir subunits
 - single-cell RT-PCR, 324
- mRNA
 - isolation, 316–317
 - patch-clamp with RT-PCR, 303–304
 - quantification, 315–316
- Multiple electrodes
 - simultaneous recordings, 174–175
- N
 - N1E-115 cells, 250
 - Nembutal, 152
 - Nernst equation, 78
 - Neuroblastoma cells
 - cGMP
 - real-time measurements, 253–258
 - Neuro-Corder, 184–185
 - Neurons
 - dead, 155–157
 - healthy, 157
 - IR-DIC videomicroscopy, 156f, 158–185
 - grounding and shielding, 161–162
 - liquid-liquid junction potentials, 163–164
 - patch pipet solutions, 158–161
 - oxidative damage, 137
 - recovery, 148f
 - unhealthy, 155–157
 - Neuron visualization
 - IR-DIC, 152–158
 - selection, 155–158
 - Neuroprotective cutting solutions
 - brain slices, 139
 - Neurotransmitter-activated
 - currents, 52
 - NIH image, 129, 184
 - supplier, 131
 - Nitric oxide, 246
 - Nitric oxide synthase (NOS), 254
 - NMDA receptor-channels
 - burst length distribution, 106f
 - current-voltage plot, 86f
 - shut time, 106f
 - NMDA receptors
 - burst length distribution, 105–108
 - NMDA single-channels
 - one-channel patch, 107f
 - Noise
 - borosilicate glasses, 15–16
 - dielectric, 19f, 22–25
 - distributed RC, 18–22, 21
 - low, 14
 - pipet, 17–18
 - pipet capacitance, 16
 - RC, 19f
 - $R_e - C_p$, 26
 - RMS, 22–25
 - seal, 26–27
 - soda lime glasses, 15
 - sources
 - whole-cell voltage clamping, 29–32
 - Normarski optics, 41
 - NOS, 254
 - NR1a/NR2a. *See* NMDA receptor-channels
 - Nucleated patch configuration, 172
 - Numerical aperture
 - fluorometric and electrophysiological recordings, 115
 - Nyquist Sampling Theorem, 44–46
 - Nystatin, 197, 199–200, 206f
 - pipet filling solutions, 206
 - O
 - Objectives
 - fluorometric and electrophysiological recordings, 113
 - Odyssey scanner, 112
 - Optical properties
 - glasses, 3

Oregon Green BAPTA-1, 124–125

Oscilloscope, 38

 Gould digital, 185

 Tektronix analog storage, 185

 traces, 42f

Osmolarity matching

 brain slices, 150–151

Outside-out patch, 83–85

 concentration jump, 85f

 solutions, 75f

Oxotremorine-M, 80f, 81

P

Patch-clamp

 amplifiers, 38, 252

 single-channel recording,
 71–72

 electrodes

 recent developments, 32–33

 technology, 1–33

 measurement

 steps, 2

 recordings

 fluorometric and electro-
 physiological, 126–127

 with RT-PCR, 301–327

 contamination, 312–314

 multiplex and nested PCR,
 314–315

 optimizing RT-PCR, 302–307

 real-time PCR, 315–318

 restriction analysis, 306–307

Patch-clamp techniques, 135–185.

See also Perforated patch
 clamp technique

 brain slices

 cutting, 143–144

 preparation, 135–152

 incubation chambers, 140–143

 neurons recording, 158–185

 perirhinal cortex, 175–181

Patch-clamping, 246f

 cyclic GMP, 245–261

 response time, 254f

 detector ion channels, 247–249,
 248f

vs. fluorescent indicators

 cyclic GMP, 254–255

 procedure, 249–251

 set-up, 251–253

Patch current sealing and recording

 loose patch voltage-clamp,
 274–275

Patch electrode

 fast drug application, 221

 single-channel recording

 fabrication, 8–15

 coating single-channel pipet,
 10–12

 firepolishing single-channel
 pipet, 12

 glass choice, 8–10

 low-noise recording, 13–15

 patch pipet noise properties,
 15–32

 pulling single-channel
 electrodes, 10

 quartz fabrication methods,
 12–13

Patch voltage-clamp

 loose. *See* Loose patch voltage-
 clamp

PCR

 hippocampal astrocytes

 Kir currents, 322–324

 real-time

 single-cell transcript analysis,
 315–318

 two-round

 patch-clamp with RT-PCR,
 304–306

 two-round nested

 genomic DNA, 313f

Peak IV curves, 53

Pentobarbital, 144

Perforated patch clamp technique,
 195–228. *See also* Patch-
 clamp technique

- electrical access formation
 - time course, 212f
- electrode construction, 209–210
- pipet filling solutions, 205–208
- polyene antibiotics, 199–200
- principles, 196–203
- problems, 213–214
- protocol, 210–212
- Perforated patch-recordings
 - membrane, 198f
- Perforated vesicle patch-clamp, 203–205
 - schematic, 204f
- Periosteal elevator, 145
- Perirhinal cortex
 - layer V pyramidal neuron, 183f
 - patch-clamp techniques, 175–181
- Perirhinal neurons
 - voltage-clamp analysis, 180f
- Phospholipase C (PLC), 254
- Photodamage
 - fluorometric and electrophysiological recordings, 127–128
- Piezo
 - fast drug application, 218–220, 219f
- Pipet, 2
 - back-filling, 171
 - capacitance, 73
 - noise, 16
 - dielectric noise, 22–25
 - distributed RC noise, 18–22
 - fabrication, 268–270
 - macropatch recording, 290–291
 - fast drug application, 220
 - firepolishing, 73–74
 - glass
 - general properties, 4–5
 - ground electrode
 - macropatch recording, 293
 - loose patch voltage-clamp, 270–271
 - macropatch recording, 290–293
 - noise, 17–18
 - simplified circuit, 19f
 - perfusion, 231–243
 - accessories, 241–242
 - applications, 232–234
 - components, 238f
 - construction, 237–241
 - Cull-Candy, Miledi, Parker
 - design, 234–235
 - double-barreled glass, 236–237
 - fluid path length, 238–239
 - inlet tube, 237, 239–241
 - Lapointe and Szabo design, 235–236
 - reservoir, 237, 239
 - schematic diagram, 240f
 - Soejima and Noma design, 235
 - solution, 237, 239, 241
 - Tang, Wang, Quandt, and Eisenberg design, 236
 - R_e - C_p noise, 26
 - seal noise, 26–27
 - single-channel recording, 73–74
 - size
 - macropatch recording, 291
 - solutions
 - chloride intracellular, 159
 - K-methylsulfate intracellular, 159
 - neurons, 158–161
 - perforated patch clamp
 - technique, 205–208
 - perfusion, 237, 239, 241
 - storage
 - macropatch recording, 293
 - thin film noise, 18
 - tip
 - firepolishing, 166–167
 - typical noise, 28–29
 - whole-cell recording, 6, 37
- Planar electrode
 - techniques, 32

- Platinum wire, 8
- PLC, 254
- Plexiglas recording chamber, 41
- Point-scan mode, 121f
- 4 pole Bessel filters, 39
- Polishing
 - pipet
 - macropatch recording, 291–293
- Polyene antibiotics
 - perforated patch clamp technique, 199–200
- Power spectral density (PSD), 17
 - distributed RC noise, 21
- Primers
 - patch-clamp with RT-PCR, 303
 - single-cell transcript analysis
 - real-time PCR, 317
- Probes
 - single-cell transcript analysis
 - real-time PCR, 317
- Protein, 69
- PSD, 17
 - distributed RC noise, 21
- Puller, 4
 - DMZ Universal, 221
 - Flaming/Brown micropipet, 166
- Q**
- Quantitative Kir transcript analysis
 - epilepsy astrocytes, 324–327
- Quartz, 9
 - dissipation factor, 16
 - fabrication methods, 12–13
- Quartz pipet, 4
- QX-314, 159
- R**
- Rat brain slices
 - recording and cutting solutions, 136–137
- RCM 80000, 116
- RC noise, 19f
- RC time constant, 36
- Real-time PCR
 - single-cell transcript analysis, 315–318
- Recording. *See also* Fluorometric and electrophysiological recordings; Macropatch recording; Single-channel recording; Whole-cell patch clamp recordings; Whole-cell recording (WCR)
 - current-clamp, 169–171
 - electrophysiological, 111–131
 - low-noise, 13–15
 - macropatch recording, 293–295
 - patch-clamp, 126–127
 - patch current
 - loose patch voltage-clamp, 274–275
 - perforated patch
 - membrane, 198f
 - visually guided whole-cell, 182f
- Recording chamber
 - Plexiglas, 41
- Recording setup
 - fluorometric and electrophysiological recordings, 112–131
- Recording solutions
 - brain slices, 136–139
 - selection, 137–138
 - single-channel recording, 74
- R_e - C_p noise
 - patch pipet, 26
- Regions-of-interests (ROIs), 129
- Regular spiking cells, 176
- Reservoir
 - pipet perfusion, 237, 239
- Resolution setting
 - single-channel recording, 91–92
- Restriction analysis
 - patch-clamp with RT-PCR, 306–307
- Reverse transcription

- hippocampal astrocytes
 - Kir currents, 319–322
- RNA
 - patch-clamp with RT-PCR, 312–314
- RMS noise, 22–25
 - meter, 14
- RNA
 - reverse transcription
 - patch-clamp with RT-PCR, 312–314
- RNA harvesting
 - single-cell RT-PCR, 307–312
- ROIs, 129
- Rongeurs, 145
- RON-S2, 248
- RT-PCR. *See* Patch-clamp with RT-PCR
 - sensitivity and specificity, 305f
 - single-cell. *See* Single-cell RT-PCR
- RTV615A, 11
- S**
- SCAN, 90
- Schott 8250, 6, 9
- Schott 83300, 6, 9
- Seals
 - high-resistance, 71
 - loose patch voltage-clamp, 270–273
 - macropatch recording, 294
 - noise, 26–27
- Series resistance
 - measurement, 168–169
 - whole-cell patch clamp recordings, 60–62
- Shielded holders, 17
- Shielding
 - neurons, 161–162
- Signal sampling rate
 - whole-cell patch clamp recordings, 44–45
- Signal-to-noise ratio
 - fluorometric and electrophysiological recordings, 127–128
- Silastic MDX-4, 11
- Silastic tubing
 - pipet perfusion, 242
- Silicone fluid, 14
- Silver chloride ground wire, 161–162
- Simplex algorithm, 58
- Simulator, 38
- Single-cell RT-PCR
 - Kir subunits
 - mouse hippocampal astrocytes, 324
 - peculiarities, 307–318
 - real time, 324–325
 - RNA harvesting, 307–312
- Single-cell transcript analysis
 - quantitative optimization, 317–318
 - real-time PCR, 315–318
- Single-Channel Analysis (SCAN), 90
- Single-channel currents
 - resolving, 70
- Single-channel data
 - del Castillo-Katz reaction
 - scheme, 97f
- Single-channel electrodes
 - pulling, 10
- Single-channel pipet
 - elastomer coating, 10–12
 - firepolishing, 12
- Single-channel recording, 69–108
 - amplitudes, 87–88
 - bursts properties, 102–108
 - channel open times, 98–100
 - channel shut times, 100–102
 - conductance, 85–87
 - current configurations, 76–85
 - data analysis, 88–108, 96–98
 - dwell time intervals, 88–89
 - electrophysiological current

- (*cont.*) conventions, 74–76
- life-times distribution, 92–95
- patch-clamp amplifiers, 71–72
- patch electrode fabrication, 8–15
- patch-pipets, 73–74
- recording solutions, 74
- resolution setting, 91–92
- resolving currents, 70–71
- two-state model, 95–96
- Single-channels
 - NMDA
 - one-channel patch, 107f
- Single spiking cells, 176, 178f
- Skull
 - removal, 145
- Sleeve
 - pipet perfusion, 242
- Slow whole-cell configurations
 - schematic representation, 197f
- Soda lime glasses, 5
 - noise, 15
- Sodium chloride cutting solutions
 - brain slices, 138–139
- Soejima and Noma design
 - pipet perfusion, 235
- Software
 - acquisitions, 131
 - COMO, 184
 - fast drug application, 221–222
 - graphing and analysis, 131
 - image analysis, 131
 - whole-cell patch-clamp studies, 181–185
- Solutions
 - calibration, 252
 - chloride intracellular, 159
 - cutting
 - brain slices, 136–139
 - fluorometric and electrophysiological recordings, 125–126
 - K-methylsulfate intracellular, 159
 - macropatch recording, 293
 - outside-out patch recordings, 75f
 - perforated patch clamp technique, 205–208
 - pipet perfusion, 237, 239, 241
 - recording
 - brain slices, 136–139
 - single-channel recording, 74
 - temperatures
 - brain slices, 150–151
- Sonicating
 - glass, 10
- Space clamp, 171–172
 - limitations, 62–63
- Steady-state inactivation curves, 56, 57f
- Steady-state IV curves, 53
- Strathclyde Electrophysiology Software, 90
- Sucrose cutting solutions
 - brain slices, 138–139, 150
- Suction line, 14
- Suppliers
 - fluorometric and electrophysiological recordings, 131
- Sylgard 184, 10, 18, 24–25, 73, 292
- T**
- Tail-current analysis, 57f
- Tang, Wang, Quandt, and Eisenberg design
 - pipet perfusion, 236
- TaqMan probe, 316, 324
- Tektronix analog storage oscilloscope, 185
- Test slides
 - supplier, 131
- Thermal properties
 - glasses, 3
 - pipet glass, 4
- Thin film
 - noise, 18
- Threshold-crossing method, 89–90
- Time-constant fitting

- (*cont.*) whole-cell patch clamp recordings, 56–58
- Time-course fitting method, 90
- Tissue chopper
 - vs.* vibrating microtome
 - cutting brain slices, 143–144
- Transistor-transistor logic (TTL), 122
- Transmittance
 - fluorometric and electrophysiological recordings, 115
- Triphenyltetrazolium chloride (TTC), 143
- TTC, 143
- TTL, 122
- Tubing
 - fast drug application, 220
- Two-electrode voltage-clamp
 - design
 - introduction, 36
- Two-photon microscopy, 121
- Two-round nested PCR
 - genomic DNA, 313f
- Two-round PCR
 - patch-clamp with RT-PCR, 304–306
- U**
- UltraClean PCR Clean-up Kit, 305
- Uncoated pipet
 - dielectric noise, 22
- Universal Image Corporation
 - website, 131
- V**
- VCR recorder, 38
- Vesicle patch clamp
 - perforated, 203–205
- Vibrating microtome
 - vs.* tissue chopper
 - cutting brain slices, 143–144
- Vibration artifacts, 224f
- Videomicroscopy
 - with DIC microscopy
 - development, 154
- Videotape, 88–89
- Visually guided whole-cell recordings, 182f
- Voltage-clamp, 171–172
 - analysis
 - perirhinal neurons, 180f
 - errors
 - whole-cell patch clamp recordings, 62–65
 - limitations, 63
 - rationale, 35–36
- W**
- Wavemetrics
 - website, 131
- WCR, 139
 - brain slices, 160f, 165–175
 - cell-resting membrane potential, 202f
 - pipet, 6
 - schematic diagram, 233f
- Websites, 131
- Whole-cell electrodes
 - elastomer coating, 7
 - firepolishing, 7–8
 - pulling, 6
- Whole-cell loose-patch voltage clamp, 276–278
 - estimating patch potential, 277–279
 - high-frequency patch-current component recovery, 279–283
 - low-frequency patch-current component recovery, 279
 - schematic, 278f
 - theory, 277
- Whole-cell patch clamp recordings, 35–66
 - aliasing, 45–46
 - cell capacitance, 47–49, 48f
 - configuration, 39–41
 - current component dissecting, 49–52

- data filtering, 43–44
- data presentation, 58–60
- data storage, 46
- electronic components, 38–39
- experimental procedure, 41–43
- I–V curves, 53–56
- leak/subtraction, 46–47
- pipet, 37
- principals, 35–36
- series resistance, 60–62
- setup, 40f
- signal sampling rate, 44–45
- special applications, 65–66
- time-constant fitting, 56–58
- voltage-clamp errors, 62–65
- Whole-cell patch-clamp studies
 - hardware, 181–185
 - software, 181–185
- Whole-cell patch pipet
 - dimple, 167f
 - Whole-cell patch technique, 36–37
- Whole-cell pipet
 - glass choice, 5–6
 - properties, 5–8
- Whole-cell recording (WCR), 139
 - brain slices, 160f, 165–175
 - cell-resting membrane potential, 202f
 - pipet, 6
 - schematic diagram, 233f
- Whole-cell voltage clamping
 - noise sources, 29–32
- X, Z
 - Xenopus* muscle cell
 - micrographs, 289f
 - Zeiss Axioskop, 154, 182
- Z-stage
 - fluorometric and electrophysiological recordings, 114